Spring 2022

Tailored Nanomaterials for Advancing Fast-Charge Research

Wessel van den Bergh

TAILORED NANOMATERIALS FOR ADVANCING FAST-CHARGE RESEARCH

by

Wessel van den Bergh

Bachelor of Science
Hope College, 2017

Submitted in Partial Fulfillment of the Requirements

For the Degree of Doctor of Philosophy in

Chemistry

College of Arts and Sciences

University of South Carolina

2022

Accepted by:

Morgan Stefik, Major Professor

Brian Benicewicz, Committee Member

Donna Chen, Committee Member

Ralph White, Committee Member

Tracey L. Weldon, Interim Vice Provost and Dean of the Graduate School

Abstract

The demand for fast, energy-dense storage has driven research into nanoscale intercalation materials. Nanoscale materials not only accelerate kinetics but also can modify reaction path thermodynamics, intercalant solubility, and diffusivity. Pioneering works have revealed such nanoscale changes, often without the need to separately probe each fundamental transport process. While electrodes can be designed to have one transport processes dominant, there remain opportunities to better understand energy-dense designs with multiple concomitant transport constraints. The contents herein highlight emerging an method using tailored, energy-dense nanomaterials and the process of elimination to clearly correlate architectural features to performance. For example, this method revealed the dependance of intercalation pseudocapacitive kinetics upon the intercalation length scale for multiple materials. In addition, this approach can isolate material-specific effects such as how amorphization modifies both insertion and diffusion kinetics for multiple materials exhibiting intercalation pseudocapacitance. A recently developed current-model deconvolves changes to surface-limited and diffusion-limited processes while at the same time revealing avenues to achieve markedly faster intercalation. Future directions are suggested including synthetic methods emphasizing tailored defects, characterization methods with minimal assumptions, and computer simulations that include diffusion with non-uniform concentrations.

Table of Contents

List of Tables

List of Figures

List of Schemes

List of Symbols

α	fit term for the MCT model
A	area
a	coefficient or lattice dimension for MCT model
β	convolved density term for MCT model
b	power-law term
C	fit parameter
δ	NMR shift
$Đ$	polymer mass dispersity
D	diffusivity or pore diameter
d	d-spacing or micelle to micelle spacing
f	volume fraction
γ	unit cell distortion for MCT model
I or i	current
i_p	peak current

j	imaginary number
k	wave number
k_1	capacitive contribution and/or surface impedance
k_2	diffusive contribution and/or diffusion impedance
L	thickness
m	mass
M_n	number average molecular weight
N	polymer chain length, analogous to repeat units
ϕ	porosity
ρ	*density*
R	resistance
r	template radius
S	micelle to micelle spacing, d-spacing ratio
t	time
t_{SLT}	sweep time at SLT
w	wall thickness
ν	voltage sweep rate

v_{SLT} voltage sweep rate at SLT

χ interaction parameter

x intercalation length or MT ratio

Z impedance

List of Abbreviations

ALD ..... atomic layer deposition

APS ..... Advanced Photon Source

CV ..... cyclic voltammetry

DFT ..... density functional theory

DI ..... de-ionized

DLT ..... diffusion-limited threshold

EDLC ..... electrochemical double layer capacitor

EIS ..... electrochemical impedance spectroscopy

EPR ..... electron paramagnetic resonance

EQ or EQN ..... equation

FTO ..... fluorine-doped tin oxide

GGA-PBE ..... generalized gradient approximation of Perdew-Burke-Ernzerhof

GI-WAXS ..... grazing incidence wide-angle x-ray scattering

GPC..... gel permeation chromatography

HR-TEM .....high resolution transmission electron microscopy

ICP-MS .....inductively coupled plasma mass spectrometry

IPA .....isopropyl alcohol

LCA.....linear combination analysis

LIBs.....lithium-ion batteries

LID.....layer integration via diffusion

MCT.....micelle core template model

M:T ..... material to template ratio

NMR ..... nuclear magnetic resonance

PAW..... projector augmented wave

PBA.....poly(butyl acrylate)

PEO ..... poly(ethylene oxide)

PHA..... poly(hexyl acrylate)

PMT .....persistent micelle template

PPO ..... poly(propylene oxide)

PS ..... polystyrene

RPM ..... revolutions per minute

RT ..... room temperature

SAXS ..... small-angle x-ray scattering

SCSC ..... South Carolina SAXS Collaborative

SEM ..... scanning electron microscopy

SLT ..... surface-limited threshold

TEM ..... transmission electron microscopy

TGA ..... thermal gravimetric analysis

THF ..... tetrahydrofuran

TTIP ..... titanium isopropoxide

WAXS ..... wide-angle X-ray scattering

XAFS or EXAFS ..... extended X-ray absorption fine structure

XPS ..... X-ray photoelectron spectroscopy

CHAPTER 1: Introduction

1.1 Overview

Consumer and ecological pressures have increased the demand for societal implementation of electrochemical energy storage. This rate of transition from mature technologies such as internal combustion engines to battery-based drivetrains in automobiles is unprecedented. The US Department of Energy predicts that annual sales of passenger electric vehicles will increase 10-fold (>50 million) in less than 20 years.[1] Correspondingly, new electrochemical materials research has been subject of intense work. One subset of this research direction has been the ambition to utilize nanoscale materials which not only accelerate diffusion and surface kinetics attributed to their shortened pathlengths and high surface-to-volume ratio but also exhibit non-trivial properties otherwise not observed in at larger length scales.[2] Research comparing nanoparticle size in relation to specific phenomena has been common method to observe structure-behavior. These studies have made qualitative observations such as a transition from plateaus to pseudolinear curves in galvanostatic profiles in multiple materials.[3–6] Underlying this observation, careful examinations of intercalation (i.e. lithiation) induced phases transitions has been found to depend on the particle size which dictates solubility limits of high and low intercalated (lithiated) phases in Li_xFePO_4, TiO_2 and $LiMn_2O_4$.[7–13] Linear relationships between particle size and solid-state diffusivity have been observed in many materials and has been typically attributed to stress gradient behavior.[14,15] Such investigations have developed mutualistic theoretical works providing new models and computational insights which propel understanding. From a series of seminal works including TiO_2(B), $LiCoO_2$, and T-Nb_2O_5, new phenomena such as intercalation pseudocapacitance have been categorized.[3,16–18] A design-dependent behavior which

exhibits kinetics dominated by surface-limitations, yet the mechanism is a diffusive ion insertion process yielding faradaic charge storage. This combination of high-power and high-energy capabilities makes intercalation pseudocapacitance and its accompanying materials design research a compelling avenue to meeting EU and US energy storage targets and has had its own influx of research using particle size, defect chemistry, and computational methods to gain a mechanistic understanding. Parallel to these, are preparations of "pseudocapacitors" which exploit abovementioned size-dependent suppression of phase transitions, high-surface area morphologies, and short diffusion paths to report high energy-densities and rate-capabilities. However, in either mechanistic studies or performance-centric works, the experimental conditions are such that the active material is cradled in additives which eliminate concerns for limiting contributions of concomitant processes yet subject to their own complications.[19,20] Furthermore, nanomaterials synthesis beyond particles, able to independently tune specific architectural features has been lacking and limiting quantitative understanding of structure-behavior relationships.

Energy storage via electrochemical intercalation, including pseudocapacitive behavior, depends on multiple diffusion and surface processes which when carefully balanced in investigations provide the closest analogue to applied devices.[2] Nanomaterials synthesis, with the exception of nanoparticles, has lacked a design philosophy of tunable and systematic architectures. Rather, methods report a plethora of synthetic procedures accompanied by a comparable number of descriptive morphologies. Yet this lack in systemic design prevents comparison between nanomaterials and how changes in specific architectural features affect observed performance therefor no relationship between structure and behavior can be made. This gap can only be rectified by single-parameter

changes to a material nanostructure for proper comparison as accompanying electrochemical analysis cannot compensate as exemplified by four popular techniques: 1) cyclic voltammetry may use a power-dependent relationship[21] between current response and voltage sweep rate to indicate whether the electrochemical kinetics are surface-limited ($i = av^b$, $b = 1.0$), diffusion-limited ($i = av^b$, $b = 0.5$, semi-infinite diffusion), or a convolution of the two. However, such a relationship is unable to describe the specific, influential diffusive process. 2) Impedance spectroscopy (EIS) can interpret an electrochemical response using representative electrical circuits. Though similarly quantitative, the data can be interpreted by multiple circuits whose individual components and what they represent are subject to conflicting claims. 3) Extensions of EIS methods such as 3D-Bode analysis[22,23] does provide metrics which are open descriptors which can be used to compare rate constants and onsets of diffusion-limited behavior yet must depend on a basis of systematic comparison that is the previously stated gap. 4) Physiochemical models[24–26] stand as a computational alternative to experimental ambiguity yet is met with its own challenges, simple geometries require a computational cluster, numerous known values, and its own set of assumptions for an unambiguous answer as to which processes contribute to what degree with regards to a materials surface-limited rate capability. Each of these methods *with* a systematic series of nanomaterials made from controlled adjustments to architectural features can provide profound and unambiguous insights into structure behavior relationships as this review will demonstrate. Furthermore, a lack of systematic materials design has manifested in a misattribution to the categorization of pseudocapacitance as it relates to material properties.[27–31] Works which attribute intercalation pseudocapacitance as an intrinsic property to the material,[28] this is often done

with T-Nb_2O_5, which is not subject to lithiation induced phase transitions of typical battery material (Anatase TiO_2, Li_xFePO_4, Li_xCoO_2), has low volumetric changes upon lithiation, and exhibits high solid-state diffusivity. Despite these advantages T-Nb_2O_5 has, it cannot be intrinsically surface-limited when prepared as particles whose length scale cause diffusion processes to dominate! As will be shown in the following chapters, intercalation pseudocapacitance is explicitly a phenomenon which a material can exhibit and is ultimately dependent upon its architecture and preparation conditions.

Persistent micelle templates (PMTs)[14,32–40] stand as a method which tuned intercalation material features have allowed electrochemical analysis to elucidate relationships between those features and resultant pseudocapacitive response and provide a platform for new perspectives and understanding. Prepared from block polymer templates under solution conditions which induce micellization and effectively freeze the kinetics of chain exchange and subsequently templates size, a series of tuned nanomaterials can be assembled by varying ratios of precursor material and template. This inhibition of shifting template size during preparation and tailored material-to-template (M:T) ratio what has enabled a divergence from other methodologies to quantitatively investigate design-behavior relationships. In Chapter 2, it will be demonstrated how a series of porous T-Nb_2O_5 architectures with varied wall and constant pore sizes whose subsequent CV kinetic analysis found an unambiguous length scale dependency between wall size (intercalation length) and loss of intercalation pseudocapacitive response.[38] In chapters 3 and 4 there will be examples of recent works which, with the same use of PMTs, have been able to disambiguate the contributions of amorphization to material performance from coinciding structural effects for multiple materials.[39,40] In addition, in chapter 4 itwill be highlighted

how PMTs provided a platform to demonstrate a revised perspective on how individual capacitive and diffusive contributions to current is calculated and whose modelling better matches experimental observations.[39] In consideration of future perspectives, chapter 6 will discuss how systematic nanomaterials approaches can utilize advances in electrochemical analysis and compliment current computational research to ease assumptions and verify predictions.

1.2 References

[1] National Blueprint for Lithium Batteries 2021-2030, Department of Energy, **2021**.

[2] C. Zhu, R. E. Usiskin, Y. Yu, J. Maier, *Science* **2017**, *358*.

[3] M. Okubo, E. Hosono, J. Kim, M. Enomoto, N. Kojima, T. Kudo, H. Zhou, I. Honma, *J. Am. Chem. Soc.* **2007**, *129*, 7444.

[4] A. V. der Ven, M. Wagemaker, *Electrochemistry Communications* **2009**, *4*, 881.

[5] J. W. Kang, D. H. Kim, V. Mathew, J. S. Lim, J. H. Gim, J. Kim, *J. Electrochem. Soc.* **2010**, *158*, A59.

[6] R. Wang, J. Lang, Y. Liu, Z. Lin, X. Yan, *NPG Asia Mater* **2015**, *7*, e183.

[7] M. Okubo, Y. Mizuno, H. Yamada, J. Kim, E. Hosono, H. Zhou, T. Kudo, I. Honma, *ACS Nano* **2010**, *4*, 741.

[8] M. Wagemaker, *Structure and dynamics of lithium in anatase TiO2: study of interstitial Li-ion intercalation in anatase TiO2 at the atomic level*, Delft Univ. Press, Delft, **2003**.

[9] M. Wagemaker, F. M. Mulder, *Acc. Chem. Res.* **2013**, *46*, 1206.

[10] M. Wagemaker, R. van de Krol, A. P. M. Kentgens, A. A. van Well, F. M. Mulder, *J. Am. Chem. Soc.* **2001**, *123*, 11454.

[11] M. Wagemaker, D. P. Singh, W. J. H. Borghols, U. Lafont, L. Haverkate, V. K. Peterson, F. M. Mulder, *J. Am. Chem. Soc.* **2011**, *133*, 10222.

[12] M. Wagemaker, W. J. H. Borghols, F. M. Mulder, *J. Am. Chem. Soc.* **2007**, *129*, 4323.

[13] A. Yamada, H. Koizumi, S. Nishimura, N. Sonoyama, R. Kanno, M. Yonemura, T. Nakamura, Y. Kobayashi, *Nature Mater* **2006**, *5*, 357.

[14] K. A. Lantz, N. B. Clamp, W. van den Bergh, A. Sarkar, M. Stefik, *Small* **2019**, *15*, 1900393.

[15] Y. Choi, S. Pyun, *Solid State Ionics* **1997**, *99*, 173.

[16] K. Brezesinski, J. Wang, J. Haetge, C. Reitz, S. O. Steinmueller, S. H. Tolbert, B. M. Smarsly, B. Dunn, T. Brezesinski, *J. Am. Chem. Soc.* **2010**, *132*, 6982.

[17] T. Brezesinski, J. Wang, S. H. Tolbert, B. Dunn, *Nature Materials* **2010**, *9*, 146.

[18] M. Zukalová, M. Kalbáč, L. Kavan, I. Exnar, M. Graetzel, *Chem. Mater.* **2005**, *17*, 1248.

[19] T. Marks, S. Trussler, A. J. Smith, D. Xiong, J. R. Dahn, *J. Electrochem. Soc.* **2011**, *158*, A51.

[20] V. Murray, D. S. Hall, J. R. Dahn, *J. Electrochem. Soc.* **2019**, *166*, A329.

[21] H. Lindström, S. Södergren, A. Solbrand, H. Rensmo, J. Hjelm, A. Hagfeldt, S.-E. Lindquist, *J. Phys. Chem. B* **1997**, *101*, 7717.

[22] J. S. Ko, M. B. Sassin, D. R. Rolison, J. W. Long, *Electrochimica Acta* **2018**, *275*, 225.

[23] J. S. Ko, C.-H. Lai, J. W. Long, D. R. Rolison, B. Dunn, J. Nelson Weker, *ACS Appl. Mater. Interfaces* **2020**, *12*, 14071.

[24] B.-A. Mei, L. Pilon, *Electrochim. Acta* **2017**, *255*, 168.

[25] B.-A. Mei, J. Lau, T. Lin, S. H. Tolbert, B. S. Dunn, L. Pilon, *J. Phys. Chem. C* **2018**, *122*, 24499.

[26] B.-A. Mei, O. Munteshari, J. Lau, B. Dunn, L. Pilon, *J. Phys. Chem. C* **2018**, *122*, 194.

[27] V. Augustyn, P. Simon, B. Dunn, *Energy Environ. Sci.* **2014**, *7*, 1597.

[28] J. Come, V. Augustyn, J. W. Kim, P. Rozier, P.-L. Taberna, P. Gogotsi, J. W. Long, B. Dunn, P. Simon, *J. Electrochem. Soc.* **2014**, *161*, A718.

[29] S. Fleischmann, J. B. Mitchell, R. Wang, C. Zhan, D. Jiang, V. Presser, V. Augustyn, *Chem. Rev.* **2020**, *120*, 6738.

[30] C. Costentin, J.-M. Savéant, *Chemical Science* **2019**, *10*, 5656.

[31] C. Costentin, T. R. Porter, J.-M. Savéant, *ACS Appl. Mater. Interfaces* **2017**, *9*, 8649.

[32] H. N. Lokupitiya, A. Jones, B. Reid, S. Guldin, M. Stefik, *Chem. Mater.* **2016**, *28*, 1653.

[33] A. Sarkar, M. Stefik, *J. Mater. Chem. A* **2017**, *5*, 11840.

[34] E. R. Williams, P. L. McMahon, J. E. Reynolds, J. L. Snider, V. Stavila, M. D. Allendorf, M. Stefik, *Mater. Adv.* **2021**, 10.1039.D1MA00146A.

[35] K. A. Lantz, A. Sarkar, K. C. Littrell, T. Li, K. Hong, M. Stefik, *Macromolecules* **2018**, *51*, 6967.

[36] H. N. Lokupitiya, M. Stefik, *Nanoscale* **2017**, *9*, 1393.

[37] W. van den Bergh, E. R. Williams, N. A. Vest, P.-H. Chiang, M. Stefik, *Langmuir* **2021**.

[38] W. van den Bergh, H. N. Lokupitiya, N. A. Vest, B. Reid, S. Guldin, M. Stefik, *Adv. Funct. Mater.* **2021**, *31*, 2007826.

[39] W. van den Bergh, S. Wechsler, H. N. Lokupitiya, L. Jarocha, S. Heald, M. Stefik, *Accepted,* **2021**.

[40] W. van den Bergh, T. Larison, M. J. Fornerod, S. Guldin, M. Stefik, *In Review* **2021**.

CHAPTER 2: Nanostructure Dependence of T-Nb_2O_5 Intercalation Pseudocapacitance Probed using Tunable Isomorphic Architectures[1]

---

[1]van den Bergh, W.; Lokupitiya, H.; Vest, N.; Reid, B.; Guldin, S.; Stefik, M. *Advanced Functional Materials*, 2021, 31, 2007826

2.1 Abstract

Intercalation pseudocapacitance has emerged as a promising energy storage mechanism that combines the energy density of intercalation materials with the power density of capacitors. Niobium pentoxide was the first material described as exhibiting intercalation pseudocapacitance. The electrochemical kinetics for charging/discharging this material are surface-limited for a wide-range of conditions despite intercalation via diffusion. Investigations of niobium pentoxide nanostructures are diverse and numerous; however, none have yet compared performance while adjusting a single architectural parameter at a time. Such a comparative approach reduces the reliance upon models and the associated assumptions when seeking nanostructure-property relationships. Here we examine a tailored isomorphic series of niobium pentoxide nanostructures with constant pore size and precision tailored wall thickness. The sweep rate at which niobium pentoxide transitions from being surface-limited to being diffusion-limited is shown to depend sensitively upon the nanoscale dimensions of the niobium pentoxide architecture. Subsequent experiments probing the independent effects of electrolyte concentration and film thickness unambiguously identify solid state lithium diffusion as the dominant diffusion constraint even in samples with just 48.5-67.0 nm thick walls. The resulting architectural dependencies from this type of investigation are critical to enable energy-dense nanostructures that are tailored to deliver a specific power density.

2.2 Introduction

Electrical energy storage materials with high power density and high energy density are in demand for applications spanning from fast-charging mobile electronics and electric

vehicles to fast-discharge emergency actuators. Each of these examples benefits from high power density. Electric double layer capacitors (EDLCs) and lithium ion batteries (LIBs) do not yet meet the demand for simultaneous energy and power densities. EDLCs' operate based upon surface electrostatic absorption, a rapid short-range mechanism that provides high power density (5-10 kW kg^{-1}) and durability (10^4-10^6 cycles), albeit with relatively low energy density.[1,2] In contrast, batteries are based upon faradaic reactions via intercalation or conversion reactions, providing high energy densities (160 mAh g^{-1} for $Li(Ni_{1/3}Co_{1/3}Mn_{1/3})O_2$).[3] For such batteries, the power density is generally limited by sluggish solid state diffusion, resulting in low power densities.

Pseudocapacitance, in contrast, combines a faradaic charge storage mechanism with rapid surface-limited kinetics, enabling high energy density and high power density simultaneously. Early pseudocapacitors, such as RuO_2[4], relied on reversible surface redox reactions that were highly dependent upon the surface architecture. Recently, a new behavior termed intercalation pseudocapacitance was reported where these surface-limited faradaic reactions extend through the volume of material.[5] T-Nb_2O_5 was the first material identified as exhibiting intercalation pseudocapacitance, which was attributed to the lack of a crystallographic phase change combined with its relatively fast solid state diffusion of lithium. In this example, T-Nb_2O_5 combined a capacity 130 mAh g^{-1} with a high power rate of 10C, corresponding to a 6-minute charge/discharge time. There remains a need to achieve such high rates within device architectures that have a significant weight and volume fraction of active material,[6–12] a task that requires knowledge of nanostructure-performance relationships to carefully balance multiple transport processes.

All electrochemical reactions, including intercalation pseudocapacitance, rely upon the concomitant transport of electrons, the transport of ions, and the interconversion between reduced and oxidized states. With lithiation of T-Nb_2O_5 the steps include a surface step where the lithium traverses between electrolyte and T-Nb_2O_5 and also include three diffusion steps: ion transport through the electrolyte, electron transport through the electrode, and lithium intercalation through T-Nb_2O_5 (Scheme 2.1). It follows that the electrochemical response will depend upon the relative rates of each of these steps, all of which are influenced by the way the material is organized in space, *i.e.* the nanoscale architecture.[13–19] A wide range of T-Nb_2O_5 nanoscale architectures[20,21] have been investigated to date with most demonstrations including remarkable charge/discharge rates. Materials architectures investigated to-date include nanoparticles,[8,22–25] nanotubes,[12,26,27]nanofibers,[28] nanorods,[29,30] nanowires,[6,31] nanosheets,[9,10,32–37] nanocomposites,[38–44] and related nanostructures.[7,37,45–54] Only few of the above works attempted a rational performance comparison of different nanostructures.[23,52–54] These studies relied on either the simultaneous variation of multiple spatial parameters or were based on single parameter architectures, thus obfuscating the study of nanostructure-property relationships. Prior works on T-Nb_2O_5 have also included theoretical studies,[55] comparisons of different crystallographic phases,[36,53,56] and correlated the high diffusion coefficient of Li in T-Nb_2O_5 with its crystallographic features.[8,57,58] In contrast to recent reports of rapid lithium intercalation into nanostructured T-Nb_2O_5, the first investigation of this system by Bard *et al* in 1981 without deliberate nanoscale porosity resulted in a sluggish electrochemical response, requiring 24 hrs for lithium intercalation to

complete.[59] This body of works demonstrates that one should reasonably expect the electrochemical kinetics of T-Nb_2O_5 to depend upon the dimensions of the architectural features albeit without yet clear correlations to specific architectural features.

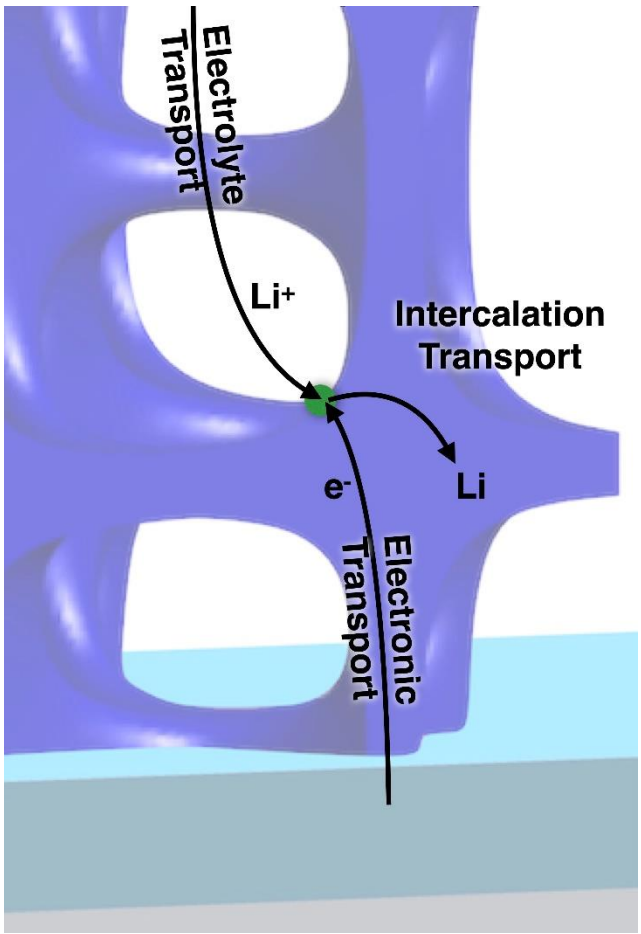

Scheme 2.1. The charging/discharging process involves three concomitant transport processes, including lithium intercalation into the wall thickness, ion transport through the electrolyte, and electron transport through the electrode. Ion insertion from the electrolyte to the electrode occurs at the interface. The rate-limiting step(s) could include any of the transport processes, which are diffusive in nature, or the insertion process which is surface limited. Each of these effects can be deconvolved using an architectural approach with minimal electrochemical modeling.

A novel nanomaterial synthesis approach termed persistent micelle templates (PMT) was recently developed to produce materials with tailored series of isomorphic architectures with nanoscale pores.[60–64] Here, block polymers form micelles that serve as templates for material precursors. Subsequent thermal processing converts the precursors to crystalline materials while the removal of the polymer produces a well-defined porosity. Conventional approaches involving micelle templates typically exhibit a dependence of the micelle size on the amount of material precursor, convolving alterations to both the pore size and wall thickness simultaneously. In contrast, PMT relies upon kinetic-control of the template size where variation of the amount of material precursors results in monotonic variation of the wall thickness alone. Thus, PMT enables the synthesis of sample series with constant pore size and tailored wall thickness. Furthermore, since the spherical micelles are kinetically trapped, the resulting series is isomorphic owing to simple sphere packing. The use of an isomorphic series, with constant morphology eliminates tortuosity changes[15,65–71] that come with transitions to cylindrical, lamellar, and other bulk block polymer morphologies.[72] In this work we investigate the electrochemical kinetics within a tailored and systematic series of niobium pentoxide nanostructures. We show that the transition of niobium pentoxide from surface limited kinetics towards diffusion limited kinetics is controlled by the underlying nanoscale architecture. The methodology described herein relaxes the dependence upon models and enables the evaluation of the rate-sensitivity of each diffusion process.

2.3 Results and Discussion

The effect of specific feature dimensions on the capability of material to exhibit rapid intercalation pseudocapacitance remains challenging to identify. Understanding these nanostructure dependencies would enable designer nanomaterials where each architectural feature is deliberately tailored to meet the specific power and energy requirements. A general challenge when probing devices with electrochemical analytical methods is ambiguity in identifying the specific diffusion process that corresponds to a rate-dependent response, particularly when multiple diffusive processes have similar rates as is typical for the sake of high energy density. This challenge will now be elaborated in the contexts of four popular analytical approaches. For cyclic voltammetry (CV), the current response, I, varies with a power-dependence of voltage sweep rate, v, where devices are either surface-limited ($I \propto v$), semi-infinite diffusion-limited ($I \propto v^{0.5}$), or a convolution thereof.[73] Although this approach can identify transitions between these regimes, it cannot alone determine the underlying diffusive process. Likewise, impedance spectroscopy data are often interpreted using equivalent circuits where a set of resistors, capacitors, diffusion elements, and other circuit elements represent the electrochemical system. Though quantitative and informative, a significant drawback is that the resulting Nyquist plots are often equally well fitted by multiple equivalent circuits. Even after selecting a circuit model, Nyquist interpretation is often ambiguous as to which of the fitted values correspond to each underlying process.[74–84] Furthermore, equivalent circuits neglect non-uniform ion/electron concentrations throughout the electrode and electrolyte.[80–84] An alternative approach using physicochemical models can numerically address non-uniform

concentration gradients, enabling unequivocal interpretations of EDLC[84,85] and pseudocapacitive materials[83,86] from cyclic voltammetry and impedance spectroscopy, albeit one needs to already have a large number of known parameters. Physicochemical models are also challenging to apply to realistic architectures since even simple 3D geometries required a computational cluster for the calculations.[85] Another analysis method based on 3D Bode plots was recently applied to T-Nb_2O_5 to identify rate constants and diffusion limitations.[87] This study noted that there was either a semi-infinite diffusion limitation of lithium intercalating into the Nb_2O_5 lattice or a diffusion limitation of electrolyte ions reaching the electrode-electrolyte interface. However, the applied analytical technique was unable to distinguish between these two possibilities. The above studies highlight the general deconvolution challenge for all of the above electrochemical analyses. Here we describe the use of a simple approach that resolves this ambiguity by using a series of nanoscale architectures where a single spatial variable is altered at a time to clearly isolate cause and effect.

Persistent micelle templates were used to prepare a tailored set of porous T-Nb_2O_5 samples. The use of custom block polymers and carefully controlled solution conditions enables the self-assembly of micelle templates under kinetic-control where chain exchange between micelles is suppressed and the resulting materials thus have a constant pore size distribution.[62] Electron micrographs of representative samples are shown in **Figure 2.1** as a function of the ratio of final material mass relative to the micelle template (M:T ratio). Visible in these images is the relatively constant pore size of 109 nm and increasing wall thickness from 48.5 to 67.0 nm corresponding to the increasing M:T ratio. These

statistically significant SEM metrics from **Figure 2.2** are summarized in **Table 2.1**. The SEM images also reveal the dominant short-range ordering, consistent with randomly packed spheres. The electron micrographs (**Figure A.1**) also clearly revealed that the porosity had an open and interconnected network with at least 4 layers of pores apparent from the top view. Such solution processed films typically exhibit compression in the out-of-plane direction since the heat treatments induce contraction.[62,88,89] Thus these films are expected to exhibit ~5 pores across the film thickness based upon cross-sectional SEM of similar samples.[62] Small-angle X-ray scattering (SAXS) of these samples generally had a primary observed peak with a secondary shoulder having an approximate q-ratio of 1:2, also consistent with randomly packed spheres.[90] The main SAXS peak shifts to lower q-spacing as the M:T ratio increases (**Figure 2.3**), consistent with the expected lattice expansion predicted by the previously established paracrystalline micelle core template (MCT) model (**Equations A.1-A.3, Table A.2)**.[61,63] The corresponding shifting d-spacings are shown in Table 2.1. The resulting best-fit also closely matched the SEM values for wall thickness with a goodness of fit R^2=0.95 (Figure 2.2a). The GIWAXS measurements confirmed all the Nb_2O_5 samples to be crystalline and consistent with the orthorhombic crystal structure (PDF No. 01-071-0336) of T-Nb_2O_5 (**Figure 2.4**). Scherrer analysis of these diffractograms indicated all samples had a nominal crystallite size of ~12 nm (see Table 2.1). Thus a tailored series of isomorphic T-Nb_2O_5 architectures were prepared for electrochemical investigation.

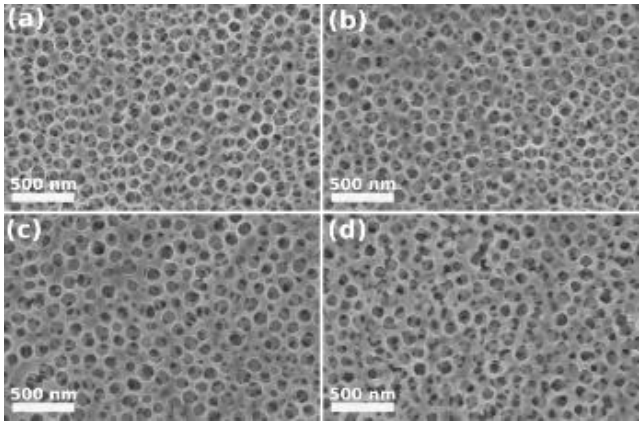

Figure 2.1. SEM images of isomorphic series of porous samples prepared with persistent micelle templates using different Material:Template ratios: MT1.2 (a), MT1.8 (b), MT2.4 (c), MT3.0 (d).

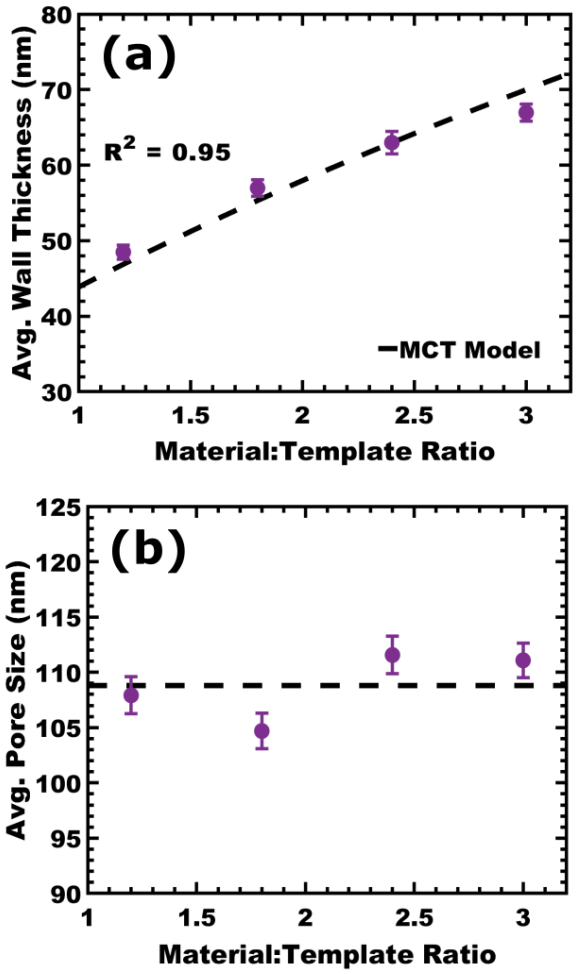

Figure 2.2. Wall thickness (a) and pore size (b) statistics were measured from SEM images as a function of the Material:Template ratio. The dashed line in (a) corresponds the best fit of the MCT model. The dashed line in (b) is the overall average of the pore diameter. The error bars correspond to the standard-error-of-the-mean.

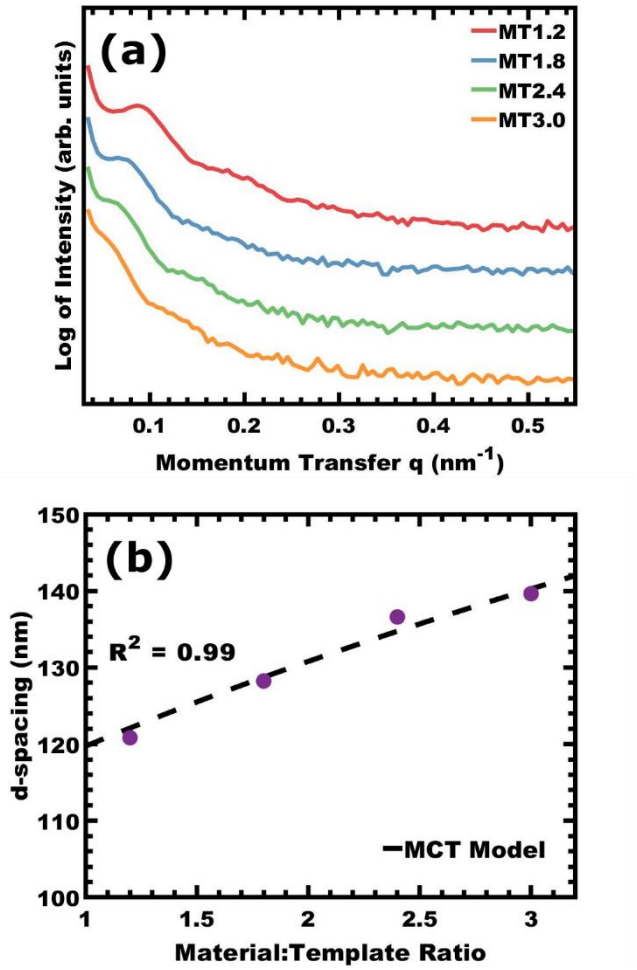

Figure 2.3. Representative SAXS data to characterize the average nanostructure for each sample in the series (a). Data are offset vertically for clarity. The trends in SAXS peak position (d-spacing=2π/q) as a function of the Material:Template ratio were well fitted by the MCT model (b).

Table 2.1. Statistical measures from the isomorphic sample series including average values and the associated error as well as the dimension distributions of each architectural feature.

Condition Name	Material-to-template ratio [M:T]	Average Pore Size [nm][a]	Pore Size Stdev. [nm][b]	Average Wall Thickness [nm][a]	Wall Thickness Stdev. [nm]	Crystallite Size [nm][c]	SAXS d-spacing [nm]	Porosity [vol%] [d]
MT1.2	1.2	107.9 ± 1.7	23.8	48.5 ± 1.0	9.2	12.8	121.5	60%
MT1.8	1.8	104.7 ± 1.6	22.9	57.0 ± 1.1	10.0	12.7	129.5	47%
MT2.4	2.4	111.6 ± 1.7	24.1	63.0 ± 1.5	12.8	12.1	135.2	27%
MT3.0	3.0	111.0 ± 1.6	22.1	67.0 ± 1.1	10.2	11.7	139.6	10%

[a)] The average values are reported ± the standard-error-of-the-mean (standard deviation divided by the square root of the number of measurements) to indicate the error of the mean value; [b)] The standard deviation reflects the distribution width of the measured dimensions; [c)] Crystallite size was determined using Scherrer analysis of the (001) peak; [d)] Volume fractions of pores calculated from eqn. A.4.

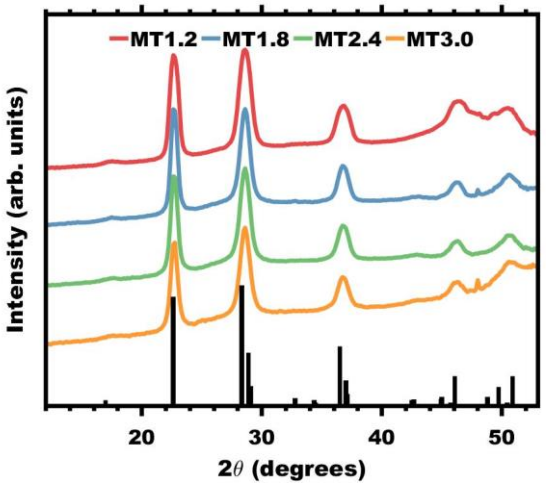

Figure 2.4. GI-WAXS data characterize the inorganic crystal structure for each sample condition in the series. The reference pattern corresponds to T-Nb_2O_5 (PDF No. 01-071-0336). Data were offset vertically for clarity. The peak at 47.3º (MT1.2, MT 1.8, and MT3.0) corresponds to the (220) peak of the Si substrate.

The electrochemical behavior of each sample was investigated using CV over a range of voltage sweep rates. All samples exhibited qualitatively similar CV curves from 2.0 to 1,000 mV s^{-1}. We will first describe the CV characteristics for sample MT1.2 before making comparisons across various sample architectures. The CV curves of MT1.2 (**Figure 2.5**) exhibit a box-like shape that is characteristic of pseudocapacitance, having broad peaks with narrow separation between the anodic and cathodic peaks. For example, the 2 mV s^{-1} sweep had an anodic peak at 1.826 ± 0.003 V vs Li/Li^+ with the corresponding cathodic peak at 1.811 ± 0.001 V vs Li/Li^+ in addition to a second broad cathodic peak at 1.559 ± 0.004 V vs Li/Li^+ as expected for nanoscale T-Nb_2O_5.[8,32] Please note that the correspondence of these peaks to specific events remains an open topic of investigation outside the scope of this manuscript.[55–57] Faster sweep rates increased the peak separation gradually from 16.3 ± 4.0 mV at 2 mV s^{-1} to 627.9± 22.0 mV at 200 mV s^{-1}, particularly

apparent CVs with normalized current (Figure 2.5b). Sweep rates exceeding 100 mV s^{-1} exhibited sufficient cathodic shift for the cathodic peak to be non-visible within the voltage window. The trends in anodic peak position are shown for all sweep rates in **Figure A.2**. All sample conditions, with wall thickness from 48.5 ± 1.0 to 67.0 ± 1.1 nm were measured by CV. Selected sweep rates are shown in **Figure 2.6** comparing the sample conditions with these different wall thicknesses. The CV trends reveal monotonically increasing peak separation with wall thickness (increasing M:T ratio) and is suggestive of an increasing diffusion limitation, *vide infra* (Figure 2.5b and Figure 2.2). This isomorphic series also exhibited a corresponding trend where the samples with lowest M:T ratio sustained faster sweep rates before lithiation capacity decreases (**Figure A.3**). The nominal capacities averaged 364.8 ± 7.7 C g^{-1} Nb_2O_5. While all samples exhibited pseudocapacitive behavior, further inquiry was needed to explain the performance differences.

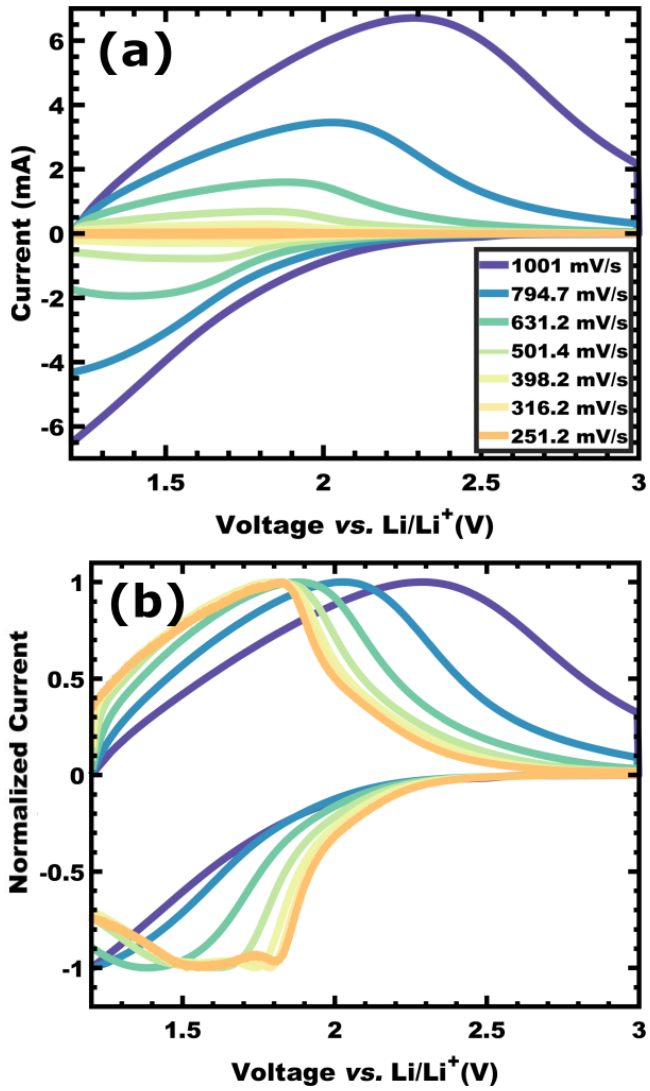

Figure 2.5. Cyclic voltammetry data from sample MT1.2 showing with logarithmically spaced sweep rates ranging from 250-1,000 mV s^{-1} (a). Normalization of this data (b) clarifies the corresponding peak shifts.

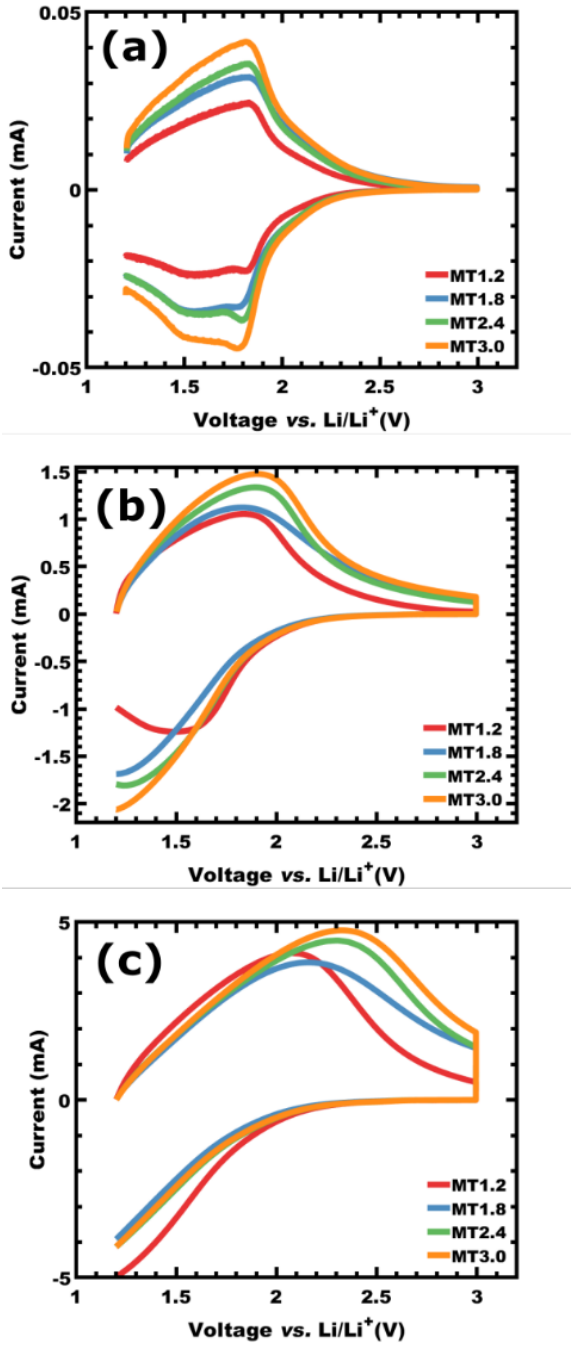

Figure 2.6. Comparison of cyclic voltammograms for the sample series at sweep rates of 2 mV s^{-1} (a), 100 mV s^{-1} (b), and 500 mV s^{-1} (c).

The type of rate governing process was assessed using the rate-dependence of the CV responses. The rate governing step was determined using the previously described power-law relation. Here the rate dependence of the peak current is:

$$I = v^b \tag{2.1}$$

where I is the current, v is the sweep rate, and b corresponds to a power law relationship.[91] Surface-limited processes such as capacitance exhibit a current that is directly proportional to the sweep rate (b=1). In contrast, diffusion-limited processes (semi-infinite) exhibit a current response that is proportional to the square root of sweep rate (b=0.5). The anodic peak current as a function of sweep rate is shown in **Figure 2.7a** on a log-log scale where the local slope corresponds to the b-value at each sweep rate. The derivative of this graph is thus the rate-dependent b-value that identifies transitions in the type of rate governing process (**Figure 2.7b**). For example, sample MT1.2 maintains b>0.9 from 2-100 mV s^{-1}, consistent with a surface-limited process. Further increasing the sweep rate leads to monotonic decline of the b-value, reaching b=0.64 ± 0.004 at 1,000 mV s^{-1}, consistent with a transition towards a semi-infinite diffusion-limited process. Again, we note that b-values non-proximal to 1.0 or 0.5 are ambiguous to interpret, *i.e*. a convolution of multiple rate-limiting processes, and thus limit the discussion to the transition points of b=0.9 and b=0.6. These values then indicate the thresholds for the maximum v for a surface-limited response (b>0.9) as well as the minimum v for a semi-infinite diffusion-limited response. We term these two conditions as the Surface-Limited Threshold (SLT) and the Diffusion-Limited Threshold (DLT). We note that all samples, when measured at sweep rates maintaining b>0.9, exhibited greater than 95% relative lithiation capacity with respect to that measured

at the slowest sweep rate of 2 mV s^{-1}. Thus, the SLT for any sample serves as a proxy for the onset of capacity loss, *i.e.* "rate-sensitivity." The trends between samples with different wall thicknesses (Figure 2.7b) show that conditions with higher M:T ratios are increasingly rate-sensitive (**Table 2.2**). For example, sample condition MT1.2 had a SLT of v=114.60 ± 0.48 mV s^{-1} whereas MT3.0 had a SLT of v=37.77 ± 0.27 mV s^{-1}; that is a factor of 3 change in SLT despite just an 18.5 nm change in wall thickness. This trend, however, is consistent with two possible interpretations: either 1) the diffusive lithium intercalation is rate-limiting, or 2) the ion transport in the electrolyte is rate-limiting since the pore volume fraction decreases as the M:T ratio increases (**Scheme 2.1**). With any porous system, two independent degrees of freedom exist: e.g. pore size and wall thickness, where their adjustment results in variation of other dependent descriptors such as the volume fraction of pores and the volume fraction of material. This ambiguity is next addressed with additional single-variable experiments.

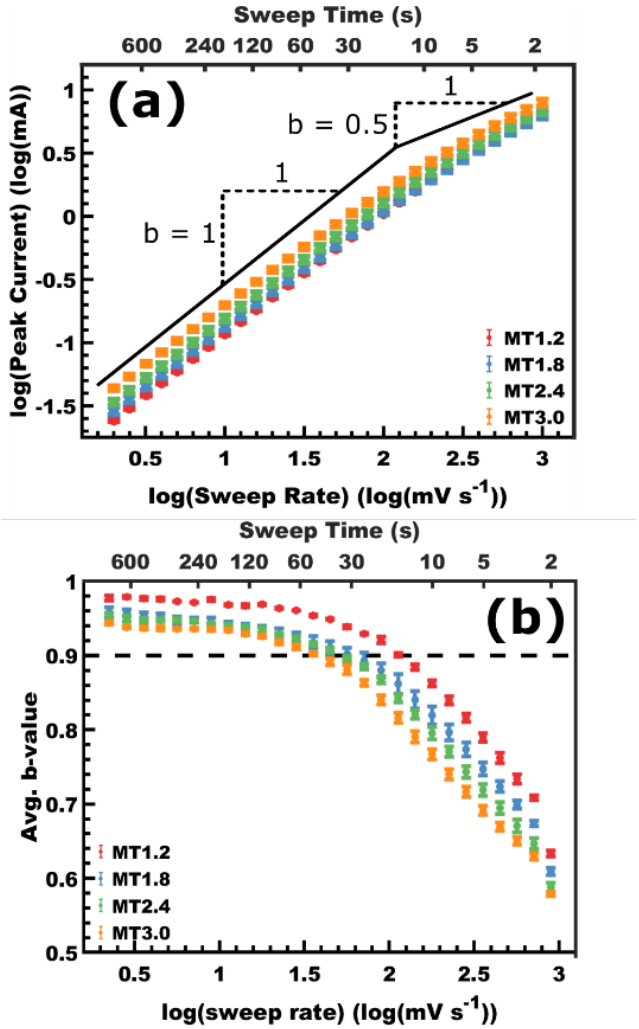

Figure 2.7. Rate-limiting step analysis was based upon the power-relationship between peak current and sweep rate. A log-log plot of the anodic peak current vs sweep rate for each sample condition is presented with characteristic slopes of 1.0 (surface limited) and 0.5 (diffusion limited) indicated (a). The derivative of panel a is termed the b-value and is plotted in panel b. The dashed line at *b*=0.9 represents the Surface-Limited Threshold. Error bars correspond to the standard-error-of-the-mean.

Table 2.2. Statistical measures of average film thickness as a function of spin-coating speed.

Condition Name	**Spin-coating speed [rpm]**	**Film thickness [nm][a]**	**Sweep rate @ b = 0.9 [mV s^{-1}][b]**	**Sweep time [s][c]**	**Sweep rate @ b = 0.6 [mV s^{-1}][b]**	**Sweep time @b=0.6 [s][c]**
MT1.2	1,000	80.4 ± 2.2	114.60 ± 0.48	15.70 ± 0.07	993.69 ± 38.63[4]	1.81 ± 0.07
MT1.2 (Thick)	400	91.0 ± 1.7	75.12 ± 0.22	23.93 ± 0.07	927.83 ± 28.10	1.94 ± 0.06
MT1.8	1,500	78.6 ± 2.7	59.48 ± 0.30	30.26 ± 0.15	926.73 ± 30.95[4]	1.94 ± 0.06
MT2.4	2,000	66.7 ± 1.4	52.13 ± 0.39	34.53 ± 0.26	856.71 ± 25.20	2.10 ± 0.06
MT3.0	2,150	65.2 ± 2.6	37.77 ± 0.27	47.66 ± 0.34	814.59 ± 26.23	2.21 ±0.07
MT3.0 (Thick)	400	163.0 ± 4.9	24.02 ± 0.25	74.95 ± 0.77	714.77 ± 10.84	2.52 ± 0.04

[a)]Average film thickness values are reported ± the standard-error-of-the-mean; [b)]Sweep rate values were linearly interpolated between nearest experimental values in the lin-log coordinate space of Figure 2.8b. Sweep rate values are reported ± the bounding limits for error propagation based on Rolle's Theorem; [c)]Sweep times were calculated as the voltage window divided by the sweep rate. Sweep time values are reported ± the error propagated from the sweep rate.

As depicted in **Scheme 2.1**, there are three diffusion-based processes: ion transport by the electrolyte through the pores, electron transport along the walls, and lithium intercalation into the walls. The sensitivity towards the first two processes was probed by altering the electrolyte concentration and film thickness respectively. The next set of experiments repeated the same rate-dependent CV analysis with a 50% reduced electrolyte concentration of 0.5 M (**Figure 2.8**). The rate-dependence of the b-values are nearly identical for 1 M and 0.5 M measurements for both samples MT1.2 and MT3.0, only having minor variations within the error of the calculations. Thus, it can be concluded that the diffusion-limited process observed above is not associated with the electrolyte. Please note that all sample comparisons made above used porous T-Nb_2O_5 films with comparable thickness (Table 2.2). Next the performance dependence upon film thickness was examined. Here, increasing the film thickness will increase both the average electrolyte path length as well as the average electron path length (Scheme 2.1). Having excluded sensitivity of these samples towards electrolyte resistance, differences found herein can be attributed to electron transport alone. Slower spin coating speeds were thus used to prepare thicker analogs of the films presented above (Table 2.2). For condition MT1.2, increasing the film thickness by 13.2% caused the SLT to decrease by 34.4% to v=75.12 ± 0.22 mV s^{-1} (Table 2.2 and **Figure 2.9a**). Similarly, with condition MT3.0, increasing the film thickness by 150% caused the SLT to decrease by 36.4% (**Figure 2.9b**). This moderate effect of film thickness is attributable to the diffusive transport of electrons through the film. In contrast, the previously described 3x change in SLT with wall thickness alone was a far more significant effect. In summary, the architectures examined here had the SLT

largely determined by the intercalation length scale, the SLT had a minor dependence upon the electron transport distance, and the samples were free from electrolyte transport limitations (no SLT dependence).

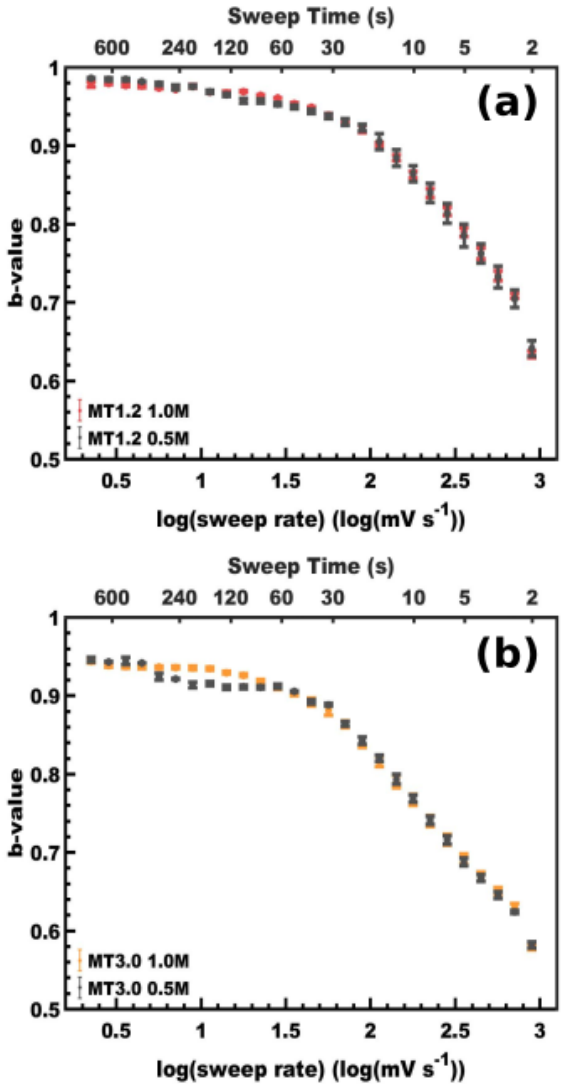

Figure 2.8. The sweep-rate dependent b-values were compared as a function of the $LiClO_4$ electrolyte concentration (0.5 and 1.0 M) for sample conditions MT1.2 (a) and MT3.0 (b). Error bars correspond to the standard-error-of-the-mean.

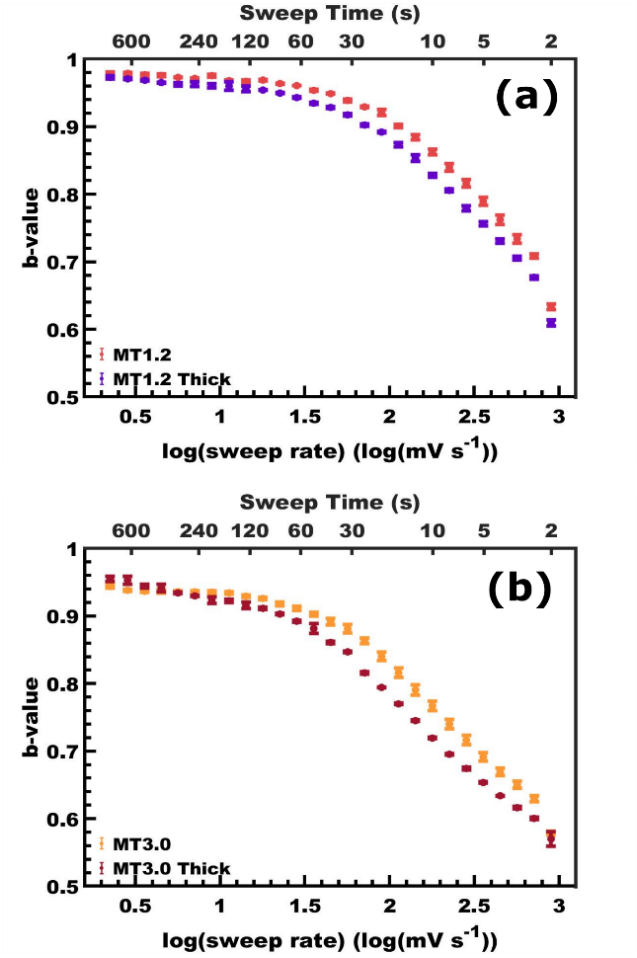

Figure 2.9. The sweep-rate dependent b-values were compared as a function of film thickness for sample conditions M:T1.2 (a) and M:T3.0 (b). Error bars correspond to the standard-error-of-the-mean.

The SLT values, as well as the sweep rate at other b-values were compared as a function of the wall-thickness. Here, it is convenient to divide the voltage window by the sweep rate to yield the sweep time for a particular b-value. Time dependent diffusion processes follow Fick's second law where the one-dimensional diffusion length with infinite source is:

$$x = \sqrt{Dt} \tag{2.2}$$

where x is the diffusion length (half the concentration of the source), D is the diffusion coefficient, and t is time. Thus, a plot of $t^{0.5}$ versus diffusion length yields a straight line. This relationship is used to approximate the time dependence upon intercalation length scale. When considering half of the wall thickness as the diffusion length, we find remarkably linear trends from b=0.6-0.9, with corresponding R^2 values >0.97 (**Figure 2.10**). As expected for a diffusion-based process, the length-time relationship for the DLT is well modeled by **Equation 2.2**. Interestingly, the length-time dependence of the SLT is equally well fitted by Equation 2.2. These data suggest that the relative value of the SLT reflects a balance of a surface process and a diffusive process. Furthermore, we note that the best-fit lines in Figure 2.10 enable one to choose the length scale needed for a particular time-dependent behavior, assuming there are no other kinetic constraints. This length-scale dependent correlation thus enables one to "nano-optimize" a device for a specific performance target. The numerous correlations presented here highlight that T-Nb_2O_5 intercalation pseudocapacitance is an extrinsic property that depends delicately on the dimensions of the porous architecture.

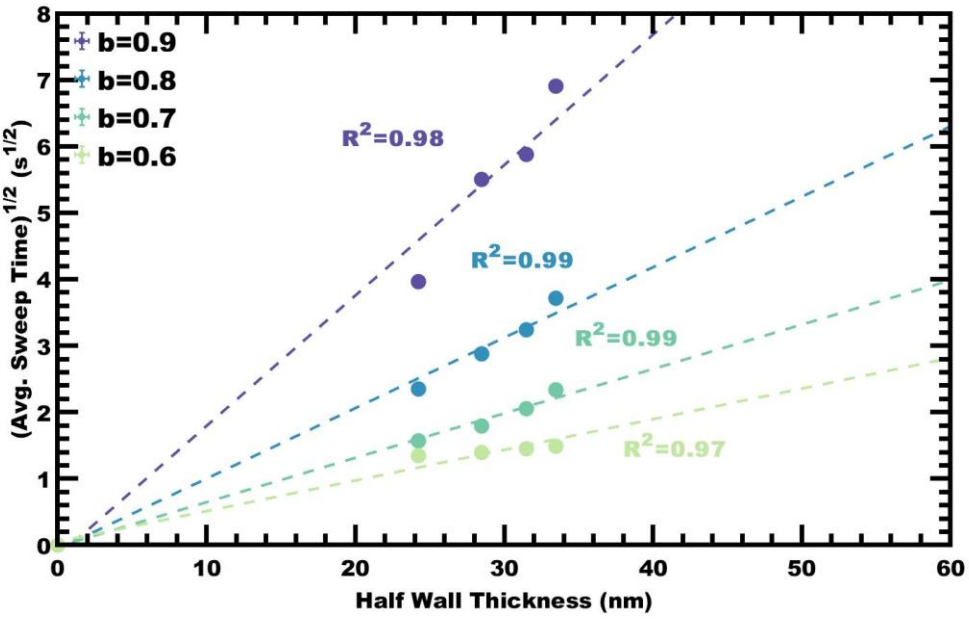

Figure 2.10. Plot correlating the intercalation length scale (half the wall thickness) to the square root of the average sweep time corresponding to specific b-values. Linear trends here are consistent with the generalized diffusion relationship of $x \propto \sqrt{(Dt)}$, where x is the diffusion length, t is time, and D is the diffusivity. Error bars correspond to the standard-error of each measure.

2.4 Conclusion

Devices that combine intercalation with pseudocapacitance are attractive for applications needing high energy and power density simultaneously. Orthorhombic niobium pentoxide stands out as the first material termed as exhibiting intercalation pseudocapacitance, yet its performance dependence upon nanoscale feature sizes has remained ambiguous. All intercalation-based charging mechanism involve charges entering a surface and subsequent diffusion into the material. Many electrochemical analytical methods struggle to unambiguously deconvolve these contributions since diffusion-limited steps often exhibit similar time-dependent responses. The studies of T-

Nb_2O_5 to date have used either 1) a single nanoscale architecture or 2) a set of nanoscale architectures with multiple spatial variables changing for each sample. Here we demonstrate the use of persistent micelle templates to prepare a series of tunable isomorphic architectures that enable the variation of single spatial variable at a time. This approach reduces the dependence upon models and can establish unambiguous nanostructure-property relationships. Two regime transitions were identified, the maximum sweep rate for surface-limited kinetics (Surface-Limited Threshold) and the minimum sweep rate for diffusion-limited kinetics (Diffusion-Limited Threshold). For the T-Nb_2O_5 architectures investigated here, it was revealed that both the SLT and DLT sensitively depend upon the intercalation length-scale, have a moderate dependence on the electron transport length, and were not affected by electrolyte transport constraints. These types of performance dependencies upon architecture are critical to enable energy-dense nanostructures that are "nano-optimized" to deliver a specific power density.

2.5 Experimental Methods

Materials. Ethanol (EtOH 200 proof, 100%, Fisher) was dried at room temperature by storage over 30% w/v of molecular sieves (3Å, 8-12 mesh, Acros Organics) for a week.[92] Concentrated hydrochloric acid (HCl, 37% w/w, ACS grade, VWR) and (HCl, 37% w/w, trace metal grade, Fisher Scientific), concentrated hydrofluoric acid (HF, 48% w/w, trace metal grade, Sigma-Aldrich), poly(ethylene glycol)methyl ether (PEO-OH, M_n = 20,000 $gmol^{-1}$, Aldrich), 2-bromopropionic acid (>99%, Aldrich), and 4-(dimethylamino) pyridine (99%, Aldrich) were used as received. Niobium(V) Ethoxide (NbOEth, 99.9%, Fisher), copper(I) bromide (99.99%, Aldrich), tris-(2-dimethylaminoethyl) amine (97%,

Aldrich), anhydrous lithium perchlorate ($LiClO_4$, 99.99%, Aldrich), concentrated nitric acid (HNO_3, 70%, Fisher Scientific), and anhydrous propylene carbonate (99.7%, Aldrich) were used as received and stored inside a glove box. Hexyl acrylate (96%, VWR) monomer was passed through a basic alumina column just prior to use. Chloroform (>99%, Aldrich), hexane (>98.5%, Fisher), tetrahydrofuran (Fisher), and dimethylformamide (97%, Aldrich) were used as received.

Polymer synthesis. Poly(ethylene oxide-*b*-hexyl acrylate), PEO-*b*-PHA, diblock polymer was synthesized by a two-step synthesis. A Steglich esterification of poly(ethylene glycol)methyl ether was used to form a macroinitiator, followed by atom transfer radical polymerization (ATRP) to grow the PHA block. The procedure is described elsewhere in detail.[60] The molar mass of PHA was determined using a Bruker Avance III HD 300 ^{1}H NMR by comparison to the known PEO (M_n = 20.0 kg mol^{-1}) (**Figure A.4a** and **Table A.1**). The molar mass dispersity was characterized using a Waters gel permeation chromatograph (GPC) equipped with a Waters 1525 binary pump, three styragel columns (HR1, HR3, HR5 in the effective molecular weight range of 0.1-5, 0.5-30, and 2-400 kg mol^{-1}, respectively), and a Waters 2414 refractive index detector. The GPC was calibrated with poly(styrene) standards (1.50, 3.28, 10.00, 17.40, 32.70, 120.00, 214.00, 545.00, 1010.00 kg mol^{-1}) obtained from Polymer Standards Service GmbH. GPC samples were prepared in THF at concentrations of 5 mg mL^{-1}, filtered through a 0.2 μm syringe filter prior to injection (**Figure 2.4b** and Table A.1).[62,93]

Synthesis of Porous Materials with Persistent Micelle Templates. A micelle stock solution was prepared by dispersing PEO-*b*-PHA (25 mg) in EtOH (2.5 mL) at room temperature with gentle agitation. Then to ensure full dissolution, the 20 mL scintillation vial for each solution was placed in an oven at 80 ºC for 30 min and was subsequently cooled to room temperature overnight. Concentrated HCl (~0.060 g) was added slowly to reach 1.8 wt% with respect to the total mixture (PEO-*b*-PHA, EtOH, and HCl). We note that ethanol was recently found to result in minimal microporosity within the final Nb_2O_5 walls.[61] After acid addition, the solution was placed in a water bath at 35 ºC to maintain dispersion of the polymer micelles. A prescribed quantity of NbOEth was added to each solution to reach the target Material:Template ratio (M:T).[63] Here the M:T is a mass ratio of the final anticipated Nb_2O_5 mass relative to the mass of block polymer. Each film was spin coated for 30 seconds at 1000, 1500, 2000, and 2150 rpm under 15% relative humidity for each M:T condition of 1.2, 1.8, 2.4, and 3.0 respectively as described in detail elsewhere.[61,63,94] Immediately after the end of spin coating, each sample was removed from the humidity-controlled chamber and placed on a 110 ºC hot plate overnight to crosslink the oxide, termed as "aging." The room humidity during aging was not found to have an effect. Aging conditions were optimized to prevent initial dewetting and to assure sufficient oxide connectivity to survive calcination. After each spin coating process, the spin coating chamber (Tupperware) was replaced to avoid effects of residual solvent vapor, as noted previously.[61] Glass, silicon, and FTO substrates were used for SAXS, SEM, and electrochemistry, respectively. After aging, the films were calcined, 5 ºC min^{-1} to 200 ºC followed by 10 ºC min^{-1} to 600 ºC with a 1 hr soak.

Electrode Preparation. FTO substrates (TEC-15, Hartford Glass, CT) were rinsed and scrubbed with DI water using Kimwipes until scrubbing produces an audible squeaking noise followed by rinsing and scrubbing with IPA wetted Kimwipes again in the same manner. The substrates were then sonicated in a soapy water bath (2 g/L deconex) for 30 minutes. The water and alcohol scrub and rinse steps were repeated as before. The resulting substrates were stored submerged in IPA until near the time of spin coating. Just prior to coating, the FTO substrates were removed from IPA, blown dry, and then calcined to 450 ºC for 3 hr to remove trace organics. After calcination, the FTO substrates were held at 110 ºC until the moment they were used for spin coating. An uncoated area for electrical contact was maintained by masking part of the substrate with high temperature Kapton tape (**Figure A.5**). After spin coating and aging as described above, the edges of the FTO substrates were cleaved to remove edge effects[63] where residual template solution can collect at the substrate edges, resulting in a locally varied film thickness. The back of each film was engraved with identifying marks for M:T, recipe number, and film number. The Kapton mask was then removed. The ~1 mm portion of the film proximal to the Kapton mask exhibited an edge effect with local variation of film thickness and was removed by scraping away oxide film with glass prior to calcination (Figure A.5). The final active area of each sample was determined by photography over a ruled grid and was analyzed using ImageJ.

X-ray Scattering Experiments. X-ray experiments were conducted using a SAXSLab Ganesha at the South Carolina SAXS collaborative (SCSC). A Xenocs GeniX 3D microfocus source was used with a copper target to produce monochromatic beam with

a 0.154 nm wavelength. The instrument was calibrated prior to measurements using National Institute of Standards and Technology (NIST) reference material, 640d silicon powder with peak position at $2\theta = 28.44^{\circ}$. A Pilatus 300k detector (Dectris) was used to collect the 2D scattering patterns with nominal pixel dimensions of 172x172 μm. SAXS data were acquired with an X-ray flux of ~1.41 M photon per second upon the sample and a detector-to-sample distance of 1,400 mm. Transmission small-angle X-ray scattering (SAXS) data were measured to observe the purely in-plane morphology. The 2D images were azimuthally integrated to yield the scattering vector and intensity. Peak positions were fitted using custom MATLAB software. Grazing incidence wide-angle X-ray scattering (GIWAXS) measurements were conducted with an incident angle (α_i) of 7º relative to the incident beam. The GIWAXS sample-to-detector distance was 112.1 mm with an X-ray flux of ~39.2 M photon per second upon the sample. The 2D WAXS data were masked to remove diffuse reflectance before integration and analysis of the resulting 1D data. A Gaussian point-spread function was utilized to interpret scattering data as a result of grain-size broadening per the Scherrer formula.[95,96]

Scanning Electron Microscopy (SEM). Top-view images of calcined films were acquired with a Zeiss Ultraplus thermal field emission SEM using an accelerating voltage of 5 keV and an in-lens secondary electron detector. The working distance was maintained at ~3 mm and images were acquired at constant magnification of 300k. At least 100 measurements were made upon each feature (pore and walls) to derive statistical metrics. These measures were conducted in numerous directions on numerous images to yield average values. The wall thickness was measured as the diameter on an inscribed circle

between neighboring pores as described elsewhere.[60] Pore size and wall-thickness data are presented as average values with the standard-error-of-the-mean. Cross-sectional SEM was used to determine film thickness.

Inductively Coupled Plasma Mass Spectrometry (ICP-MS). A series of films prepared on FTO substrates were cut to ~1 cm^2 of the Nb_2O_5 coating. A photograph was used to account for the specific substrate area as previously described. These films along with FTO blanks were heated in a Teflon vessel containing 70% HNO_3 (trace metal grade), 37% HCl (trace metal grade), and 48% HF (trace metal grade) (1:3:0.5 mL) respectively at 180 ºC for 12 hours before solutions were diluted with water (18.2 MΩ cm) to 50 mL volume and measured using a Thermo-Finnigan Element XR ICP-MS. The instrument was calibrated using a range of concentrations spanning those of the measured samples in conjunction with FTO blanks. A range of HF contents was screened to assure efficient Nb_2O_5 digestion (**Figure A.6**). These data were used to calculate the Nb_2O_5 mass-per-area metric for each sample condition.

Electrochemical Analysis. Electrochemical measurements were conducted using a three-electrode setup with a BioLogic SP-150 potentiostat. All measurements were performed in an argon-filled glovebox (<1 ppm O_2, <1 ppm H_2O). The working electrodes were porous Nb_2O_5 prepared using PMT on FTO substrates as described above. The working electrode was held by a home-built titanium metal clamp to assure ohmic contact to the FTO. All potentials are reported vs a Li/Li^+ reference electrode. The counter electrode was also lithium foil approximately 540 mm^2 in surface area. All lithium foils

were scraped until shiny just prior to immersion in electrolyte. The electrolyte solution was 1.0 M $LiClO_4$ in propylene carbonate. A series of diagnostic cyclic voltammograms and electric impedance spectroscopy measurements were used to verify ohmic contact. The working electrode was then held at 1.2 V for 20 minutes before cycling from 1.2 V to 3.0 V repeatedly 20 times at 10 mV/s to remove trace contaminants. A series of 28 logarithmically spaced sweeps ranging in rate from 1000 mV s^{-1} to 2 mV s^{-1} were run in sequence starting from 1.2 V vs Li/Li^+. There was a 3 min hold period at the end of each sweep to allow the electrode to equilibrate. Mass normalized was based upon the film area and ICP-MS measurements with identical samples.

2.6 References

[1] A. Borenstein, O. Hanna, R. Attias, S. Luski, T. Brousse, D. Aurbach, *J. Mater. Chem. A* **2017**, *5*, 12653.

[2] A. G. Pandolfo, A. F. Hollenkamp, *J. Power Sources* **2006**, *157*, 11.

[3] K. M. Shaju, G. V. Subba Rao, B. V. R. Chowdari, *Electrochim. Acta* **2002**, *48*, 145.

[4] S. Trasatti, G. Buzzanca, *J. Electroanal. Chem. Interfacial Electrochem.* **1971**, *29*, A1.

[5] V. Augustyn, J. Come, M. A. Lowe, J. W. Kim, P.-L. Taberna, S. H. Tolbert, H. D. Abruña, P. Simon, B. Dunn, *Nat. Mater* **2013**, *12*, 518.

[6] H. Yang, H. Xu, L. Wang, L. Zhang, Y. Huang, X. Hu, *Chem. - A Eur. J.* **2017**, *23*, 4203.

[7] S. Zhang, J. Wu, J. Wang, W. Qiao, D. Long, L. Ling, *J. Power Sources* **2018**, *396*, 88.

[8] J. W. Kim, V. Augustyn, B. Dunn, *Adv. Energy Mater.* **2012**, *2*, 141.

[9] S. Lou, X. Cheng, L. Wang, J. Gao, Q. Li, Y. Ma, Y. Gao, P. Zuo, C. Du, G. Yin, *J. Power Sources* **2017**, *361*, 80.

[10] D. Li, J. Shi, H. Liu, C. Liu, G. Dong, H. Zhang, Y. Yang, G. Lu, H. Wang, *Sustain. Energy Fuels* **2019**, *3*, 1055.

[11] J. Lin, Y. Yuan, Q. Su, A. Pan, S. Dinesh, C. Peng, G. Cao, S. Liang, *Electrochim. Acta* **2018**, *292*, 63.

[12] S. Hemmati, G. Li, X. Wang, Y. Ding, Y. Pei, A. Yu, Z. Chen, *Nano Energy* **2019**, *56*, 118.

[13] C. Zhu, R. E. Usiskin, Y. Yu, J. Maier, *Science* **2017**, *358*, eaao2808.

[14] J. W. Long, B. Dunn, D. R. Rolison, H. S. White, *Chem. Rev.* **2004**, *104*, 4463.

[15] A. Vu, Y. Qian, A. Stein, *Adv. Energy Mater.* **2012**, *2*, 1056.

[16] J. Maier, *Faraday Discuss.* **2015**, *176*, 17.

[17] H. Liu, Z. Bi, X.-G. Sun, R. R. Unocic, M. P. Paranthaman, S. Dai, G. M. Brown, *Adv. Mater.* **2011**, *23*, 3450.

[18] J. K. Shon, H. S. Lee, G. O. Park, J. Yoon, E. Park, G. S. Park, S. S. Kong, M. Jin, J. M. Choi, H. Chang, S. Doo, J. M. Kim, W. S. Yoon, C. Pak, H. Kim, G. D. Stucky, *Nat. Commun.* **2016**, *7*, 1.

[19] J. M. Szeifert, J. M. Feckl, D. Fattakhova-Rohlfing, Y. Liu, V. Kalousek, J. Rathousky, T. Bein, *J. Am. Chem. Soc.* **2010**, *132*, 12605.

[20] Q. Deng, Y. Fu, C. Zhu, Y. Yu, *Small* **2019**, *15*, 1804884.

[21] C. Li, Q. Li, Y. V. Kaneti, D. Hou, Y. Yamauchi, Y. Mai, *Chem. Soc. Rev.* **2020**, *49*, 4681.

[22] E. Lim, C. Jo, H. Kim, M.-H. Kim, Y. Mun, J. Chun, Y. Ye, J. Hwang, K.-S. Ha, K. C. Roh, K. Kang, S. Yoon, J. Lee, *ACS Nano* **2015**, *9*, 7497.

[23] X. Ge, C. Gu, Z. Yao, J. Sun, X. Wang, J. Tu, *Chem. Eng. J.* **2018**, *338*, 211.

[24] L. Kong, X. Liu, J. Wei, S. Wang, B. B. Xu, D. Long, F. Chen, *Nanoscale* **2018**, *10*, 14165.

[25] W. Luo, Y. Li, J. Dong, J. Wei, J. Xu, Y. Deng, D. Zhao, *Angew. Chem.* **2013**, *125*, 10699.

[26] Y. Lian, D. Wang, S. Hou, C. Ban, J. Zhao, H. Zhang, *Electrochim. Acta* **2020**, *330*, 135204.

[27] G. Luo, H. Li, D. Zhang, L. Gao, T. Lin, *Electrochim. Acta* **2017**, *235*, 175.

[28] J. Y. Cheong, J.-W. Jung, D.-Y. Youn, C. Kim, S. Yu, S.-H. Cho, K. R. Yoon, I.-D. Kim, *J. Power Sources* **2017**, *360*, 434.

[29] B. Deng, T. Lei, W. Zhu, L. Xiao, J. Liu, *Adv. Funct. Mater.* **2018**, *28*, 1704330.

[30] C. Shi, K. Xiang, Y. Zhu,, X. Chen, W. Zhou, H. Chen, *Ceram. Int.* **2017**, *43*, 12388.

[31] H. Song, J. Fu, K. Ding, C. Huang, K. Wu, X. Zhang, B. Gao, K. Huo, X. Peng, P. K. Chu, *J. Power Sources* **2016**, *328*, 599.

[32] K. Brezesinski, J. Wang, J. Haetge, C. Reitz, S. O. Steinmueller, S. H. Tolbert, B. M. Smarsly, B. Dunn, T. Brezesinski, *J. Am. Chem. Soc.* **2010**, *132*, 6982.

[33] S. Jiang, S. Dong, L. Wu, Z. Chen, L. Shen, X. Zhang, *J. Electroanal. Chem.* **2019**, *842*, 82.

[34] Y. Jiao, H. Zhang, H. Zhang, A. Liu, Y. Liu, S. Zhang, *Nano Res.* **2018**, *11*, 4673.

[35] Y. Li, R. Wang, W. Zheng, Q. Zhao, S. Sun, G. Ji, S. Li, X. Fan, C. Xu, *Mater. Technol.* **2020**, 1.

[36] J. Liao, R. Tan, Z. Kuang, C. Cui, Z. Wei, X. Deng, Z. Yan, Y. Feng, F. Li, C. Wang, J. Ma, *Chinese Chem. Lett.* **2018**, *29*, 1785.

[37] S. Kim, J. Hwang, J. Lee, J. Lee, *Sci. Adv.* **2020**, *6*, eabb3814.

[38] E. Lim, C. Jo, M. S. Kim, M.-H. Kim, J. Chun, H. Kim, J. Park, K. C. Roh, K. Kang, S. Yoon, J. Lee, *Adv. Funct. Mater.* **2016**, *26*, 3711.

[39] P. Nagaraju, R. Vasudevan, A. Alsalme, A. Alghamdi, M. Arivanandhan, R. Jayavel, *Nanomaterials* **2020**, *10*, 160.

[40] M. Y. Song, N. R. Kim, H. J. Yoon, S. Y. Cho, H.-J. Jin, Y. S. Yun, *ACS Appl. Mater. Interfaces* **2017**, *9*, 2267.

[41] L. Kong, C. Zhang, S. Zhang, J. Wang, R. Cai, C. Lv, W. Qiao, L. Ling, D. Long, *J. Mater. Chem. A* **2014**, *2*, 17962.

[42] G. Ma, K. Li, Y. Li, B. Gao, T. Ding, Q. Zhong, J. Su, L. Gong, J. Chen, L. Yuan, B. Hu, J. Zhou, K. Huo, *ChemElectroChem* **2016**, *3*, 1360.

[43] W. Hu, S. Zhang, W. Zhang, M. Wang, F. Feng, *J. Nanoparticle Res.* **2020**, *22*, 57.

[44] H. Sun, L. Mei, J. Liang, Z. Zhao, C. Lee, H. Fei, M. Ding, J. Lau, M. Li, C. Wang, X. Xu, G. Hao, B. Papandrea, I. Shakir, B. Dunn, Y. Huang, X. Duan, *Science* **2017**, 599.

[45] F. Idrees, J. Hou, C. Cao, F. K. Butt, I. Shakir, M. Tahir, F. Idrees, *Electrochim. Acta* **2016**, *216*, 332.

[46] Z. Chen, H. Li, X. Lu, L. Wu, J. Jiang, S. Jiang, J. Wang, H. Dou, X. Zhang, *ChemElectroChem* **2018**, *5*, 1516.

[47] J. Zhai, Y. Wu, X. Zhao, Q. Yang, *J. Alloys Compd.* **2017**, *715*, 275.

[48] J. W. Kim, S. Kim, H. Kim, *Int. J. Energy Res.* **2019**, *43*, 4359.

[49] J. Hu, J. Li, K. Wang, H. Xia, *Electrochim. Acta* **2020**, *331*, 135364.

[50] X. Xu, B. Tian, S. Zhang, J. Kong, D. Zhao, B. Liu, *Anal. Chim. Acta* **2004**, *519*, 31.

[51] E. Lim, H. Kim, C. Jo, J. Chun, K. Ku, S. Kim, H. I. Lee, I.-S. Nam, S. Yoon, K. Kang, J. Lee, *ACS Nano* **2014**, *8*, 8968.

[52] A. L. Viet, M. V. Reddy, R. Jose, B. V. R. Chowdari, S. Ramakrishna, *J. Phys. Chem. C* **2010**, *114*, 664.

[53] S. Li, Q. Xu, E. Uchaker, X. Cao, G. Cao, *CrystEngComm* **2016**, *18*, 2532.

[54] S. Ouendi, C. Arico, F. Blanchard, J.-L. Codron, X. Wallart, P. L. Taberna, P. Roussel, L. Clavier, P. Simon, C. Lethien, *Energy Storage Mater.* **2019**, *16*, 581.

[55] A. A. Lubimtsev, P. R. C. Kent, B. G. Sumpter, P. Ganesh, *J. Mater. Chem. A* **2013**, *1*, 14951.

[56] K. J. Griffith, A. C. Forse, J. M. Griffin, C. P. Grey, *J. Am. Chem. Soc.* **2016**, *138*, 8888.

[57] D. Chen, J.-H. Wang, T.-F. Chou, B. Zhao, M. A. El-Sayed, M. Liu, *J. Am. Chem. Soc.* **2017**, *139*, 7071.

[58] J. Come, V. Augustyn, J. W. Kim, P. Rozier, P.-L. Taberna, P. Gogotsi, J. W. Long, B. Dunn, P. Simon, *J. Electrochem. Soc.* **2014**, *161*, A718.

[59] B. Reichman, A. J. Bard, *J. Electrochem. Soc.* **1981**, *128*, 344.

[60] K. A. Lantz, N. B. Clamp, W. van den Bergh, A. Sarkar, M. Stefik, *Small* **2019**, *15*, 1900393.

[61] A. Sarkar, L. Evans, M. Stefik, *Langmuir* **2018**, *34*, 5738.

[62] H. N. Lokupitiya, A. Jones, B. Reid, S. Guldin, M. Stefik, *Chem. Mater.* **2016**, *28*, 1653.

[63] A. Sarkar, M. Stefik, *J. Mater. Chem. A* **2017**, *5*, 11840.

[64] A. Sarkar, A. Thyagarajan, A. Cole, M. Stefik, *Soft Matter* **2019**, *15*, 5193.

[65] P. Sutton, P. Bennington, S. N. Patel, M. Stefik, U. B. Wiesner, P. F. Nealey, U. Steiner, I. Gunkel, *Adv. Funct. Mater.* **2019**, *29*, 1905977.

[66] R. Dehmel, J. A. Dolan, Y. Gu, U. Wiesner, T. D. Wilkinson, J. J. Baumberg, U. Steiner, B. D. Wilts, I. Gunkel, *Macromolecules* **2017**, *50*, 6255.

[67] O. Kim, S. Y. Kim, J. Lee, M. J. Park, *Chem. Mater.* **2016**, *28*, 318.

[68] P. Docampo, S. Guldin, M. Stefik, P. Tiwana, M. C. Orilall, S. Hüttner, H. Sai, U. Wiesner, U. Steiner, H. J. Snaith, *Adv. Funct. Mater.* **2010**, *20*, 1787.

[69] E. J. W. Crossland, P. Cunha, S. Ludwigs, M. A. Hillmyer, U. Steiner, *ACS Appl. Mater. Interfaces* **2011**, *3*, 1375.

[70] E. J. W. Crossland, M. Nedelcu, C. Ducati, S. Ludwigs, M. A. Hillmyer, U. Steiner, H. J. Snaith, *Nano Lett.* **2009**, *9*, 2813.

[71] M. Nedelcu, J. Lee, E. J. W. Crossland, S. C. Warren, M. C. Orilall, S. Guldin, S. Hüttner, C. Ducati, D. Eder, U. Wiesner, U. Steiner, H. J. Snaith, *Soft Matter* **2009**, *5*, 134.

[72] M. Stefik, J. Song, H. Sai, S. Guldin, P. Boldrighini, M. C. Orilall, U. Steiner, S. M. Gruner, U. Wiesner, *J. Mater. Chem. A* **2015**, *3*, 11478.

[73] H. Lindström, S. Södergren, A. Solbrand, H. Rensmo, J. Hjelm, A. Hagfeldt, S.-E. Lindquist, *J. Phys. Chem. B* **1997**, *101*, 7717.

[74] B. E. Conway, W. G. Pell, *J. Power Sources* **2002**, *105*, 169.

[75] S. Yoon, J. H. Jang, B. H. Ka, S. M. Oh, *Electrochim. Acta* **2005**, *50*, 2255.

[76] O. Bohlen, J. Kowal, D. U. Sauer, *J. Power Sources* **2007**, *172*, 468.

[77] S. Yoon, C. W. Lee, S. M. Oh, *J. Power Sources* **2010**, *195*, 4391.

[78] M. Kaus, J. Kowal, D. U. Sauer, *Electrochim. Acta* **2010**, *55*, 7516.

[79] R. L. Spyker, R. M. Nelms, *IEEE Trans. Aerosp. Electron. Syst* **2000**, *36*, 829.

[80] M. Z. Bazant, K. Thornton, A. Ajdari, *Phys. Rev. E* **2004**, *70*, 021506.

[81] K. T. Chu, M. Z. Bazant, *Phys. Rev. E* **2006**, *74*, 011501.

[82] L. Højgaard Olesen, M. Z. Bazant, H. Bruus, *Phys. Rev. E* **2010**, *82*, 011501.

[83] B.-A. Mei, J. Lau, T. Lin, S. H. Tolbert, B. S. Dunn, L. Pilon, *J. Phys. Chem. C* **2018**, *122*, 24499.

[84] B.-A. Mei, O. Munteshari, J. Lau, B. Dunn, L. Pilon, *J. Phys. Chem. C* **2018**, *122*, 194.

[85] B.-A. Mei, L. Pilon, *Electrochim. Acta* **2017**, *255*, 168.

[86] H.-L. Girard, B. Dunn, L. Pilon, *Electrochim. Acta* **2016**, *211*, 420.

[87] J. S. Ko, C.-H. Lai, J. W. Long, D. R. Rolison, B. Dunn, J. Nelson Weker, *ACS Appl. Mater. Interfaces* **2020**, *12*, 14071.

[88] S. Dutta, K. C.-W. Wu, T. Kimura, *Chem. Mater.* **2015**, *27*, 6918.

[89] S. Guldin, P. Docampo, M. Stefik, G. Kamita, U. Wiesner, H. J. Snaith, U. Steiner, *Small* **2012**, *8*, 432.

[90] C. Robertus, W. H. Philipse, J. G. H. Joosten, Y. K. Levine, *J. Chem. Phys.* **1989**, *90*, 4482.

[91] S. Ardizzone, G. Fregonara, S. Trasatti, *Electrochim. Acta* **1990**, *35*, 263.

[92] D. B. G. Williams, M. Lawton, *J. Org. Chem.* **2010**, *75*, 8351.

[93] L. J. Fetters, D. J. Lohse, D. Richter, T. A. Witten, A. Zirkel, *Macromolecules* **1994**, *27*, 4639.

[94] H. N. Lokupitiya, M. Stefik, *Nanoscale* **2017**, *9*, 1393.

[95] A. L. Patterson, *Phys. Rev.* **1939**, *56*, 978.

[96] P. Scherrer, *Math. Phys.* **1918**, *2*, 98.

CHAPTER 3: Faster Intercalation Pseudocapacitance Enabled by Adjustable Amorphous Titania where Tunable Isomorphic Architectures Reveal Accelerated Lithium Diffusivity[1]

[1]van den Bergh, W.; Larison, T.; Fornerod, M. J.; Guldin, S.; Stefik, M., **2022** *In Review*.

3.1 Abstract

Intercalation pseudocapacitance is a faradaic electrochemical phenomenon with high power and energy densities, combining the attractive features of capacitors and batteries respectively. Intercalation pseudocapacitive responses exhibit surface-limited kinetics by definition, without restriction from the collective of diffusion-based processes. The surface-limited threshold (SLT) corresponds to the maximum voltage sweep rate (v_{SLT}) exhibiting a predominantly surface-limited current response prior to the onset of diffusion-limitations. Prior studies have shown increased solid-state lithium diffusivity for amorphous TiO_2 compared to anatase. Here a granular series of calcination temperatures yielded TiO_2 nanostructures with tailored amorphous character and content. The corresponding amorphous-phase v_{SLT} was found to increase monotonically by 317% as a result of lowered calcination temperatures changing the character of the amorphous phase. Subsequent isomorphic comparisons varying a single transport parameter at a time identified solid-state lithium diffusion as the dominant diffusive constraint. Thus, performance improvements were linked to increasing the lithium diffusivity of the amorphous phase with decreased calcination temperature. This remarkably enabled 95% capacity retention (483 ± 17 C/g) within a 30s discharge (120C equivalent). These results highlight how isomorphic sample series can reveal previously unidentified trends by reducing ambiguity and reiterate the potential of amorphization to realize increased performance in known materials.

3.2 Introduction

Electrochemical energy storage is growing quickly with increased demand for new materials with higher energy densities and higher power densities for faster (dis)charging

capabilities.[1–3] This demand is particularly high for mobile devices and electric vehicles where faster charging is desired. These concomitant requirements reveal a gap between typical batteries and capacitors which offer, respectively, only high energy density or only high power density.[4–6] Typically intercalation, defined as the insertion of a species between interstitial gaps in a material, observed in batteries is a sluggish process. However, intercalation pseudocapacitive responses combine the high energy density of faradaic energy storage via intercalation with high power density via rapid diffusive processes. Intercalation pseudocapacitive responses exhibit surface-limited kinetics by definition, where the current response is proportional to the voltage sweep rate (v).[7,8] Materials that have exhibited intercalation pseudocapacitive responses have sufficiently fast solid-state diffusion and an absence of phase transitions upon intercalation.[7–14] The introduction of dopants or other defects have been used to increase the rates of solid-state diffusion with examples for $Cu[Fe(CN)_6]_{0.63}\bullet\square_{0.37}\bullet 3.4H_2O$,[15] T-$Nb_2O_5$,[16–18] MoO_3,[19] TiO_2,[20,21] and others.[22,23] Nanoscale materials can also differ from bulk analogs, for example, nanoscale anatase can lithiate as a solid solution whereas larger anatase crystals undergo a phase separation of discrete lithium rich and lithium poor domains.[24,25] The observation of intercalation pseudocapacitance depends upon both the intrinsic material properties (insertion rate, diffusivity, etc) and on extrinsic architectural properties (surface area, transport constraints for electrons, electrolyte ions, and intercalation).[26–30] Generally pseudocapacitive current responses are observed from low v up until v is sufficiently high to onset diffusive-constraints, termed the surface-limited threshold (SLT, v_{SLT}, t_{SLT}). It often remains a challenge, however, to identify which specific diffusive process(es) limits the v_{SLT}. It follows that many works on nanoscale pseudocapacitive devices emphasize

performance without identifying limitations from a specific diffusive process. From a perspective of electrochemical characterization, most diffusive processes (electron transport, electrolyte ion transport, and lithium intercalation) follow Fick's second law and thus all have similar $(Dt)^{0.5}$ dependence which adds ambiguity to cyclic voltammetry (CV),[31] electrochemical impedance spectroscopy (EIS),[32–37] and 3D bode plot interpretations.[28,38] Though computational models[39–41] can in principle explain each aspect of device performance, they unfortunately require most parameters to be known, limiting their utility for studying unknown materials. From an architectural perspective, the ambiguity from concomitant diffusive processes sharing the same $(Dt)^{0.5}$ dependence may be resolved by comparing samples where a single transport process is altered at a time, e.g. by comparing series of isomorphic samples.[27] In contrast, most methods used for preparing nanomaterials for electrochemical devices result in multiple architectural parameters changing at the same time, e.g. simultaneous changes to both the intercalation length and the pore size. For example, a series of T-Nb_2O_5 nanoscale architectures were recently examined one variable at a time to identify that v_{SLT} was principally limited by solid-state lithium diffusion and varied with the intercalation length.[27] This extrinsic dependence is important to understand performance limitations as well as to support the optimization of energy devices.

Amorphization has emerged as an approach to modify, and sometimes increase, the rate of solid-state diffusion within known materials. Here amorphization is broadly defined and spans the continuum from disorder to perfect crystals. For example, the deliberate introduction of oxygen vacancies and dopants to intercalation materials have increased Li diffusivity,[16,17,23] electronic conductivity,[42,43] or both.[18–20] Dopants can provide shallow

electron donors for enhanced electronic conductivity.[18,42,44] Improved electronic conductivity can improve ionic conductivity when lithium diffusion is coupled with electron transport in cases where $D_{Li} > D_{e^-}$.[45] Vacancies similarly provide shallow electron donors which can increase electronic conductivity[16,19,20,43] and increase free-volume,[19] both of which can enhance Li diffusivity. Oxygen vacancies were reported to increase the interlayer spacing and the corresponding lithium diffusivity of MoO_{3-x},[19] and simulations of oxygen vacancies in V_2O_5 found a lower energetic hopping barrier thus greater lithium diffusivity.[46] Similar comparisons were made between amorphous and crystalline TiO_2 which identified amorphization as route to lower the activation energy for solid-state diffusion.[29,47,48] It is worth emphasizing that there exists a continuum between an amorphous solid and a perfect crystal. While binary comparisons of "crystalline" vs "amorphous" material have provided inspiration, there remain few insights from more granular investigations. For example, of the infinite versions of "amorphous" material it is not clear yet if they exhibit markedly different electrochemical behaviors. For materials, such as nanoscale TiO_2 architectures which has been observed to stubbornly consist of a mixture of amorphous and crystalline components,[49–53] it is challenging to isolate the contribution and character of each phase.[7,54,55] Here a sol-gel process was used to prepare amorphous TiO_2 from precursors where the extent of amorphization was monotonically reduced with a progressive series of calcination heat treatments. The well-known and distinct voltametric profiles for amorphous and anatase TiO_2 enable changes within the amorphous phase to be independently tracked. Comparing the performance of a tailored series of isomorphic architectures is ideal to limit ambiguity by identifying specific diffusion-limited contributions when examining the effects of amorphization.

Persistent micelle templates (PMTs) enable the synthesis of tunable isomorphic architectures with nanoscale pores.[27,56–62] In brief, PMTs use kinetically trapped block polymer micelles as templates that yield sample series with constant pore size. Varying the ratio of material precursors to micelle templates (material:template ratio, M:T) directly controls the final wall thickness while preserving constant templated pore size. Such independent control is in contrasts with other block polymer-based approaches where equilibration often couples such material additions to changing pore sizes and often also changing morphologies.[63,64] Furthermore since PMTs preserve spherical templates, the resulting porous materials are of a consistent morphology and isomorphic due to the simple sphere packing arrangement which maintains relatively constant tortuosity.[65–72] Here, PMTs are used to derive isomorphic TiO_2 architectures absent of electrochemical additives prone to side reactions which may confound architectural and material contributions.[73,74] These architectures are calcined at different temperatures to identify granular changes in the lithium diffusivity and pseudocapacitive kinetics of amorphous TiO_2.

3.3 Results and Discussion

First the physical characterization for the series of isomorphic architectures is described before examining their electrochemistry. The inclusion of series of isomorphic architectures that vary a single spatial parameter at a time is important later to support the deconvolution of concomitant processes and thus reduce the ambiguity of interpretations. Here PMTs were used to prepare the desired series of architectures based upon poly(ethylene oxide-*b*-butyl acrylate) (PEO-*b*-PBA) micelle templates dispersed in methanol (**Figure B.1, SI Table B.1**). In brief, the inclusion of a controlled water content was used prevent polymer chain exchange and thus impose a constant template

diameter.[27,56–60] Material precursors (TiO_2 nanoparticles) were prepared *ex-situ* to preserve the necessary water content for kinetic micelle control.[56] These material precursors were added in various quantities to PMT solutions (material:template ratio, M:T) to independently control the material wall thickness while preserving constant average pore size. The prepared sample conditions spanned a 2-parameter matrix with M:T = 1.6, 2.1, or 2.6 and with calcination temperatures of 280 °C, 380 °C, or 600 °C. It is noted that previous works reported residual carbon can remain after calcination of inorganic-organic mixtures to yet higher temperatures.[75,76] Scanning electron microscope (SEM) images of the resulting samples are shown in **Figure 3.1**. Please note that a uniform color scheme is used throughout this manuscript with each M:T ratio having a distinct shade and each calcination temperature having a distinct hue. The SEM images showed randomly packed spherical, open pores (dark regions) with short-range order and material walls (light regions) that vary with M:T ratio. Small-angle X-ray scattering (SAXS) data from these samples are shown in **Figure 3.2a-c**. These SAXS patterns exhibited a ~1:2 peak q-ratio which is consistent with the random sphere packing observed in SEM.[77] The SAXS patterns exhibited a similar number of structure factor peaks for all calcination temperatures indicating preservation of the nanostructure order. Furthermore, the SAXS peaks shifted to lower q-values (nm^{-1}) with increasing M:T ratio. The corresponding trend in d-spacing values ($d = 2\pi/q$) thus indicates lattice expansion with increasing M:T ratio which is typical under PMT conditions and was well fitted by the PMT model (**eqn B.1**, **Figure 3.2d**). The corresponding best-fit parameters are shown in **Table B.4**. Numerous measurements were taken from SEM images to quantify the distribution of pore and wall dimensions. The average pore diameter was constant for each M:T series at constant

calcination temperature. The average pore size increased somewhat with increasing calcination temperature (16.1% rel change), likely corresponding to further densification of the wall material (**Figure 3.2e)**. The porosity of these samples had little effect on electrolyte transport, *vide infra*. The increasing average wall thickness with M:T measured by SEM was also well-matched by the best-fit of the PMT model (**Figure 3.2f, eqn B.3**). For each given M:T value, the wall thickness decreased somewhat with increasing calcination temperature and was attributed to densification of the TiO_2 during crystallization. The amorphous/crystalline character was evaluated using X-ray and electron scattering. Grazing-incidence wide-angle X-ray scattering (GI-WAXS) of M:T = 1.6 samples with many calcination conditions are shown in **Figure 3.3a**. The scattering/diffraction pattern for the 280 °C calcination temperature had broad features (~22-34°) that are consistent with the short-range atomic ordering of amorphous material. For calcination temperatures from 380 °C and higher there are peaks consistent with anatase crystallites (PDF 65-5714). The average anatase crystallite sizes are shown in **Figure 3.3b** based on Scherrer analysis of the (101) peak. The general trend was that increased M:T ratio and increased calcination temperature led to larger average crystallite sizes as expected, albeit with some deviations such as MT1.6-600°C. The anatase crystallite dimensions were smaller than the wall thicknesses, for example, MT1.6-600°C had 8.6 nm crystallites (Scherrer) within the 15.15 ± 0.23 nm thick walls. This relationship was also apparent in brightfield and darkfield TEM, where MT1.6-600°C exhibited an average of 6-7 nm crystallites (**Figure B.2a-b**). Close examination of HR-TEM images also indicated random crystal placement throughout the nanostructure (**Figure B.2c)**. With a large fraction of amorphous phase in all samples determined electrochemically, *vide*

infra, it is likely that the amorphous phase is also distributed throughout the nanostructure. Thus, the crystal growth observed with increasing calcination temperature was attributed to the progressive conversion of an initially amorphous phase to anatase. As the calcination temperature increases, changes are possible within the remaining amorphous phase since there is a continuum between disorder and perfect crystals that notably includes a continuum of amorphous configurations. Here we term the samples with the lowest calcination temperatures as thus having the greatest degree of amorphization for both the amorphous and anatase phases. Thus, a set of tailored isomorphic architectures were prepared with controlled pore size, TiO_2 wall thickness, and extent of amorphization.

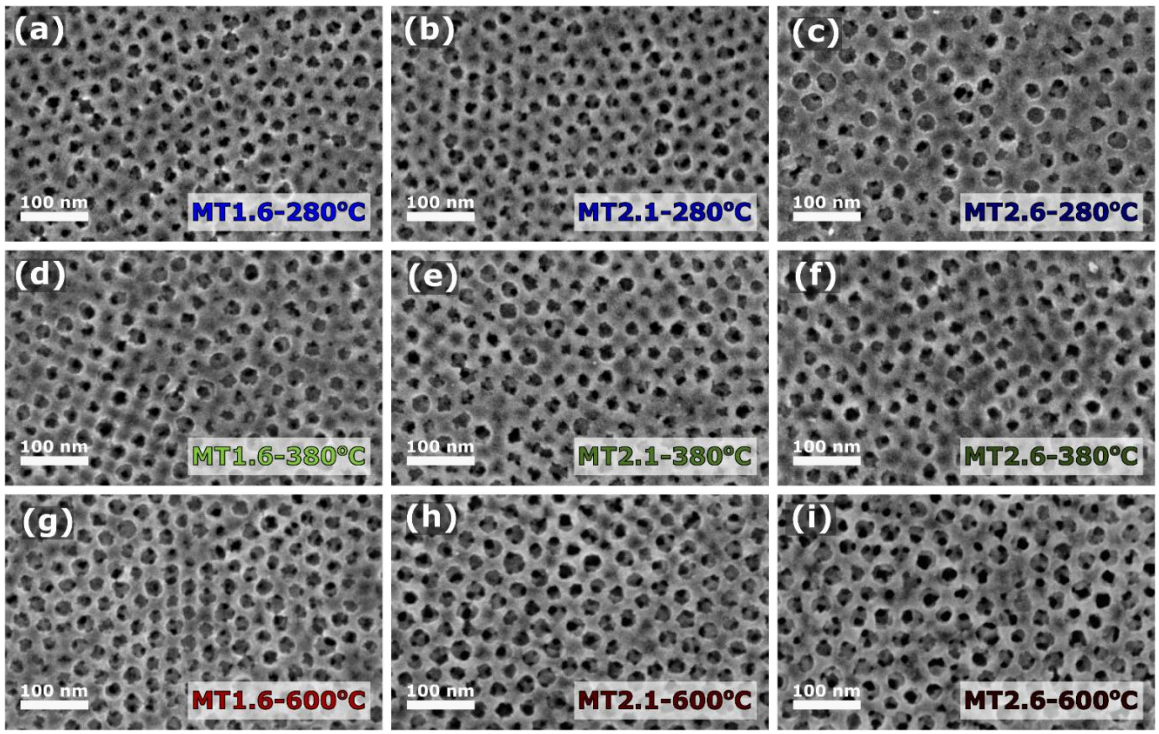

Figure 3.1. (a-i) SEM images of the isomorphic series of mesoporous TiO_2 samples prepared with persistent micelle templates using different material:template (M:T) ratios and calcined at different temperatures. The M:T ratios and calcination temperatures are labelled on each panel. Subsequent figures preserve this color scheme with the hue corresponding to the calcination temperature and the shade corresponding to the M:T ratio.

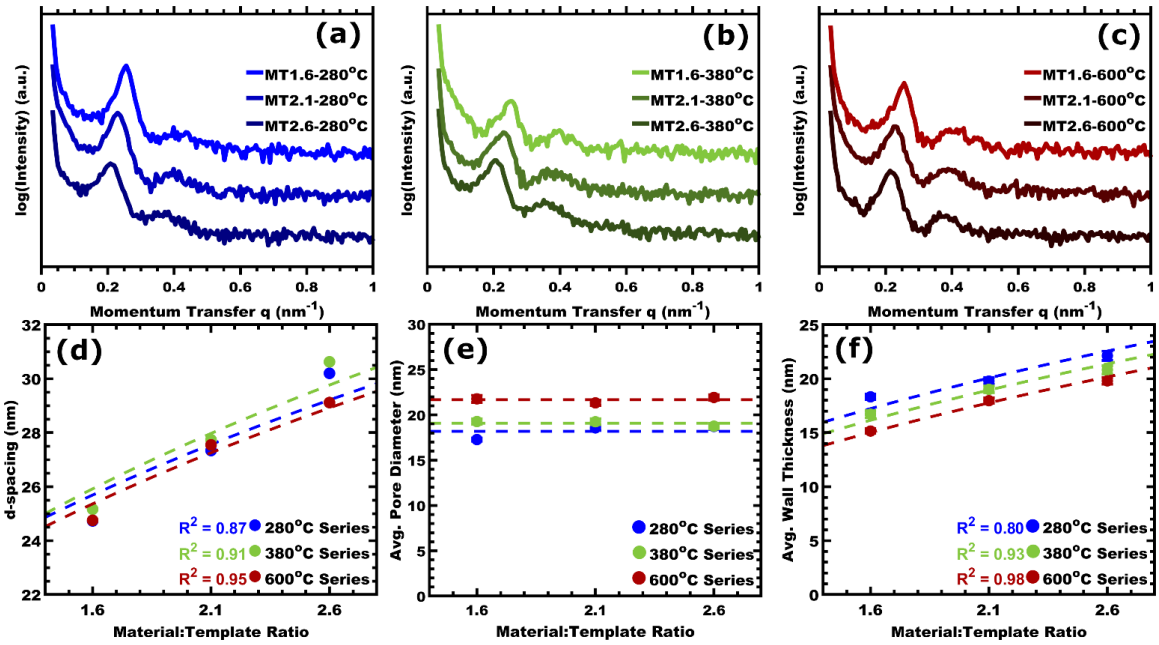

Figure 3.2. (a-c) SAXS patterns for all samples from the isomorphic series arranged by calcination temperature: (a) 280 °C, (b) 380 °C, and (c) 600 °C. SAXS data were vertically offset for clarity. (d) The corresponding d-spacing ($2\pi/q^*$) trends reveal lattice expansion upon increasing material-to-template ratio (M:T). (e) The mean pore diameters and (f) mean wall thicknesses were determined from numerous measurements upon SEM images and were compared the best-fit of the PMT model. The error bars correspond to the error-of-the-mean. (d-f) Each of these metrics were compared to the PMT model (dashed lines) with goodness-of-fit (R^2) indicated.

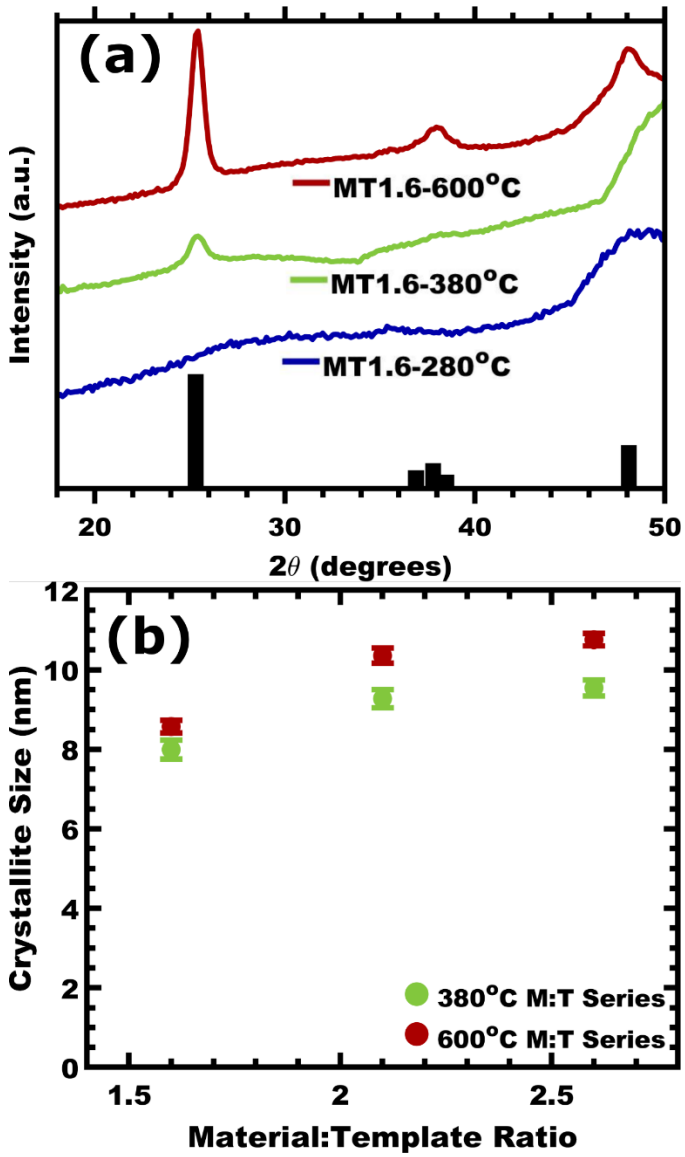

Figure 3.3. (a) GI-WAXS patterns for samples calcined at temperatures ranging from 280 °C to 600 °C with constant M:T=1.6. Data were offset vertically for clarity and include an anatase reference pattern (PDF 65-5714, black bars). (b) Average crystallite sizes were determined using Scherrer analysis of the non-convolved (101) peak at 25.3°.

Cyclic voltammetry (CV) was used to characterize lithiation behavior across the series of samples. All samples were measured with logarithmically spaced voltage sweep rates (v) within the same 1.5-2.5 V vs Li/Li^+ window using $LiClO_4$/PC electrolyte with a hold step for equilibration before reversing the voltage sweep direction. The CV data for the MT = 1.6 series at 2.0 mV/s is shown first to describe changes with calcination temperature (**Figure 3.4).** Condition MT1.6-280°C exhibited a broad peak at 1.641 ± 0.007 V. Several prior reports of sol-gel derived TiO_2 lithiation have included a similar CV feature that was sometimes ascribed to amorphous TiO_2 and was sometimes ascribed to TiO_2(B), a polymorph known to exhibit intercalation pseudocapacitance. Some of those reports described the TiO_2(B) as being "X-ray amorphous," i.e. without supporting diffraction data due to nanoscale crystals.[50–52,56,78–83] Since many definitions of "crystallinity" require observable diffraction,[84] it is suggested that such phases be termed "amorphous." For the present samples, neither X-ray diffraction data nor additional electron diffraction measurements (**Figure B.3)** were consistent with TiO_2(B) so the CV feature near 1.6V is ascribed to amorphous TiO_2. The CV of MT1.6-380°C included similar amorphous character with an additional anodic feature at 2.061 ± 0.011 V and a complimentary cathodic peak at 1.682 ± 0.002 V (379 mV peak separation), consistent with typical anatase lithiation.[24,85] Yet higher calcination temperature led MT1.6-600°C to have more prominent anatase peaks with less amorphous content (**Figure 3.4**). It is noteworthy that the amorphous peak shape seen in CV changes considerably with calcination temperature, having very broad character for MT1.6-280°C and a narrow peak for MT1.6-600°C, suggesting increased localization upon further calcination.[8,9] The total lithiation capacity for these two samples were similar at 476.8 ± 17.34 C/g_{TiO2} and 516.2 ±

15.53 C/g_{TiO2} at 280 °C and 600 °C respectively (v = 2.5 mV/s, **Figure B.4a**, **Table B.5**). Compared to the 604 C/ theoretical capacity for $Li_{0.5}TiO_2$, these capacities correspond to $Li_{0.40\text{-}0.43}TiO_2$. The fraction of lithiation current/capacity attributed to amorphous and anatase phases were determined by integration of the anatase peak upon the tail of the amorphous peak with a suitable baseline (**Figure B.5**). Since all samples had similar gravimetric capacity regardless of amorphous content, the mass of the amorphous phase (g_{amor}) was calculated as the product of the amorphous coulombic fraction (Coul.%amor) with the TiO_2 mass (g_{TiO2}) determined via integration (SI Figure S4). Repeated CV cycles at 25.0 mV/s on all samples reported here revealed relatively constant lithiation capacity without apparent degradation **(Figure B.6**). While both amorphous and anatase contributions were recorded, this manuscript focuses on the changes to the character and performance of the amorphous phase.

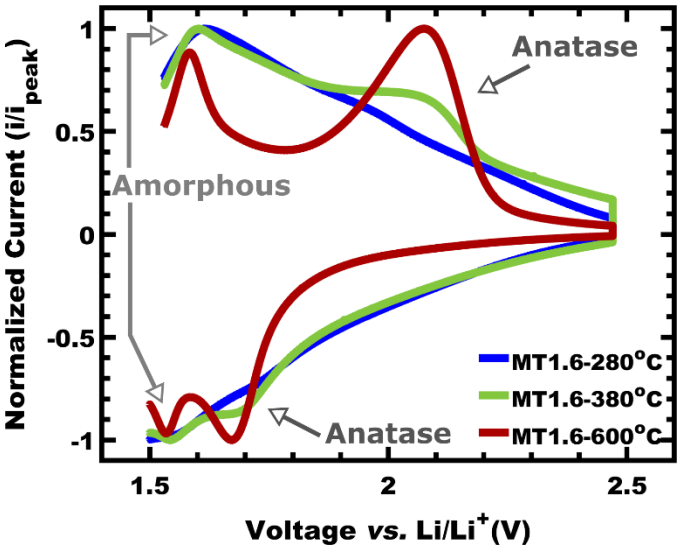

Figure 3.4. Normalized cyclic voltammograms of representative samples (M:T = 1.6) calcined at 280 °C, 380 °C, and 600 °C. The voltage window was 1.5 – 2.5 V vs Li/Li^+ with an electrolyte of 1 M $LiClO_4$ in propylene carbonate (PC) and a voltage sweep rate of 2 mV/s. The corresponding peaks from amorphous TiO_2 and anatase TiO_2 are indicated with arrows.

The electrochemical kinetics were analyzed by comparing peak current densities to the voltage sweep rates. Series of CV data were acquired over a range of v (**Figure 3.5a**), and the corresponding amorphous phase peak currents were plotted on log-log axes (**Figure 3.5b)**. First representative data from MT1.6-280°C are described before making comparisons between sample conditions. CV current responses are often modeled with a power law relationship:[31]

$$\boldsymbol{i_p = av^b} \quad (1)$$

where i_p is the peak current, a is a coefficient, and b ("b-value") is a power dependence. The b-value is useful to ascribe the type of rate-limiting process(es) where $i \propto v$ (b = 1.0) indicates a dominant surface-limited process, $i \propto v^{0.5}$ (b = 0.5) indicates a dominant semi-infinite diffusion-limited process, and intermediate values can indicate a convolution thereof. The noted log-log axes are convenient since the corresponding derivative yields the b-value as a function of v (b-value(v)) and can thus indicate transitions of the type of rate-limiting process (**Figure 3.5c**). For example, the b-value for the amorphous phase is proximal to 1.0 for sweep rates up to ~40 mV/s, indicating surface-limited behavior. The combination of surface-limited kinetics with energy storage via intercalation warrant the behavior classification as intercalation pseudocapacitance. As v increases further, the b-value lowers from 0.9 to 0.7, indicating a progressively increasing contribution from a diffusion-limited process. Condition MT1.6-280°C departs from surface-limited kinetics (b = 0.9) at v_{SLT} = 42.86 ± 0.04 mV/s where b = 0.9.[27] The v_{SLT} thus corresponds to the onset of diffusive limitations to the overall kinetics. Isomorphic series will later be compared to assign these diffusive limitations with specificity. Next attention is turned to changes within a given architecture as function of extent of amorphization.

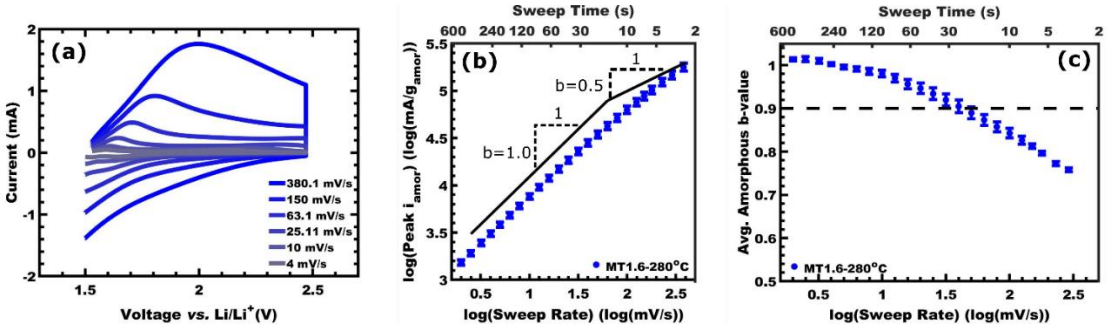

Figure 3.5. (a) Representative cyclic voltammograms at different voltage sweep rates for sample MT1.6-280°C. (b) A log-log plot of the anodic amorphous peak current vs. voltage sweep rate. The amorphous current was normalized per g of total TiO_2 and per the coulombic % amorphous (Table B.5). The slope (b-value) of this log-log plot identifies the type of rate-limiting process. (c) The corresponding derivative plots the b-value as a function of voltage sweep rate. The surface-limited threshold (SLT) denotes the departure from surface-limited kinetics (dashed line, b=0.9). Plotted points correspond to mean values ± the standard error-of-the-mean.

Samples with constant M:T ratio have nearly identical architecture and thus comparisons of the effects of different calcination temperatures largely reveal changes to the material itself. The amorphous peak current values and b-values(ν) with calcination temperature alone are shown in **Figure3.6**. Comparing peak currents with amorphous mass normalization at the lowest ν ($b \approx 1.0$, 2.5 mV/s) provides an indication of the rate of the surface-limited step (**Figure 3.6a**, **Figure B.7**). The temperature series MT1.6-280°C-12hr and MT1.6-290°C-12hr conditions, both purely amorphous by WAXS and CV, had no significant difference in peak current (ν = 2.5 mV/s) indicating a similar surface reaction rate (**Figure 3.6a**). In contrast, the ν_{SLT} for MT1.6-280°C-12hr was 57.6% higher than that for MT1.6-290°C-12hr (**Figure 3.6b-c**, **Table B.5**), indicating a significant acceleration in the diffusion-limited process. Considering the nearly identical nanostructures, this change is most likely associated with the solid-state lithium diffusivity, an assessment that is later supported with additional experiments. With further increasing calcination temperature, the amorphous CV shape narrows (**Figure 3.4**), limiting peak current comparisons between

the lowest and highest calcination temperatures. Comparison of amorphous mass normalized peak currents for MT1.6-420°C-12hr, MT1.6-450°C-12hr, and MT1.6-600°C-1hr revealed no statistically significant difference, in contrast, MT1.6-420°C-12hr had a 21.5% higher amorphous ν_{SLT} than MT1.6-600°C-1hr, again indicating that the diffusion-limited process was fastest with the lowest calcination temperatures (**Figure 3.6b-c**, **Table B.5**). Prior computational and experimental studies identified that amorphous TiO_2 can have faster solid-state lithium diffusion than anatase (binary comparison).[29,47,48] The present data indicate a further granular trend where the solid-state lithium diffusivity within the amorphous phase decreases monotonically with calcination temperature. The identity of this specific diffusion-limited process is examined next amongst several candidates.

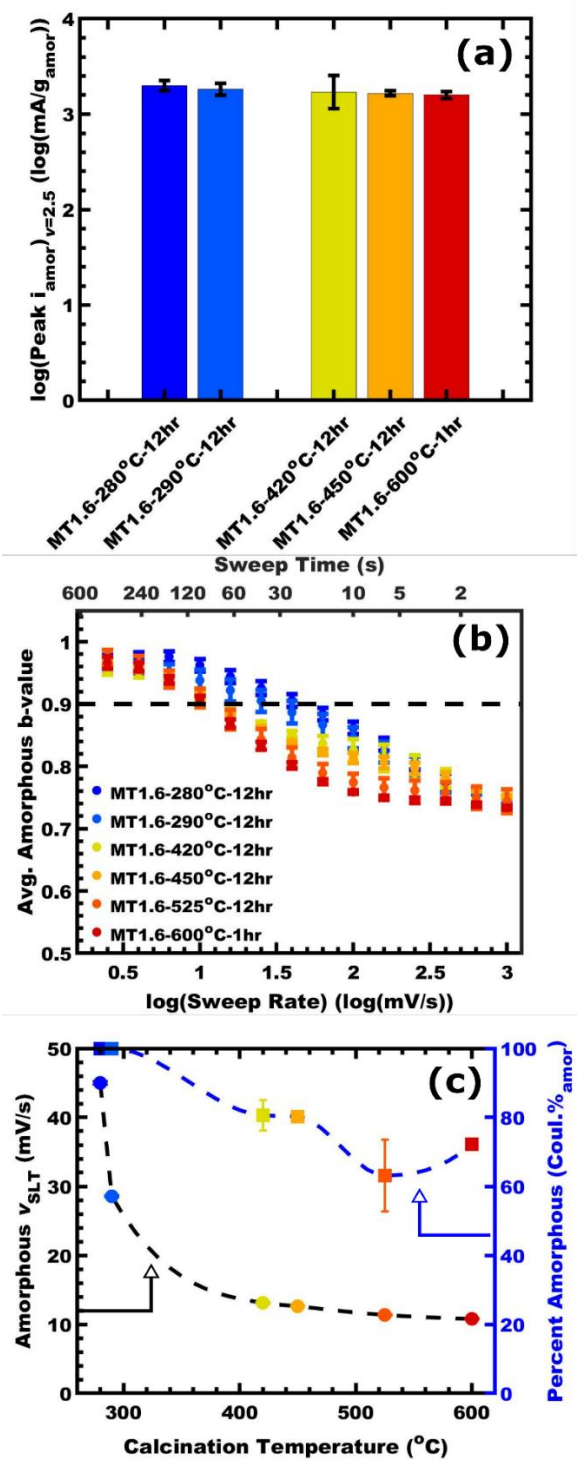

Figure 3.6. Comparisons of M:T=1.6 samples calcined at different temperatures: (a) amorphous peak currents at v=2.5 mV/s, (b) amorphous b-value(v), (c) v_{SLT}, and (c) amorphous content. All plotted points correspond to mean values ± the standard error-of-the-mean.

A series of CV experiments controlling electrolyte concentration, film thickness, and wall thickness were performed to identify the effects of each diffusive transport process upon the electrochemical kinetics. The lithium-ion transport rate from the electrolyte depends upon the pathlength, the volume fraction of pores, and the Li ion concentration. To determine electrolyte transport contributions, the same CV and b-value analysis were performed for conditions, associated with reduced volume fraction of pores that geometrically accompanies thickening of walls, MT2.6-280°C, MT2.6-380°C, and MT2.6-600°C in both 1.0 and 0.5M $LiClO_4$ (**Figure B.8a-d, Figure B.9d-f** and **Table B.6)**. The change in electrolyte concentration did not lead to any significant changes in amorphous peak current nor in ν_{SLT}, indicating that these electrolyte concentrations neither alter the surface-limited reaction rate nor the diffusive electrolyte lithium-ion transport. Next electron transport was examined by altering the film thickness. A 28% increase in film thickness (**Figure B.8**) did not significantly affect the amorphous mass normalized peak current and lead to a general, minor (few mV/s) decreases in the amorphous ν_{SLT} for MT2.6-280°C, MT2.6-380°C(**Figure B.8a, B.8e-f**, **Table B.6, Figure B.9g-i**). For completeness' sake it is noted that the film thickness affects both electrolyte transport and electron transport, however the lack of electrolyte constraints with a larger 50% change in concentration suggests that the observed minor diffusive constraint from film thickness is associated with electron transport alone. Lastly, wall thickness was independently adjusted to vary the solid-state diffusion pathlength by comparing three different M:T ratios at each calcination temperature. Starting with the 280°C M:T series, there was no significant change in amorphous peak current which was surprising that the surface-limited process did not slow down with the reduction of specific surface area associated with reduced

volume fraction of pores that geometrically accompanies thickening of walls (**Figure 3.7a**). Here the similar surface-limited kinetics could be associated with microporosity within the walls and pore roughness due to the limited thermal coarsening, thus the surface area may increase with M:T (Table B.7). For this series the amorphous ν_{SLT} increased significantly from 23.48 ± 0.073 to 42.86 ± 0.04 mV/s with decreasing M:T, corresponding to thinning the wall and decreasing the intercalation length (**Figure 3.7b**, **Table B.6, Figure B.8a**). The maximum ν preserving 95% of the total capacity ($\nu_{95\%}$) similarly increased from 96.89 ± 0.48 to 203.4 ± 2.82 mV/s with thinner walls (Figure 3.7e). Both of these large kinetic changes with wall thickness confirm that solid-state lithium diffusion is the dominant diffusive limiting process. The M:T series calcined at 380°C and 600°C both exhibited a decrease in amorphous mass normalized peak current, indicating the expected decrease in the surface-limited rate when the specific surface area is reduced (**Figure 3.7a**, **c-d, Table B.6, Figure B.8b-c**). The 380°C series exhibited a similarly large increases in amorphous ν_{SLT} and increase in total $\nu_{95\%}$ with decreasing wall thickness, again indicating that solid-state lithium diffusion is the dominant diffusive constraint. The 600°C series, however, exhibited minor variation of amorphous ν_{SLT} and an increase in total $\nu_{95\%}$ with decreasing wall thickness. The lack of a simple ν_{SLT} trend for the 600°C series may be associated with changes to the spatial distribution of the amorphous phase at this high calcination temperature however determination of such is subject for future work and beyond the scope of the report herein. Please note that the amorphous ν_{SLT} trend for the 600°C series was consistent across multiple samples, multiple batches, and repeated measurements and is similar to the value for the closely related sample MT1.6-600°C-1hr (Figure 3.6c). The trend in total $\nu_{95\%}$ for the 600°C series is likely associated with the significant anatase

13.4% increase of the total capacity. These changes in ν_{SLT} and $\nu_{95\%}$ are next compared to quantitative expectations.

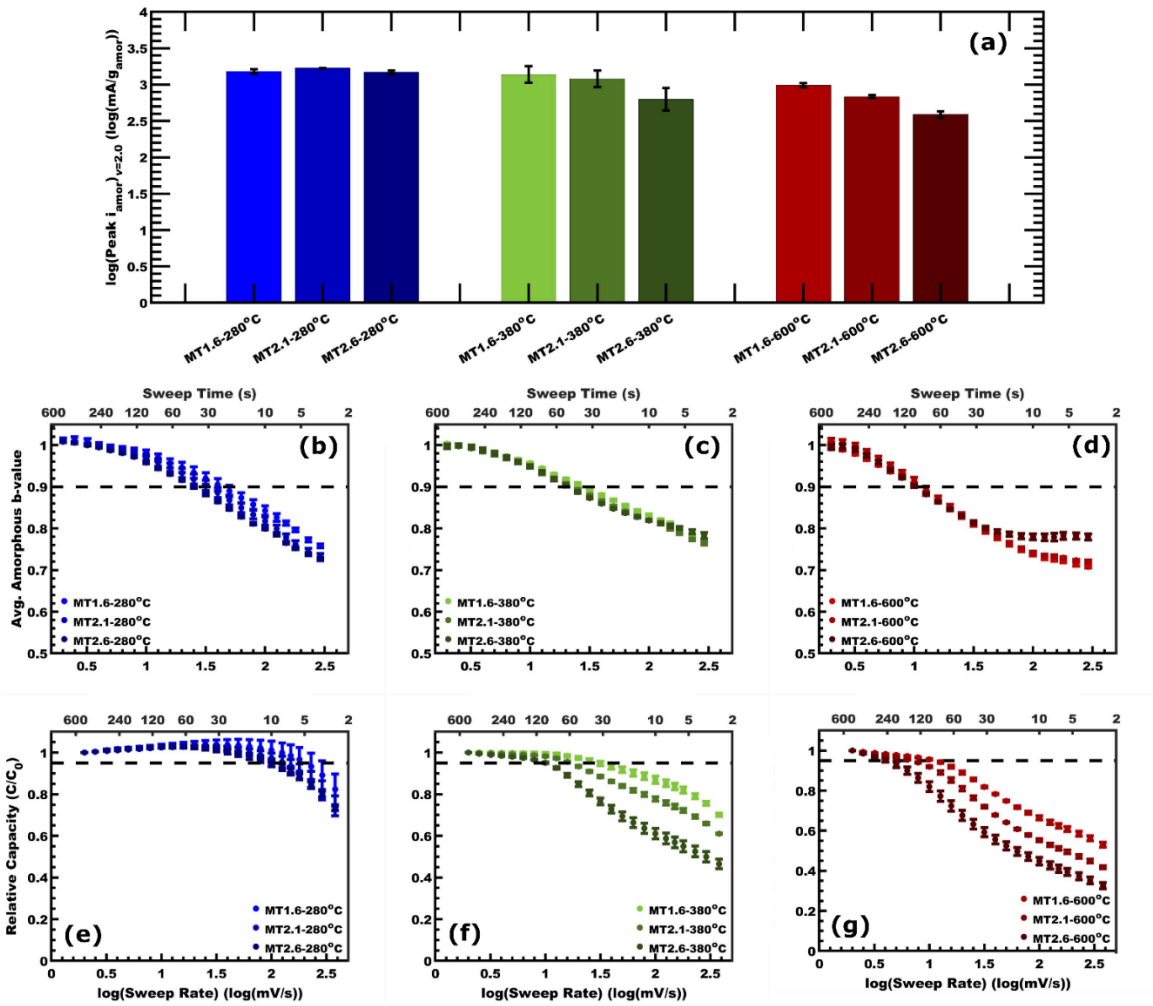

Figure 3.7. Amorphous TiO_2 kinetic constraints from the intercalation length (wall thickness) were examined over a range of isomorphic architectures (indicated M:T values) with different calcination conditions: (b,e) 280 °C, (c,f) 380 °C, and (d,g) 600 °C. Comparisons include (a) amorphous peak currents (b-d) amorphous b-values(ν) and (e-f) relative capacity values(ν). Values are presented as the mean ± standard error-of-the-mean.

The generalized relationship of spatial dimensions to the rates of diffusion-limited process may be estimated using Fick's second law for 1D diffusion with an infinite source[27]:

$$\boldsymbol{x} \propto (\boldsymbol{Dt})^{\mathbf{0.5}} \quad (2)$$

where x is the diffusion length (half the concentration of the source), D is diffusivity, and t is time. With CV the time may be calculated as the voltage window divided by v. Likewise the maximum diffusion length corresponds to half of the wall thickness. Plots of $t^{0.5}$ vs the intercalation length (half wall thickness) are thus expected to yield a linear trend. The amorphous v_{SLT} follows these expectations (**Eqn 3.2**) for both the 280°C and 380°C sample series both with R^2 values of 0.99. As noted earlier the 600°C series did not exhibit monotonic variation of v_{SLT} (**Figure 3.8a)**. Comparison of samples MT1.6-600°C to MT2.6-380°C with similar amorphous content and thicker walls emphasizes the significant increase in solid-state lithium diffusivity for lower temperature calcinations where there is an 86.1% increase in the amorphous v_{SLT} (**Figure B.12)**. The trends for $t_{95\%}$ cleanly corresponded to the linear expectations of EQ2 with $R^2 > 0.94$, again supporting solid state lithium diffusion as the dominant diffusive constraint (**Figure 3.8b)**. Please note that the amorphous t_{SLT} values correspond to the behavior of the amorphous phase alone since the peak currents were not convolved with anatase contributions until higher v-values exceeding the v_{SLT} (see **Figure B.11**). Briefly, the trends in crystalline anatase behavior are examined. Both the 380°C and 600°C series exhibited similar crystalline anatase peak currents for all calcination temperatures within the error of the measures (**Figure B.13, 14a).** In both cases, the b-value(v) decreases monotonically towards b=0.6 with thicker walls, consistent with increasing rate limitation by solid-state diffusion. Comparing the

600°C b-values(v) to those for 380°C suggests faster solid state lithium diffusion for crystalline anatase with more amorphization or alternatively accelerated kinetics from faster nearby amorphous regions.[86] Thus the collection of electrochemical kinetic data indicate that solid state lithium diffusion was the dominant diffusive constraint for these architectures.

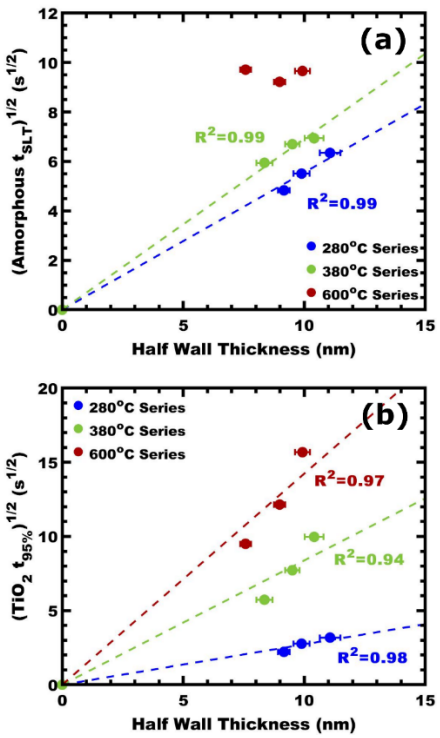

Figure 3.8. Amorphous TiO_2 electrochemical kinetic metrics were compared as a function of the intercalation length (M:T ratio) and calcination temperature. Both plots of (a) $t_{SLT}^{0.5}$ and (b) $t_{95\%}^{0.5}$ vs half wall thickness (intercalation length) should yield linear generalized diffusion-limited processes with $x \propto \sqrt{Dt}$, see EQN 3.2. Values are presented as the mean ± standard error-of-the-mean.

Lastly, the material performance of MT1.6-280°C-12hr, consisting of only active material on a current collector, was compared to high-performing TiO_2 precedents reported in the literature.[29,87–90] This includes ALD-prepared macroporous (2nm) amorphous TiO_2 on Au,[29] hydrothermal TiO_2(B) nanowires (75:18:7, Active:Carbon:Binder),[87]

anatase/graphene (50:2 weight ratio, 80:10:10, Active:Carbon:Binder),[88] electrospun anatase nanotubes (direct deposit on Cu),[89] and amorphous TiO_2/graphene (150:1 weight ratio, 85:10:5, Active:Carbon:Binder).[90] **Figure 3.9** shows the C-rate dependent capacity of these materials. Here C-rate is defined with respect to the inverse of the (dis)charge time, e.g., a 1 hr (dis)charge is a 1C rate whereas a 1-minute ($1/60^{th}$ hr) (dis)charge corresponds to a 60C rate. While C-rate capacities are often measured under galvanostatic conditions, CV data can be analogously presented in terms of C-rate based on the inverse of the sweep time. The general trend is a decrease in capacity with increasing C-rate where the literature precedents here reached 400 C/g between 15-80C-rate, generally due to diffusion constraints. In contrast, condition MT1.6-280°C-12hr with enhanced amorphous TiO_2 diffusivity maintained >400C/g up to an 800C-rate (4.5s). This performance is remarkable considering that the sample was free from conductive additives and was ~50% dense oxide yet demonstrated significant capacity retention with an order of magnitude faster charge rates. With the performance of amorphous materials depending significantly upon the underlying atomic structure (i.e., the extent of amorphization), there is a significant opportunity for future works to characterize the specific atomic structure aspects that lead to such improved electrochemical behaviors as well as synthetic opportunities to prepare pure amorphous (also pure crystalline) samples with deliberately tuned extents of amorphization. The granular extents of amorphization examined here suggest a rich area for additional materials research advancing energy storage devices.

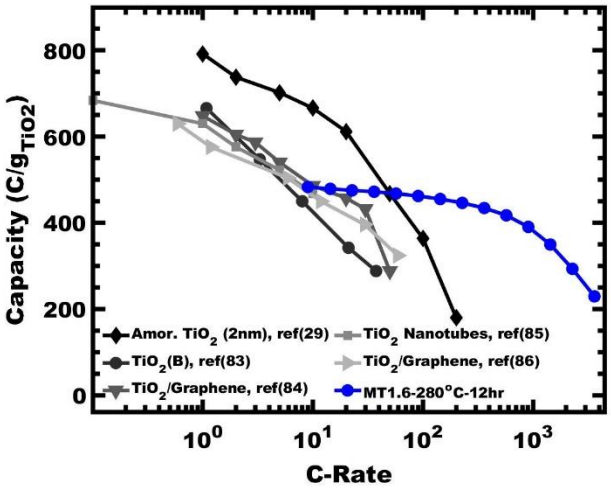

Figure 3.9. The rate-dependent lithiation capacity of MT1.6-280°C is compared to published TiO_2 precedents as a function of C-rate.

3.4 Conclusion

Amorphization is a promising approach to accelerate lithium diffusivity in both amorphous and anatase TiO_2. The increase of lithium diffusivity enables amorphous TiO_2 to exhibit an intercalation pseudocapacitive response with higher voltage sweep rates, enabling access to faster (dis)charge rates with comparable capacity. Going beyond prior binary comparisons, the present study reveals granular changes to both amorphous and anatase TiO_2 as a function of calcination conditions, reflecting the underlying extended continuum between perfect crystals and amorphous disorder. A 317% increase in amorphous v_{SLT}, corresponding to an increase in lithium diffusivity, was found for samples calcined at 280 °C as compared to those at 600 °C. Notably, there were not apparent changes in the surface reaction rate for the amorphous phase as a function of the calcination temperature (fixed M:T, constant nominal specific surface area). The kinetic effects resulting from changes to each of the underlying diffusive transport processes revealed no sensitivity to electrolyte transport, a minor sensitivity to electron transport and a dominant

diffusive constrain from intercalation through the wall thickness. Multiple kinetic metrics were compared to the distance-time (intercalation length $\propto t^{0.5}$) relationship estimated from a simple solution to Fick's second law of diffusion. The temperature dependent behavior of the amorphous phase revealed that its character is sensitive to its degree of disorder, i.e., the degree of amorphization. The corresponding top performer MT1.6-280°C exhibited 95% capacity retention (483 ± 17C/g) with sweep times less than 30 seconds, comparable to a remarkable C-rate of 120C. This study shows how isomorphic sample series can reveal previously unidentified trends and reduce ambiguity amongst diffusion-limited processes that all share the same fundamental $Dt^{0.5}$ dependence.

3.5 Experimental Methods

Materials. Methanol (MeOH, 99.8%, Fisher) was dried at room temperature by storage over 30% w/v of molecular sieves (3 Å, 8-12 mesh, Acros Organics) for a week.[91] Copper(I) bromide (99.99%, Aldrich), tris-(2-dimethylaminoethyl) amine (97%, Aldrich), dry lithium perchlorate ($LiClO_4$, 99.99%, Aldrich), anhydrous propylene carbonate (99.7%, Aldrich), titanium(IV) isopropoxide (TTIP, ≥98%, Acros Organics) were used as received and stored inside an argon-filled glove box. n-Butyl acrylate (+99%, Acros Organics) monomer was passed through basic alumina column just prior to use. 2-Bromopropionic acid (>99%, Aldrich), chloroform (>99.8%, VWR) stabilized with amylene, 4-(dimethylamino) pyridine (+99.0%, TCI America), dimethylformamide (97%, Aldrich), poly(ethylene glycol) methyl ether (PEO-OH, M_n = 5,000 $gmol^{-1}$, Aldrich), hexane (>98.5%, Fisher), concentrated hydrochloric acid (HCl, 37% w/w, ACS grade, VWR), tetrahydrofuran (Fisher, Certified) were used as received.

Polymer Synthesis. Poly(ethylene oxide)-*b*-poly(n-butyl acrylate), PEO-*b*-PBA, diblock polymer was synthesized by a two-step synthesis. A Steglich esterification of poly(ethylene glycol) methyl ether synthesized the macroinitiator, followed by an atom transfer radical polymerization to create the PHA block. The synthesis is described elsewhere in detail.[56] The molar mass of PBA was determined using a Bruker Avance III HD 300 ^{1}H NMR by comparing it to the PEO methyl ether starting material (M_n = 5.0 kg mol^{-1}) (Figure B.1a). The molar mass dispersity was characterized using a Waters gel permeation chromatograph (GPC) equipped with a Waters 1525 binary pump, three styragel columns (HR1, HR3, HR5 in the effective molecular weight range of 0.1–5, 0.5–30, and 2–400 kg mol^{-1}, respectively), and a Waters 2414 refractive index detector with THF as the carrier solvent. The GPC was calibrated with poly(styrene) standards (1.50, 3.28, 10.00, 17.40, 32.70, 120.00, 214.00, 545.00, 1010.00 kg mol^{-1}) obtained from Polymer Standards Service GmbH. GPC samples were prepared in THF at concentrations of 5 mg mL^{-1}, filtered through a 0.2 µm PTFE syringe filter prior to injection (Figure B.1b).

PMT synthesis. A micelle template stock solution was prepared by dispersing PEO-*b*-PBA (25 mg) in MeOH (2.5 mL) before adding concentrated HCl was added slowly to reach 0.7 wt% with respect to the total mixture (PEO-*b*-PBA, MeOH, and HCl). After acid addition, the solution was placed in sonication bath Fisher ultrasonic bath (Cat. no. FS-28) operated continuously at full power (225 W) and frequency of 40 kHz for 10 min at room temperature to enable chain exchange under kinetically limited condition.[60,92]

An *ex-situ* TiO_2 sol stock was used as described in detail elsewhere.[56]Briefly, 5 mL of titanium isopropoxide (TTIP) was added to 1.2 mL of rapidly stirring concentrated HCl

(37% wt %), creating a solution with a 3:1 H_2O/Ti ratio. Note that this reaction is very exothermic. After being allowed to cool for a few minutes, 2 mL of anhydrous MeOH was added to dilute the sol stock solution. This dilute sol stock solution was combined with the micelle template stock solutions described above in varying ratios, depending on the target material to template (M:T) ratio. Here, the M:T ratio is calculated by comparing the anticipated final oxide mass (TiO_2) relative to the mass of the block polymer template. Each film was spin coated for 30 sec at 1,100, 1,100, and 2,00 rpm under 36% relative humidity for each M:T ratio of 1.6, 2.1, and 2.6, respectively as described elsewhere in detail.[58,60,93] Immediately after spin coating, each sample was removed from the humidity-controlled chamber and placed on a 250 °C hot plate overnight, after which the samples were aged at 110 °C until they were prepared for calcination. This processes, termed as "aging," is meant to crosslink the metal oxide were optimized to prevent dewetting and sufficient crosslinking to survive calcination. After each spin coating of a sample, the humidity-controlled spin coating chamber was replaced to avoid residual solvent vapor, as described previously.[58] Glass, silicon, and fluorine doped tin oxide (FTO) substrates were used for SAXS; SEM, Ellipsometry, and TEM; and electrochemistry and ICP-MS, respectively. All samples were calcined with a ramp rate of 5 °C/min to 200 °C followed by a ramp rate of 10 °C/min to the specified temperature denoted by sample name, which was held for 12 hrs, except for MT1.6-600C-1hr which was held for 1hr and allowed to cool to room temperature.

Ellipsometry. Visible light ellipsometry measurements were done with a J.A. Woollam Co. V-VASE ellipsometer. Si substrates coated with TiO_2 architectures calcined at 450 °C for 0.1 hr at a ramp rate of 5 °C/min to 200 °C followed by a ramp rate of 10

°C/min, prepared at different spin coating RPM, were measured from 450 to 1000 nm (Δ2nm) at incident angles of 64, 69, and 74 degrees intending to be below, near, and above Brewster's angle for TiO_2 collecting both Δ and Ψ data. Data analysis was done using Semilab's Spectroscopic Ellipsometry Analyzer (v1.6.6) with the optical model consisting of a Si substrate and a single phase on top whose thickness was determined via Cauchy's dispersion law.[94] The refractive indices used to determine porosity was estimated from literature for both nanoscale anatase,[95] amorphous,[96] and their effective mean contributions[97,98] at 632.8 nm.

X-Ray Scattering Experiments. X-ray experiments were conducted using the SAXSLab Ganesha at the South Carolina SAXS collaborative (SCSC). A Xenocs GeniX 3D microfocus source was used with a copper target to produce monochromatic beam with a 0.154 nm wavelength. The instrument was calibrated prior to measurements using National Institute of Standards and Technology (NIST) reference material, 640d silicon powder with peak position at $2\theta = 28.44°$. A Pilatus 300k detector (Dectris) was used to collect the 2D scattering patterns with nominal pixel dimensions of 172 × 172 μm. SAXS data were acquired with an X-ray flux of ≈3.0 M photon per second upon the sample and a detector-to-sample distance 950 mm. Transmission SAXS data were measured to observe the purely in-plane morphology. The 2D images were azimuthally integrated to yield the scattering vector and intensity. GI-WAXS measurements were conducted with an incident angle (a) of 8° relative to the incident beam. The GI-WAXS sample-to-detector distance was X mm with an X-ray flux of ≈38.0 M photon per second upon the sample. A Gaussian point-spread function was utilized to interpret scattering data from grain-size broadening per the Scherrer formula.[99,100]

Scanning Electron Microscopy. Top-view images of calcined films were acquired with a Zeiss Gemini500 field emission SEM using an accelerating voltage of 5 keV and an in-lens secondary electron detector. The working distance was maintained at ≈4.5 mm and images were acquired at constant 1500 kX magnification. At least 100 measurements were made for each feature (pores and walls) for each condition (temperature and M:T ratio) to determine their statistical metrics using ImageJ software. The wall thickness was measured as the diameter on an inscribed circle between neighboring pores as described elsewhere,[56,62] in addition pore diameter was measured using an inscribed circle method. Pore size and wall thickness are presented as an average ± standard-error-of-the-mean.

Transmission Electron Microscopy. TEM images were acquired using a JEOL 1400 Plus TEM operated in bright field, dark field, and diffraction mode with an accelerating voltage of 120 keV. Samples were prepared by placing a single drop of solution containing suspended mesoporous film, scraped from their substrates with glass, onto a carbon coated 300 mesh copper grids purchased from Electron Microscopy Sciences. The solution was allowed to evaporate to dryness. Samples were collected by first focusing on a single sample area using the selective area aperture in bright field at a magnification of 60,000 X. The instrument was then placed in diffraction mode to observe the diffraction rings at a camera length of 40 cm. Using the objective area aperture, the beam was focused on the outer diffraction rings to avoid amorphous signal near the first diffraction ring. The instrument was then placed in dark field mode to collect an image at that unique position. This process was repeated in a clockwise manner to obtain data for each position around the entire diffraction ring for a single sample.

Inductively Coupled Plasma Mass Spectrometry. A series of films prepared on FTO substrates were cut to ≈1 cm^2 in size with a uniform TiO_2 coating. ImageJ analysis was used to account for the specific substrate area. These films in addition to FTO samples absent of TiO_2 coating were heated at 180 °C for 6 hrs in a Teflon-lined bomb with a 1:3:0.05 mL solution of 70% wt% nitric acid, 37% wt% trace metal grade HCl, 48% wt% trace metal grade HF, respectively. After heating the solutions were diluted with X purity water to a 50 mL total volume and subsequently measured using a Thermo-Finnigan Element XR ICP-MS. The instrument was calibrated using a range of concentrations spanning those of the measured samples (~0 – 30 ug of TiO_2). The resulting mass data were used to determine the average mass per area for each M:T condition. There was no significant difference in mass between calcination temperatures for each M:T.

Electrode Preparation. FTO substrates (TEC-15, Hartford Glass, CT) were rinsed and scrubbed with DI water using Kimwipes until scrubbing produces an audible squeaking noise followed by rinsing and scrubbing with IPA wetted Kimwipes again in the same manner. The substrates were then sonicated in a soapy water bath (2 g L^{-1} deconex) for 30 min. The water and alcohol scrub and rinse steps were repeated as before. The resulting substrates were stored submerged in IPA until near the time of spin coating. Just prior to coating, the FTO substrates were removed from IPA, blown dry. The FTO substrates were held at 110 °C until the moment they were used for spin coating. An uncoated area for electrical contact was maintained by masking part of the substrate with high-temperature Kapton tape as described previously.[27] After spin coating and aging as described above, the edges of the FTO substrates were cleaved to remove edge effects[58] where residual template solution can collect at the substrate edges, resulting in a locally varied film

thickness. The back of each film was engraved with identifying marks for M:T, recipe number, and film number. The Kapton mask was then removed. The ≈1 mm portion of the film proximal to the Kapton mask exhibited an edge effect with local variation of film thickness and was removed by scraping away oxide film with glass prior to calcination as described in previous work.[27] The final active area of each sample was determined by photography over a ruled grid and was analyzed using ImageJ.

Electrochemical analysis. Electrochemical measurements were conducted using a three-electrode setup with a BioLogic SP-150 potentiostat. All measurements were performed in an argon-filled glovebox (<1 ppm O_2, <1 ppm H_2O). The working electrodes were porous TiO_2 prepared using PMT on FTO substrates. The working electrode was held by a home-built titanium metal clamp to assure ohmic contact to the FTO. All potentials are reported versus a Li/Li^+ reference electrode. The counter electrode was also lithium foil ≈540 mm^2 in surface area. All lithium foils were scraped until shiny just prior to immersion in electrolyte. The electrolyte solution was 1.0 M $LiClO_4$ in propylene carbonate. A series of diagnostic cyclic voltammograms and electric impedance spectroscopy measurements were used to verify ohmic contact. The working electrode was then held at 1.5 V for 20 min before cycling from 1.5 to 2.5 V repeatedly 20 times at 25 mV s^{-1} to remove trace contaminants. For the MT1.6 sample temperature series, a series of 14 logarithmically spaced sweeps ranging in rate from 2.5 to 1000 mV/s in order from low to high were run, starting at 1.5 V vs. Li/Li^+. There was a 3-minute voltage hold period at the end of each period, sufficient to intercalate or deintercalation ≥ 99% of reversible Li species in all cases. For the M:T sample series, a series of 24 logarithmically spaced sweeps ranging in rate from 380 to 2.0 mV/s in order from high to low were run, starting at 1.5 V vs Li/Li^+. There

was a 3-minute voltage hold period at the end of each period, sufficient to intercalate or deintercalation ≥ 99% of reversible Li species in all cases. Mass normalization of data was based upon the film area and ICP-measurements of representative samples for each M:T sample condition. Coulombic phase content was calculated by a MATLAB baseline function using linear interpolation between the inflection point after the amorphous peak and the "tail" after the anatase peak (see **Figure B.5**), this curve was used as a "baseline correction" to subtract amorphous CV contribution. Anatase and amorphous coulombic content were assigned as a fraction of the integrated curve assigned to anatase relative to the CV data and the difference thereof, respectively.

3.6 References

[1] D. Larcher, J.-M. Tarascon, *Nature Chem* **2015**, *7*, 19.

[2] J.-M. Tarascon, M. Armand, In *Materials for Sustainable Energy*, Co-Published with Macmillan Publishers Ltd, UK, **2010**, pp. 171–179.

[3] J.-M. Tarascon, *Joule* **2020**, *4*, 1616.

[4] H. Li, A. Liu, N. Zhang, Y. Wang, S. Yin, H. Wu, J. R. Dahn, *Chem. Mater.* **2019**, *31*, 7574.

[5] C. Choi, D. S. Ashby, D. M. Butts, R. H. DeBlock, Q. Wei, J. Lau, B. Dunn, *Nat. Rev. Mater.* **2020**, *5*, 5.

[6] J. B. Goodenough, *Acc. Chem. Res.* **2013**, *46*, 1053.

[7] S. Fleischmann, J. B. Mitchell, R. Wang, C. Zhan, D. Jiang, V. Presser, V. Augustyn, *Chem. Rev.* **2020**, *120*, 6738.

[8] C. Costentin, T. R. Porter, J.-M. Savéant, *ACS Appl. Mater. Interfaces* **2017**, *9*, 8649.

[9] G. Z. Chen, *Prog. Nat. Sci.* **2013**, *23*, 245.

[10] E. Lim, H. Kim, C. Jo, J. Chun, K. Ku, S. Kim, H. I. Lee, I.-S. Nam, S. Yoon, K. Kang, J. Lee, *ACS Nano* **2014**, *8*, 8968.

[11] E. Lim, W.-G. Lim, C. Jo, J. Chun, M.-H. Kim, K. Chul Roh, J. Lee, *J. Mater. Chem. A* **2017**, *5*, 20969.

[12] T. Brezesinski, J. Wang, S. H. Tolbert, B. Dunn, *Nature Materials* **2010**, *9*, 146.

[13] K. Lan, L. Liu, J.-Y. Zhang, R. Wang, L. Zu, Z. Lv, Q. Wei, D. Zhao, *J. Am. Chem. Soc.* **2021**, jacs.1c03433.

[14] E. Lim, C. Jo, J. Lee, *Nanoscale* **2016**, *8*, 7827.

[15] X. Wu, J. J. Hong, W. Shin, L. Ma, T. Liu, X. Bi, Y. Yuan, Y. Qi, T. W. Surta, W. Huang, J. Neuefeind, T. Wu, P. A. Greaney, J. Lu, X. Ji, *Nat. Energy* **2019**, *4*, 123.

[16] S. Zhang, G. Liu, W. Qiao, J. Wang, L. Ling, *J. Colloid Interface Sci.* **2020**, *562*, 193.

[17] Z. Liu, W. Dong, J. Wang, C. Dong, Y. Lin, I.-W. Chen, F. Huang, *iScience* **2020**, *23*, 100767.

[18] X. Zhai, J. Liu, Y. Zhao, C. Chen, X. Zhao, J. Li, H. Jin, *Appl. Surf. Sci.* **2020**, *499*, 143905.

[19] H.-S. Kim, J. B. Cook, H. Lin, J. S. Ko, S. H. Tolbert, V. Ozolins, B. Dunn, *Nat. Mater.* **2017**, *16*, 454.

[20] J.-Y. Shin, J. H. Joo, D. Samuelis, J. Maier, *Chem. Mater.* **2012**, *24*, 543.

[21] T. Xia, W. Zhang, J. B. Murowchick, G. Liu, X. Chen, *Advanced Energy Materials* **2013**, *3*, 1516.

[22] Y. Liu, Z. Wang, J.-P. M. Veder, Z. Xu, Y. Zhong, W. Zhou, M. O. Tade, S. Wang, Z. Shao, *Adv. Energy Mater.* **2018**, *8*, 1702604.

[23] D. Yan, A.-H. Lu, Z.-Y. Chen, L. He, W.-C. Li, *ACS Appl. Energy Mater.* **2021**, *4*, 1824.

[24] M. Wagemaker, W. J. H. Borghols, F. M. Mulder, *J. Am. Chem. Soc.* **2007**, *129*, 4323.

[25] L. Zhong, Y. Liu, W.-Q. Han, J. Y. Huang, S. X. Mao, *Advanced Materials* **2017**, *29*, 1700236.

[26] C. Zhu, R. E. Usiskin, Y. Yu, J. Maier, *Science* **2017**, *358*.

[27] W. van den Bergh, H. N. Lokupitiya, N. A. Vest, B. Reid, S. Guldin, M. Stefik, *Adv. Funct. Mater.* **2021**, *31*, 2007826.

[28] J. S. Ko, C.-H. Lai, J. W. Long, D. R. Rolison, B. Dunn, J. Nelson Weker, *ACS Appl. Mater. Interfaces* **2020**, *12*, 14071.

[29] J. Ye, P. Shea, A. C. Baumgaertel, S. A. Bonev, M. M. Biener, M. Bagge-Hansen, Y. M. Wang, J. Biener, B. C. Wood, *Chem. Mater.* **2018**, *30*, 8871.

[30] J. W. Long, B. Dunn, D. R. Rolison, H. S. White, *Adv. Energy Mater.* **2020**, *10*, 2002457.

[31] H. Lindström, S. Södergren, A. Solbrand, H. Rensmo, J. Hjelm, A. Hagfeldt, S.-E. Lindquist, *J. Phys. Chem. B* **1997**, *101*, 7717.

[32] S. Yoon, C. W. Lee, S. M. Oh, *J. Power Sources* **2010**, *195*, 4391.

[33] M. Kaus, J. Kowal, D. U. Sauer, *Electrochim. Acta* **2010**, *55*, 7516.

[34] R. L. Spyker, R. M. Nelms, *IEEE Trans. Aerosp. Electron. Syst.* **2000**, *36*, 829.

[35] M. Z. Bazant, K. Thornton, A. Ajdari, *Phys. Rev. E* **2004**, *70*, 021506.

[36] K. T. Chu, M. Z. Bazant, *Phys. Rev. E* **2006**, *74*, 011501.

[37] L. Højgaard Olesen, M. Z. Bazant, H. Bruus, *Phys. Rev. E* **2010**, *82*, 011501.

[38] J. S. Ko, M. B. Sassin, J. F. Parker, D. R. Rolison, J. W. Long, *Sustainable Energy & Fuels* **2018**, *2*, 626.

[39] B.-A. Mei, J. Lau, T. Lin, S. H. Tolbert, B. S. Dunn, L. Pilon, *J. Phys. Chem. C* **2018**, *122*, 24499.

[40] B.-A. Mei, L. Pilon, *Electrochim. Acta* **2017**, *255*, 168.

[41] B.-A. Mei, O. Munteshari, J. Lau, B. Dunn, L. Pilon, *J. Phys. Chem. C* **2018**, *122*, 194.

[42] Z. Chen, H. Li, X. Lu, L. Wu, J. Jiang, S. Jiang, J. Wang, H. Dou, X. Zhang, *ChemElectroChem* **2018**, *5*, 1516.

[43] G. Wang, Y. Ling, Y. Li, *Nanoscale* **2012**, *4*, 6682.

[44] M. Dieterle, G. Weinberg, G. Mestl, *Phys. Chem. Chem. Phys.* **2002**, *4*, 812.

[45] J.-Y. Shin, D. Samuelis, J. Maier, *Solid State Ion.* **2012**, *225*, 590.

[46] D. Lee, H. Lee, Y.-T. Kim, K. Lee, J. Choi, *Electrochim. Acta* **2020**, *330*, 135192.

[47] J. A. Yuwono, P. Burr, C. Galvin, A. Lennon, *ACS Appl. Mater. Interfaces* **2021**, *13*, 1791.

[48] C. Arrouvel, T. C. Peixoto, M. E. G. Valerio, S. C. Parker, *Computational and Theoretical Chemistry* **2015**, *1072*, 43.

[49] H. Kaper, S. Sallard, I. Djerdj, M. Antonietti, B. M. Smarsly, *Chem. Mater.* **2010**, *22*, 3502.

[50] D. Fattakhova-Rohlfing, M. Wark, T. Brezesinski, B. M. Smarsly, J. Rathouský, *Adv. Funct. Mater.* **2007**, *17*, 123.

[51] J. Procházka, L. Kavan, M. Zukalová, O. Frank, M. Kalbáč, A. Zukal, M. Klementová, D. Carbone, M. Graetzel, *Chem. Mater.* **2009**, *21*, 1457.

[52] M. Zukalová, M. Kalbáč, L. Kavan, I. Exnar, M. Graetzel, *Chem. Mater.* **2005**, *17*, 1248.

[53] L. Kavan, M. Kalbáč, M. Zukalová, I. Exnar, V. Lorenzen, R. Nesper, M. Graetzel, *Chem. Mater.* **2004**, *16*, 477.

[54] V. Augustyn, P. Simon, B. Dunn, *Energy Environ. Sci.* **2014**, *7*, 1597.

[55] J. Xie, P. Yang, Y. Wang, T. Qi, Y. Lei, C. M. Li, *Journal of Power Sources* **2018**, *401*, 213.

[56] K. A. Lantz, N. B. Clamp, W. van den Bergh, A. Sarkar, M. Stefik, *Small* **2019**, *15*, 1900393.

[57] H. N. Lokupitiya, A. Jones, B. Reid, S. Guldin, M. Stefik, *Chem. Mater.* **2016**, *28*, 1653.

[58] A. Sarkar, M. Stefik, *J. Mater. Chem. A* **2017**, *5*, 11840.

[59] A. Sarkar, A. Thyagarajan, A. Cole, M. Stefik, *Soft Matter* **2019**, *15*, 5193.

[60] A. Sarkar, L. Evans, M. Stefik, *Langmuir* **2018**, *34*, 5738.

[61] E. R. Williams, P. L. McMahon, J. E. Reynolds, J. L. Snider, V. Stavila, M. D. Allendorf, M. Stefik, *Mater. Adv.* **2021**, 10.1039.D1MA00146A.

[62] W. van den Bergh, E. R. Williams, N. A. Vest, P.-H. Chiang, M. Stefik, *Langmuir* **2021**.

[63] M. C. Orilall, U. Wiesner, *Chem. Soc. Rev.* **2011**, *40*, 520.

[64] M. Stefik, *J. Mater. Res.* **2021**.

[65] E. J. W. Crossland, P. Cunha, S. Ludwigs, M. A. Hillmyer, U. Steiner, *ACS Appl. Mater. Interfaces* **2011**, *3*, 1375.

[66] E. J. W. Crossland, M. Nedelcu, C. Ducati, S. Ludwigs, M. A. Hillmyer, U. Steiner, H. J. Snaith, *Nano Lett.* **2009**, *9*, 2813.

[67] R. Dehmel, J. A. Dolan, Y. Gu, U. Wiesner, T. D. Wilkinson, J. J. Baumberg, U. Steiner, B. D. Wilts, I. Gunkel, *Macromolecules* **2017**, *50*, 6255.

[68] P. Docampo, S. Guldin, M. Stefik, P. Tiwana, M. C. Orilall, S. Hüttner, H. Sai, U. Wiesner, U. Steiner, H. J. Snaith, *Adv. Funct. Mater.* **2010**, *20*, 1787.

[69] O. Kim, S. Y. Kim, J. Lee, M. J. Park, *Chem. Mater.* **2016**, *28*, 318.

[70] M. Nedelcu, J. Lee, E. J. W. Crossland, S. C. Warren, M. C. Orilall, S. Guldin, S. Hüttner, C. Ducati, D. Eder, U. Wiesner, U. Steiner, H. J. Snaith, *Soft Matter* **2008**, *5*, 134.

[71] P. Sutton, P. Bennington, S. N. Patel, M. Stefik, U. B. Wiesner, P. F. Nealey, U. Steiner, I. Gunkel, *Adv. Funct. Mater.* **2019**, *29*, 1905977.

[72] A. Vu, Y. Qian, A. Stein, *Adv. Energy Mater.* **2012**, *2*, 1056.

[73] T. Marks, S. Trussler, A. J. Smith, D. Xiong, J. R. Dahn, *J. Electrochem. Soc.* **2011**, *158*, A51.

[74] V. Murray, D. S. Hall, J. R. Dahn, *J. Electrochem. Soc.* **2019**, *166*, A329.

[75] P. Mohapatra, S. Shaw, D. Mendivelso-Perez, J. M. Bobbitt, T. F. Silva, F. Naab, B. Yuan, X. Tian, E. A. Smith, L. Cademartiri, *Nat. Commun.* **2017**, *8*, 2038.

[76] B. Reid, A. Taylor, A. Alvarez-Fernandez, M. H. Ismael, S. Sharma, B. Schmidt-Hansberg, S. Guldin, *ACS Appl. Mater. Interfaces* **2019**, *11*, 19308.

[77] C. Robertus, W. H. Philipse, J. G. H. Joosten, Y. K. Levine, *J. Chem. Phys.* **1989**, *90*, 4482.

[78] L. Kavan, J. Rathouský, M. Grätzel, V. Shklover, A. Zukal, *J. Phys. Chem. B* **2000**, *104*, 12012.

[79] R. Marchand, L. Brohan, M. Tournoux, *Mater. Res. Bull.* **1980**, *15*, 1129.

[80] M. Kobayashi, V. V. Petrykin, M. Kakihana, K. Tomita, M. Yoshimura, *Chem. Mater.* **2007**, *19*, 5373.

[81] A. G. Dylla, J. A. Lee, K. J. Stevenson, *Langmuir* **2012**, *28*, 2897.

[82] L. Kavan, *Chem. Rec.* **2012**, *12*, 131.

[83] Y. Chimupala, P. Junploy, T. Hardcastle, A. Westwood, A. Scott, B. Johnson, R. Brydson, *J. Mater. Chem. A* **2016**, *4*, 5685.

[84] W. V. Metanomski, Ed., *Compendium of Macromolecular Nomenclature*, 1st ed., International Union of Pure and Applied Chemistry., **1991**.

[85] S. Liang, X. Wang, Y.-J. Cheng, Y. Xia, P. Müller-Buschbaum, *Energy Storage Materials* **2021**.

[86] G. Gregori, R. Merkle, J. Maier, *Progress in Materials Science* **2017**, *89*, 252.

[87] A. R. Armstrong, G. Armstrong, J. Canales, R. García, P. G. Bruce, *Advanced Materials* **2005**, *17*, 862.

[88] X. Xin, X. Zhou, J. Wu, X. Yao, Z. Liu, *ACS Nano* **2012**, *6*, 11035.

[89] H. Han, T. Song, E.-K. Lee, A. Devadoss, Y. Jeon, J. Ha, Y.-C. Chung, Y.-M. Choi, Y.-G. Jung, U. Paik, *ACS Nano* **2012**, *6*, 8308.

[90] W. Li, F. Wang, S. Feng, J. Wang, Z. Sun, B. Li, Y. Li, J. Yang, A. A. Elzatahry, Y. Xia, D. Zhao, *J. Am. Chem. Soc.* **2013**, *135*, 18300.

[91] D. B. G. Williams, M. Lawton, *J. Org. Chem.* **2010**, *75*, 8351.

[92] K. A. Lantz, A. Sarkar, K. C. Littrell, T. Li, K. Hong, M. Stefik, *Macromolecules* **2018**, *51*, 6967.

[93] H. N. Lokupitiya, M. Stefik, *Nanoscale* **2017**, *9*, 1393.

[94] Z. Qi, I. Honma, H. Zhou, *J. Phys. Chem. B* **2006**, *110*, 10590.

[95] Y. Sheng, L. Liang, Y. Xu, D. Wu, Y. Sun, *Optical Materials* **2008**, *30*, 1310.

[96] W. Shimizu, S. Nakamura, T. Sato, Y. Murakami, *Langmuir* **2012**, *28*, 12245.

[97] D. J. Kim, S. H. Hahn, S. H. Oh, E. J. Kim, *Materials Letters* **2002**, *57*, 355.

[98] E. Haimi, H. Lipsonen, J. Larismaa, M. Kapulainen, J. Krzak-Ros, S.-P. Hannula, *Thin Solid Films* **2011**, *519*, 5882.

[99] P. Scherrer, *Math. Phys.* **1918**, *2*, 98.

[100] A. L. Patterson, *Phys. Rev.* **1939**, *56*, 978.

CHAPTER 4: Disambiguation of Structure and Amorphization Effects on Performance of T-Nb_2O_5 Architectures[1]

[1] v. d. Bergh, W.; Wechsler, S.; Lokupitiya, H. N.; Jarocha, L.; Kim, K.; Chapman, J.; Kweon, K. E.; Wood, B. C.; Heald, S.; Stefik, M. *Batteries & Supercaps*, 2022, ASAP.

4.1 Abstract

Intercalation pseudocapacitance can combine capacitor-like power densities with battery-like energy densities. Such surface-limited behavior requires rapid diffusion where amorphization can increase solid-state diffusivity. Here intercalation pseudocapacitance with tailored extents of amorphization in T-Nb_2O_5 is first reported. Amorphization was characterized with WAXS, XPS, XAFS, and EPR which suggested a peroxide-rich (O_2^{2-}) surface that was consistent with DFT predictions. A series of tunable isomorphic architectures enabled comparisons while independently varying transport parameters. Through process of elimination, solid-state lithium diffusion was identified as the dominant diffusive-constraint dictating the maximum voltage sweep rate for surface-limited kinetics (v_{SLT}), termed the Surface-Limited Threshold (SLT). The v_{SLT} increased with amorphization however stable cycling required crystalline T-Nb_2O_5. A current-response model using series-impedances well-matched these observations. This perspective revealed that amorphization of T-Nb_2O_5 enhanced solid-state diffusion by 12.2% and increased surface-limitations by 17.0% (stable samples). This approach enabled retaining 95% lithiation capacity at ~800 mV s^{-1} (1,600 C-rate equivalent).

4.2 Introduction

The broad demand for electrochemical energy storage materials with high energy density and rapid (dis)charge times has motivated widespread research into new electrode chemistries and tailored electrode architectures.[1–6] Current lithium-ion batteries and electrochemical double-layer capacitors do not meet these simultaneous demands with the former suffering from sluggish solid-state kinetics and the latter from low energy density.[7–9] Pseudocapacitive[10–15] behavior combines rapid surface-limited kinetics with faradaic

energy storage mechanisms and is a path towards concomitant high power and energy densities. Early studies[16–18] on RuO_2 were the first reports of pseudocapacitance based upon faradaic surface reactions[16] but more recent work on orthorhombic ("Tief") T-Nb_2O_5 have identified a similar kinetic response with an intercalation-based mechanism.[19,20] Here the rate of lithiation naturally depends upon the nanoscale architecture and the implied transport pathlengths for electrons, electrolytes, and solid-state ion intercalation.[21] This concomitant set of transport processes along with the surface reaction determine the overall rate capability which may be limited by either diffusion processes or the surface reaction. With increasing voltage sweep rate (v), the transition from the surface-limited regime towards the diffusion-limited regime reflects the balance of these processes and was recently termed the surface-limited threshold (SLT).[21] Surface-limited kinetics are possible when the overall rate is not limited by diffusive processes and there is an absence of a crystallographic phase changes upon intercalation.[22–26] Numerous nanoscale niobia structures have been reported with an emphasis on individual performance metrics.[27–74] A few investigations have approached the relationship between nanostructure and T-Nb_2O_5 performance using computational models,[75] advanced electrochemical techniques,[76] tunable nanotubes,[77] and core-shell particles[78,79] without experimentally isolating the rate-limiting process(es). In contrast, changing a single transport parameter at a time recently enabled the first unambiguous identification of solid-state lithium diffusion as the dominant diffusion-limited process in T-Nb_2O_5 lithiation as a function of the extrinsic nanostructure.[21]

Solid-state lithium diffusivities vary widely with composition and crystal structure where amorphization is recently being explored as a route to accelerate known materials.

Amorphization is broadly defined here as the deliberate inclusion of defects where the extent of amorphization spans the continuous gamut from perfect crystals to amorphous materials.[80] While the specific electrochemical observations vary widely, amorphization has sometimes led to increased performance[45,64,68,81–84] with diverse intercalation materials. Many past works have examined oxygen vacancies and dopants. Dopants are usually introduced to improve electrical conductivity with electron donating species[45,68] while oxygen vacancies have also improved electrical conductivity[81–83,85] in addition to enhanced lithium diffusivity,[64,82] increased lithiation capacity,[64,68,81–83] and enhanced stability[82] depending on the vacancy concentration. A recent comparison of crystalline anatase and amorphous TiO_2 reported the latter's higher diffusivity due to lower activation energy for Li hops between sites.[84,86] For T-Nb_2O_5 lithiation, some reports indicated amorphization of T-Nb_2O_5 via oxygen vacancies enhanced performance[64,68,83] whereas the amorphous phase itself had greatly lowered lithiation capacity and/or slower kinetics.[19,22,24,25,62,71] Past works have also compared lithiation performance of different Nb_2O_5 crystallographic phases.[22,24,25,57,62,71,87,88] Thermal treatments are conventionally used for crystallization (lowered amorphization). It should be recognized however that there is a continuum for the extent of amorphization along the path from an amorphous solid to a perfect crystal. One of the challenges when comparing samples from different heat treatments is that the nanoscale architecture may simultaneously change, convolving multiple variables and adding causal ambiguity. Here changes in specific electrochemical processes are attributed to tailored extent of T-Nb_2O_5 amorphization by comparing series of isomorphic nanoscale architectures to enable unambiguous interpretation.

The use of persistent micelle templates (PMT) enables the production of tunable isomorphic architectures that alter a single spatial-variable at a time.[21,89–93] With PMT, the material wall thickness is independently tailored while preserving a constant average pore diameter by using kinetically trapped micelles as templates. PMTs are based upon kinetic control where the solution conditions impose a large enthalpic barrier to polymer chain exchange between micelles.[21,89–93] Furthermore, the preservation of spherical micelle templates leads to isomorphic series with relatively constant tortuosity owing to simple sphere packing.[94] In contrast, typical block polymer-based methods rely upon equilibration which couples all architectural attributes as well as the morphology to free-energy minimization.[95,96] With PMT, the subsequent thermal treatment removes the micelle template and converts the material precursors to the desired material. The time and the temperature of this heat treatment reduces the extent of amorphization as the material further crystalizes. Here the effect of tailored amorphization upon the pseudocapacitive response of orthorhombic niobia nanostructures is systematically elaborated. Furthermore, a revised i(v) model for CV is shown to be congruent with observations and enables quantitative parsing of surface-limited and diffusion-limited contributions.

4.3 Results and Discussion

Both material and architecture determine electrode performance. Amorphization is known to augment material performance however the assessment of that change independently is challenging since modifications to heat treatments can simultaneously alter architectural parameters, for example, the pore size and wall thickness. On the other hand, the use of tunable isomorphic architectures provides a unique perspective to reveal architectural effects alone. Thus, a strategy combining material modifications

(amorphization) in concert with controlled architectural variations can yield more direct insights to nanoscale cause-and-effect relationships. Here tunable isomorphic architectures were produced using PMTs composed of poly(ethylene oxide-*b*-hexyl acrylate) (**Figure C.1**) dispersed in EtOH/HCl(aq). A material precursor (niobium ethoxide) was added in various proportions to determine the material:template (M:T) ratio. For PMT conditions, the M:T ratio directly determines the wall thickness while maintaining a constant template/pore diameter. The resulting sample series were heated to different calcination temperatures to adjust the extent of amorphization while removing the polymer micelles and producing porosity. Scanning electron microscope (SEM) images are shown for a series of samples in **Figure 4.1** with M:T = 1.2-3.0 and calcination temperatures from 520-600 °C. The samples are named using these two attributes in sequence (e.g. MT1.2-520°C) and a consistent color scheme is used throughout where the hue corresponds to the calcination temperature and the shade corresponds to the M:T ratio. The SEM images were all consistent with disordered packing of ~95 nm spherical pores (dark) with an average wall thickness (light) that ranged from ~45-80 nm, increasing with M:T ratio (**Figure 4.2e-f**). Small-angle X-ray scattering patterns from the samples exhibited 2-3 peaks with approximate q-ratios of 1:2:3, consistent with randomly packed spheres.[97] The main SAXS peak shifts to lower q-spacing with increasing M:T ratio, corresponding to the lattice expansion that is expected with PMT behavior (Figure 4.2a-c). The corresponding d-spacing ($2\pi/q^*$) trends were all well fitted using a PMT model (**SI Equations C.1-C.3**, Figure 4.2d). The resulting best-fit parameters are shown in **SI Table C.3** where the average pore size increased slightly with calcination temperature due to further densification of the wall material. This densification is associated with reduced extent of

amorphization where for example, grain boundaries and vacancies are anticipated to be reduced in prevalence. Thus, several sample series with isomorphic architectures were prepared with independent variation of wall thickness and nearly independent variation of amorphization extent.

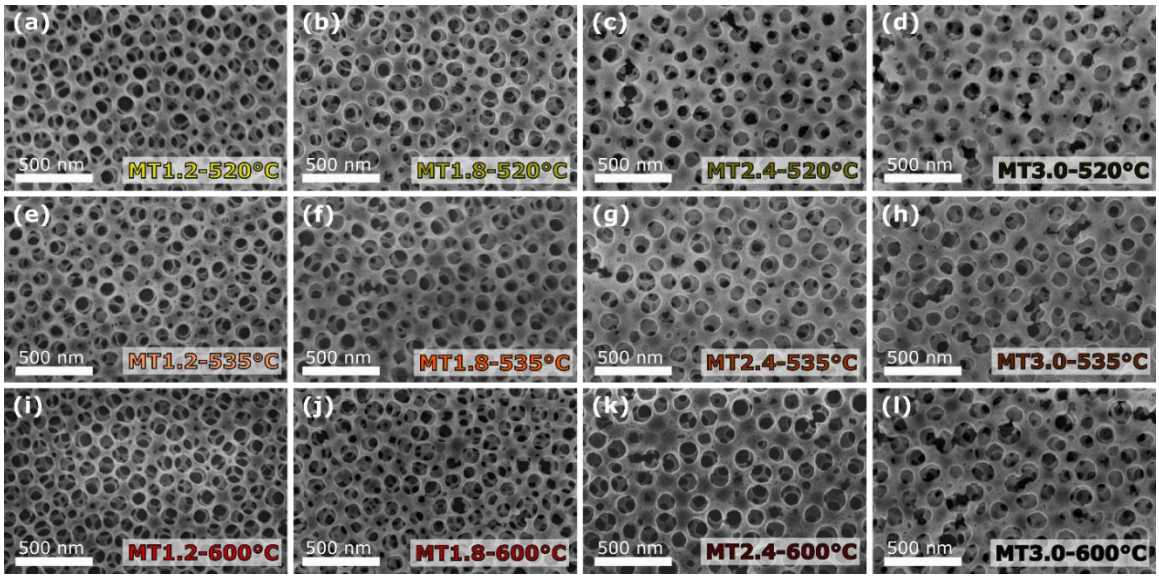

Figure 4.1. (a-l) SEM images of the isomorphic series of porous niobia samples prepared with persistent micelle templates using different material:template (M:T) ratios and different calcination temperatures. The M:T ratios and calcination temperatures are noted in each panel. Subsequent figures preserve this color scheme with the hue corresponding to the calcination temperature and the shade corresponding to the M:T ratio.

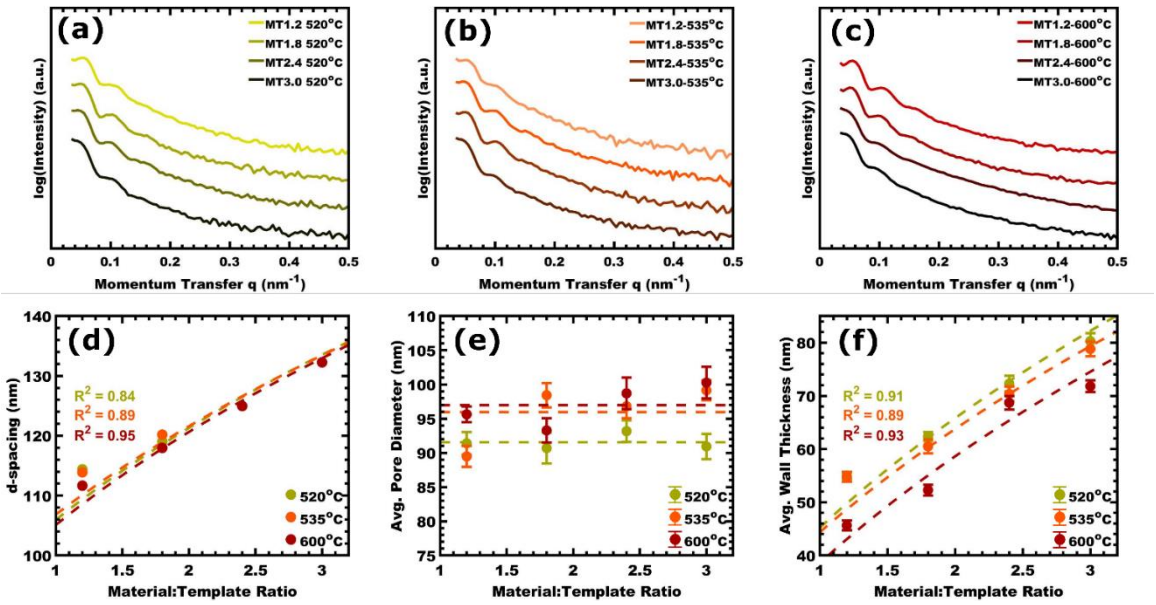

Figure 4.2. (a-c) SAXS patterns for all samples from the isomorphic series arranged by calcination temperature: (a) 520 °C, (b) 535 °C, (c) 600 °C. SAXS data were offset vertically for clarity. (d) The corresponding d-spacing ($2\pi/q^*$) trends reveal lattice expansion upon increasing material-to-template ratio (M:T). (e) The mean pore diameters and (f) mean wall thicknesses were determined from numerous measurements upon SEM images and were compared the best-fit of the PMT model. The error bars correspond to the error-of-the-mean. (d-f) Each of these metrics were compared to the PMT model (dashed lines) with goodness-of-fit (R^2) indicated. Values presented as mean ± standard error-of-the-mean.

The extent of amorphization was characterized by X-ray scattering, X-ray adsorption spectroscopy, X-ray photoelectron spectroscopy (XPS), and electron paramagnetic resonance (EPR). Grazing-incidence wide-angle X-ray scattering (GIWAXS) patterns for fixed M:T = 1.8 and calcination temperature ranging from 475-600 °C are shown in **Figure 4.3a**. Whereas MT1.8-475°C was largely amorphous in character, the samples with higher calcination temperatures exhibited a series of peaks consistent with the orthorhombic T-Nb_2O_5. The peaks generally were narrower with higher temperature calcination. Scherrer analysis quantified the average crystallite size (without considering strain effects) where e.g. the samples with M:T = 1.8 exhibited an increasing

average crystallite size trend of 12.8, 13.7, 13.5, 13.9, and 14.3 nm when calcined at 500, 520, 535, 550, and 600 °C, respectively (Figure 4.3b). Such growth of progressively larger crystals can be accomplished either by the crystallization of amorphous regions or by Ostwald ripening of existing crystals. There was also an overall trend of increasing crystallite size with M:T ratio (increasing wall thickness). These observations indicate, as expected, that calcination promotes crystallization where the highest extent of amorphization occurs with the lowest calcination temperatures. Extended X-ray absorption fine structure (EXAFS) measurements were acquired near the Nb K-edge for samples spanning M:T = 1.2-3.0 and calcination temperatures spanning 300-600 °C (**Figure C.2a**). The k^2-weighted Fourier transform of $\chi(k)$ data exhibited known[20,98–100] Nb-O and Nb-Nb peaks with atomic distances at ~0.8 - 2 Å and ~2.4 - 4 Å, respectively (**Figure 4.4c**). Sample changes were compared using linear combination analysis (LCA) between the calcination endpoints of 300 °C (most amorphous) and 600 °C (most crystalline). The k^2-weighted $\chi(k)$ EXAFS data were similar within most M:T conditions (Figure C.2a) thus the corresponding average deconvolutions (crystalline vs amorphous) were compared. The resulting Figure 4f reveals a sigmoidal transition for niobia from amorphous to crystalline character that onsets around 500°C, similar to the GIWAXS trend, and the majority of samples were adequately fitted with two endpoint components. A few samples had significant residuals when fitted using these two components, where principle component analysis identified a third unknown component in these cases. The third component was not consistent with either pseudohexagonal TT-Nb_2O_5 nor T-Nb_2O_5 prepared via solid state synthesis[24] (Figure C.2b) with the former standard having negligible contribution to additional LCA analysis (**Table C.4**). The third component could perhaps be a distinct

amorphous motif, but its further study is beyond the scope of this manuscript. Analysis of niobia crystal structures remains complex with multiple Nb-sites, partial occupancies, and a diversity of similar phases with minor differences in diffraction patterns.[99,100] XPS spectra were acquired on samples spanning from 520-600 °C (Figure 4.4a-b). One notable feature was the gradual decrease in Nb $3d_{5/2}$ energy with increasing calcination temperature. A recent XPS study identified a similar shift in the Nb $3d_{5/2}$ peak location upon a calcination induced amorphous-crystalline transition, attributed to the addition of oxygen vacancies. In that report the amorphous phase Nb $3d_{5/2}$ peak appeared at 207.46 eV whereas the corresponding T-Nb_2O_5 peak was at 206.98 eV.[101,102] These reference positions were used to estimate the amorphous and crystalline content of PMT films. This analysis (Figure 4.4e) suggests an increase in crystalline content from 68.4 ± 3.2% to 86.4 ± 1.7% for calcination at 520 to 600 °C, respectively, similar to the EXAFS analysis. The O 1s region is often interpreted as a convolution of lattice oxygen, non-lattice oxygen, and H_2O or OH species with corresponding energies of 530.0, 531.2, and 532.6 eV, respectively (Figure 4.4a). The quantitative O/Nb composition, excluding non-lattice and hydrous species contributions, decreased from 3.96-2.13 with increasing calcination temperature, indicating progressive removal of O (Figure 4.4d). The implied sample stoichiometries of $Nb_2O_{4.3\text{-}8.0}$ were unexpected. The XPS calibration was validated using both commercial Nb_2O_5, NbO_2, and a T-Nb_2O_5 reference sample prepared by solid-state synthesis, the standard error of which was ±5% of the expected lattice-O/Nb stoichiometry. Assuming an upper limit oxidation state of Nb^{5+}, this stoichiometry suggests a significant presence of oxygen in forms other than oxide O^{2-}, such as interstitial O^0, electron deficient oxygen anion O^-, superoxide anion O_2^-, peroxide anion O_2^{2-}, or ozonide anion O^{3-}. Several reports

have claimed interstitial O^x species in diverse metal oxides,[103–107] however related XPS observations noted those between the lattice O peak and non-lattice O peak.[104–106] EPR analysis of samples calcined between 475-600 °C were conducted to detect paramagnetic oxygen species containing unpaired electrons. The resulting spectra did not exhibit detectable signal associated with any paramagnetic oxygen species nor oxygen vacancies (**Figure C.3**).[64,108–112] This observation suggests an absence of the considered paramagnetic oxygen species (O^-, O_2^-, O^{3-}) where the combination of XPS and EPR is most consistent with oxygen present dominantly as diamagnetic species, including oxide O^{2-}, hydroxide OH^-, and peroxide O_2^2 which are not observable by EPR. Density functional theory (DFT) calculations were performed on the O-rich niobia surface to better understand the excess oxygen configurations observed with low calcination temperatures (**Figure C.4**), assuming that excess oxygen is likely to be located in the near-surface region. The DFT calculation revealed two different types of O-O bonds on the relaxed (001) surface as shown in Figure C.4. The computed O-O bond distance in O_{po1} and O_{po2} is 1.44 Å and 1.39 Å, respectively, suggesting that both O_{po1} and O_{po2} are peroxide (O_2^{2-}). Prediction of energetically favorable peroxide formation on the relaxed O-rich surface is consistent with the measurements indicating excess diamagnetic oxygen species. Thus, the combination of experimental and DFT suggest that the amorphous niobia may be rich in peroxide defects that are gradually removed with increasing calcination temperature. Thus, several changes to the composition and atomic structure of orthorhombic niobia varied with calcination temperature.

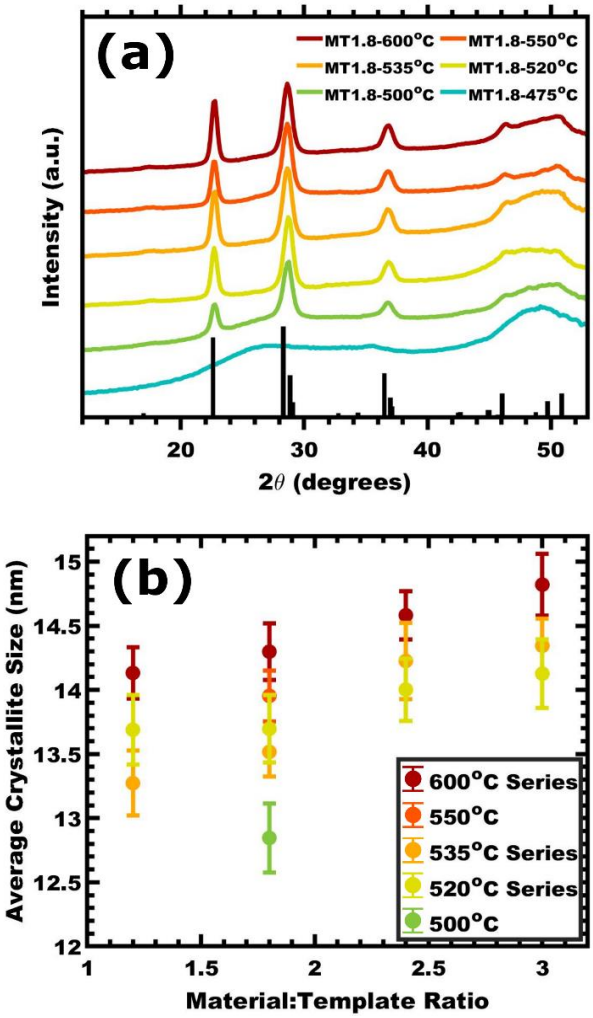

Figure 4.3. (a) GI-WAXS patterns for samples calcined at temperatures ranging from 475-600°C with constant M:T = 1.8. Data were offset vertically for clarity and include a T-Nb_2O_5 reference pattern (PDF No. 01-071-0336, black bars). (b) The average crystallite size was calculated using Scherrer analysis of the non-convolved (001) peak at 22.6° for different sample conditions. Values in panel (b) are presented as the mean ± standard error-of-the-mean.

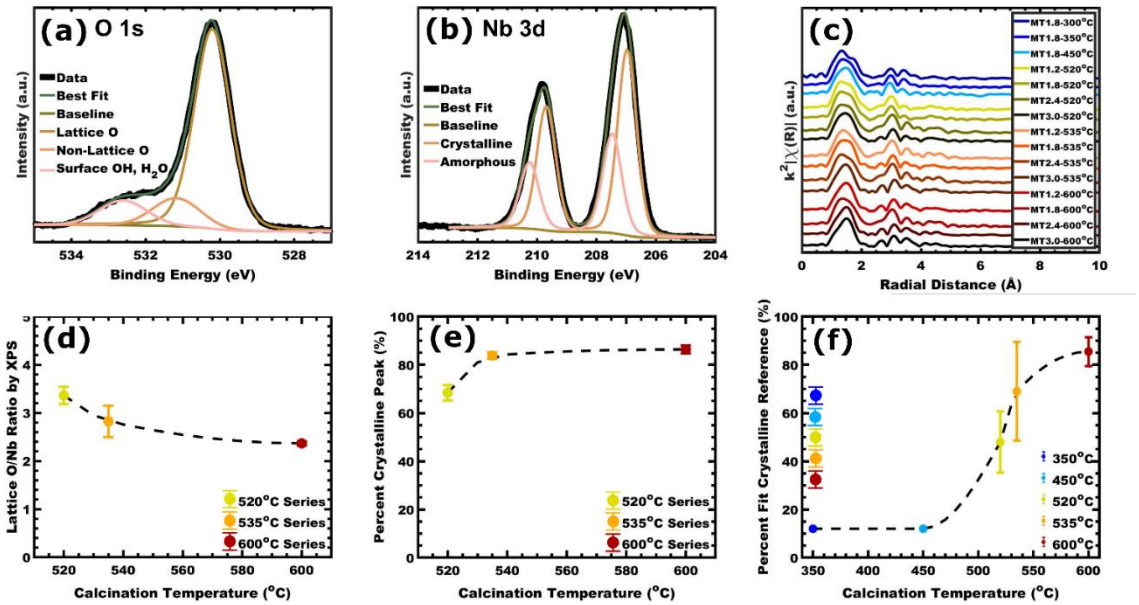

Figure 4.4. Representative XPS data from MT1.2-520°C with showing the (a) O 1s and (b) Nb 3d regions. The oxygen peaks were termed as lattice (530.1 eV), non-lattice (531.1 eV), or surface OH/H_2O (532.5 eV). The Nb peaks were deconvolved as amorphous (210.28, 207.46 eV) and crystalline (209.68, 206.98 eV) contributions based on prior work. (c) The EXAFS data are presented as k^2-weighted Fourier-transformed Nb K-edge. (d) The XPS derived O/Nb ratio and the (e) crystalline/amorphous ratio are shown. (f) The EXAFS data were analyzed through a linear combination of MT1.8-300°C as the amorphous references and MT2.4-600°C as the crystalline reference to derive the percent crystallinity. Values presented with error bars represent the mean ± standard error-of-the-mean.

The cyclic voltammetry (CV) methods used to characterize the electrochemical behavior associated with each calcination temperature. The general approach is first described using a representative sample (MT1.2-600°C) before comparing samples. A fixed voltage window from 1.2 to 3.0 V was scanned using series of voltage sweep rates (v) ranging from 3.2 mV s^{-1} to 1,000 mV s^{-1} and the current (i) response was recorded with a three-electrode configuration (**Figure 4.5a**). The resulting CV curves were characteristic of pseudocapacitance[10,113] with broad peaks having a box-like shape with narrow separation between anodic and cathodic peaks (see normalized data **SI Figure C.5d-f**). The anodic peaks were apparent for all v's investigated however the cathodic peaks became

unobservable beyond 199.5 mV s^{-1} due to ohmic shift outside of the voltage window. The trends in anodic peak current are shown in Figure 5b. A power law relationship[114] is often used to identify the type of rate-limiting process:

$$i = a * v^b \quad (4.1)$$

Where i is peak current, and a and b ("b-value") are fit terms. Surface-limited behavior such as ideal capacitance exhibit $i \propto v$ (b = 1.0) whereas semi-infinite diffusion-limited behavior exhibits $i \propto v^{0.5}$ (b = 0.5). The anodic $i(v)$ is shown in Figure 5b on a log-log scale where the slope corresponds to the b-value. The derivative of Figure 5b is shown as a plot of b-value(v) in Figure 5c. Here MT1.2-600°C exhibits a b-value > 0.9 for $v \leq 87.1$ mV s^{-1}, indicative of surface-limited behavior, i.e., pseudocapacitance. The departure from surface-limited kinetics with increasing v-values was previously termed the surface limited threshold (SLT, v_{SLT}, t_{SLT}) defined as b = 0.9.[21] Please note that b-values that are non-proximal to 1.0 and 0.5 are ambiguous to interpret due to the convolution of multiple rate-limiting processes. Thus, the SLT represents the point where diffusion-limited processes become apparent. Condition MT1.2-600°C had v_{SLT} = 87.1 ± 0.3 mV s^{-1}, corresponding to a charge time (t_{SLT}) of 20.66 ± 0.08 s. For the samples investigated here, the v_{SLT} also corresponds to the onset of diffusion-limited capacity loss (**Figure C.6**). This methodology thus identifies the transitions in type of rate limiting process where further comparisons are needed to identify the specific diffusive process.

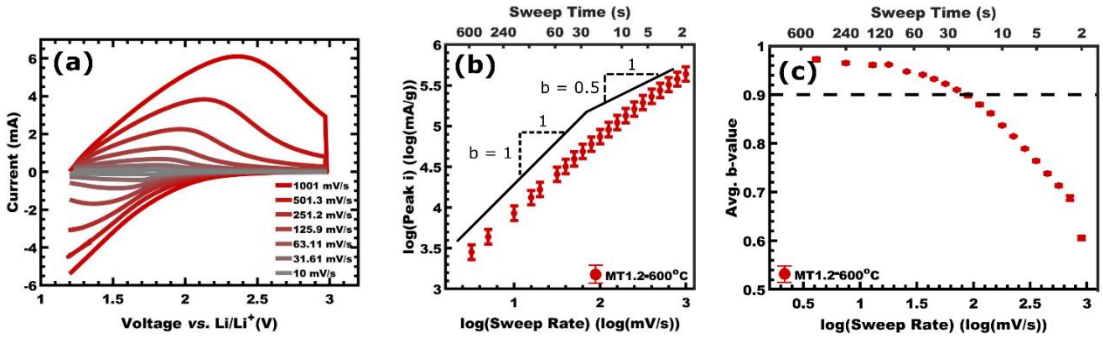

Figure 5. (a) Representative cyclic voltammograms at different voltage sweep rates for sample MT1.2-600°C at different voltage sweep rates. (b) A log-log plot of anodic, mass-normalized peak current vs. voltage sweep rate. The slope (b-value) of this log-log plot identifies the type of rate limiting process. (c) The corresponding derivative shows b-value changes with the voltage sweep-rate. The surface-limited threshold (SLT) denotes the departure from surface-limited kinetics ($b = 0.9$, dashed line). Values are presented as mean ± standard error-of-the-mean.

This kinetic analysis combined with control experiments were used to interpret the specific diffusive process that limits the v_{SLT} for each temperature series. First the 520 °C series is elaborated before turning attention to the other calcination temperatures. Four samples spanning M:T = 1.2-3.0 were compared with similar film thicknesses (**Figure 4.6a-b,** Figure C.6, **Table C.5 and C.6, Figure C.7**). Performance changes may be associated with changes to the surface-limited process, the diffusion-limited process(es), or some combination thereof. Thus, the analytical strategy examines both possible changes. For the 520 °C series, the peak currents at $v = 3.2$ mV s^{-1} were varied less than the error of the measurement, not indicating a marked change in the rate of the surface-limited process with M:T. With respect to the diffusion-limited processes, the b-value(v) trends were compared where $v > v_{SLT}$ contains diffusion-limited contributions of varying magnitudes. For these samples the v_{SLT} monotonically shifted to higher v with lower M:T (Figure 4.6b). For example, MT1.2-520°C and sample MT3.0-520°C exhibited v_{SLT} values of 136.3 ± 2.1 and 56.0 ± 0.5 mV s^{-1}, respectively. This 143% increase is quite large for a 25.5 nm

(33.8%) reduction in wall thickness. These data alone, however, are not yet definitive towards a specific diffusive process. For example, the increase of wall thickness is geometrically coupled to a decrease in the pore volume fraction which will decrease the effective conductivity of the electrolyte phase. To check for this constraint sample MT3.0-520°C with the thickest walls and lowest volume fraction of porosity was examined with an electrolyte of half the prior concentration. The 50% decrease in electrolyte concentration was found to have no marked effect upon the peak current nor b-value(v), indicating that electrolyte transport was not rate limiting for these samples (Figure 4.6e). For due diligence, the sensitivity of the architecture towards film thickness was next investigated which affects both electrolyte and electron transport. Having previously excluded sensitivity towards electrolyte constraints, differences here should be attributed to electron transport alone. Samples of MT3.0-520°C were compared to samples of MT3.0-520°C-Thick which had the film thickness increased from 65.2 to 163.0 nm, a ~150% increase. The corresponding peak currents found a 2.6% decrease however, the b-value(v) plots revealed some effect of film thickness with the v_{SLT} shifting from 56.0 ± 0.5 to 40.6 ± 0.3 mV s^{-1}, a 28% decrease (Figure 4.6h, **Figure 4.7a**). Thus, the minor restriction from electron transport and minor changes in overall sample thickness with M:T do not explain the significant 143% increase in v_{SLT} found with decreasing M:T conditions with similar thicknesses (Table C.6). Thus, by the process of elimination one can conclude that dominant diffusion-limited process at v_{SLT} is solid-state lithium intercalation with a minor contribution from electron transport. The other calcination temperature series at 535 °C and 600 °C exhibited similar trends overall including: 1) similar peak currents (mA g^{-1}) with changing M:T ratio (Figure 4.6a); 2) a shift in b-value(v) corresponding to increasing

v_{SLT} with decreasing M:T ratio (Figure 4.6c-d); 3) no significant change in peak current nor v_{SLT} with changing the electrolyte concentration from 1.0 M to 0.5 M (Figure 6f-g); and 4) a minor reduction of peak current and a ~28% decrease in v_{SLT} with increased film thickness (Figure 4.6i-j). Thus, all sample series calcined from 520-600 °C were concluded to have solid-state lithium diffusion as the dominant diffusive constraint and are further analyzed with diverse models (*vide infra*). Figure 4.7a presents the corresponding t_{SLT} values (t_{SLT} = voltage window ÷ v_{SLT}) showing how both thinner walls from lower M:T ratios and lower calcination temperatures both lead to faster t_{SLT} times, ranging from ~13-35 s. Despite the onset of a diffusive contribution for $v > v_{SLT}$, the samples retain excellent rate-capability (**Figure 4.7b**). For example, MT1.2-520°C maintained 95% of its capacity (577.4 ± 17.0 C g^{-1}) with a sweep time of 2.25 s (1600 C-rate equivalent) exceeding many literature precedents for T-Nb_2O_5. Furthermore, many of these comparison reports included conductive additives for particle-based slurries (typically not included in mass-normalization),[115,116] whereas our thin films were purely composed of orthorhombic niobia. The limits to amorphization of orthorhombic niobia are next discussed with a larger temperature range.

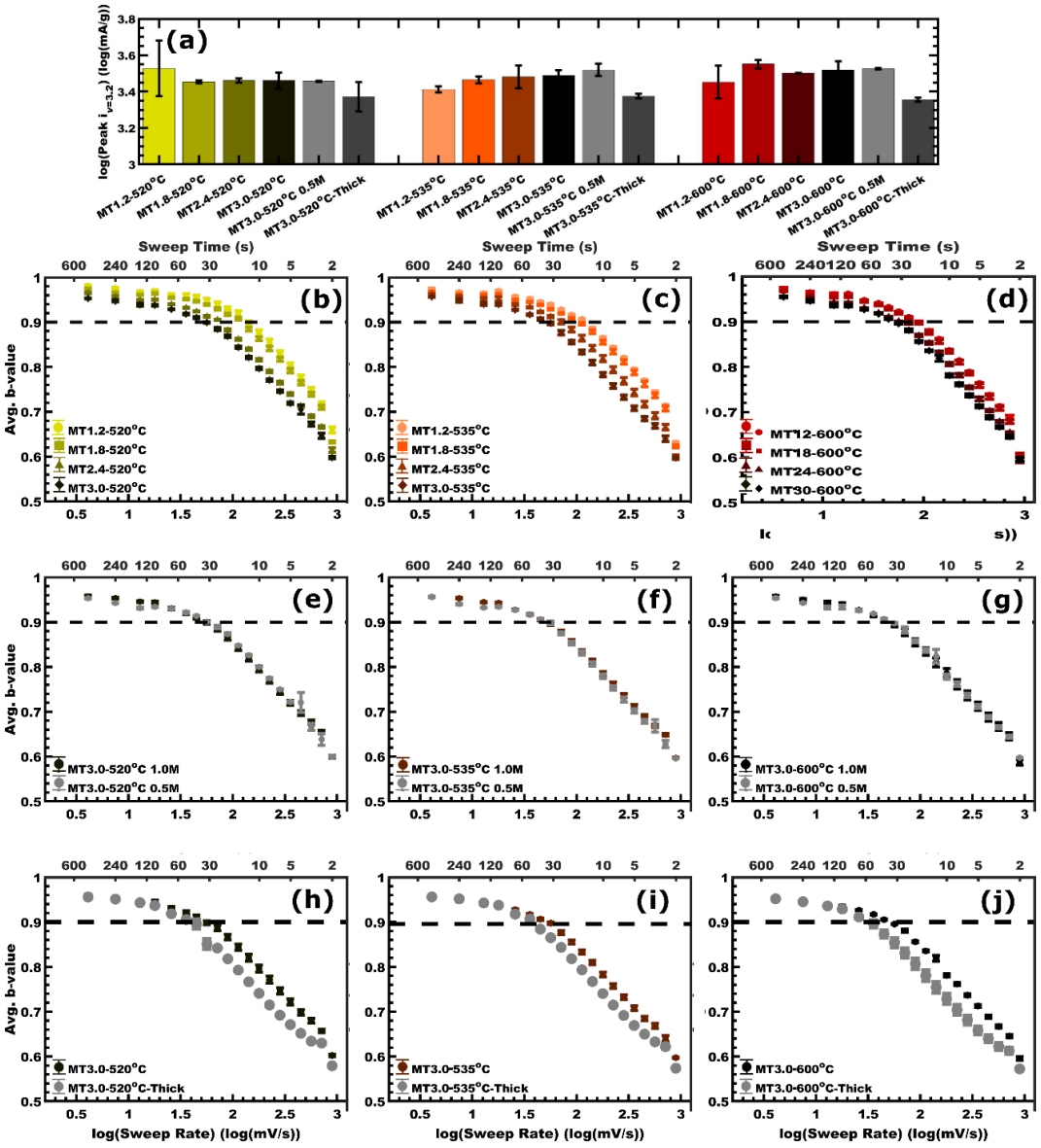

Figure 4.6. Examination of possible kinetic constraints from the intercalation length, electrolyte transport, and electron transport for a range of samples with calcination temperatures of 520 °C, 535 °C, and 600 °C. Comparisons include (a) the peak current at v = 3.2 mV s^{-1}, (b-d) b-value(v) with wall thickness (M:T ratio), (e-f) b-value(v) with 1.0 M vs 0.5 M electrolyte, (h-i) b-value(v) with standard thickness (~75 nm) vs thicker films (~120% thicker). Values are presented as the mean ± standard error-of-the-mean.

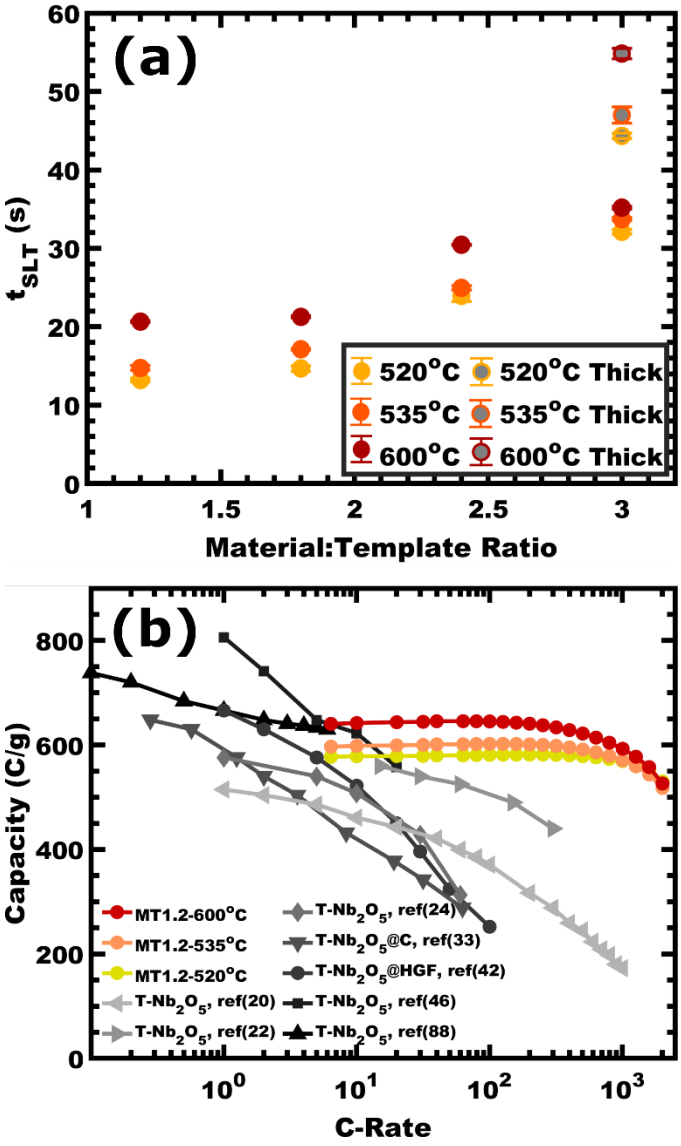

Figure 4.7. (a) Comparison of the CV sweep times corresponding to the surface-limited threshold (t_{SLT}) for all sample conditions presented thus far. Values are presented as the mean ± standard error-of-the-mean. (b) The rate-dependent lithiation capacity of for the M:T = 1.2 series are compared to published precedents as a function of C-rate or effective C-rate.

The electrochemical behavior of lower calcination temperatures was examined down to 300 °C. The CV curves for samples from 300-500 °C exhibited profiles that were considerably broader, spanning a larger voltage range, than T-Nb_2O_5 similar to prior reports of amorphous niobia (**Figure 4.8a**).[19,22,24,25,62,71] Curiously this CV peak breadth

increased somewhat with calcination temperature up to a maximum width at 500 °C, corresponding to the GIWAXS onset of crystallization (Figure 4.3), then substantially narrowing with further increasing calcination temperature. This CV trend suggests increasing charge localization as crystalline samples are heated at higher calcination temperatures,[10] i.e. increasing delocalization with T-Nb_2O_5 amorphization. The CV-character as well as the GIWAXS, EXAFS, and XPS trends were clustered into two groups, the mostly-amorphous samples calcined between 300-475 °C and the mostly-crystalline samples calcined between 520-600 °C. Whereas the mostly-crystalline samples exhibited reproducible lithiation capacity upon cycling, the mostly-amorphous samples all exhibited a marked ~30-40% decline in lithiation capacity (Figure 4.8b) and were thus only briefly examined. Having noted the limited stability of mostly-amorphous samples, their electrochemical kinetics were examined as described before. As shown in **Figure 4.9a**, there was an increase in low-v peak currents with increasing calcination temperature, suggesting an accelerated surface reaction rate (*vide infra*). While comparisons among the mostly-crystalline samples and the mostly-amorphous samples are both consistent with this trend, caution should be taken in comparing the end points since the CV curve shapes simultaneously varied which alters the peak current values. The b-value(v) data for a set of samples with M:T = 1.8 are presented spanning all calcination temperatures investigated here (Figure 4.9b). Again, the mostly-amorphous and mostly-crystalline samples clustered into two distinct groups with the mostly-amorphous samples exhibiting the highest v_{SLT} values. The corresponding t_{SLT} value exhibited a sigmoidal trend with the fastest time found for the mostly-amorphous samples (Figure 4.9b). The most interesting region of this amorphization continuum is the 520-600 °C samples that were mostly-crystalline,

electrochemically stable, and revealed monotonic kinetics changes (Figure 4.9b-c). A general increase in lithiation capacity was noted with increased calcination temperature with average values (all M:T ratios) of 625.8 ± 29.7 C g^{-1} at 520 °C, 669.7 ± 47.8 C g^{-1} at 535 °C, 727.5 ± 60.9 C g^{-1} at 600 °C (Figure C.6) approaching the theoretical capacity of 726 C g^{-1} for $Li_2Nb_2O_5$.[117] Thus the mostly-crystalline samples (520-600 °C) were found to have the most compelling collection of attributes including stable lithiation capacity and adjustable kinetics via calcination temperature.

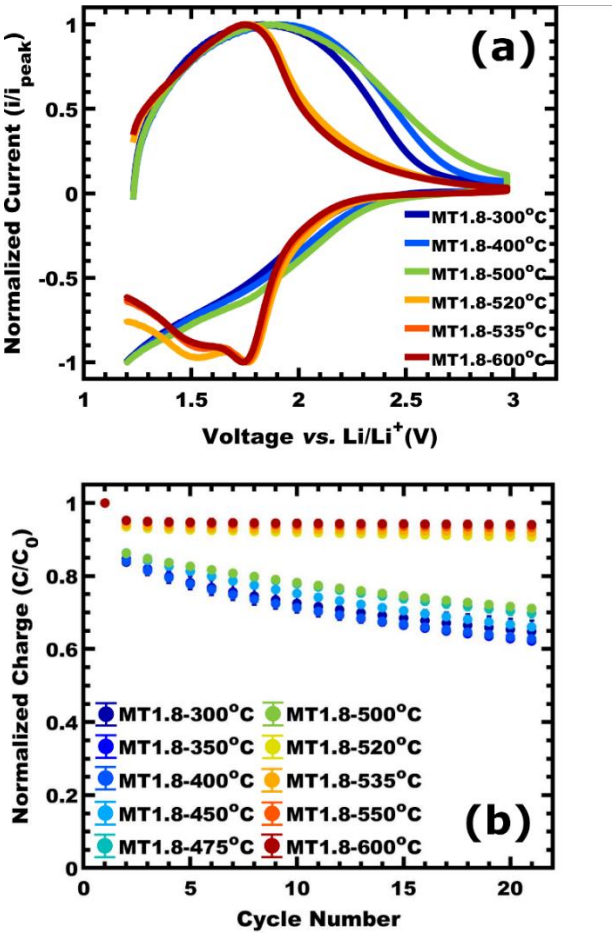

Figure 4.8. (a) Comparison of normalized CV data for wide range of calcination temperatures with constant MT = 1.8 measured at v = 3.2 mV s^{-1}. (b) Comparison of the corresponding normalized charge with repeated electrochemical cycling at 10 mV s^{-1} reveals that samples calcined at 500 °C or below are unstable. Values are presented as mean ± standard error-of-the-mean.

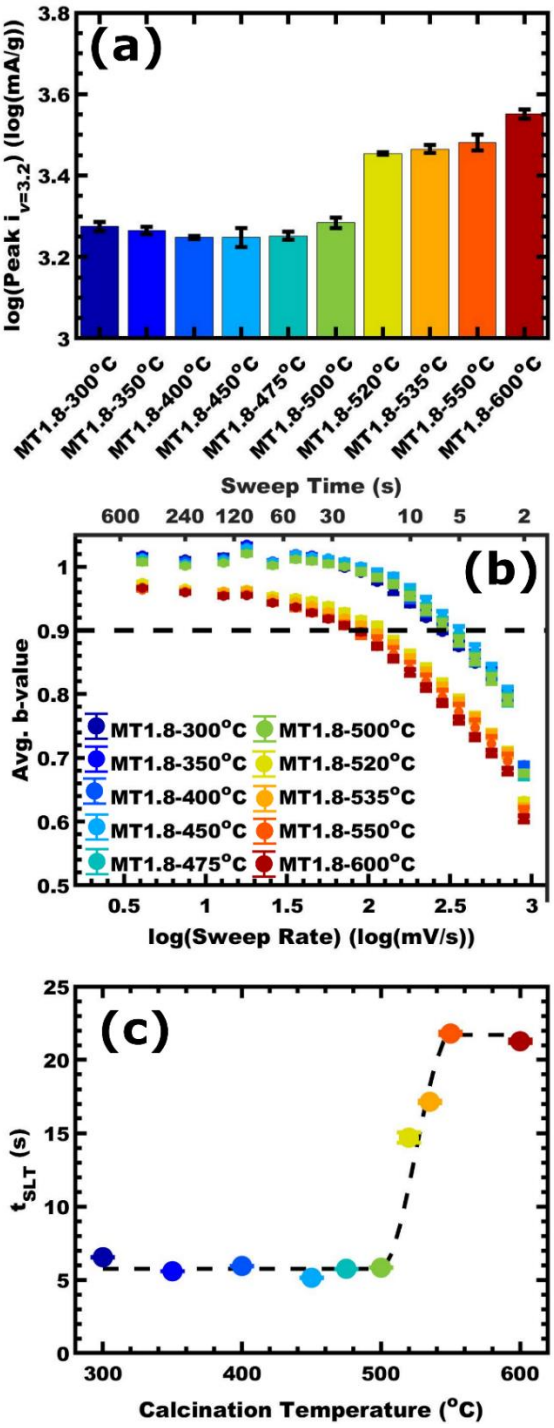

Figure 4.9. Comparisons of electrochemical kinetics for initial measurements on MT=1.8 samples with calcination temperatures ranging from 300 °C to 600 °C. Comparisons include (a) the peak current at v = 3.2 mV s^{-1} (b), b-value(v), (c) and sweep times at the corresponding surface-limited thresholds (t_{SLT}). Values are presented as mean ± standard error-of-the-mean.

Further insights into the differences in electrochemical kinetics were elucidated with a simple current model. As noted above, the SLT reflects the tipping point from surface-limited kinetics towards a convolution that includes diffusion-limited contributions where increases in v_{SLT} could in principle be attributed to either a decrease in the surface-limited reaction rate or an increase in the diffusion-limited reaction rate. A popular model was developed for $i(v)$ surface-redox pseudocapacitive materials[118] where surface-limited and diffusion-limited contributions were parametrized with:

$$\boldsymbol{i = k_1 v + k_2 v^{0.5}} \tag{4.2}$$

where k_1 and k_2 are fit parameters that are analogous to admittance (larger k values lead to larger current). This expression includes two separate sources of current that operate in parallel and are added together (termed here "parallel model"). This parallel model includes a surface-limited current from the charging of the "near surface" material and a separate diffusion-limited current from the rest of the material. The corresponding theoretical plot on a log-log scale shows how the dashed lines for k_1-alone and k_2-alone add together to yield the total current (**Figure 4.10a**). This functional form fundamentally transitions from diffusion-limited behavior at low v to surface-limited behavior at high v (Figure 4.10a). That trend is most apparent by examining the corresponding derivative i.e., b-value(v) for the parallel model (Figure 4.10c). This behavior trend however does not match the experimental data here. A revised perspective is proposed where both a surface-limited process and a diffusion-limited process operate in series, here termed the "series model" (Derivation in **Equations C.4-C.10** with $R = 0$):

$$i = \left[\left(\frac{k_2}{\sqrt{v}}\right)^2 + \left(\frac{k_1}{v} + \frac{k_2}{\sqrt{v}}\right)^2\right]^{-0.5} \quad (4.3)$$

where k_1 and k_2 are fit parameters that are analogous to impedance (lower values lead to higher currents). Notably the k_1 term corresponds to the impedance of a surface-limited process and the k_2 term corresponds to the impedance of a diffusion-limited process. The corresponding theoretical plot on a log-log scale shows how the total current remains below both the k_1-alone and k_2-alone contributions (dashed lines), reflecting that both processes restrict current (Figure 4.10b). In contrast to the parallel model, the series model thus fundamentally transitions from surface-limited behavior to diffusion-limited behavior with increasing *v*. Again, the corresponding derivative reveals a b-value(*v*) trend (Figure 4.10d) which closely matches the samples investigated here (compare to Figure 4.6). Notably, the series model does not presume the existence of a special near-surface region[10] and does not assume that the diffusion-limited current operates in the absence of a surface-limited contribution (consider Occam's razor). Thus, a parallel model for current is proposed to quantify surface and diffusion contributions which matches experimental observations.

The utility of these models is compared with one dataset. The M:T = 1.2 series calcined at 520, 535, and 600 °C are presented as i(*v*) and b-value(*v*) in **Figure 4.11** using best fits from each model. Since the log-log plot of *i*(*v*) is mostly linear, both models yield an excellent fit in this coordinate space with goodness-of-fit R^2 values > 0.99 (Figure 4.11a,b). In contrast, the parallel model is unable to track the general shape of b-value(*v*) due to its functional form, *vide supra*, giving very poor fits with goodness-of-fit $R^2 \leq -1.1$ (Figure 4.11d). Given the poor congruence between the parallel model and b-value(*v*) observations, it is questionable how much faith should be put to its use to separate surface-

limited capacity and diffusion-limited capacities. The series model, on the other hand, closely matches experimental b-value(v) trends for all samples with goodness-of-fit $R^2 \geq 0.82$ (Figure 4.11e). The addition of a single additional fit term corresponding to a series resistor improved the goodness-of-fit for b-value(v) with $R^2 \geq 0.98$ for these samples (Figure 11c,f). Several modifications were examined, including implementation of a constant phase element, inclusion of a second diffusion-limited process, and the addition of a resistor term were examined where the latter was selected due to the improved fit. In the interest of matching data trends with minimal complexity the series model was limited to three terms here where (Derivation in SI Equations C.4-C.10 with $R \neq 0$):

$$\boldsymbol{i} = \left[\left(\frac{\boldsymbol{k_2}}{\sqrt{\boldsymbol{v}}} + \boldsymbol{R}\right)^{\mathbf{2}} + \left(\frac{\boldsymbol{k_1}}{\boldsymbol{v}} + \frac{\boldsymbol{k_2}}{\sqrt{\boldsymbol{v}}}\right)^{\mathbf{2}}\right]^{\mathbf{-0.5}} \tag{4.4}$$

where R corresponds to the impedance of a resistor. The effects of a range of theoretical parameters upon $i(v)$ and b-value(v) are presented in **Figure C.8**. As expected, increasing the k_2 impedance reduces the $i(v)$ in the high-v regime and similarly increasing the k_1 impedance reduces the $i(v)$ in the low-v regime (Figure C.8a-d). A perhaps surprising feature is that the b-value(v) trends and the implied v_{SLT} depend largely on the ratio of k_1/k_2 (constant $R = 0$) despite significant changes in $i(v)$ performance (Figure C.8e,f). Lastly the effect of increasing R is presented where $i(v)$ decreases and b-value(v) exhibits increasing curvature and reaches b-values < 0.5 (Figure C.8g,h). A notable advantage is that the use of either series model enables the independent assessment of the rates (impedances) of the surface-limited process and the diffusion-limited process.

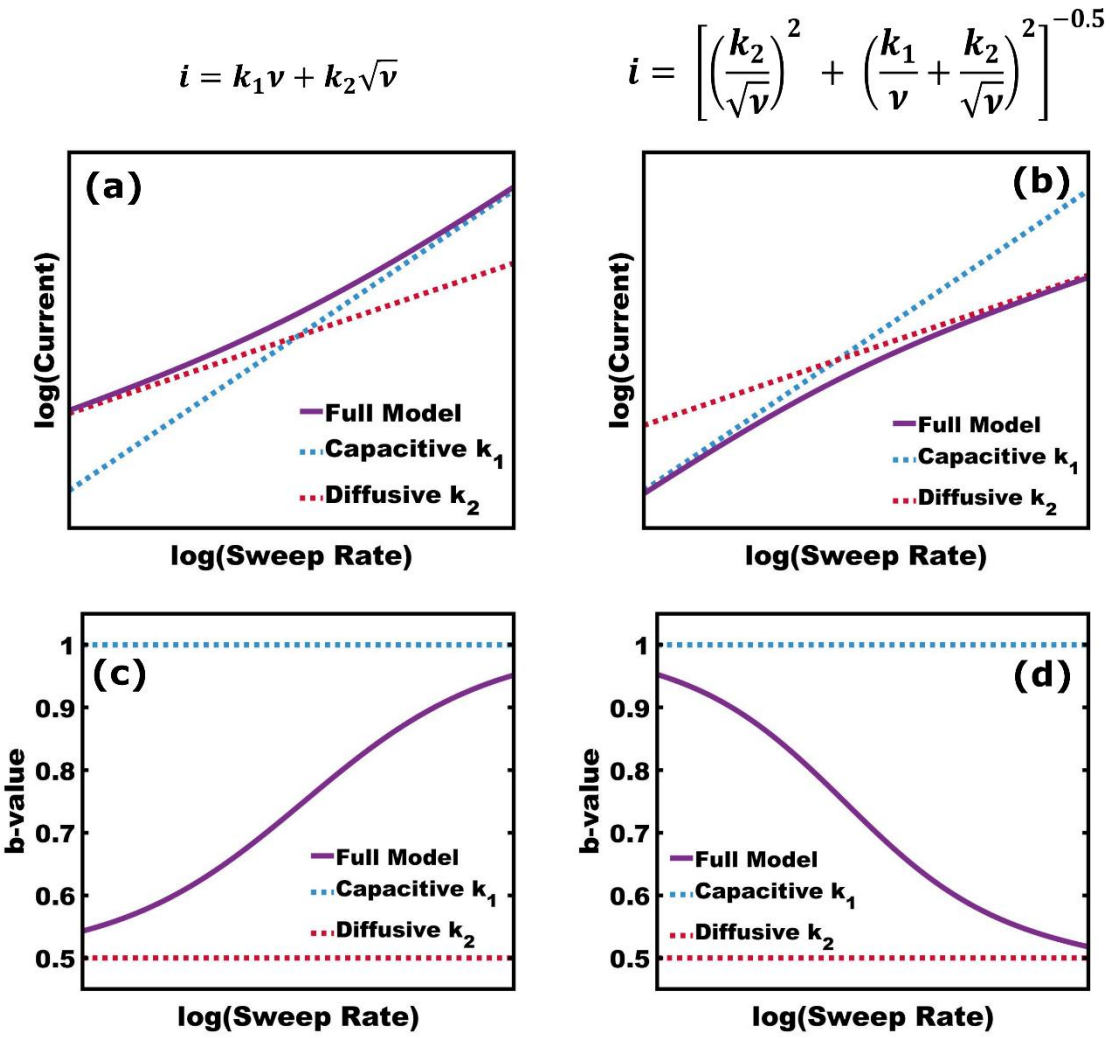

Figure 4.10. Comparison of current models as a function of voltage sweep rate with surface-limited and diffusion-limited elements connected in either (a) parallel or (b) series. (c,d) The corresponding derivative plots present b-value(v) which identify the type of the dominant rate-limiting process as surface-limited (b ~ 1.0), diffusion-limited (b ~ 0.5), or a mixture thereof.

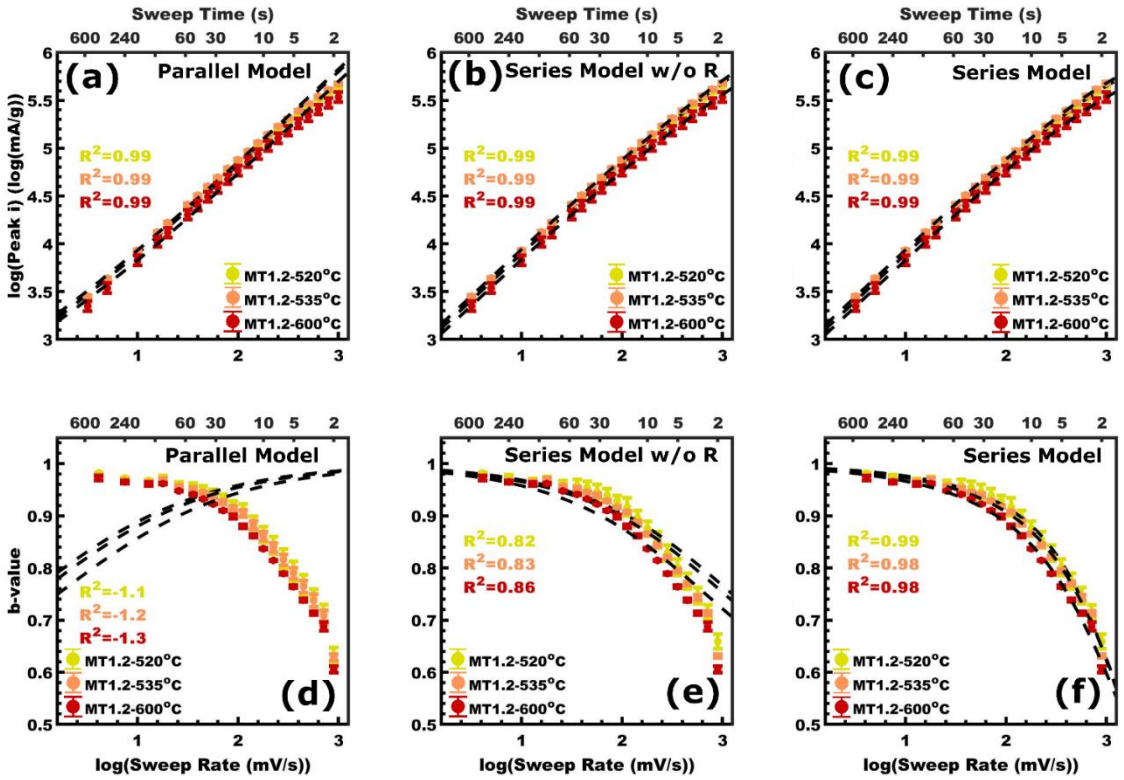

Figure 4.11. Comparison of three current models where the best-fits had similar goodness-of-fit values $R^2 > 0.99$ for (a) the parallel model, (b) the series model without a resistor, and (c) the series model with a resistor. (d-f) The corresponding derivatives show b-value(v) relative to each model where only the series models are similar to the data. (f) The resistor addition to the series model improves the goodness-of-fit $R^2 \geq 0.98$ for all three sample conditions. Values presented as mean ± standard error-of-the-mean.

The best-fits of the series model (**Equation 4.4**) were compared to quantify changes to rates of surface and diffusion processes across many sample conditions. Samples spanning M:T = 1.2-3.0 and calcination temperatures 520-600 °C were all well-fitted in the $i(v)$ coordinate space with the corresponding b-value(v) plots included for comparison (**Figure C.9**). **Figure 4.12** shows the trends for best-fit parameters k_1, k_2, and R as a function of the calcination temperature (different colors) and the intercalation length (horizontal axis, half the wall thickness). Please note all current data was mass-normalized before fitting. Starting with the surface process the k_1 impedance decreases (faster surface process) with increasing calcination temperature. The accelerated surface process with

calcination temperature may be associated with the increased extent of crystallization, or the removal of defects associated with excess oxygen noted by XPS. For example, interstitial oxygen species could act as an additional Li-O coordination motif which have been calculated to increase the energy for lithium adsorption.[23] Within each temperature series, the k_1 impedance generally decreased (faster surface process) with increasing wall thickness despite the naturally accompanying decrease in mass-normalized surface area (Figure 4.12a). This trend may be associated with the increased crystallite size found with thicker walls (higher M:T) within each temperature series. The implied trends for a faster surface process with increasing M:T, however, were not apparent when comparing the individual low-v peak current values for each temperature series, a small change that is perhaps better revealed by fitting each full i(v) dataset. Second, the diffusive process k_2 impedance generally decreased (faster diffusion process) with lowered calcination temperatures. This is consistent with the prior discussion where solid state lithium diffusion was identified as the dominant diffusive process where lowering the calcination temperature was found to increase the rate of lithium diffusivity (Figure 4.12b, **Table 4.1**). Within each temperature series, the k_2 impedance generally increased with wall thickness (or M:T), likely associated with the increased diffusion length which fit reasonably to a linear trend. This diffusion-length kinetic dependence is also revealed for each temperature series in a plot of $t_{SLT}^{0.5}$ vs diffusion length where a straight line is expected for a 1D general solution (half concentration of source) to Fick's second law with an infinite source[21] ($x \propto (Dt)^{0.5}$) (Figure 4.12d). The $t_{SLT}^{0.5}$ plot is also consistent with the diffusivity trend where decreasing calcination temperature led to lower slopes corresponding to faster t_{SLT} values and higher lithium diffusivity (Figure 4.12d). Thus, there is agreement upon this conclusion

from both the t_{SLT} and the k_2 perspectives with an observed 21.34% decrease, and 12.17% decrease in slope of the 520 °C condition relative to the 600 °C condition, respectively (Figure 12b,d). Previous work comparing amorphous and crystalline metal oxide counterparts suggest lithium diffusivity is improved when amorphization lowers the energy barrier for lithium site hopping.[25,73,84,86,119–123] The granular kinetic changes resulting from variation of calcination temperature could be the result of an ensemble of phases or alternatively a granular change in the average local atomic environment. Lastly, the resistive impedance *R* was relatively constant for all samples with a minor reduction with increasing calcination temperature as observed in amorphized T-Nb_2O_5[64] or perhaps indicative of improved contact resistance between the niobia film and the FTO substrates (Figure 4.12c **Table 4.1**) similar to that observed elsewhere when comparing anatase and amorphous TiO_2 films.[124] Thus the use of the series model to interpret lithiation kinetic changes provided evidence that decreasing the calcination temperature, i.e. increasing the extent of amorphization, both accelerates the solid-state diffusion of lithium ions and decelerates the surface reaction.

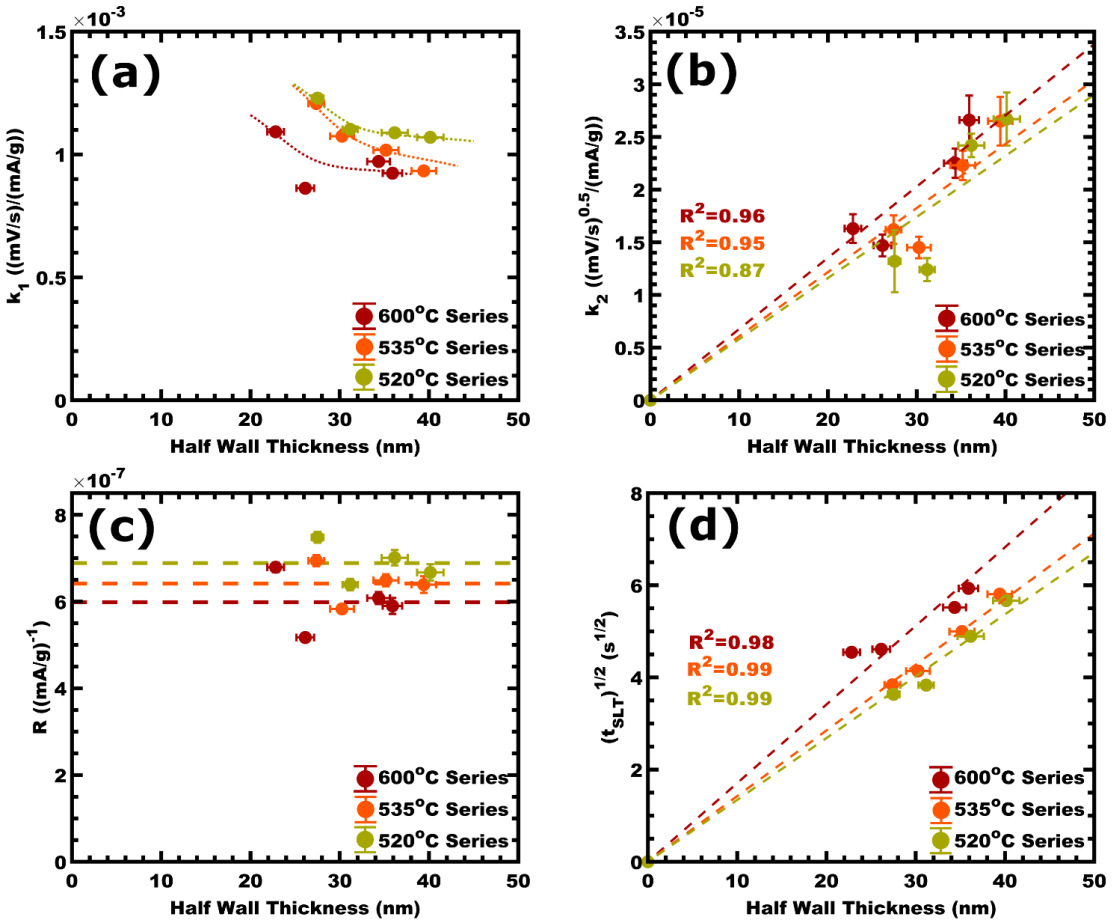

Figure 4.12. (a-c) The peak currents for all sample conditions were fitted using the series-model and the best-fit parameters were compared as a function of half the wall thickness (intercalation pathlength). (a) The k_1 term corresponds to the impedance of a surface-limited process with a dotted line to guide the eye. (b) The k_2 term corresponds to the impedance of a diffusion-limited process with dashed lines corresponding to linear best-fits. (c) The R term corresponds to a resistance with a dashed line to represent the average for each series. (d) For comparison to (b) $t_{SLT}^{0.5}$ is plotted vs the intercalation length where a linear trend is consistent with a generalized diffusion relationship from Fick's second law. Values are presented as mean ± standard error-of-the-mean.

Table 4.1. Comparison of kinetic descriptors for sample series with different calcination temperatures.

Sample Series	Slope of Figure 12b k_2 [((mV $s^{-1})^{0.5}$(mA $g^{-1})^{-1}$) nm^{-1}][a]	Slope of Figure 12d [$(s)^{0.5}$ nm^{-1}][a]	Average R value [(mA $g^{-1})^{-1}$][a]
520°C Series	7.183E-7 (-12.17%)	0.1342 (-21.34%)	6.888E-7 (15.09%)
535°C Series	7.218E-7 (-11.74%)	0.1425 (-16.47%)	6.413E-7 (7.151%)
600°C Series	8.178E-7 (0%)	0.1706 (0%)	5.985E-7 (0%)

[a] The percent change relative to the 600 °C Series is noted in parentheses

4.4 Conclusion

Amorphization provides an avenue to enhance diffusion rates for improved rate capability with intercalation pseudocapacitance. The identification and quantification of such amorphization effects are challenging when the experimental samples contain multiple simultaneous variations. Here, PMTs enabled the production of niobia sample series with tunable isomorphic architectures calcined over a range of temperatures. Using GIWAXS, XAFS, XPS, and EPR, the degree of amorphization was found to increase with lower calcination temperatures and was consistent with increasing peroxide as supported by DFT calculations. While the mostly-amorphous samples were not stable to cyclic lithiation, the mostly-crystalline samples were and exhibited marked kinetic changes with calcination temperature. Through process of elimination and variation of a single transport parameter at a time, solid-state lithium diffusion was identified as the dominant diffusive

process which limits v_{SLT}. A series model for $i(v)$ was proposed which closely matched experimental observations while simultaneously quantifying the impedance of the surface process and the dominant diffusion process. This in-series model revealed that amorphization led to a 12.2% decreased diffusion-limitation and a 17.0% increased surface-limitation amongst the stable samples. The use of isomorphic architectures that vary a single spatial parameter at a time uniquely support the disambiguation of fundamental kinetic processes. Lastly, these results reveal a new high-performance material which achieved 577 ± 17 C g-1 capacity (95% retention) with a 2.25 s response time, corresponding to an effective C-rate of 1600 C.

4.5 Experimental Methods

Materials. Ethanol (EtOH 200 proof, 100%, Fisher) was stored over 30% w/v of molecular sieves (3Å, 8–12 mesh, Acros Organics) for a week.[125] 2-bromopropionic acid (>99%, Aldrich), chloroform (>99%, Aldrich), dimethylformamide (97%, Aldrich), hexane (>98.5%, Fisher), concentrated hydrochloric acid (HCl, 37% w/w, ACS grade, VWR) and (HCl, 37% w/w, trace metal grade, Fisher Scientific), concentrated hydrofluoric acid (HF, 48% w/w, trace metal grade, Sigma-Aldrich), niobium(IV) oxide (>99%, metal basis, Alfa Aesar), concentrated nitric acid (HNO_3, 70%, Fisher Scientific), poly(ethylene glycol)methyl ether (PEO-OH, M_n = 20,000 $gmol^{-1}$, Aldrich), 4-(dimethylamino) pyridine (99%, Aldrich), tetrahydrofuran (Fisher, certified), and were used as received. Niobium(V) ethoxide (NbOEth, 99.9%, Fisher), copper(I) bromide (99.99%, Aldrich), tris-(2-dimethylaminoethyl) amine (97%, Aldrich), anhydrous lithium perchlorate (LiClO4, 99.99%, Aldrich), and anhydrous propylene carbonate (99.7%, Aldrich) were used as

received and stored inside an argon-filled glove box. Hexyl acrylate (96%, VWR) monomer was passed through a basic alumina column just prior to use for polymerization.

Polymer Synthesis. Poly(ethylene oxide-*b*-hexyl acrylate), PEO-*b*-PHA, diblock polymer was synthesized by a two-step synthesis. A Steglich esterification of poly(ethylene glycol)methyl ether synthesized the macroinitiator, followed by an atom transfer radical polymerization to create the PHA block. The synthesis is described elsewhere in detail.[89] The molar mass of PHA was determined using a Bruker Avance III HD 300 ^{1}H NMR by comparing it to the PEO methyl ether starting material (M_n = 20.0 kg mol^{-1}) (Figure S4a and Table S1, Supporting Information). The molar mass dispersity was characterized using a Waters gel permeation chromatograph (GPC) equipped with a Waters 1525 binary pump, three styragel columns (HR1, HR3, HR5 in the effective molecular weight range of 0.1–5, 0.5–30, and 2–400 kg mol^{-1}, respectively), and a Waters 2414 refractive index detector with THF as the carrier solvent. The GPC was calibrated with poly(styrene) standards (1.50, 3.28, 10.00, 17.40, 32.70, 120.00, 214.00, 545.00, 1010.00 kg mol^{-1}) obtained from Polymer Standards Service GmbH. GPC samples were prepared in THF at concentrations of 5 mg mL^{-1}, filtered through a 0.2 µm PTFE syringe filter prior to injection (Figure C.1b and Table C.1).[90,126]

Synthesis of Porous Materials with Persistent Micelle Templates. A micelle template stock solution was prepared by dispersing PEO-*b*-PHA (25 mg) in EtOH (2.5 mL) at 80 °C in a sealed 20 mL scintillation vial with a PTFE lined cap then allowed to cool to room temperature overnight. Concentrated HCl (37 wt%) (≈0.060 g) was added slowly to reach 1.8 wt% with respect to the total mixture (PEO-*b*-PHA, EtOH, and HCl). We note that ethanol was found to result in minimal microporosity within the final niobia walls.[93]

After acid addition, the solution was placed in a water bath at 35 °C to maintain dispersion of the polymer micelles. A prescribed quantity of NbOEth was added to a 20 mL scintillation in an argon-filled glovebox (<1 ppm O_2, <1 ppm H_2O) and once removed from the glovebox was mixed with a prescribed amount of micelle template solution via injection through PTFE lined cap to reach the target material-to-template ratio, M:T ratio.[89] Once mixed, the solution was placed back in the water bath. Here the M:T ratio is a mass ratio of the final anticipated niobia mass relative to the mass of block polymer. Each film was spin coated for 30 s at 1,000, 1,500, 2,000, and 2,150 rpm under 36% relative humidity for each M:T condition of 1.2, 1.8, 2.4, and 3.0, respectively, a procedure described in detail elsewhere.[89,93,127] Immediately after spin coating, each sample was removed from the humidity-controlled chamber and placed on a 110 °C hot plate with a minimum period of 12 hrs to crosslink the oxide, termed as "aging." Aging conditions were optimized to prevent initial dewetting and to assure sufficient oxide connectivity to survive calcination. After each spin coating of a film, the spin coating chamber (generic "Tupperware") was replaced to avoid effects of residual solvent vapor, as observed previously.[89] Glass, silicon, and fluorine-doped tin (FTO) substrates were used for SAXS, SEM, and electrochemistry, respectively. After aging, the films were calcined, 5 ^{o}C min^{-1} to 200 ^{o}C followed by 10 ^{o}C min^{-1} to variable temperatures ranging from 300 °C to 550 °C for a 12 hr soak whereas the 600 °C samples had a 1 hr soak.

Electrode Preparation. FTO substrates (TEC-15, Hartford Glass, CT) were rinsed and scrubbed with DI water using Kimwipes until scrubbing produces an audible squeaking noise followed by rinsing and scrubbing with IPA wetted Kimwipes again in the same manner. The substrates were then sonicated in a soapy water bath (2 g L^{-1} deconex) for 30

min. The water and alcohol scrub and rinse steps were repeated as before. The resulting substrates were stored submerged in IPA until near the time of spin coating. Just prior to coating, the FTO substrates were removed from IPA, blown dry. The FTO substrates were held at 110 °C until the moment they were used for spin coating. An uncoated area for electrical contact was maintained by masking part of the substrate with high-temperature Kapton tape. After spin coating and aging as described above, the edges of the FTO substrates were cleaved to remove edge effects[89] where residual template solution can collect at the substrate edges, resulting in a locally varied film thickness. The uncoated side of each film was engraved with identifying marks for M:T, recipe number, and film number. The Kapton mask was then removed. The ≈1 mm portion of the film proximal to the Kapton mask exhibited an edge effect with local variation of film thickness and was removed by scraping away oxide film with glass prior to calcination. The final active area of each sample was determined by photography over a ruled grid and was analyzed using ImageJ.

X-Ray Scattering Experiments. X-ray experiments were conducted using the SAXSLab Ganesha at the South Carolina SAXS collaborative (SCSC). A Xenocs GeniX 3D microfocus source was used with a copper target to produce monochromatic beam with a 0.154 nm wavelength. The instrument was calibrated prior to measurements using National Institute of Standards and Technology (NIST) reference material, 640d silicon powder with peak position at $2\theta = 28.44°$. A Pilatus 300k detector (Dectris) was used to collect the 2D scattering patterns with nominal pixel dimensions of 172 × 172 μm. SAXS data were acquired with an X-ray flux of ≈1.41 M photon per second upon the sample and a detector-to-sample distance of 1400 mm. Transmission SAXS data were measured to

observe the purely in-plane morphology. The 2D images were azimuthally integrated to yield the scattering vector and intensity. GI-WAXS measurements were conducted with an incident angle (α_i) of 8° relative to the incident beam. The GI-WAXS sample-to-detector distance was 112.1 mm with an X-ray flux of ≈39.2 M photon per second upon the sample. A Gaussian point-spread function was utilized to interpret scattering data as a result of grain-size broadening per the Scherrer formula.[128,129]

X-Ray Adsorption Spectroscopy Experiments. The M:T series at 520, 535, and 600 °C were measured at beamline 20-ID at the Advanced Photon Source (APS) using a Si (111) monochromator. The beam was focused using a Rh coated toroidal mirror at 2.5 mrad. The incident and transmitted X-Rays were monitored with ion chambers filled with 80% He and 20% N_2 gas. The samples were mounted at about 15° incident angle and the Nb fluorescence detected with a 4-element silicon drift detector. Since the substrate glass had a strong Zn fluorescence signal, the signal was attenuated with 300 μm of Al foil in front of the detector. Multiple scans (5-6) were summed to achieve good signal-to-noise which also verified that sample damage from the beam was negligible as no change was observed. MT1.8 films at 300, 350, and 450 °C in addition to the solid-state T-Nb_2O_5 and TT- Nb_2O_5 standards (*vide infra*) were measured at APS beamline 20-BM using a Si (111) monochromator and similar Rh coated toroidal mirror focusing arrangement. Here, the fluorescence was measured using a 13 element Ge detector with 10-12 scans for good signal-to-noise. The solid-state samples were finely ground powders mounted on Scotch® Magic™ tape (3M), with 16 layers giving a good signal in transmission. The data were analyzed using the Demeter software package.[130] Considering a smooth transition between the endpoints of MT1.8-300^{o}C and MT2.4-600^{o}C samples with the latter selected

for its strong Nb-O signal in the Fourier transform (|χ(R)|). Intermediate sample data (χ(k)) were fitted as a linear combination of the two endpoints.

Electron Paramagnetic Resonance. EPR samples were prepared using PMT stock described previously. Once an M:T=3.0 template solution was prepared, aliquots were cast into 20 mL scintillation vials and allowed to evaporate to dryness at room temperature under 25 L min^{-1} of flowing dry air inside a generic Tupperware container. Once dry, samples were aged at 110 ^{o}C for a minimum of 24 hours before calcined with conditions described previously. EPR data were collected on a Bruker EMX spectrometer operating at X-band. The resonant frequency was 9.78 GHz with a modulation amplitude of 5.0 G and a microwave power of 2.0 mW. Data represent an average of 16 measurements. Results are baseline corrected using measurements made in an empty resonator.

Scanning Electron Microscopy. Top-view images of calcined films were acquired with a Zeiss Gemini500 field emission SEM using an accelerating voltage of 5 keV and an in-lens secondary electron detector. The working distance was maintained at ≈4.5 mm and images were acquired at constant magnification of 500k. At least 85 measurements were made upon each feature (pore and walls) to derive statistical metrics. The wall thickness was measured as the diameter on an inscribed circle between neighboring pores as described elsewhere,[91] in addition pore diameter was measured using an inscribed circle. Pore size and wall-thickness data are presented as mean values with the standard-error-of-the-mean. Cross-sectional SEM was used to determine film thickness.

Inductively Coupled Plasma Mass Spectrometry. A series of films prepared on FTO substrates were cut to ≈1 cm^2 of the niobia coating. ImageJ analysis was used to account

for the specific substrate area as previously described. These films along with FTO blanks were heated in a Teflon vessel containing 70% HNO_3 (trace metal grade), 37% HCl (trace metal grade), and 48% HF (trace metal grade) (1:3:0.5 mL) respectively at 180 °C for 12 h before solutions were diluted with water (18.2 MΩ cm) to 50 mL volume and measured using a Thermo-Finnigan Element XR inductively coupled plasma mass spectrometry (ICP-MS). The instrument was calibrated using a range of concentrations spanning those of the measured samples. A range of digestion solutions were screened in a previous work, demonstrating the above solution is sufficient for complete digestion of niobia. These data were used to calculate the niobia mass per unit area for each sample condition.[21]

Electrochemical Analysis. Electrochemical measurements were conducted using a three-electrode setup with a BioLogic SP-150 potentiostat. All measurements were performed in an argon-filled glovebox (<1 ppm O_2, <1 ppm H_2O). The working electrodes were porous niobia prepared using PMT on FTO substrates as described above. The working electrode was held by a home-built titanium metal clamp to assure ohmic contact to the FTO. All potentials are reported versus a Li/Li^+ reference electrode. The counter electrode was also lithium foil ≈540 mm^2 in surface area. All lithium foils were scraped until shiny just prior to immersion in electrolyte. The electrolyte solution was 1.0 M $LiClO_4$ in propylene carbonate. A series of diagnostic cyclic voltammograms and electrochemical impedance spectroscopy measurements were used to verify ohmic contact. The working electrode was then held at 1.2 V for 20 min before cycling from 1.2 to 3.0 V repeatedly 20 times at 10 mV s^{-1} to remove trace contaminants. A series of 21 logarithmically spaced sweeps ranging in rate from 1000 to 3.2 mV s^{-1} were run in sequence starting from 1.2 V versus Li/Li^+. There was a 3 min hold period at the end of each sweep to allow the electrode

to equilibrate. Mass normalization was based upon the film area and ICP-MS measurements with identical samples.

Electrochemical data was imported into MATLAB 2018b using custom scripts and functions. The b-value metrics were determined as a difference between anodic peak currents and their corresponding voltage sweep rates; the corresponding voltage sweep rate for each b-value was the moving mean between the used voltage sweep rates. The determination of surface-limited threshold (SLT) was interpolated between b-value points as a function of corresponding voltage sweep rate. The standard error of this interpolation was estimated using Rolle's theorem. Parallel and series model fitting was done using the MATLAB non-linear regression function with the corresponding equations for each model. Non-linear fitting used mass-normalized current data, initial values close to expected values, a Cauchy weighting function for robust fitting, and a maximum number of iterations of 250,000. Fitting values generated from the non-linear regression function were passed through a gradient function to determine the corresponding predicted b-value of each model.

Solid-state synthesis of Nb_2O_5. Synthesis was adapted from elsewhere.[24] In brief, NbO_2 powder were calcined in alumina crucibles for 24 hrs with a 10 °C min^{-1} ramp rate at 350 and 600 °C to yield TT-Nb_2O_5 and T-Nb_2O_5 polymorphs respectively before allowed to cool to room temperature.

DFT Calculations. Spin polarized DFT calculations were performed using the VASP[131] with projector augmented wave (PAW) pseudo potentials.[132] The generalized gradient approximation of Perdew-Burke-Ernzerhof (GGA-PBE) was used for the

exchange-correlation functional.[133] The calculated lattice parameters for orthorhombic Nb_2O_5 are a = 6.333 Å, b = 29.584 Å, and c = 3.813 Å, which agree well with previously calculated values.[26] The O-rich (001) surface was modeled using a periodic slab containing five unit cells along the *c*-direction with one unit each along the *a*- and *b*-direction as shown in Figure C.4 (a). A vacuum gap of 15 Å was used along the surface normal direction (*c*-direction) to separate the slab from its periodic image. During geometry optimization, the atoms in the middle layer were fixed at their relaxed bulk positions to maintain the bulk phase, whereas all other atoms were allowed to fully relax until the residual forces become smaller than 0.02 eV $Å^{-1}$. A plane-wave energy cutoff of 500 eV was used and the Brillouin zone of the (001) surface model was sampled using a (4 × 2 × 1) Monkhorst-Pack[134] k-point mesh.

4.6 References

[1] J. W. Long, B. Dunn, D. R. Rolison, H. S. White, *Adv. Energy Mater.* **2020**, *10*, 2002457.

[2] P. F. Smith, K. J. Takeuchi, A. C. Marschilok, E. S. Takeuchi, *Acc. Chem. Res.* **2017**, *50*, 544.

[3] P. Albertus, V. Anandan, C. Ban, N. Balsara, I. Belharouak, J. Buettner-Garrett, Z. Chen, C. Daniel, M. Doeff, N. J. Dudney, B. Dunn, S. J. Harris, S. Herle, E. Herbert, S. Kalnaus, J. A. Libera, D. Lu, S. Martin, B. D. McCloskey, M. T. McDowell, Y. S. Meng, J. Nanda, J. Sakamoto, E. C. Self, S. Tepavcevic, E. Wachsman, C. Wang, A. S. Westover, J. Xiao, T. Yersak, *ACS Energy Lett.* **2021**, 1399.

[4] S. Fleischmann, J. B. Mitchell, R. Wang, C. Zhan, D. Jiang, V. Presser, V. Augustyn, *Chem. Rev.* **2020**, *120*, 6738.

[5] J. Maier, *Faraday Discuss.* **2015**, *176*, 17.

[6] J. M. Szeifert, J. M. Feckl, D. Fattakhova-Rohlfing, Y. Liu, V. Kalousek, J. Rathousky, T. Bein, *J. Am. Chem. Soc.* **2010**, *132*, 12605.

[7] J. B. Goodenough, Y. Kim, *Chem. Mater.* **2010**, *22*, 587.

[8] J.-M. Tarascon, M. Armand, In *Materials for Sustainable Energy*, Co-Published with Macmillan Publishers Ltd, UK, **2010**, pp. 171–179.

[9] H. Li, A. Liu, N. Zhang, Y. Wang, S. Yin, H. Wu, J. R. Dahn, *Chem. Mater.* **2019**, *31*, 7574.

[10] C. Costentin, T. R. Porter, J.-M. Savéant, *ACS Appl. Mater. Interfaces* **2017**, *9*, 8649.

[11] T. Brousse, D. Bélanger, J. W. Long, *J. Electrochem. Soc.* **2015**, *162*, A5185.

[12] V. Augustyn, P. Simon, B. Dunn, *Energy Environ. Sci.* **2014**, *7*, 1597.

[13] B. E. Conway, V. Birss, J. Wojtowicz, *J. Power Sources* **1997**, *66*, 1.

[14] B. E. Conway, *J. Electrochem. Soc.* **1991**, *138*, 1539.

[15] C. Choi, D. S. Ashby, D. M. Butts, R. H. DeBlock, Q. Wei, J. Lau, B. Dunn, *Nat. Rev. Mater.* **2020**, *5*, 5.

[16] S. Trasatti, G. Buzzanca, *J. Electroanal. Chem. Interf. Electrochem.* **1971**, *29*, A1.

[17] J. P. Zheng, T. R. Jow, *J. Electrochem. Soc.* **1995**, *142*, L6.

[18] J. P. Zheng, P. J. Cygan, T. R. Jow, *J. Electrochem. Soc.* **1995**, *142*, 2699.

[19] K. Brezesinski, J. Wang, J. Haetge, C. Reitz, S. O. Steinmueller, S. H. Tolbert, B. M. Smarsly, B. Dunn, T. Brezesinski, *J. Am. Chem. Soc.* **2010**, *132*, 6982.

[20] V. Augustyn, J. Come, M. A. Lowe, J. W. Kim, P.-L. Taberna, S. H. Tolbert, H. D. Abruña, P. Simon, B. Dunn, *Nat. Mater.* **2013**, *12*, 518.

[21] W. van den Bergh, H. N. Lokupitiya, N. A. Vest, B. Reid, S. Guldin, M. Stefik, *Adv. Funct. Mater.* **2021**, *31*, 2007826.

[22] J. W. Kim, V. Augustyn, B. Dunn, *Adv. Energy Mater.* **2012**, *2*, 141.

[23] A. A. Lubimtsev, P. R. C. Kent, B. G. Sumpter, P. Ganesh, *J. Mater. Chem. A* **2013**, *1*, 14951.

[24] K. J. Griffith, A. C. Forse, J. M. Griffin, C. P. Grey, *J. Am. Chem. Soc.* **2016**, *138*, 8888.

[25] S. Li, Q. Xu, E. Uchaker, X. Cao, G. Cao, *CrystEngComm* **2016**, *18*, 2532.

[26] D. Chen, J.-H. Wang, T.-F. Chou, B. Zhao, M. A. El-Sayed, M. Liu, *J. Am. Chem. Soc.* **2017**, *139*, 7071.

[27] Q. Deng, Y. Fu, C. Zhu, Y. Yu, *Small* **2019**, *15*, 1804884.

[28] C. Li, Q. Li, Y. V. Kaneti, D. Hou, Y. Yamauchi, Y. Mai, *Chem. Soc. Rev.* **2020**, *49*, 4681.

[29] X. Xu, B. Tian, S. Zhang, J. Kong, D. Zhao, B. Liu, *Anal. Chim. Acta* **2004**, *519*, 31.

[30] W. Luo, Y. Li, J. Dong, J. Wei, J. Xu, Y. Deng, D. Zhao, *Agnew. Chem.* **2013**, *125*, 10699.

[31] L. Kong, C. Zhang, S. Zhang, J. Wang, R. Cai, C. Lv, W. Qiao, L. Ling, D. Long, *J. Mater. Chem. A* **2014**, *2*, 17962.

[32] E. Lim, H. Kim, C. Jo, J. Chun, K. Ku, S. Kim, H. I. Lee, I.-S. Nam, S. Yoon, K. Kang, J. Lee, *ACS Nano* **2014**, *8*, 8968.

[33] E. Lim, C. Jo, H. Kim, M.-H. Kim, Y. Mun, J. Chun, Y. Ye, J. Hwang, K.-S. Ha, K. C. Roh, K. Kang, S. Yoon, J. Lee, *ACS Nano* **2015**, *9*, 7497.

[34] F. Idrees, J. Hou, C. Cao, F. K. Butt, I. Shakir, M. Tahir, F. Idrees, *Electrochim. Acta* **2016**, *216*, 332.

[35] G. Ma, K. Li, Y. Li, B. Gao, T. Ding, Q. Zhong, J. Su, L. Gong, J. Chen, L. Yuan, B. Hu, J. Zhou, K. Huo, *ChemElectroChem* **2016**, *3*, 1360.

[36] H. Song, J. Fu, K. Ding, C. Huang, K. Wu, X. Zhang, B. Gao, K. Huo, X. Peng, P. K. Chu, *J. Power Sources* **2016**, *328*, 599.

[37] J. Y. Cheong, J.-W. Jung, D.-Y. Youn, C. Kim, S. Yu, S.-H. Cho, K. R. Yoon, I.-D. Kim, *J. Power Sources* **2017**, *360*, 434.

[38] S. Lou, X. Cheng, L. Wang, J. Gao, Q. Li, Y. Ma, Y. Gao, P. Zuo, C. Du, G. Yin, *J. Power Sources* **2017**, *361*, 80.

[39] G. Luo, H. Li, D. Zhang, L. Gao, T. Lin, *Electrochim. Acta* **2017**, *235*, 175.

[40] C. Shi, K. Xiang, Y. Zhu, W. Zhou, X. Chen, H. Chen, *Ceram. Int.* **2017**, *43*, 12388.

[41] M. Y. Song, N. R. Kim, H. J. Yoon, S. Y. Cho, H.-J. Jin, Y. S. Yun, *ACS Appl. Mater. Interfaces* **2017**, *9*, 2267.

[42] H. Sun, L. Mei, J. Liang, Z. Zhao, C. Lee, H. Fei, M. Ding, J. Lau, M. Li, C. Wang, X. Xu, G. Hao, B. Papandrea, I. Shakir, B. Dunn, Y. Huang, X. Duan, *Science* **2017**, *356*, 599.

[43] H. Yang, H. Xu, L. Wang, L. Zhang, Y. Huang, X. Hu, *Chem. - Eur. J.* **2017**, *23*, 4203.

[44] J. Zhai, Y. Wu, X. Zhao, Q. Yang, *J. Alloys Compd.* **2017**, *715*, 275.

[45] Z. Chen, H. Li, X. Lu, L. Wu, J. Jiang, S. Jiang, J. Wang, H. Dou, X. Zhang, *ChemElectroChem* **2018**, *5*, 1516.

[46] B. Deng, T. Lei, W. Zhu, L. Xiao, J. Liu, *Adv. Funct. Mater.* **2018**, *28*, 1704330.

[47] Y. Jiao, H. Zhang, H. Zhang, A. Liu, Y. Liu, S. Zhang, *Nano Res.* **2018**, *11*, 4673.

[48] L. Kong, X. Liu, J. Wei, S. Wang, B. B. Xu, D. Long, F. Chen, *Nanoscale* **2018**, *10*, 14165.

[49] J. Liao, R. Tan, Z. Kuang, C. Cui, Z. Wei, X. Deng, Z. Yan, Y. Feng, F. Li, C. Wang, J. Ma, *Chin. Chem. Lett.* **2018**, *29*, 1785.

[50] S. Zhang, J. Wu, J. Wang, W. Qiao, D. Long, L. Ling, *J. Power Sources* **2018**, *396*, 88.

[51] S. Hemmati, G. Li, X. Wang, Y. Ding, Y. Pei, A. Yu, Z. Chen, *Nano Energy* **2019**, *56*, 118.

[52] S. Jiang, S. Dong, L. Wu, Z. Chen, L. Shen, X. Zhang, *J. Electroanal. Chem.* **2019**, *842*, 82.

[53] J. W. Kim, S.-O. Kim, H.-S. Kim, *Int. J. Energy Res.* **2019**, *43*, 4359.

[54] D. Li, J. Shi, H. Liu, C. Liu, G. Dong, H. Zhang, Y. Yang, G. Lu, H. Wang, *Sustain. Energy Fuels* **2019**, *3*, 1055.

[55] J. Hu, J. Li, K. Wang, H. Xia, *Electrochim. Acta* **2020**, *331*, 135364.

[56] W. Hu, S. Zhang, W. Zhang, M. Wang, F. Feng, *J. Nanopart. Res.* **2020**, *22*, 57.

[57] Z. Hu, Q. He, Z. Liu, X. Liu, M. Qin, B. Wen, W. Shi, Y. Zhao, Q. Li, L. Mai, *Sci.* **2020**, *65*, 1154.

[58] J. Kang, H. Zhang, Z. Zhan, Y. Li, M. Ling, X. Gao, *ACS Appl. Energy Mater.* **2020**, *3*, 11841.

[59] S. Kim, J. Hwang, J. Lee, J. Lee, *Sci. Adv.* **2020**, *6*, eabb3814.

[60] Y. Li, Y. Wang, G. Cui, T. Zhu, J. Zhang, C. Yu, J. Cui, J. Wu, H. H. Tan, Y. Zhang, Y. Wu, *ACS Appl. Energy Mater.* **2020**, *3*, 12037.

[61] Y. Li, R. Wang, W. Zheng, Q. Zhao, S. Sun, G. Ji, S. Li, X. Fan, C. Xu, *Mater. Technol.* **2020**, *35*, 625.

[62] Y. Lian, D. Wang, S. Hou, C. Ban, J. Zhao, H. Zhang, *Electrochim. Acta* **2020**, *330*, 135204.

[63] D. Liang, L. Hu, L. Wang, L. Liu, S. Liang, L. Yang, N. Zhou, C. Liang, *ChemNanoMat* **2020**, *6*, 73.

[64] Z. Liu, W. Dong, J. Wang, C. Dong, Y. Lin, I.-W. Chen, F. Huang, *iScience* **2020**, *23*, 100767.

[65] P. Nagaraju, R. Vasudevan, A. Alsalme, A. Alghamdi, M. Arivanandhan, R. Jayavel, *Nanomaterials* **2020**, *10*, 160.

[66] X. Qu, Y. Liu, B. Li, B. Xing, G. Huang, C. Zhang, S. W. Hong, J. Yu, Y. Cao, *Energy Fuels* **2020**, *34*, 3887.

[67] L. She, F. Zhang, C. Jia, L. Kang, Q. Li, X. He, J. Sun, Z. Lei, Z.-H. Liu, *J. Colloid Interface Sci.* **2020**, *573*, 1.

[68] X. Zhai, J. Liu, Y. Zhao, C. Chen, X. Zhao, J. Li, H. Jin, *Appl. Surf. Sci.* **2020**, *499*, 143905.

[69] H. Ding, Z. Song, K. Feng, H. Zhang, H. Zhang, X. Li, *J. Solid State Chem.* **2021**, *299*, 122136.

[70] J. Jin, J. Cai, X. Wang, Z. Sun, Y. Song, J. Sun, *FlatChem* **2021**, *27*, 100236.

[71] S. Ouendi, C. Arico, F. Blanchard, J.-L. Codron, X. Wallart, P. L. Taberna, P. Roussel, L. Clavier, P. Simon, C. Lethien, *Energy Storage Mater.* **2019**, *16*, 581.

[72] R. Kang, S. Li, B. Zou, X. Liu, Y. Zhao, J. Qiu, G. Li, F. Qiao, J. Lian, *J. Alloys Compd.* **2021**, *865*, 158824.

[73] E. Lim, C. Jo, M. S. Kim, M.-H. Kim, J. Chun, H. Kim, J. Park, K. C. Roh, K. Kang, S. Yoon, J. Lee, *Adv. Funct. Mater.* **2016**, *26*, 3711.

[74] R. Bi, N. Xu, H. Ren, N. Yang, Y. Sun, A. Cao, R. Yu, D. Wang, *Angew. Chem.* **2020**, *132*, 4895.

[75] B.-A. Mei, J. Lau, T. Lin, S. H. Tolbert, B. S. Dunn, L. Pilon, *J. Phys. Chem. C* **2018**, *122*, 24499.

[76] J. S. Ko, C.-H. Lai, J. W. Long, D. R. Rolison, B. Dunn, J. Nelson Weker, *ACS Appl. Mater. Interfaces* **2020**, *12*, 14071.

[77] N. Li, X. Lan, L. Wang, Y. Jiang, S. Guo, Y. Li, X. Hu, *ACS Appl. Mater. Interfaces* **2021**, *13*, 16445.

[78] X. Ge, C. Gu, Z. Yao, J. Sun, X. Wang, J. Tu, *Chem. Eng. J.* **2018**, *338*, 211.

[79] Z. Song, H. Li, W. Liu, H. Zhang, J. Yan, Y. Tang, J. Huang, H. Zhang, X. Li, *Adv. Mater.* **2020**, *32*, 2001001.

[80] W. V. Metanomski, Ed., *Compendium of Macromolecular Nomenclature*, 1st ed., International Union of Pure and Applied Chemistry., **1991**.

[81] J.-Y. Shin, J. H. Joo, D. Samuelis, J. Maier, *Chem. Mater.* **2012**, *24*, 543.

[82] H.-S. Kim, J. B. Cook, H. Lin, J. S. Ko, S. H. Tolbert, V. Ozolins, B. Dunn, *Nat. Mater.* **2017**, *16*, 454.

[83] S. Zhang, G. Liu, W. Qiao, J. Wang, L. Ling, *J. Colloid Interface Sci.* **2020**, *562*, 193.

[84] J. Ye, P. Shea, A. C. Baumgaertel, S. A. Bonev, M. M. Biener, M. Bagge-Hansen, Y. M. Wang, J. Biener, B. C. Wood, *Chem. Mater.* **2018**, *30*, 8871.

[85] G. Wang, Y. Ling, Y. Li, *Nanoscale* **2012**, *4*, 6682.

[86] J. A. Yuwono, P. Burr, C. Galvin, A. Lennon, *ACS Appl. Mater. Interfaces* **2021**, *13*, 1791.

[87] A. L. Viet, M. V. Reddy, R. Jose, B. V. R. Chowdari, S. Ramakrishna, *J. Phys. Chem. C* **2010**, *114*, 664.

[88] J. Meng, Q. He, L. Xu, X. Zhang, F. Liu, X. Wang, Q. Li, X. Xu, G. Zhang, C. Niu, Z. Xiao, Z. Liu, Z. Zhu, Y. Zhao, L. Mai, *Adv. Energy Mater.* **2019**, *9*, 1802695.

[89] A. Sarkar, M. Stefik, *J. Mater. Chem. A* **2017**, *5*, 11840.

[90] H. N. Lokupitiya, A. Jones, B. Reid, S. Guldin, M. Stefik, *Chem. Mater.* **2016**, *28*, 1653.

[91] K. A. Lantz, N. B. Clamp, W. van den Bergh, A. Sarkar, M. Stefik, *Small* **2019**, *15*, 1900393.

[92] A. Sarkar, A. Thyagarajan, A. Cole, M. Stefik, *Soft Matter* **2019**, *15*, 5193.

[93] A. Sarkar, L. Evans, M. Stefik, *Langmuir* **2018**, *34*, 5738.

[94] A. Vu, Y. Qian, A. Stein, *Adv. Energy Mater.* **2012**, *2*, 1056.

[95] M. Stefik, *J. Mater. Res.* **2021**.

[96] M. C. Orilall, U. Wiesner, *Chem. Soc. Rev.* **2011**, *40*, 520.

[97] C. Robertus, W. H. Philipse, J. G. H. Joosten, Y. K. Levine, *J. Chem. Phys.* **1989**, *90*, 4482.

[98] M. A. Sahiner, A. Nabizadeh, D. Rivella, L. Cerqueira, J. Hachlica, R. Morea, J. Gonzalo, J. C. Woicik, *J. Phys.: Conf. Ser.* **2016**, *712*, 012103.

[99] M. T. Vandenborre, B. Poumellec, J. Livage, *J. Solid State Chem.* **1989**, *83*, 105.

[100] M. T. Vandenborre, B. Poumellec, C. Alquier, J. Livage, *J. Non. Cryst. Solids* **1989**, *108*, 333.

[101] I. Andoni, J. M. Ziegler, G. Jha, C. A. Gadre, H. Flores-Zuleta, S. Dai, S. Qiao, M. Xu, V. T. Chen, X. Pan, R. M. Penner, *ACS Appl. Energy Mater.* **2021**, acsaem.1c00580.

[102] N. Özer, T. Barreto, T. Büyüklimanli, C. M. Lampert, *Sol. Energy Mater. Sol. Cells* **1995**, *36*, 433.

[103] A. S. Foster, A. L. Shluger, R. M. Nieminen, *Phys. Rev. Lett.* **2002**, *89*, 225901.

[104] H.-W. Huang, Z.-G. Ye, M. Dong, W.-L. Zhu, X.-Q. Feng, *Jpn. J. Appl. Phys.* **2002**, *41*, L713.

[105] E. Talik, J. Kisielewski, P. Zajdel, A. Guzik, E. Wierzbicka, A. Kania, J. Kusz, S. Miga, M. Szubka, *Opt. Mater.* **2019**, *91*, 355.

[106] A. Sahai, N. Goswami, *Ceram. Int.* **2014**, *40*, 14569.

[107] J.-W. Sun, L.-S. Kang, J.-S. Kim, M.-R. Joung, S. Nahm, T.-G. Seong, C.-Y. Kang, J.-H. Kim, *Acta Mater.* **2011**, *59*, 5434.

[108] J. Cao, D. Zhang, Y. Yue, T. Pakornchote, T. Bovornratanaraks, M. Sawangphruk, X. Zhang, J. Qin, *Mater. Today Energy* **2021**, *21*, 100824.

[109] S. Yang, Y. Liu, Y. Hao, X. Yang, W. A. Goddard III, X. L. Zhang, B. Cao, *Adv. Sci.* **2018**, *5*, 1700659.

[110] E. Knözinger, O. Diwald, M. Sterrer, *J. Mol. Catal. A Chem.* **2000**, *162*, 83.

[111] M. Sterrer, O. Diwald, E. Knözinger, *J. Phys. Chem. B* **2000**, *104*, 3601.

[112] J. M. Coronado, A. J. Maira, J. C. Conesa, K. L. Yeung, V. Augugliaro, J. Soria, *Langmuir* **2001**, *17*, 5368.

[113] M. R. Lukatskaya, B. Dunn, Y. Gogotsi, *Nat. Commun.* **2016**, *7*, 12647.

[114] H. Lindström, S. Södergren, A. Solbrand, H. Rensmo, J. Hjelm, A. Hagfeldt, S.-E. Lindquist, *J. Phys. Chem. B* **1997**, *101*, 7717.

[115] V. Murray, D. S. Hall, J. R. Dahn, *J. Electrochem. Soc.* **2019**, *166*, A329.

[116] T. Marks, S. Trussler, A. J. Smith, D. Xiong, J. R. Dahn, *J. Electrochem. Soc.* **2011**, *158*, A51.

[117] N. Kumagai, K. Tanno, T. Nakajima, N. Watanabe, *Electrochim. Acta* **1983**, *28*, 17.

[118] T.-C. Liu, W. G. Pell, B. E. Conway, S. L. Roberson, *J. Electrochem. Soc.* **1998**, *145*, 1882.

[119] H. Kim, E. Lim, C. Jo, G. Yoon, J. Hwang, S. Jeong, J. Lee, K. Kang, *Nano Energy* **2015**, *16*, 62.

[120] D. Chao, R. DeBlock, C.-H. Lai, Q. Wei, B. Dunn, H. J. Fan, *Adv. Mater.* **2021**, *33*, 2103736.

[121] S. Moitzheim, S. D. Gendt, P. M. Vereecken, *J. Electrochem. Soc.* **2019**, *166*, A1.

[122] V. Daramalla, G. Venkatesh, B. Kishore, N. Munichandraiah, S. B. Krupanidhi, *J. Electrochem. Soc.* **2018**, *165*, A764.

[123] J. Han, A. Hirata, J. Du, Y. Ito, T. Fujita, S. Kohara, T. Ina, M. Chen, *Nano Energy* **2018**, *49*, 354.

[124] W. S. Shih, S. J. Young, L. W. Ji, W. Water, H. W. Shiu, *J. Electrochem. Soc.* **2011**, *158*, H609.

[125] D. B. G. Williams, M. Lawton, *J. Org. Chem.* **2010**, *75*, 8351.

[126] L. J. Fetters, D. J. Lohse, D. Richter, T. A. Witten, A. Zirkel, *Macromolecules* **1994**, *27*, 4639.

[127] H. N. Lokupitiya, M. Stefik, *Nanoscale* **2017**, *9*, 1393.

[128] A. L. Patterson, *Phys. Rev.* **1939**, *56*, 978.

[129] P. Scherrer, *Math. Phys.* **1918**, *2*, 98.

[130] B. Ravel, M. Newville, *J. Synchrotron Rad.* **2005**, *12*, 537.

[131] G. Kresse, J. Furthmüller, *Comput. Mater. Sci.* **1996**, *6*, 15.

[132] P. E. Blöchl, *Phys. Rev. B* **1994**, *50*, 17953.

[133] J. P. Perdew, K. Burke, M. Ernzerhof, *Phys. Rev. Lett.* **1996**, *77*, 3865.

[134] H. J. Monkhorst, J. D. Pack, *Phys. Rev. B* **1976**, *13*, 5188.

[135] F. Crameri, G. E. Shephard, P. J. Heron, *Nat. Commun.* **2020**, *11*, 5444.

[136] F. Crameri, *Geosci.* **2018**, *11*, 2541.

CHAPTER 5: Mesoporous TiO_2 Microparticles with Tailored Surface, Pore, Wall, and Particle Dimensions using Persistent Micelle Templates[1]

---

[1]van den Bergh, W.; Williams, E.; Vest, N.; Chiang, P.-H.; Stefik, M. *Langmuir*, 2021, 37(44), 12874–12886

5.1 Abstract

Mesoporous microparticles are an attractive platform to deploy high surface area nanomaterials in a convenient particulate form that is broadly compatible with diverse device manufacturing methods. The applications for mesoporous microparticles are numerous, spanning the gamut from drug delivery to catalysis and energy storage. For most applications, the performance of the resulting materials depends upon the architectural dimensions including the mesopore size, wall thickness, and microparticle size yet a synthetic method to control of all these parameters has remained elusive. Furthermore, some mesoporous microparticle reports noted a surface skin layer which has not been tuned before despite the important effect of such a skin layer upon transport/encapsulation. In the present study, material precursors and block polymer micelles are combined to yield mesoporous materials in a microparticle format due to phase separation from a homopolymer matrix. The skin layer thickness was kinetically controlled where a layer integration via diffusion (LID) model explains its production and dissipation. Furthermore, the independent tuning of pore size and wall thickness for mesoporous microparticles is shown for the first time using persistent micelle templates. Lastly, the kinetic effects of numerous processing parameters upon the microparticle size are shown.

5.2 Introduction

Mesoporous microparticles enable convenient integration of nanomaterials with popular manufacturing methods based on micron-scale powders. Applications of mesoporous microparticles include drug delivery,[1–5] chemical sensors,[6–9] catalytic structures,[10–22] and energy devices.[23–43] The application performance depends upon the architecture of the nanostructure where the transport and storage of drugs or intercalation

of ions are influenced by the pathways and interfaces. The presence of a less-porous skin layer can further tailor chemical transport rates to/from the microparticle *e.g.*, adjusting the rate of controlled release.[1–3,13,44,45] Thus, the ability to custom tailor each aspect of the mesoporous microparticle architecture determines their ultimate performance. For example, when mesoporous microparticles are applied in battery electrodes, each architectural dimension contributes towards a specific function: the wall thickness determines the ion intercalation length scale, the particle size and porosity determine the electrolyte diffusion length, and the surface area influences the insertion kinetics. Efficient electrode design balances these concomitant processes to achieve the greatest gravimetric and volumetric energy/power densities.[46] Such tailored mesoporous microparticles could also provide a platform for investigating emergent nanoscale phenomena using fully tailorable nanomaterials to deconvolve contributions from concomitant processes.[47] Synthetic routes for both soft and hard templates have widely enabled mesoporous microparticles.[4,5,9,14–18,25–29,48–65] Soft templates are advantageous in terms of the lower cost, simpler preparation, and synthetic versatility. Soft template routes span a wide gamut, including hydro/solvothermal synthesis,[14,19–21,30–35,43,48,49,66–70] spray pyrolysis,[5,18,25,27,52–61,63,65] and evaporative casting.[9,15–17,26,28,29,50,51,71] Generally the microparticle structure is controlled via the dispersion of precursors. For example, spray pyrolysis techniques quickly form microparticles from the evaporation of aerosols, however the nanostructures are often poorly defined and the microparticles are sometimes covered with a skin layer with a speculative formation pathway.[53,54,56–58,63,64] Hydro/solvothermal synthesis techniques and simple evaporative casting processes produce microparticles via phase separation of precursors from a solvent or a non-volatile species such as a homopolymer.

These approaches have demonstrated many different morphologies and numerous different nanoscale dimensions via soft templates; however, none have yet demonstrated independent control of the pore and wall dimensions. This lack of one-variable at a time tailoring is in part due to the changing of micelle template dimensions with alterations to processing conditions. A fully tunable strategy must be able to adjust all feature sizes in a controlled and predictable manner.

Persistent micelle templates (PMT) uniquely enable nanostructures with independent tunability of the pore and wall dimensions.[47,72–76] Most processes using block polymer structure-directing agents are based upon equilibration and thus the architectural dimensions are determined by free-energy minimization. In contrast, the PMT strategy is based upon kinetic control where block polymer micelles are used as templates with an invariant size. Here it is important to inhibit chain exchange processes which would otherwise cause the micelles to change size in response to changing solution conditions. The equilibrium size of a micelle is a balance of enthalpic and entropic contributions, largely tied to interfacial energy (favoring larger micelles) and chain stretching entropy (favoring smaller micelles). The activation energy for chain exchange naturally determines its rate. For the single chain exchange mechanism, the rate has a double exponential dependence on χN where N scales with core block molecular mass and χ is the Flory-Huggins interaction parameter, a largely enthalpic term corresponding to the two component interface of the core block with the solution ($\chi_{core\text{-}solution}$).[77,78] The use of such high-χN conditions was shown to enable the kinetic entrapment of persistent micelles to yield constant template dimensions.[73] The material wall thickness may be tailored monotonically by changing the amount of material precursors relative to the amount of

template (M:T ratio) and the resulting feature sizes follow a simple geometric model.[72] PMT thus diverges from dynamic (non-persistent) micelle templates which undergo size changes due to equilibration anytime the M:T ratio is altered which leads to chaotic trends of the feature sizes[72] as well as changes to the morphology.[79] In the past, PMT approaches were mostly used for thin films where the rapid material crosslinking ensured preservation of kinetic micelle control after evaporation.[47,72–75]

The development of fully tunable bulk mesoporous microparticles with PMT thus poses several design challenges. Here an evaporative strategy is adopted based upon micelles templates, material precursors, and a phase-separating homopolymer. The evaporative processing of microparticles from bulk solution is inherently slower than thin-film spin coating and thus provides numerous challenges towards preserving kinetic control of micelle templates. Both the removal of solvents that inhibit chain exchange (particularly water) and the subsequent heat treatments to crosslink the material precursors enable additional time for a loss of kinetic-control via equilibration. Here, it is shown that simple translation of prior PMT protocols towards mesoporous microparticles resulted in a loss of kinetic micelle control. This lack of independent pore and wall thickness control is a general feature of other evaporative casting works. An improved PMT strategy was developed to yield the first mesoporous microparticles prepared from block polymers that independently control the pore and wall thickness based upon micelles with glassy cores (glassy-PMT).[76] This use of micelles with robust kinetic entrapment was necessary to preserve the micelle shape and size throughout the full synthesis. This contrasts with prior evaporative casting works which were subject to multiparameter changes when glassy templates were plasticized[9,26] or when low-T_g templates were used.[14–17,28,29,50,51,71] While

there are a broad range of mesoporous carbon,[22,23,30,37,66,76,80] metal,[55,81–83] oxide,[1–5,7–13,20,21,24,25,31,34,35,40–42,44,45,47,51–54,57–62,64,67,70,72,73,79,84,85] hydroxide,[65,71] sulfide,[32,69] and polyanion[10,43] materials reported, TiO_2 was selected here as a model material due to its broad use in catalysis,[14–19,48,50,56,63] energy storage,[26,68,74] sensing,[38,86] and other applications.[27–29,33,36,49] Furthermore, processing factors that determine skin layer thickness and particle size were identified. A model is presented to explain skin layer formation and is used to tailor the microparticle surface. Thus, a comprehensive set of conditions are elaborated to enable custom tuning of all architectural aspects of mesoporous microparticles.

5.3 Results and Discussion

Ideally the synthesis of mesoporous microparticles supports independent tailoring of each feature size, including skin layer thickness or absence thereof, pore size, wall thickness, and microparticle size. Prior works have demonstrated the ability to adjust several of these dimensions, though generally coupled at the same time with changes to other feature sizes.[16,26,28,48,57,66,80] The independent adjustment of the pore size, wall thickness, or skin layer thickness has remained elusive for mesoporous microparticles produced using soft templates. Here we employ a polymer-based soft template strategy to produce mesoporous microparticles by combining a block polymer with a phase separating homopolymer. Through evaporative processing with a common solvent, the block polymer and material precursors phase separate from the homopolymer. Several important design criteria must be considered to realize mesoporous microparticles with independent feature tunability in this context. 1) The mixture of polymers must use a majority of homopolymer such that the other components (a mixture of block polymer and material precursors) phase

separates as a minority suspension of discrete microparticles. Most prior examples employ a 5-10x ratio of homopolymer to other reagents to inhibit coarsening of the minority phase by avoiding percolation and extending the distance between the microparticles. 2) The homopolymer composition must be selected to phase separate from both the block polymer ($\chi_{homopolymer\text{-}template}$>0.5) and material precursors ($\chi_{homopolymer\text{-}precursor}$>0.5). Selecting a homopolymer with a different chemical composition than the block polymer generally will lead to the desired phase separation, otherwise the homopolymer may swell the block polymer phase.[84] Furthermore, popular material precursors, *e.g.* metal oxide nanoparticles, are hydrophilic due to hydrogen bonding interactions and have limited solvent options. Thus, the homopolymer must be processable from common hydrophilic solvents yet be sufficiently hydrophobic to phase separate from the material precursors. The homopolymer poly(propylene oxide) satisfies all of these considerations. 3) The block polymer within the microparticle minority phase also must satisfy several concomitant criteria. A portion of the block polymer must phase separate ($\chi_{core\text{-}precursor}$>0.5) from the material precursors to produce a nanostructure, eventually leading to mesoporosity after thermal removal of the polymers. Furthermore, the other portion of the block polymer must selectively interact with the material precursors ($\chi_{corona\text{-}precursor}$<0), typically via hydrogen bonding. Lastly, the block polymer must also be dispersible in the same solvent used for the other components, often lower alcohols. PEO-*b*-PBA satisfies all these criteria and *vide infra*, PEO-*b*-PS can also satisfy these criteria when pre-micellized. 4) Considering that multiple materials are undergoing simultaneous phase separation and rearrangement; the timescale of evaporation should be controlled to tailor the spatial distribution of each component (**Scheme 5.1**). It will be shown that deliberate rate control during evaporation

enables regulation of the skin layer thickness and particle size. 5) Retaining independent control of the pore and wall dimensions requires that the block polymer template does not undergo equilibration.[72–75,84] In contrast, a kinetically trapped process called Persistent Micelle Templates (PMT) enables independent and high precision control of these dimensions with as small as 2 Å increments of adjustment demonstrated between samples.[72,74] Most prior PMT demonstrations produced thin films and relied upon arresting chain exchange between micelles by imposing a large $\chi_{core\text{-}solution}$.[73,75] In contrast to past works involving ~100-500 nm thin films which can evaporate solvent and crosslink the oxide within seconds, it is shown here that the novel use of glassy micelle cores was needed to impose persistence on the more extended time scales needed for bulk samples.

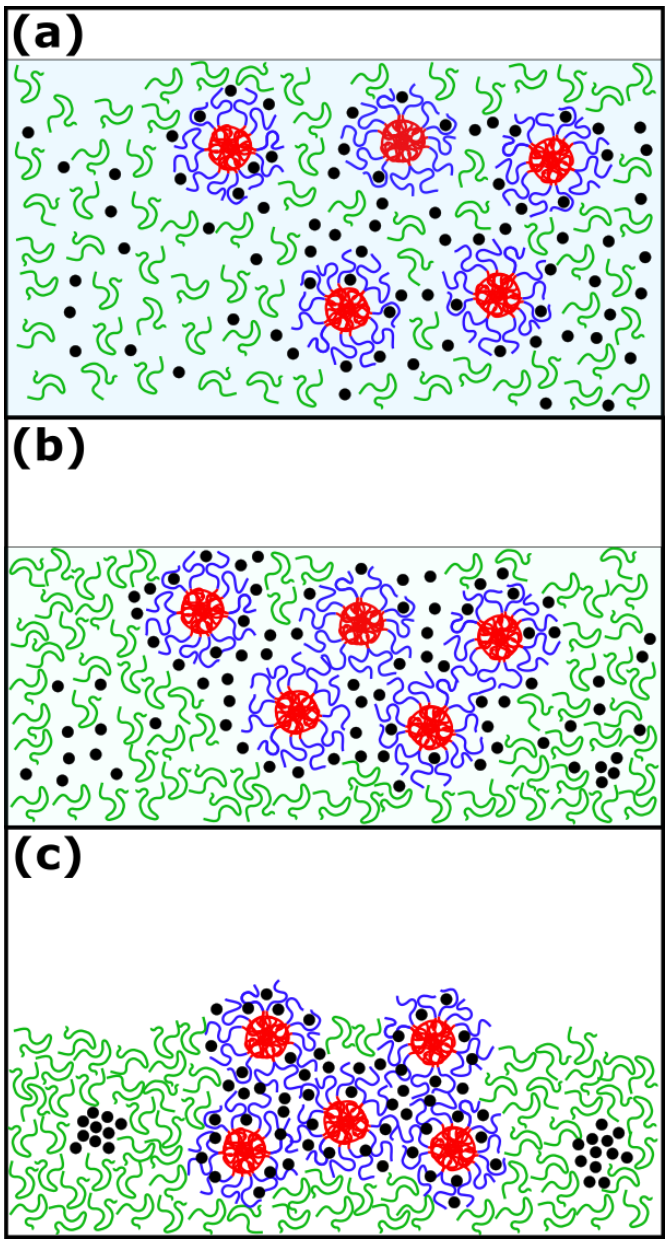

Scheme 5.1. The casting solution with homogeneous dispersion of homopolymers (green), block polymer micelles (red and blue), material nanoparticles (black), and solvent molecules (not drawn) (a). Evaporation of the solvent leads to phase separation of the nanoparticles and the micelles from the homopolymer. Here, different rates of phase separation for the nanoparticles and the micelles lead to the formation of a skin layer on the exterior of the microparticle (b). Overtime, the sol particles redistribute throughout the corona blocks of the micelles, reducing the skin layer thickness (c). Such a process would release free energy by minimizing nanoparticle contact with the homopolymer and maximizing nanoparticle contact with the corona block. Similarly, some nanoparticles could phase separate away from the micelle templates.

Surface skin layers regulate the transport of reagents to and from microparticles. Skin layers around mesoporous microparticle have been observed elsewhere, however their presence is rarely explained and is sometimes attributed to rapid evaporation of solvent[53,54,57,59] or thermodynamics.[95] While some adjustment of the skin layer has been reported, these syntheses did not independently modify other structural features.[57,63,95] The preliminary experiments leading to this report often resulted in microparticles with a significant skin layer thickness (**Figure 5.1c**). The skin layer formation was examined under different processing times as well as different evaporation conditions (purge 0.1-25 L/min). Here the term "processing time" indicates the time from the beginning of solution evaporation until the sample was transferred from the drying chamber to the aging step which promotes material crosslinking. The samples dried with 25 L/min of carrier gas exhibited a marked reduction in the skin layer thickness upon extension of this processing time. Please note that most of the solvent has left the sample within the first 5 min whereas the skin layer was found to monotonically reduce in thickness for 3 hrs, exhibiting a final average thickness of 14.2 ± 2.4 nm. The pronounced trend for processing time dependence indicates kinetic control. Furthermore, partially covering the dishes and/or reducing the gas flow rate to 16 or 0.1 L/min were all found to reduce the skin layer thickness (**Figure 5.1a**). The thinnest skin layer thickness of 1.28 ± 1.40 nm (with 71% of open porosity) was found using 0.1 L/min of carrier gas with a partially covered dish (**Figure 5.3**). Longer processing times generally lead to thinner skin layers and greater degrees of open surface porosity (no skin layer) across all conditions, except for the 120 min sample under 16 L/min. Samples dried under 16 L/min of carrier gas reached a minimal skin layer thickness of 2.25 ± 2.93 nm with 86% open porosity. Both the 16 and 0.1 L/min flow rate conditions with sufficient

processing time or 3 hrs or more produced microparticles with a majority of open mesoporosity (**Figure 5.1b,d**). The use of tailored drying gas flow rates has not been previously examined for block polymer based mesoporous microparticles. We propose that the skin layer formation is caused by different rates of phase separation for each of the microsphere components: the block polymer micelles and the material precursors. As the solvent is gradually eliminated, the initially homogeneous solution (**Scheme 5.1a**) begins to partition and phase separate during drying (**Scheme 5.1b**) as governed by the solubility and mobility of each component. These differences can lead to an uneven distribution of material precursors and block polymer micelles. Consider the process where a nanoparticle (material precursor) is added to a cluster of micelles composing a microsphere; the nanoparticle incorporation into the surface is reasonably much faster than its diffusion into the micelle corona chains. Given enough time and mobility, the nanoparticles accumulating at the surface of the microparticles can be integrated within the microspheres (**Scheme 5.1c**). While full incorporation is expected considering nanoparticle diffusion rates in polymer melts[96–99] the inability of our samples to reach that state suggests that nanoparticle crosslinking rate is competing with the nanoparticle incorporation rate to generally preserve some skin layer. Regardless, we term this process Layer Integration via Diffusion (LID). The LID model explains why skin layers are found most commonly for spray pyrolysis methods[53,54,56–60,64,65] which have rapid evaporation whereas slower methods often do not exhibit a skin layer.[16,26,28,50,51] Similarly the process examined here, spans in behavior from a tunable skin layer to mostly eliminating the skin layer. Other recent studies have demonstrated that the interfacial energetics can impose/eliminate a skin layer, albeit coupled with variation of multiple architectural parameters at the same time.[80]

The skin layer is also adjustable at later steps via thermal coarsening. **Figure 5.2** shows how progressively increasing the calcination time leads to the gradual reduction of the surface layer, likely driven by the reduction of surface area. Please note that SAXS measurements on these thermally coarsened nanostructures revealed no marked changes to the well-defined nanostructure (**Figure D.4**). Thus, the LID model and thermal coarsening enable tailoring of the skin layer thickness via kinetic control and can include a majority of open surface mesoporosity.

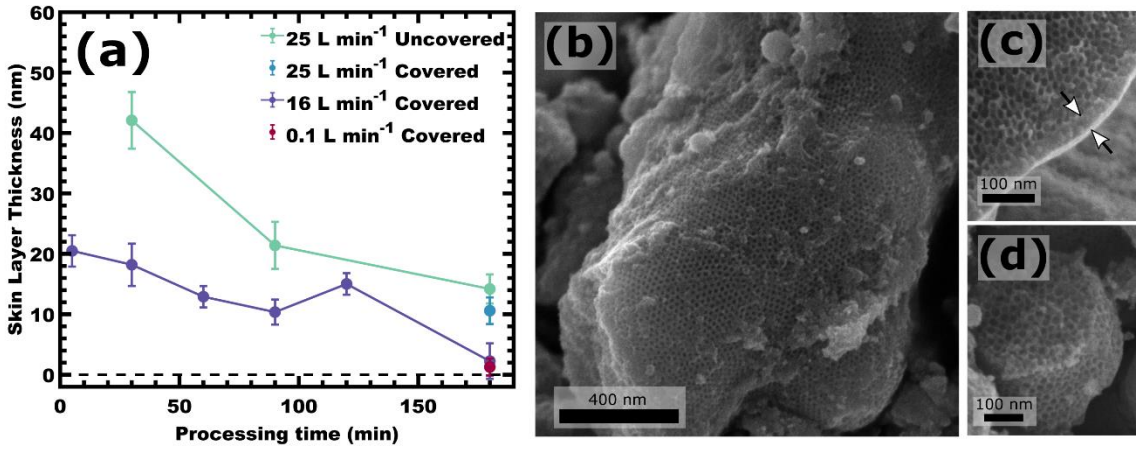

Figure 5.1. The skin layer thickness at the surface of mesoporous microparticles was varied with different processing parameters (a). SEM image of a representative microparticle without a skin layer (b) reveals accessible porosity. Cross-sectional SEM images of fractured microparticles were used to determine skin thickness statistics (c, d). Values are reported as the mean ± error-of-the-mean. Data and SEM images shown for PEO-*b*-PBA with M:T=2.5.

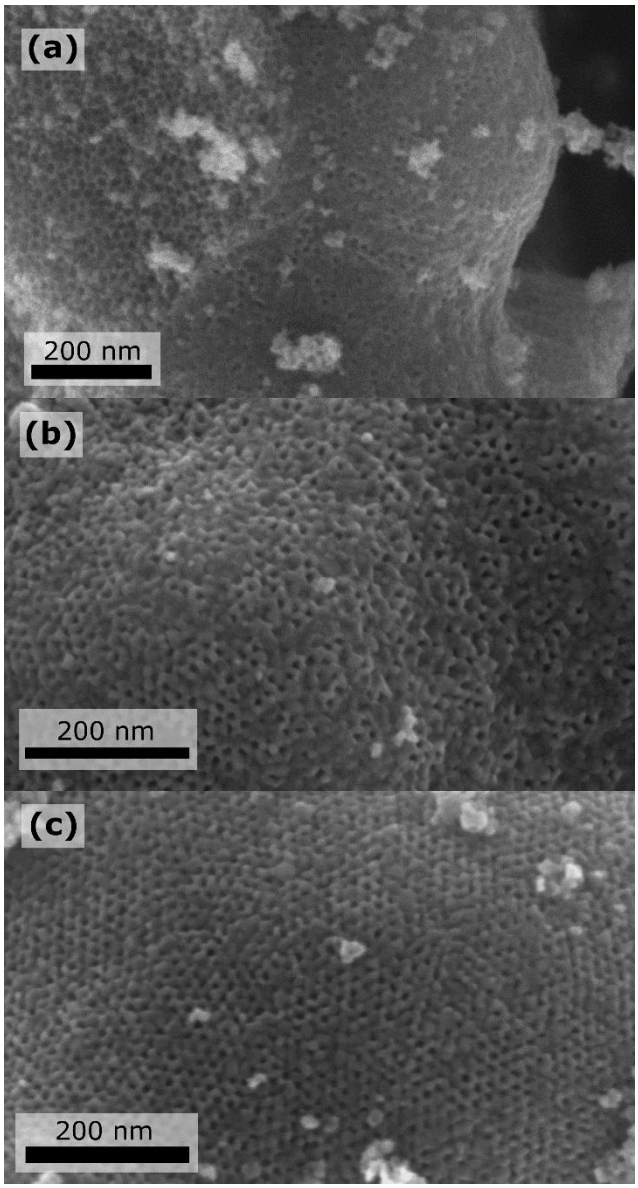

Figure 5.2. SEM images of microparticle surfaces showing the pore exposure, or lack thereof, of the same sample tailored via calcination conditions: 0.1 hr (a), 12 hr (b), and 24 hr (c) at 450 °C. The template was PEO-*b*-PBA with M:T=2.5.

The mesopore size and wall thickness are important to control since they govern intra-particle species transport through the nanostructure and intercalation transport into the nanostructure, respectively, thus significantly influencing application performance. As introduced earlier, PMT enables the independent tuning of nanoscale pore and wall dimensions by using kinetically trapped micelle templates. As quantitatively predicated by

a prior SAXS-based model a PMT series is expected to exhibit lattice expansion when the template size is held constant and material is added between micelles (increasing M:T ratio).[72] Such lattice expansion is simple to validate quantitatively via the primary SAXS peak shifting to lower-q (higher d-spacing). However, the PEO-*b*-PBA based samples did not exhibit such a trend in SAXS peak position shift (q-spacing) and was rather indicative of lattice contraction typical for dynamic micelle (not PMT) behavior (**Figure 5.3a**). Furthermore, the SAXS patterns were often bimodal, indicative of multiple morphologies and partial equilibration.[54,62] These results suggest that after evaporation, the material precursors surrounding the micelles are insufficient to hamper chain exchange, neither in terms of energetic barrier (χN) nor mobility hinderance from *e.g.* condensation reactions. This shows that the preservation of kinetic control is more challenging here than with prior thin film methods. Most prior PMT demonstrations used similar low-T_g block polymers combined with rapid crosslinking after spin coating. In contrast, the much slower process used here provides enough time to lose kinetic micelle control of the micelle templates. Increasing water content, i.e., increasing $\chi_{core\text{-}solution}$, from 5 wt% to 20 wt% did not maintain kinetic micelle control with PEO-*b*-PBA. More rapid processing likely aids in limiting chain exchange, however, the results in **Figure 5.1** demonstrate that faster processing would simultaneously thicken the skin layer and limit its extent of tailoring. In addition, changes to the skin layer thickness are expected to be convolved onto changes to the wall thickness since skin formation removes material precursors from the microparticle interiors. Thus, we adapted an alternative avenue to prevent chain exchange between micelles.

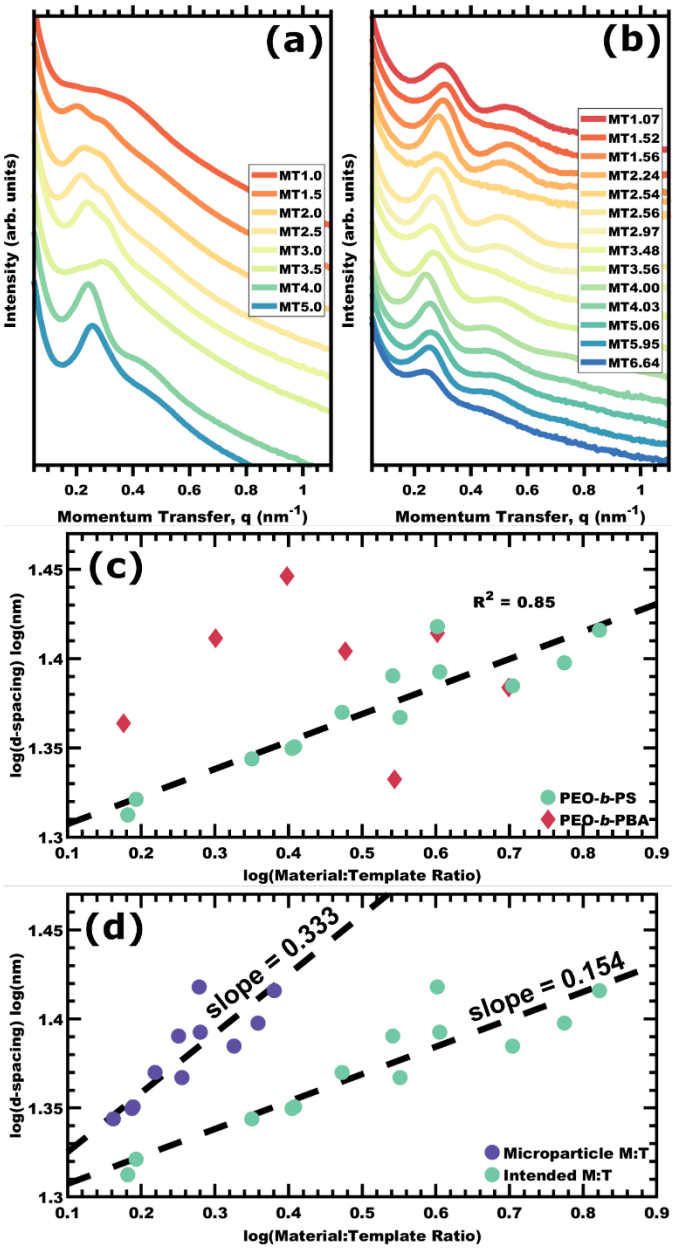

Figure 5.3. SAXS data for microparticle series with varied M:T values using PEO-*b*-PBA (a) were not consistent with PMT lattice expansion (c). In contrast, similar samples prepared using PEO-*b*-PS glassy-core micelles (b) show a peak shift to lower q, consistent with PMT lattice expansion (c). The PMT model predicts the log-log plots of SAXS d-spacing vs M:T to have an approximate slope of 1/3. The lower slope for the PEO-*b*-PS series was attributed to material phase separation partially into templated microparticles and partially into non-templated materials. The microparticle M:T was determined by fitting an empirical power law relationship to correct this slope (panel d). Best-fit lines are presented with dashes. SAXS plots were offset vertically for clarity.

To provide more robust kinetic-control, regardless of χN conditions, we used glassy persistent micelle templates (glassy-PMT). The high-T_g core block enables micelle dynamics to be arrested thermally if good solvents and plasticizers are avoided. This strategy has been employed to halt micelle chain exchange during kinetic studies,[77] for trapping diverse micelle morphologies,[100–107] and was recently expanded to the context of polymer templates with glassy-PMT.[76] Glassy-PMTs were thus prepared using an established procedure based on PEO-*b*-PS. Mesoporous microparticles were again prepared with PPO using a series of M:T values and were measured by SAXS (**Figure 5.3b**). Please note that an increased water content of 10 wt% was used to maintain a narrow particle size distribution while enabling LID to limit the skin layer thickness (*vide infra*). In contrast to PEO-*b*-PBA, the SAXS trends of this sample series exhibited lattice expansion as materials were added, consistent with PMT behavior (**Figure 5.3b,5.5a**) with an observed structure factor q-ratio of ~1:2 in SAXS, consistent with randomly packed spheres of relatively uniform size seen in SEM images (**Figure 5.4**).[108] These SEM images also revealed relatively constant pore size and increasing wall thickness with M:T with the corresponding statistical descriptors presented in **Figure 5.5**. A previously developed log-log coordinate system was used to check SAXS trends for consistency with PMT conditions based upon the quantitative trend for lattice expansion (**Equation D.2**).[75] In brief, an approximate slope of 1/3 is anticipated based upon the cube root relationship between volumetric attributes (M:T) and linear dimensions (d-spacing).[75] However, the PEO-*b*-PS sample series exhibited a slope of 0.154 in this log-log coordinate system (**Figure 5.3a**), lower than the expected value. This trend is consistent with phase separation of some material away from the micelle templates (i.e. non-templated material) (**Scheme**

5.1) or alternatively a change in material density.[75] Here the former hypothesis is supported by SEM observations of regions of non-templated TiO_2 (**Scheme 5.1c**). The placement of material precursors away from the micelles lowers the local M:T value ("microparticle M:T") and correspondingly limits the rate of lattice expansion. A power-law relationship (**Equation D.1**) was selected for convenience and simplicity to empirically resolve the discrepancy of slope by lowering the microparticle M:T value to account for material partitioning (**Figure 5.3d**). This finding suggests that all samples have some untemplated materials and that fraction increases with M:T ratio. Prior demonstrations without quantitative expectations would have easily missed such a non-templated material fraction. The increasing d-spacing trend as a function of microparticle M:T was well fitted by the PMT model[72] (**Equation D.2-4**) with a goodness-of-fit R^2 of 0.82 (**Figure 5.5a**). Consistent with PMT behavior, average SEM pore sizes were relatively constant at ~13.6 nm for all samples measured (**Figure 5.5b, Figure D.16**). Furthermore, the SEM wall thickness trend (10.2 – 17.5 nm) was well fitted by the model with a goodness-of-fit R^2 of 0.85 (**Figure 5.5c**). Please note that the change from PEO-*b*-PBA to PEO-*b*-PS did not markedly change the TGA profile suggesting a similar and likely negligible carbon yield (**Figure D.15**). Thus, glassy-PMT enabled the first mesoporous microparticles with independent wall thickness control from a block-polymer template with constant mesopore size.

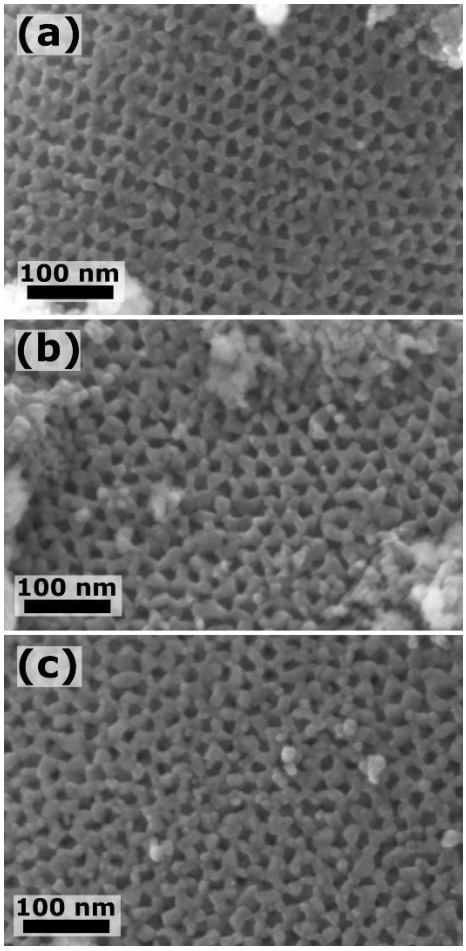

Figure 5.4. SEM images showing variation of wall thickness with constant pore size for the PS-*b*-PEO series: M:T=2.54 (a), M:T=3.48 (b), and M:T=5.06 (c). Statistical metrics from these images and others are included in Figure 5.5.

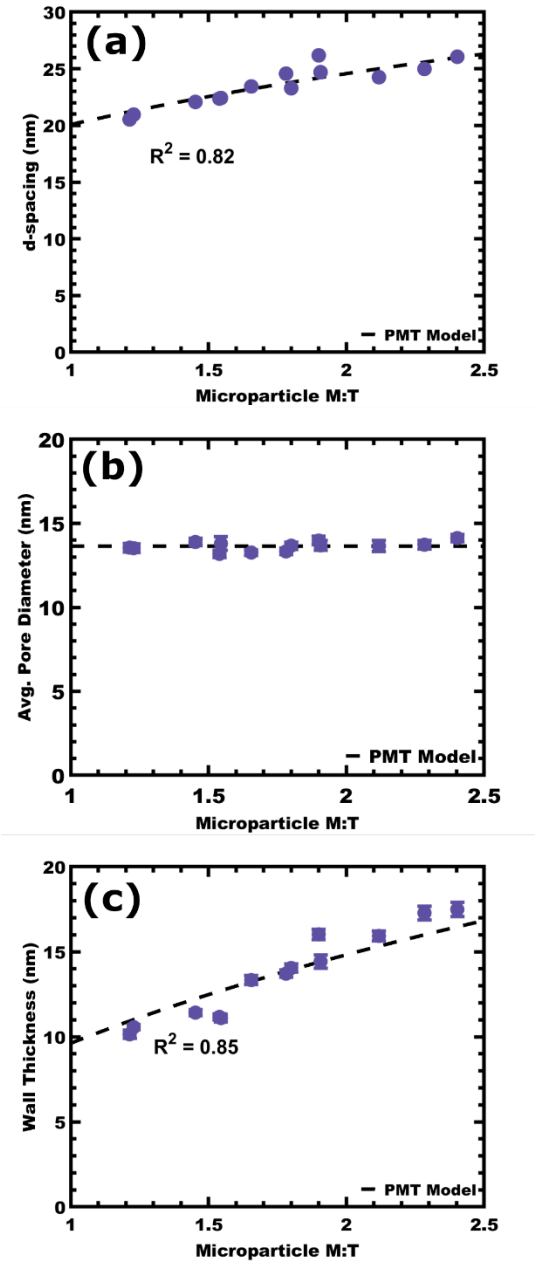

Figure 5.5. The SAXS d-spacing with increasing microparticle M:T ratio was well-fitted by the PMT model (a). Statistical SEM measures of pore diameter (b) and wall thickness (c) were also well-fitted by the PMT model. The goodness-of-fit R^2 values are indicated.

Briefly, it is noted that the tailored TiO_2 confinement within glassy-PMT led to systematic trends in crystallization behavior. After calcination, the resulting materials were measured using WAXS to identify the crystal structure as anatase, JCPDS Card no. 21-1272 (**Figure 5.6a**). The peak width narrowed slightly with increasing M:T and the Scherrer formula was used to quantify the average crystallite size (**Figure 5.6b**). The average crystallite sizes exhibited an increasing trend with the M:T ratio, corresponding to larger crystallites as the wall thickness expanded as previously reported.[74] These crystallite sizes were typically about ~80% as large as the overall wall thickness suggesting that most crystallites had a free surface. Such crystallite size control is important for many applications in energy storage.[74,109–112] Thus, the production of mesoporous microparticles with glassy-PMT enabled tailored crystallite dimensions.

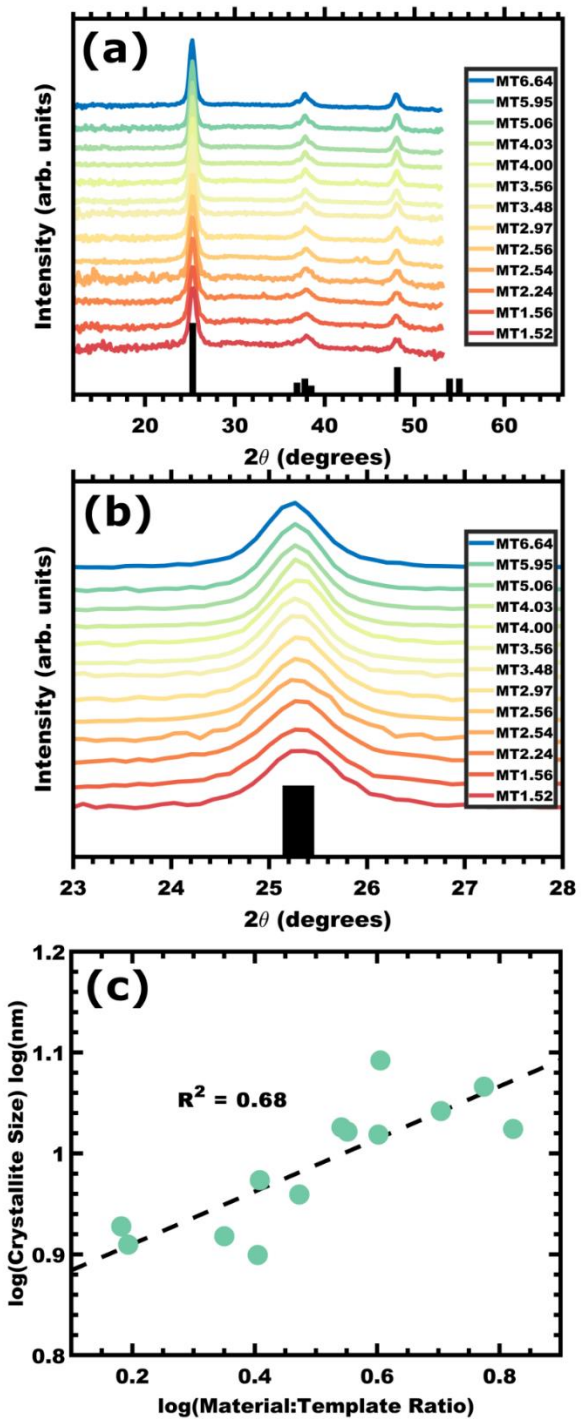

Figure 5.6. WAXS data for the PEO-*b*-PS sample series (a) where the (101) (b) and (200) anatase peaks were analyzed using the Scherrer formula to yield the average crystallite size (c) as a function of the M:T ratio. The reference anatase pattern is JCPDS Card no. 21-1272 and the dashed line in (c) is a guide for the eye.

The microparticle size distribution determines the nominal length scale for intraparticle transport processes and thus influences performance. The microparticle size is generally expected to be determined kinetically by the phase separation conditions. The homopolymer is thus intended as a medium in which to disperse microparticles and avoid the formation of much larger continuous aggregates. Thus, the combination of molecular mobility and time facilitate kinetic coarsening. The initial experiments screened a range of factors from solution composition to evaporation rate, aging conditions, and the surface energy of the casting dish. The effect of homopolymer content was first investigated, with PPO mass ratios ranging from 2.0-40.0x with respect to the mass of block polymer. The microparticle size distributions were determined by measurements on SEM images (**Figure 5.7, Figure D.5, Table 5.1**). The sample with 2.5x PPO resulted in an average microparticle size of 2.36 ± 0.24 μm, however, this sample contained a significant fraction of microparticles (≥5 μm) with uncontrolled size (**Figure D.5a**). Low amounts of PPO thus do not sufficiently separate microparticles to impede their fusion. In contrast, PPO ratios from 5.0-10.0x resulted in more uniform and smaller microparticles with average diameters of ~ 1 μm (**Table 5.1**). At the other end of the continuum, PPO ratios from 15.0-40x exhibited an unexpected increase in microparticle size, particularly considering the dilution of the minority microparticle phase (**Table 5.1**). This accelerated coarsening was attributed to the slower solvent removal from the larger sample sizes where additional time and mobility was available for coarsening. Curiously, SEM images of microparticles with >20.0x PPO (PEO-*b*-PBA templates) were found to exhibit a morphology transition from spherical micelles to a cylindrical morphology to a worm-like morphology (**Figure 5.8**). The PPO is expected to partition a fraction of the water owing to its ~1 wt% water

miscibility which lowers the water content in the microparticles and the lowered χN barrier can enable morphology transitions.[113] This interpretation is supported by samples combining both high water content and high PPO ratios (**Figure D.6**) where the micelle morphologies were preserved. This change in morphology as a function of water content and PPO ratio highlights the sensitivity of non-glassy block polymer templates such as PEO-*b*-PBA and need for glassy templates, which are less sensitive to solution conditions. Next, the effect of water content upon microparticle size was examined from 5.0-20 wt% water (**Figure 5.9 and Table 5.2**). Modest water contents from 5.0-10 wt% yielded average microparticle sizes of ~0.5 μm, whereas higher water contents from 15-20 wt% yielded larger average microparticles sizes of ~1.2 μm. These samples with higher water content were also found to exhibit a greater frequency of extended aggregates (**Figure D.7c,d**), as higher water content enhances the mobility of the metal alkoxide oligomers[114] and increasing the hydrophobic/hydrophilic contrast driving the phase separation. All of these possible effects promote coarsening of the microparticles. The effect of substrate surface energy was also found to have a concomitant role with water content. Samples prepared in glass dishes resulted in smaller microparticles and fewer extended aggregates (**Figure 5.9** and **Table 5.2**) when compared to Teflon dishes (**Figure D.8**, **D.9,** and **Table D.5**). The attraction of the material precursors to the hydrophilic substrate could impose a drag that limits horizontal microparticle mobility and impedes coarsening. Shorter processing times prior to aging led to larger microparticles again attributed to residual solvent induced coarsening (**Figure D.10**). Changing the molecular mass of PPO from 1 to 4 kg mol^{-1} was found to not have a significant effect on microparticle size, (**Figure D.11 and D.12**) suggesting that the PPO viscosity does not play a critical role in coarsening after solvent

evaporation. Similarly, variation of the aging treatments was also not found to have a significant effect on microparticle size, again suggesting that the microparticle size is determined largely during evaporation **(Figure D.13, D.14, and Table D.6)**. While conditions with large microparticles and extended aggregates exhibited some fracturing (cleaved lines) that contribute to the particle size distribution, samples with smaller microparticles rather dominantly exhibited curved surfaces, consistent with diffusive coarsening. Please note that these PEO-*b*-PBA data on microparticle size distributions were acquired prior to the development of glassy-PMT. The presence of chain exchange, however, is not expected to significantly affect microparticle formation thus these parameters which tune particle size are conditions which likely do not inhibit the independent control of pore and wall feature size with glassy-PMT. Thus, numerous parameters affect the rate of microparticle coarsening during evaporative processing.

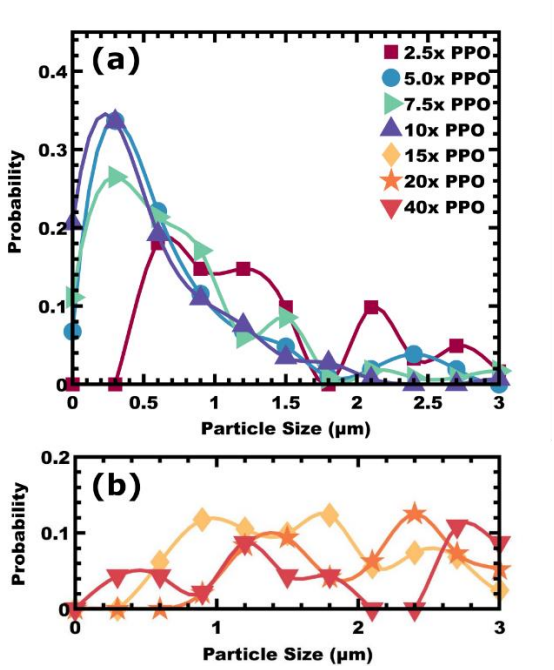

Figure 5.7. Microparticle size distributions were determined using measurements on SEM images as a function of different PPO ratios where panel (a) contains PPO ratios from 2.5 – 10x and panel (b) contains ratios from 15 – 40x. The template was PEO-*b*-PBA with M:T=2.5.

Table 5.1. Statistical measurements of average microparticle size in relation to amount of PPO added to template solutions using PEO-*b*-PBA with M:T=2.5.

PPO:Block Polymer Ratio	**Average Particle Size (µm)***	**Standard Deviation (µm)**
2.5	2.36 ± 0.24	1.85
5.0	1.07 ± 0.10	1.05
7.5	1.03 ± 0.08	0.91
10.0	0.72 ± 0.05	0.60
15.0	2.88 ± 0.19	2.36
20.0	4.60 ± 0.41	4.01
40.0	4.41 ± 0.47	3.20

*Values are reported as the average ± the error-of-the-mean

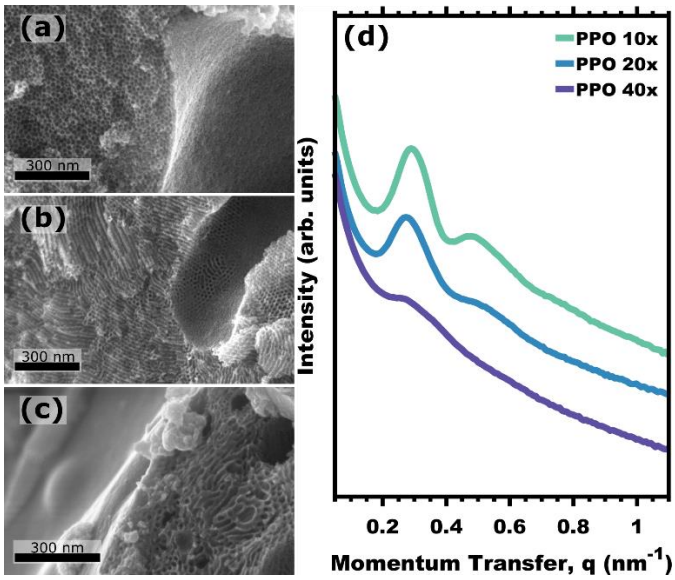

Figure 5.8. SEM images showing mesopore morphologies for microparticles prepared with different PPO ratios where the behavior spans from spherical pores 10x (a), to cylindrical pores 20x (b), and worm-like pores 40x (c). The corresponding SAXS patterns (d) were offset vertically for clarity. The template was PEO-*b*-PBA with M:T=2.5.

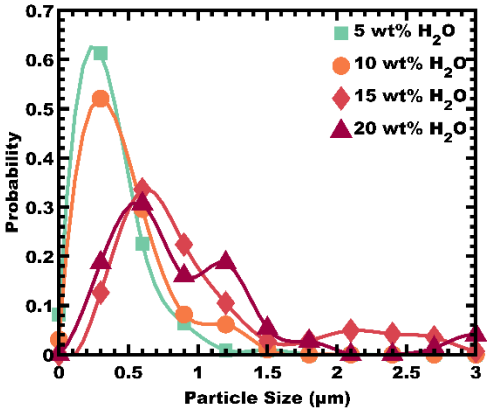

Figure 5.9. Microparticle size distributions as determined from SEM images were tailored as a function of the initial water quantity. The template was PEO-*b*-PBA with M:T=2.5.

Table 5.2. Statistical measurements of average microparticle sizes in relation to water content using PEO-*b*-PBA template solutions with M:T=2.5.

Water content (wt% of soln)	**Average Particle Size (μm)***	**Standard Deviation (μm)**
5.0	0.54 ± 0.02	0.23
10.0	0.65 ± 0.03	0.28
15.0	1.22 ± 0.06	0.77
20.0	1.18 ± 0.11	0.91

*Values are reported as an average ± error-of-the-mean

5.4 Conclusion

Mesoporous microparticles are an attractive platform for a broad set of manufacturing methods due to their convenient particulate form. The applications for TiO_2 mesoporous microparticles include catalysis, lithium-ion batteries, sensors, optoelectronics, and dye-sensitized solar cells where each application is best matched with distinct architectural dimensions. Here it is demonstrated for the first time that the pore size and wall thickness are independently tunable within mesoporous microparticles by using glassy-PMTs from PEO-*b*-PS. In contrast, the low-T_g PBA block in PEO-*b*-PBA was not sufficiently persistent to avoid changes to size and sometimes also changes to morphology during processing. In addition, an explanation is provided for reports of surface skin layer formation which dictates transport to/from microparticle interiors. A kinetic LID model was posited where the skin layer forms due to different rates of phase separation for micelles and material precursors followed by slow re-mixing. Here slower evaporation enabled the thinnest skin layers and high degrees of open surface porosity which were further tunable with coarsening heat treatments. Lastly, the effects of several processing

parameters upon the microparticle size were examined where microparticle size was largely controlled by the removal rate of solvents.

5.5 Experimental Methods

Materials. Methanol (MeOH, 99.8%, Fisher) and ethanol (EtOH, 200 proof, ACS Grade, Fisher) were dried at room temperature by storage over 30% w/v of molecular sieves (3 Å, 8-12 mesh, Acros Organics) for a week.[87] n-Butyl acrylate (≥99%, Acros Organics) and styrene (99%, Acros Organics) monomer were passed through a basic alumina column just prior to use. Poly(propylene glycol) (PPO, M_n = 1,000 g mol $^{-1}$ and 4,000 g mol^{-1}, Sigma Aldrich) were placed under vacuum overnight at room temperature before use to remove residual water. The 2-bromopropionic acid (>99%, Aldrich), 4-(dimethylamino) pyridine (99%, Aldrich), aluminum oxide (Al_2O_3, basic, Brockmann I, 50 – 200 μm, Acros Organics), chloroform (>99%, Aldrich), copper(I) bromide (99.99%, Aldrich), dimethylformamide (97%, Aldrich), hexanes (>98.5%, Fisher), concentrated hydrochloric acid (HCl, 37% w/w, ACS grade, VWR), anhydrous magnesium sulfate ($MgSO_4$, 99%, J.T. Baker), poly(ethylene glycol) methyl ether (PEO-OH, M_n = 5000 g mol^{-1}, Aldrich), tetrahydrofuran (THF, ACS Grade ≥99.0%, Fisher), titanium(IV) isopropoxide (TTIP, ≥98%, Acros Organics), tris-(2-dimethylaminoethyl) amine (97%, Aldrich) were used as received.

Polymer synthesis and characterization. Poly(ethylene oxide-*b*-butyl acrylate), PEO-*b*-PBA, and Poly(ethylene oxide-*b*-styrene), PEO-*b*-PS, diblock polymers were synthesized by a two-step synthesis. First, a Steglich esterification of poly(ethylene glycol)methyl ether was used to form a macroinitiator for atom transfer radical polymerization (ATRP). Second, ATRP was used to grow the PBA or PS block from the

macroinitiator. The procedure is described elsewhere in detail (**Table D.1**).[72] The molar mass of PBA or PS blocked was determined using a Bruker Avance III HD 300 ^{1}H NMR by comparison to the known PEO block molecular weight (**Figure D.1a, D.2a, and Table D.2**). ^{1}H NMR of PEO-b-PBA (300 MHz, $CDCl_3$) δ (ppm): 4.05 (COOC**H**$_2$), 3.67 (O-C**H**$_2$C**H**$_2$-O), 2.30 (C**H**COO), 1.92 (-C**H**$_2$CH-), convolved peaks 1.62 (-C**H**$_2$-, -C**H**$_3$), 1.39 (-C**H**$_2$-, -C**H**$_3$) and 0.96 (-C**H**$_2$-, -C**H**$_3$) with some contribution from 1.92 (-C**H**$_2$CH-). ^{1}H NMR of PEO-b-PS (300 MHz, $CDCl_3$) δ (ppm): convolved peaks 7.09 (o,p,m C-**H**) and 6.56 (o,p,m C-**H**), 3.67 (O-C**H**$_2$C**H**$_2$-O), convolved peaks 1.86 (-C**H**$_2$CH-, -CH_2C**H**-) and 1.45 (-C**H**$_2$CH-, -CH_2C**H**-). The molar mass dispersity index was characterized using a Waters gel permeation chromatograph (GPC) equipped with a Waters 1525 binary pump, three styragel columns (HR1, HR3, HR5 in the effective molecular weight range of 0.1-5, 0.5-30, and 2-400 kg mol^{-1}, respectively), and a Waters 2414 refractive index detector (**Figure D.1b, D.2b, and Table D.2**). The GPC was calibrated with poly(styrene) standards (1.50, 3.28, 10.00, 17.40, 32.70, 120.00, 214.00, 545.00, 1010.00 kg mol^{-1}) obtained from Polymer Standards Service GmbH. GPC samples were prepared in THF at concentrations of 5 mg mL^{-1} and were passed through a 0.2 μm syringe filter prior to injection. Note that the monochelic PEO-OH had a bimodal GPC trace as-received from the manufacturer (SI Figure 1b and 2b), a contaminant feature that was also apparent after further polymerization and was included in molar mass dispersity (Đ) calculations (Figure D.1b and D.2b).

Micelle template preparation. The PEO-*b*-PBA micelle stock solution was prepared by dispersing 40 mg of PEO-*b*-PBA in 4 mL of MeOH at room temperature with gentle agitation. Concentrated HCl was added slowly to achieve the target water composition of 0.7 wt% similar to prior work,[74] with respect to the total mixture unless

otherwise stated (examined 0.7% to 20%). The combined solution was sonicated using a Fisher ultrasonic bath (Cat. no. FS-28) operated continuously at full power (225 W) and frequency of 40 kHz for 10 min at room temperature, intended to temporarily enable chain exchange.[85,88] The micelle stock was then divided into aliquots containing 8 mg of polymer template in preparation of each M:T evaporative casting condition.

The PEO-*b*-PS micelles were prepared by dissolving 1.0 g of PEO-*b*-PS in 10 mL of THF in a large round bottom flask.[76] To this solution was added 10 mL of deionized water in a dropwise fashion and with frequent swirling of the flask. Next, 100 mL of anhydrous methanol was added. The THF was removed by rotary evaporation and the removed volume was replaced with anhydrous methanol to achieve a final micelle concentration of 10 mg mL^{-1}. It was previously shown that a procedure such as this is important to remove all good solvents which act as a plasticizers.[76] Subsequently, anhydrous $MgSO_4$ was added in excess to the solution until a cloudy precipitate was observed, indicating a preliminary state of dryness. The mixture was passed through a Gelman Sciences glass fiber filter paper with 1 μm pores to remove this precipitate and yield a transparent solution with much lower water content. This solution was then further dried over molecular sieves (3 Å, 8-12 mesh) and allowed to sit for at least three days before use. Similar drying conditions were shown to lead to <40 ppm levels of water.[87] Just prior to use, concentrated HCl was added slowly to 4 mL of the micelle solution to reach a desired water composition, 10 wt% with respect to the total stock solution unless otherwise stated. The resulting micelle stock solution was divided into aliquots containing 8 mg of polymer template for the preparation of each M:T evaporative casting condition.

Ex-situ sol method. An *ex-situ* TiO_2 sol stock was used as described in detail elsewhere.[74] Briefly, 5 mL of titanium isopropoxide (TTIP) was added to 1.2 mL of rapidly stirring concentrated HCl (37% wt%) creating a solution with a 3:1 H_2O:Ti ratio. Note that this reaction is very exothermic. After being allowed to cool for a few minutes, 2 mL of anhydrous MeOH was added to dilute the sol stock solution. This dilute sol stock solution was combined with one of the micelle template stock solutions described above in varying ratios, depending on the target material to template (M:T) ratio. Here the M:T ratio is calculated by comparing the anticipated final oxide mass (e.g. TiO_2) relative to the mass of block polymer template.

Mesoporous microparticle synthesis. In a typical experiment, micelle stock solution was combined with dilute ex situ sol stock solution, followed by the addition of prescribed amount of 1.0 kg mol^{-1} poly(propylene oxide). The PPO loading was reported as a mass ratio relative to the block polymer template. The PPO loading was 10x (examined 2.5x-40x) unless otherwise stated. Unless stated otherwise, the solution was bulk cast within a 9.0 cm glass dish and tilted around to assure uniform wetting of the dish. Unless otherwise noted, a glass cover was placed on the dish with a spacer made from 16G copper wire (see **Figure D.3**). The covered dish was then placed in a Tupperware chamber with a constant flow of air. Unless otherwise noted, the purge gas was 16 L/min (examined 0.1 to 25 L/min) with 15% relative humidity as controlled by a homemade system.[73] Unless otherwise noted, the dish was left to dry for 3 hrs and was then directly transferred to the "aging" process to promote cross-linking of material precursors. Samples were aged by placing them in a vacuum oven at RT and slowly reducing the pressure over 30 min to avoid damage to nanostructure. The aging treatment was customized for each polymer template. For PEO-

b-PBA templates, the samples were held for 12 hrs of RT vacuum and were then further heated to 190 ^{o}C for 12 hrs (examined 40 ^{o}C to 190 ^{o}C). For PEO-*b*-PS templates, the samples were heated in the vacuum oven to 80 ^{o}C overnight. In both cases, the resulting aged samples were then calcined at 450 ^{o}C for 0.1 hr with a 5^{o}C min^{-1} ramp, unless otherwise stated, to oxidatively remove the polymer and induce crystallization of the material. Please note that the removal of homopolymer or block polymer template by dissolution has been shown elsewhere as an alternative to removal via calcination.[82,83,89–92]

Small-Angle X-ray Scattering (SAXS) Measurements. X-ray experiments were conducted using a SAXSLab Ganesha at the South Carolina SAXS Collaborative (SCSC). A Xenocs GeniX 3D microfocus source was used with a copper target to produce monochromatic beam with a 0.154 nm wavelength. The instrument was calibrated prior to measurements using National Institute of Standards and Technology (NIST) reference material, 640d with peak position at $2\theta = 28.44^{o}$. A Pilatus 300k detector (Dectris) was used to collect the 2D scattering patterns with nominal pixel dimensions of 172x172 μm. Transmission small-angle X-ray scattering (SAXS) data were measured. SAXS data were acquired with an X-ray flux of ~3.3 M photons per second upon the sample and a detector-to-sample distance of 1,040 mm. The 2D images were azimuthally integrated to yield the scattering vector and intensity. Peak positions were fitted using custom MATLAB software. Transmission wide-angle X-ray scattering (WAXS) data were measured to identify crystalline phase of mesoporous microparticles and were acquired with an X-ray flux of ~36 M photons per second upon the sample and a detector-to-sample distance of 112 mm. The 2D images were azimuthally integrated to yield the scattering vector and

intensity. A Gaussian point-spread function was utilized to interpret scattering data as a result of grain-size broadening per the Scherrer formula.[93,94]

Scanning electron microscopy (SEM) measurements. Top-view images of calcined particles were acquired with a Zeiss Ultraplus thermal field emission SEM using an accelerating voltage of 5 keV and an in-lens secondary electron detector, the working distance was maintained at ~2.5 mm. The skin layer thickness was measured using cross-section images of fractured microparticles. For samples containing significant fractions of open and accessible porosity (no skin layer) the measured skin layer thicknesses were weighted by the area fraction of skin layer coverage. Pore and wall size measurements were carried out exclusively on images measured at 200KX magnification to eliminate calibration variation during SEM measurements. The wall thickness was measured by inscribing the largest possible circle between pores and recording the corresponding diameter.[74] The particle size distributions were determined manually by measuring 150 particles within a randomly selected image section for each condition. The full histograms are presented along with the mean, error-of-the-mean, and standard deviation. Measurements of skin layer thickness, area fraction of open surface porosity, pore, wall, and particle size were all determined using ImageJ software.

5.6 References

[1] Teruel, A. H.; Pérez-Esteve, É.; González-Álvarez, I.; González-Álvarez, M.; Costero, A. M.; Ferri, D.; Gaviña, P.; Merino, V.; Martínez-Máñez, R.; Sancenón, F. *Mol. Pharm.* **2019**, *16* (6), 2418–2429.

[2] Pavel, I.-A.; Girardon, M.; Hajj, S. E.; Parant, S.; Amadei, F.; Kaufmann, S.; Tanaka, M.; Fierro, V.; Celzard, A.; Canilho, N.; Pasc, A. *J. Mater. Chem. B* **2018**, *6* (35), 5633–5639.

[3] Qu, F.; Zhu, G.; Huang, S.; Li, S.; Sun, J.; Zhang, D.; Qiu, S. *Microporous Mesoporous Mater.* **2006**, *92* (1), 1–9.

[4] El-Boubbou, K.; Ali, R.; Al-Zahrani, H.; Trivilegio, T.; Alanazi, A. H.; Khan, A. L.; Boudjelal, M.; AlKushi, A. *Sci. Rep.* **2019**, *9* (1), 9481.

[5] Arcos, D.; López-Noriega, A.; Ruiz-Hernández, E.; Terasaki, O.; Vallet-Regí, M. *Chem. Mater.* **2009**, *21* (6), 1000–1009.

[6] Wu, Z.; Zhao, D. *Chem. Commun.* **2011**, *47* (12), 3332–3338.

[7] Qin, Z.; Zhao, Y.; Lin, L.; Zou, P.; Zhang, L.; Chen, H.; Wang, Y.; Wang, G.; Zhang, Y. *Acta* **2017**, *184* (11), 4513–4520.

[8] Kumar, A.; Park, G. D.; Patel, S. K. S.; Kondaveeti, S.; Otari, S.; Anwar, M. Z.; Kalia, V. C.; Singh, Y.; Kim, S. C.; Cho, B.-K.; Sohn, J.-H.; Kim, D. R.; Kang, Y. C.; Lee, J.-K. *Chem. Eng. J.* **2019**, *359*, 1252–1264.

[9] Zhou, X.; Zou, Y.; Ma, J.; Cheng, X.; Li, Y.; Deng, Y.; Zhao, D. *Chem. Mater.* **2019**, *31* (19), 8112–8120.

[10] Chen, L.; Hu, Z.-P.; Ren, J.-T.; Wang, Z.; Yuan, Z.-Y. *Microporous Mesoporous Mater.* **2021**, *315*, 110921.

[11] Sarkar, D.; Khare, D.; Kaushal, A.; Acharya, C.; Bahadur, J.; Prakash, J.; Donthula, H.; Dasgupta, K. *Appl. Nanosci.* **2019**, *9* (8), 1925–1937.

[12] Shang, C.; Wu, Z.; Wu, W. D.; Chen, X. D. *ACS Appl. Mater. Interfaces* **2019**, *11* (18), 16693–16703.

[13] Khodakov, A. Y.; Griboval-Constant, A.; Bechara, R.; Zholobenko, V. L. *J. Catal.* **2002**, *206* (2), 230–241.

[14] Chauhan, N.; Singh, V.; Kumar, S.; Kumari, M.; Sirohi, K. *J. Mol. Struct.* **2019**, *1185*, 219–228.

[15] Zong, L.; Zhang, G.; Zhao, H.; Zhang, J.; Tang, Z. *Chem. Eng. J.* **2018**, *354*, 295–303.

[16] Zhang, W.; He, H.; Tian, Y.; Lan, K.; Liu, Q.; Wang, C.; Liu, Y.; Elzatahry, A.; Che, R.; Li, W.; Zhao, D. *Chem. Sci.* **2019**, *10* (6), 1664–1670.

[17] Zhou, W.; Li, W.; Wang, J.-Q.; Qu, Y.; Yang, Y.; Xie, Y.; Zhang, K.; Wang, L.; Fu, H.; Zhao, D. *J. Am. Chem. Soc.* **2014**, *136* (26), 9280–9283.

[18] Tang, C.; Liu, L.; Li, Y.; Bian, Z. *Appl. Catal., B* **2017**, *201*, 41–47.

[19] Zou, M.; Xiong, F.; Ganeshraja, A. S.; Feng, X.; Wang, C.; Thomas, T.; Yang, M. *Mater. Chem. Phys.* **2017**, *195*, 259–267.

[20] Liu, Z.; Wu, B.; Zhu, Y.; Yin, D.; Wang, L. *Catal. Lett.* **2012**, *142* (12), 1489–1497.

[21] Cao, S.-W.; Zhu, Y.-J. *Nanoscale Res. Lett.* **2011**, *6* (1), 1–7.

[22] Xu, X.; Tan, H.; Wang, Z.; Wang, C.; Pan, L.; Kaneti, Y. V.; Yang, T.; Yamauchi, Y. *Environ. Sci.: Nano* **2019**, *6* (3), 981–989.

[23] Lu, H.; Dai, W.; Zheng, M.; Li, N.; Ji, G.; Cao, J. *J. Power Sources* **2012**, *209*, 243–250.

[24] Liu, Y.; Zhai, Y.; Xia, Y.; Li, W.; Zhao, D. *Small Structures* **2021**, *2* (5), 2000118.

[25] Perreault, L. L.; Colò, F.; Meligrana, G.; Kim, K.; Fiorilli, S.; Bella, F.; Nair, J. R.; Vitale-Brovarone, C.; Florek, J.; Kleitz, F.; Gerbaldi, C. *Adv. Energy Mater.* **2018**, *8* (35), 1802438.

[26] Fischer, M. G.; Hua, X.; Wilts, B. D.; Gunkel, I.; Bennett, T. M.; Steiner, U. *ACS Appl. Mater. Interfaces* **2017**, *9* (27), 22388–22397.

[27] Beitollahi, A.; Daie, A. H. H.; Samie, L.; Akbarnejad, M. M. *J. Alloys Compd.* **2010**, *490* (1), 311–317.

[28] Liu, Y.; Che, R.; Chen, G.; Fan, J.; Sun, Z.; Wu, Z.; Wang, M.; Li, B.; Wei, J.; Wei, Y.; Wang, G.; Guan, G.; Elzatahry, A. A.; Bagabas, A. A.; Al-Enizi, A. M.; Deng, Y.; Peng, H.; Zhao, D. *Sci. Adv.* **2015**, *1* (4), e1500166.

[29] Wang, Y.; Zhu, Y.; Yang, X.; Shen, J.; Li, X.; Qian, S.; Li, C. *Electrochim. Acta* **2016**, *211*, 92–100.

[30] Xiong, W.; Liu, M.; Gan, L.; Lv, Y.; Li, Y.; Yang, L.; Xu, Z.; Hao, Z.; Liu, H.; Chen, L. *J. Power Sources* **2011**, *196* (23), 10461–10464.

[31] Liu, G.; Zhao, L.; Sun, R.; Chen, W.; Hu, M.; Liu, M.; Duan, X.; Zhang, T. *Electrochim. Acta* **2018**, *259*, 20–27.

[32] Li, G.; Liu, H. *J. Mater. Chem.* **2011**, *21* (45), 18398–18402.

[33] Tu, L.; Pan, H.; Xie, H.; Yu, A.; Xu, M.; Chai, Q.; Cui, Y.; Zhou, X. *Solid State Sci.* **2012**, *14* (5), 616–621.

[34] Deng, S.; Luo, Z.; Liu, Y.; Lou, X.; Lin, C.; Yang, C.; Zhao, H.; Zheng, P.; Sun, Z.; Li, J.; Wang, N.; Wu, H. *J. Power Sources* **2017**, *362*, 250–257.

[35] Zhong, X.; Wang, X.; Wang, H.; Yang, Z.; Jiang, Y.; Li, J.; Tian, Z. *Nano Res.* **2018**, *11* (7), 3814–3823.

[36] Fattakhova-Rohlfing, D.; Zaleska, A.; Bein, T. Three-Dimensional Titanium Dioxide Nanomaterials. *Chem. Rev.* **2014**, *114* (19), 9487–9558.

[37] Juhl, A. C.; Schneider, A.; Ufer, B.; Brezesinski, T.; Janek, J.; Fröba, M. *Beilstein J. Nanotechnol.* **2016**, *7*, 1229–1240.

[38] J. Wales, D.; Grand, J.; P. Ting, V.; D. Burke, R.; J. Edler, K.; R. Bowen, C.; Mintova, S.; D. Burrows, A. *Chem. Soc. Rev.* **2015**, *44* (13), 4290–4321.

[39] Verduzco, R.; Li, X.; L. Pesek, S.; E. Stein, G. *Chem. Soc. Rev.* **2015**, *44* (8), 2405–2420.

[40] Xiao, W.; Yang, S.; Zhang, P.; Li, P.; Wu, P.; Li, M.; Chen, N.; Jie, K.; Huang, C.; Zhang, N.; Dai, S. *Chem. Mater.* **2018**, *30* (9), 2924–2929.

[41] Zhang, Z.; Yang, S.; Hu, X.; Xu, H.; Peng, H.; Liu, M.; Thapaliya, B. P.; Jie, K.; Zhao, J.; Liu, J.; Chen, H.; Leng, Y.; Lu, X.; Fu, J.; Zhang, P.; Dai, S. *Chem. Mater.* **2019**, *31* (15), 5529–5536.

[42] Wei, D.; Scherer, M. R. J.; Bower, C.; Andrew, P.; Ryhänen, T.; Steiner, U. A. *Nano Lett.* **2012**, *12* (4), 1857–1862.

[43] Mei, P.; Kaneti, Y. V.; Pramanik, M.; Takei, T.; Dag, Ö.; Sugahara, Y.; Yamauchi, Y. *Nano Energy* **2018**, *52*, 336–344.

[44] Kosuge, K.; Kubo, S.; Kikukawa, N.; Takemori, M. *Langmuir* **2007**, *23* (6), 3095–3102.

[45] Zeleňák, V.; Badaničová, M.; Halamová, D.; Čejka, J.; Zukal, A.; Murafa, N.; Goerigk, G. *Chem. Eng. J.* **2008**, *144* (2), 336–342.

[46] Zhu, C.; Usiskin, R. E.; Yu, Y.; Maier, J. *Science* **2017**, *358* (6369).

[47] van den Bergh, W.; Lokupitiya, H. N.; Vest, N. A.; Reid, B.; Guldin, S.; Stefik, M. *Adv. Funct. Mater.* **2021**, *31* (1), 2007826.

[48] Lan, K.; Wang, R.; Zhang, W.; Zhao, Z.; Elzatahry, A.; Zhang, X.; Liu, Y.; Al-Dhayan, D.; Xia, Y.; Zhao, D. *Chem* **2018**, *4* (10), 2436–2450.

[49] Tong, H.; Enomoto, N.; Inada, M.; Tanaka, Y.; Hojo, J. *Mater. Lett.* **2015**, *141*, 259–262.

[50] Liu, Y.; Luo, Y.; Elzatahry, A. A.; Luo, W.; Che, R.; Fan, J.; Lan, K.; Al-Enizi, A. M.; Sun, Z.; Li, B.; Liu, Z.; Shen, D.; Ling, Y.; Wang, C.; Wang, J.; Gao, W.; Yao, C.;

Yuan, K.; Peng, H.; Tang, Y.; Deng, Y.; Zheng, G.; Zhou, G.; Zhao, D. *ACS Cent. Sci.* **2015**, *1* (7), 400–408.

[51] Liu, Y.; Teng, W.; Chen, G.; Zhao, Z.; Zhang, W.; Kong, B.; Hozzein, W. N.; Al-Khalaf, A. A.; Deng, Y.; Zhao, D. *Chem. Sci.* **2018**, *9* (39), 7705–7714.

[52] Wu, Z.; Waldron, K.; Zhang, X.; Li, Y.; Wu, L.; Wu, W. D.; Chen, X. D.; Zhao, D.; Selomulya, C. *J. Colloid Interface Sci.* **2019**, *556*, 529–540.

[53] Waldron, K.; Wu, W. D.; Wu, Z.; Liu, W.; Selomulya, C.; Zhao, D.; Chen, X. D. *J. Colloid Interface Sci.* **2014**, *418*, 225–233.

[54] Andersson, N.; Alberius, P. C. A.; Skov Pedersen, J.; Bergström, L. *Microporous Mesoporous Mater.* **2004**, *72* (1), 175–183.

[55] Jin, Z.; Xiao, M.; Bao, Z.; Wang, P.; Wang, J. *Angew. Chem., Int. Ed.* **2012**, *51* (26), 6406–6410.

[56] Yu, Z.; Gao, X.; Yao, Y.; Zhang, X.; Bian, G.-Q.; Wu, W. D.; Chen, X. D.; Li, W.; Selomulya, C.; Wu, Z.; Zhao, D. *J. Mater. Chem. A* **2018**, *6* (9), 3954–3966.

[57] Waldron, K.; Wu, Z.; Zhao, D.; Chen, X. D.; Selomulya, C. *Chem. Eng. Sci.* **2015**, *127*, 276–284.

[58] Waldron, K.; Wu, Z.; Wu, W. D.; Liu, W.; Zhao, D.; Chen, X. D.; Selomulya, C. *J. Mater. Chem. A* **2014**, *2* (45), 19500–19508.

[59] Wei, L.; Yan, S.; Wang, H.; Yang, H. *NPG Asia Mater.* **2018**, *10* (9), 899–911.

[60] Kuai, L.; Wang, J.; Ming, T.; Fang, C.; Sun, Z.; Geng, B.; Wang, J. *Sci. Rep.* **2015**, *5* (1), 9923.

[61] Baccile, N.; Grosso, D.; Sanchez, C. *J. Mater. Chem.* **2003**, *13* (12), 3011–3016.

[62] Andersson, N.; Kronberg, B.; Corkery, R.; Alberius, P. *Langmuir* **2007**, *23* (3), 1459–1464.

[63] Oh, J. Y.; Song, S. A.; Jung, K. Y.; Chang, Y.-W.; Kim, K.; Lim, S. N.; Jeong, Y.-C. *Electrochim. Acta* **2017**, *253*, 390–395.

[64] Waldron, K.; Wu, Z.; Zhao, D.; Chen, X. D.; Selomulya, C. *Mater. Today* **2016**, *3* (2), 646–651.

[65] Tarutani, N.; Tokudome, Y.; Jobbágy, M.; Soler-Illia, G. J. A. A.; Takahashi, M. *J. Sol-Gel Sci. Technol.* **2019**, *89* (1), 216–224.

[66] Guan, B. Y.; Yu, L.; Lou, X. W. *J. Am. Chem. Soc.* **2016**, *138* (35), 11306–11311.

[67] Feng, Y.; Zhang, M.; Guo, M.; Wang, X. *Cryst. Growth Des.* **2010**, *10* (4), 1500–1507.

[68] Lan, K.; Liu, Y.; Zhang, W.; Liu, Y.; Elzatahry, A.; Wang, R.; Xia, Y.; Al-Dhayan, D.; Zheng, N.; Zhao, D. *J. Am. Chem. Soc.* **2018**, *140* (11), 4135–4143.

[69] Zhou, H.; Xiong, H.; Zhang, R.; Zhang, L.; Zhang, L.; Li, L.; Zhang, W.; Zhu, Z.; Qiao, Z.-A. *Small* **2021**, *17* (21), 2100428.

[70] Biriaei, R.; Nohair, B.; Kaliaguine, S. *Microporous and Mesoporous Materials* **2020**, *298*, 110067.

[71] Tarutani, N.; Katagiri, K.; Inumaru, K.; Ishigaki, T. *J. Phys. Chem. B* **2021**, *125* (18), 4883–4889.

[72] Sarkar, A.; Stefik, M. *J. Mater. Chem. A* **2017**, *5* (23), 11840–11853.

[73] Lokupitiya, H. N.; Jones, A.; Reid, B.; Guldin, S.; Stefik, M. *Chem. Mater.* **2016**, *28* (6), 1653–1667.

[74] Lantz, K. A.; Clamp, N. B.; Bergh, W. van den; Sarkar, A.; Stefik, M. *Small* **2019**, *15* (18), 1900393.

[75] Sarkar, A.; Evans, L.; Stefik, M. *Langmuir* **2018**, *34* (20), 5738–5749.

[76] Williams, E. R.; McMahon, P. L.; Reynolds, J. E.; Snider, J. L.; Stavila, V.; Allendorf, M. D.; Stefik, M. *Mater. Adv.* **2021**, 10.1039.D1MA00146A.

[77] Choi, S.-H.; Lodge, T. P.; Bates, F. S. *Phys. Rev. Lett.* **2010**, *104* (4), 047802.

[78] Ma, Y.; Lodge, T. P. *Macromolecules* **2016**, *49* (9), 3639–3646.

[79] Stefik, M.; Mahajan, S.; Sai, H.; Epps, T. H.; Bates, F. S.; Gruner, S. M.; DiSalvo, F. J.; Wiesner, U. *Chem. Mater.* **2009**, *21* (22), 5466–5473.

[80] Peng, L.; Hung, C.-T.; Wang, S.; Zhang, X.; Zhu, X.; Zhao, Z.; Wang, C.; Tang, Y.; Li, W.; Zhao, D. *J. Am. Chem. Soc.* **2019**, *141* (17), 7073–7080.

[81] Park, H.; Masud, M. K.; Na, J.; Lim, H.; Phan, H.-P.; Kaneti, Y. V.; Alothman, A. A.; Salomon, C.; Nguyen, N.-T.; Hossain, M. S. A.; Yamauchi, Y. *J. Mater. Chem. B* **2020**, *8* (41), 9512–9523.

[82] Iqbal, M.; Kim, Y.; Li, C.; Jiang, B.; Takei, T.; Lin, J.; Yuliarto, B.; Bando, Y.; Henzie, J.; Yamauchi, Y. *ACS Appl. Mater. Interfaces* **2019**, *11* (40), 36544–36552.

[83] Li, C.; Iqbal, M.; Jiang, B.; Wang, Z.; Kim, J.; Nanjundan, A. K.; Whitten, A. E.; Wood, K.; Yamauchi, Y. *Chem. Sci.* **2019**, *10* (14), 4054–4061.

[84] Sarkar, A.; Thyagarajan, A.; Cole, A.; Stefik, M. *Soft Matter* **2019**, *15* (26), 5193–5203.

[85] Lokupitiya, H. N.; Stefik, M. *Nanoscale* **2017**, *9* (4), 1393–1397.

[86] Amri, F.; Septiani, N. L. W.; Rezki, M.; Iqbal, M.; Yamauchi, Y.; Golberg, D.; Kaneti, Y. V.; Yuliarto, B. *J. Mater. Chem. B* **2021**, *9* (5), 1189–1207.

[87] Williams, D. B. G.; Lawton, M. *J. Org. Chem.* **2010**, *75* (24), 8351–8354.

[88] Lantz, K. A.; Sarkar, A.; Littrell, K. C.; Li, T.; Hong, K.; Stefik, M. *Macromolecules* **2018**, *51* (17), 6967–6975.

[89] Docampo, P.; Guldin, S.; Steiner, U.; Snaith, H. J. *J. Phys. Chem. Lett.* **2013**, *4* (5), 698–703.

[90] Guldin, S.; Hüttner, S.; Tiwana, P.; Orilall, M. C.; Ülgüt, B.; Stefik, M.; Docampo, P.; Kolle, M.; Divitini, G.; Ducati, C.; Redfern, S. A. T.; Snaith, H. J.; Wiesner, U.; Eder, D.; Steiner, U. *Energy Environ. Sci.* **2011**, *4* (1), 225–233.

[91] Docampo, P.; Guldin, S.; Stefik, M.; Tiwana, P.; Orilall, M. C.; Hüttner, S.; Sai, H.; Wiesner, U.; Steiner, U.; Snaith, H. J. *Advanced Functional Materials* **2010**, *20* (11), 1787–1796.

[92] Buken, O.; Mancini, K.; Sarkar, A. *RSC Adv.* **2021**, *11* (44), 27356–27368.

[93] Scherrer, P. Nachr Ges Wiss Goettingen. *Math. Phys.* **1918**, *2*, 98–100.

[94] Patterson, A. L. *Phys. Rev.* **1939**, *56* (10), 978–982.

[95] Dubinsky, S.; Park, J. I.; Gourevich, I.; Chan, C.; Deetz, M.; Kumacheva, E. *Macromolecules* **2009**, *42* (6), 1990–1994.

[96] Carroll, B.; Bocharova, V.; Carrillo, J.-M. Y.; Kisliuk, A.; Cheng, S.; Yamamoto, U.; Schweizer, K. S.; Sumpter, B. G.; Sokolov, A. P. *Macromolecules* **2018**, *51* (6), 2268–2275.

[97] Grabowski, C. A.; Adhikary, B.; Mukhopadhyay, A. *Appl. Phys. Lett.* **2009**, *94* (2), 021903.

[98] Grabowski, C. A.; Mukhopadhyay, A. *Macromolecules* **2014**, *47* (20), 7238–7242.

[99] Griffin, P. J.; Bocharova, V.; Middleton, L. R.; Composto, R. J.; Clarke, N.; Schweizer, K. S.; Winey, K. I. *ACS Macro Lett.* **2016**, *5* (10), 1141–1145.

[100] Zhu, J.; Hayward, R. C. *J. Am. Chem. Soc.* **2008**, *130* (23), 7496–7502.

[101] Yu, K.; Eisenberg, A. *Macromolecules* **1996**, *29* (19), 6359–6361.

[102] Yu, K.; Eisenberg, A. *Macromolecules* **1998**, *31* (11), 3509–3518.

[103] Yu, K.; Bartels, C.; Eisenberg, A. *Langmuir* **1999**, *15* (21), 7157–7167.

[104] Riess, G. *Progress in Polymer Science* **2003**, *28* (7), 1107–1170.

[105] Bhargava, P.; Zheng, J. X.; Li, P.; Quirk, R. P.; Harris, F. W.; Cheng, S. Z. D. *Macromolecules* **2006**, *39* (14), 4880–4888.

[106] Bhargava, P.; Tu, Y.; Zheng, J. X.; Xiong, H.; Quirk, R. P.; Cheng, S. Z. D. *J. Am. Chem. Soc.* **2007**, *129* (5), 1113–1121.

[107] Mai, Y.; Eisenberg, A. *Chem. Soc. Rev.* **2012**, *41* (18), 5969–5985.

[108] Ruland, W.; Smarsly, B. M. *J. Appl. Crystallogr.* **2007**, *40* (3), 409–417.

[109] Wang, J.; Polleux, J.; Lim, J.; Dunn, B. *J. Phys. Chem. C* **2007**, *111* (40), 14925–14931.

[110] Lesel, B. K.; Cook, J. B.; Yan, Y.; Lin, T. C.; Tolbert, S. H. *ACS Energy Lett.* **2017**, *2* (10), 2293–2298.

[111] Balaya, P.; Bhattacharyya, A. J.; Jamnik, J.; Zhukovskii, Yu. F.; Kotomin, E. A.; Maier, J. *Journal of Power Sources* **2006**, *159* (1), 171–178.

[112] Wagemaker, M.; Borghols, W. J. H.; Mulder, F. M. *J. Am. Chem. Soc.* **2007**, *129* (14), 4323–4327.

[113] Stefik, M.; Song, J.; Sai, H.; Guldin, S.; Boldrighini, P.; Orilall, M. C.; Steiner, U.; Gruner, S. M.; Wiesner, U. *J. Mater. Chem. A* **2015**, *3* (21), 11478–11492.

[114] Soler–Illia, G. J. de A. A.; Sanchez, C. *New J. Chem.* **2000**, *24* (7), 493–499.

CHAPTER 6: Future Directions for PMTs as a Tool

6.1 Overview

With the demand for fast, energy-dense storage, research has advanced into nanoscale intercalation materials. These materials not only accelerate kinetics but also can modify reaction path thermodynamics, intercalant solubility, and diffusivity. While electrodes have been designed to have one transport processes dominant, there remain opportunities to better understand energy-dense designs with multiple concomitant transport constraints. Using tailored, energy-dense nanomaterials made from persistent micelle templates (PMTs), it is possible to fulfill these opportunities. From the process of elimination to clearly correlate architectural features to performance. As shown in the previous chapters PMTs revealed the dependance of intercalation pseudocapacitive kinetics upon the intercalation length scale for multiple materials. In addition, this approach can isolate material-specific effects such as how amorphization modifies both insertion and diffusion kinetics for multiple materials exhibiting intercalation pseudocapacitance. From this body of work, we developed current-model which deconvolves changes to surface-limited and diffusion-limited processes while at the same time revealing avenues to achieve markedly faster intercalation. However, electrochemical methods beyond cyclic voltammetry present an open domain to which systematic materials can be used to understand underlying phenomena and correlate structure and material changes to performance. Two bodies of work present themselves as examples of how PMTs can advance the field of fast-charge devices. First, electrochemical impedance spectroscopy (EIS) is an advanced technique which generates data that is analyzed using equivalent electrical circuits that represent electrochemical processes.[1] There is ambiguity here as to which segments of data represent which process however, which could be better elucidated

with the comparison of tuned architectures from PMTs. In addition, akin to the in-series current model described in chapter 4, 3D bode analysis from EIS represents a tool which provides generalized descriptors of the data which can be assigned to specific processes of well understood materials.[2,3] The second body of work is physiochemical models[1,4,5] which rely on assumptions and computation clusters to provide unambiguous descriptions of a system that considers complex processes such as diffusion gradients. Any reduction in the number of assumptions or estimation of unknown variables would ease the computational demand and provide more accurate models. Conversely, PMTs stand to serve as a platform to verify computational predictions. Regardless PMTs are a tool which is unique in the field of nanoscale research and provides an essential method to produce unambiguous understanding of material phenomena and observe correlations between changes in architecture and the material itself to performance.

6.2 Current Challenges of PMT-derived Noble Metal Nanoparticles

Persistent micelle templates (PMTs) stand as a tool that can be expanded to not only other electrochemical analytics but direct applications as well. Modern electrochemical catalysis still depends upon expensive noble metals, any enhancement to which has significant impacts on chemical production on an industrial scale. Like electrochemical intercalation, catalysis has benefitted from nanoscale design. Beyond the simple increase in surface area to volume ratio with decrease particle sizes, many investigations predict and observe non-trivial improvements to performance with high surface curvature which has been assigned to low coordination atoms that are more catalytically active. In addition, a growing body of work has compared concave and convex curvature, ultimately finding concave architectures more stable with comparable catalytic

performance.[6] One such avenue of this research has been solution-based templating of mesoporous nanoparticles with block polymers.[7–12] From chemical reduction of noble metal salts, mesoporous catalysts can be made with cheap templates (Figure 1). To date, there remains a challenge to tune the feature sizes of these mesoporous metal nanoparticles. Despite employing conditions which would produce persistent templates, those used in current research causes plasticization to the PEO-*b*-PS templates with the presence of solubilizing THF. While marketed as a handle for control, such solvents prevent further control. With the use of glassy-PMTs,[13,14] such tunability could be achieved. Rather than tune wall thickness, here the emphasis would be upon tuning pore size[15] which would change degree of curvature. From a series of particles of varying pore sizes (Figure 2), it can be correlated the degree of activity to radius of curvature not well understood in concave structures. Such analysis could be extended to more novel high-entropy catalysts which have the advantage of much higher catalytic activity and tunability in the material composition itself.[16] Preliminary works[8,10] producing mesoporous metal nanoparticles have been reported with a binary composition however due to the differences in electrochemical reduction for each metal species, even these binary systems have a non-linear correlation between material addition and the resulting product composition. Recent preparation of PMTs with irreversible binding motifs (phosphonic acid) in the corona represent a method which could prevent the loss of less reactive materials, rather producing a composition of any combination of metal precursors in a simple manner.[17] Similar to single metal mesoporous catalysts, correlations between curvature and performance can be made with the addition feature adjustment of composition.

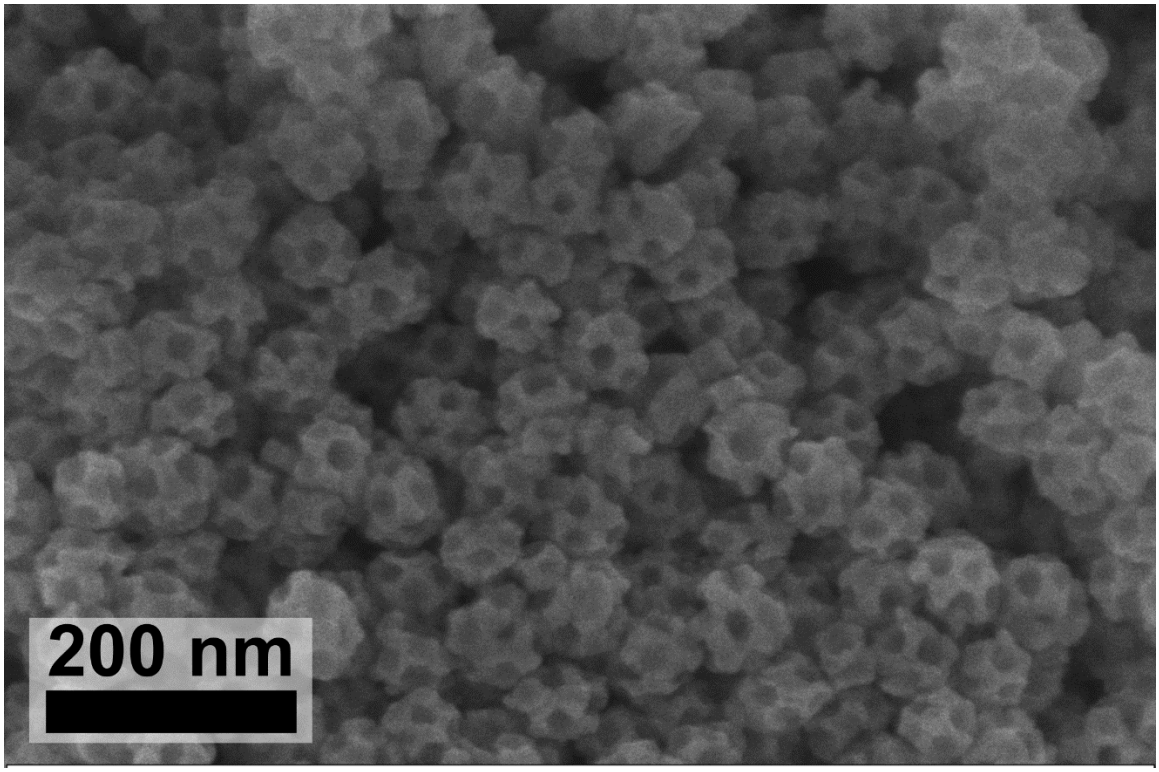

Figure 6.1. SEM image of mesoporous Pd nanoparticles prepared via chemical reduction and templated with PEO-*b*-PS

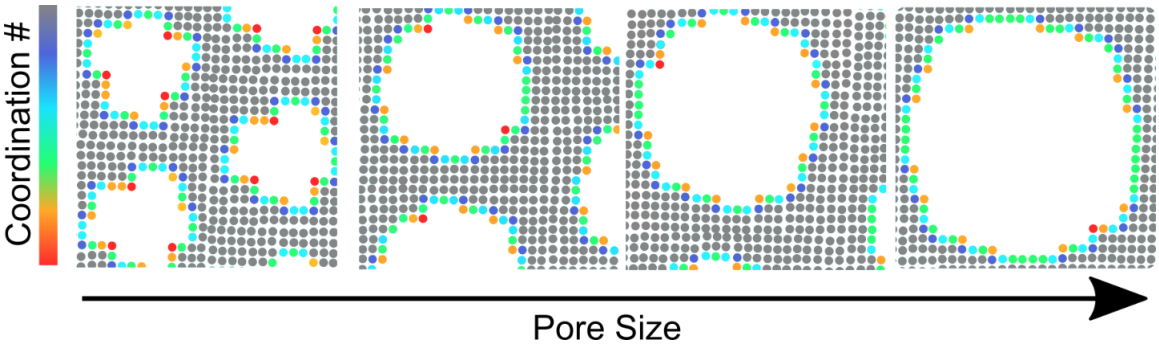

Figure 6.2. Conceptual scheme of how surface curvature can be tuned by a porous nanostructure.

6.3 References

[1] B.-A. Mei, J. Lau, T. Lin, S. H. Tolbert, B. S. Dunn, L. Pilon, *J. Phys. Chem. C* **2018**, *122*, 24499.

[2] J. S. Ko, C.-H. Lai, J. W. Long, D. R. Rolison, B. Dunn, J. Nelson Weker, *ACS Appl. Mater. Interfaces* **2020**, *12*, 14071.

[3] J. S. Ko, M. B. Sassin, D. R. Rolison, J. W. Long, *Electrochimica Acta* **2018**, *275*, 225.

[4] B.-A. Mei, L. Pilon, *Electrochim. Acta* **2017**, *255*, 168.

[5] B.-A. Mei, O. Munteshari, J. Lau, B. Dunn, L. Pilon, *J. Phys. Chem. C* **2018**, *122*, 194.

[6] M. Iqbal, Y. Bando, Z. Sun, K. C.-W. Wu, A. E. Rowan, J. Na, B. Y. Guan, Y. Yamauchi, *Advanced Materials n/a*, 2004554.

[7] V. Malgras, H. Ataee-Esfahani, H. Wang, B. Jiang, C. Li, K. C.-W. Wu, J. H. Kim, Y. Yamauchi, *Advanced Materials* **2016**, *28*, 993.

[8] M. Iqbal, Y. Kim, C. Li, B. Jiang, T. Takei, J. Lin, B. Yuliarto, Y. Bando, J. Henzie, Y. Yamauchi, *ACS Appl. Mater. Interfaces* **2019**, *11*, 36544.

[9] H. Ataee-Esfahani, J. Liu, M. Hu, N. Miyamoto, S. Tominaka, K. C. W. Wu, Y. Yamauchi, *Small* **2013**, *9*, 1047.

[10] B. Jiang, K. Kani, M. Iqbal, H. Abe, T. Kimura, Md. S. A. Hossain, O. Anjaneyulu, J. Henzie, Y. Yamauchi, *Chem. Mater.* **2018**, *30*, 428.

[11] M. Iqbal, Y. Kim, A. G. Saputro, G. Shukri, B. Yuliarto, H. Lim, H. Nara, A. A. Alothman, J. Na, Y. Bando, Y. Yamauchi, *ACS Appl. Mater. Interfaces* **2020**.

[12] C. Li, M. Iqbal, B. Jiang, Z. Wang, J. Kim, A. K. Nanjundan, A. E. Whitten, K. Wood, Y. Yamauchi, *Chem. Sci.* **2019**, *10*, 4054.

[13] W. van den Bergh, E. R. Williams, N. A. Vest, P.-H. Chiang, M. Stefik, *Langmuir* **2021**.

[14] E. R. Williams, P. L. McMahon, J. E. Reynolds, J. L. Snider, V. Stavila, M. D. Allendorf, M. Stefik, *Mater. Adv.* **2021**, 10.1039.D1MA00146A.

[15] A. Sarkar, A. Thyagarajan, A. Cole, M. Stefik, *Soft Matter* **2019**, *15*, 5193.

[16] Y. Ma, Y. Ma, Q. Wang, S. Schweidler, M. Botros, T. Fu, H. Hahn, T. Brezesinski, B. Breitung, *Energy & Environmental Science* **2021**, *14*, 2883.

[17] T. Larison, M. Stefik, *Langmuir* **2021**, *37*, 9817.

Appendix A: Supporting Information for Chapter 2

---

[1]van den Bergh, W.; Lokupitiya, H.; Vest, N.; Reid, B.; Guldin, S.; Stefik, M. *Advanced Functional Materials*, 2021, 31, 2007826

A.1 Supporting Information for Chapter 2

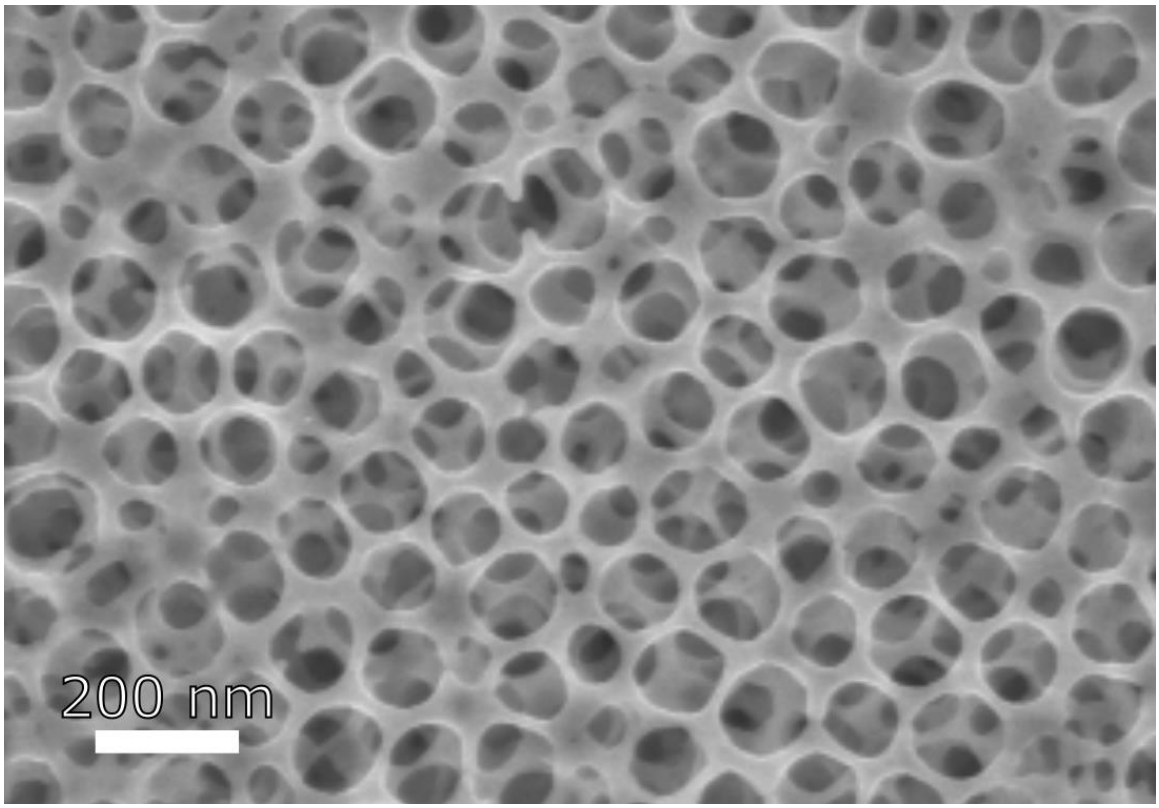

Figure A.1. SEM image of MT1.8 showing percolation of porosity deep into the nanostructure.

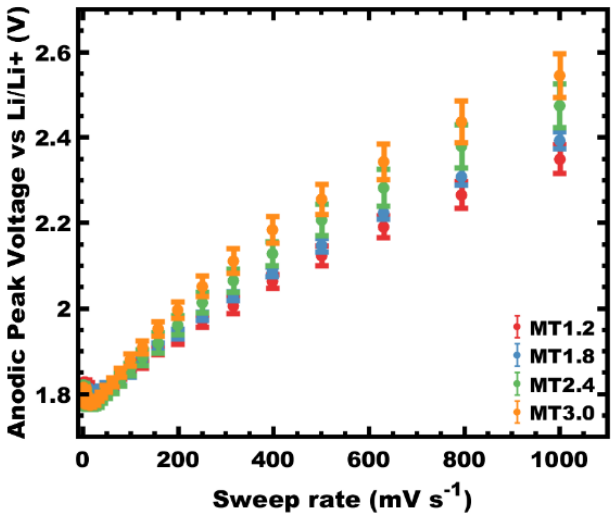

Figure A.2. Analysis of cyclic voltammetry data revealed the trend in anodic peak voltage as a function of sweep rate and nanoscale architecture (MT condition).

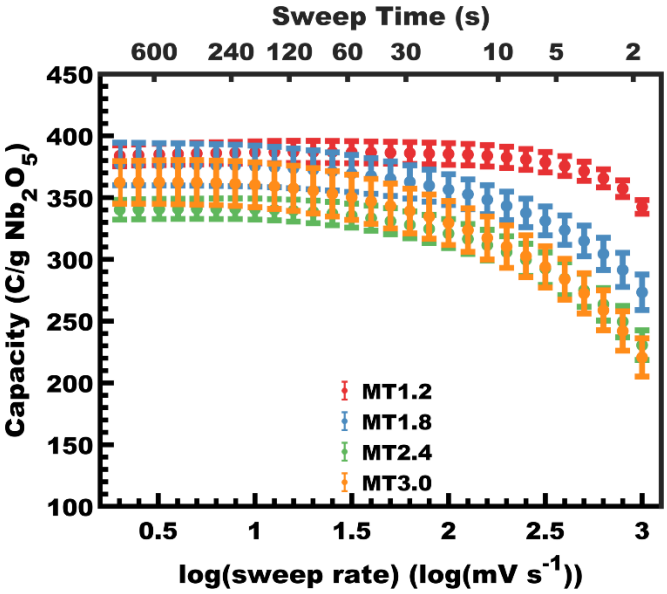

Figure A.3. The sweep-rate dependent lithiation capacity for the sample series. Error bars correspond to the standard-error-of-the-mean.

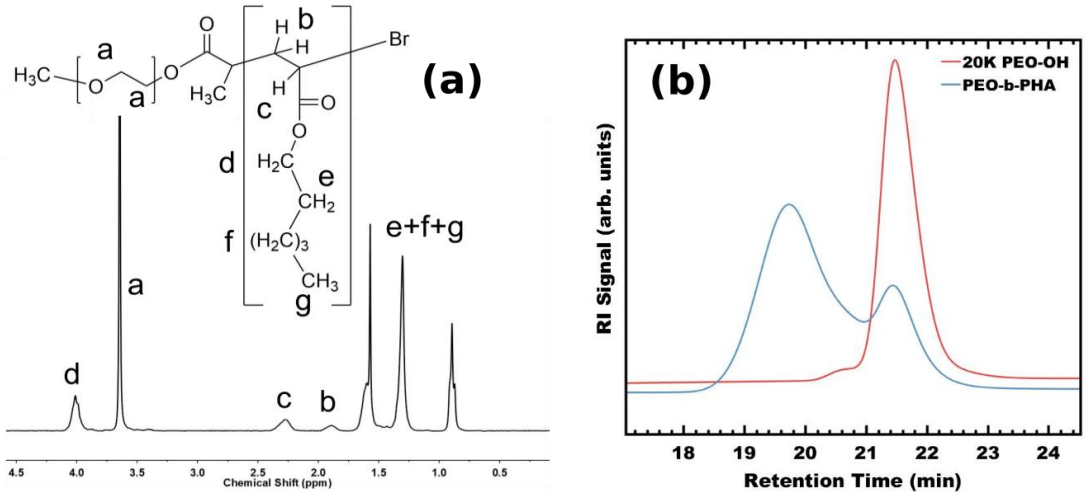

Figure A.4. ^{1}H NMR spectra (a) of PEO-*b*-PHA block copolymer and GPC (b) of PEO-OH vs PEO-*b*-PHA. ^{1}H NMR (300 MHz, $CDCl_3$, δ), 4.05 (m, 2H, COOC**H**$_2$), 3.65 (s, 4H, C**H**$_2$C**H**$_2$O), 2.30 (s, CH), 1.90 (s, 2H, CH_2), 1.55 (m, 2H, CH_2), 1.30 (m, 6H, CH_2), 0.90 (m, 3H, CH_3). Note that peaks b, e, f, and g have some convolution.

A previously developed micelle core template (MCT) model was used to model wall thickness and d-spacing changes with M:T. The wall thickness equation was:

$$w = (\alpha a - D) \quad \text{(A.1)}$$

where w is the wall thickness, α is a fit term to accommodate the variable distribution of wall thickness for different lattice planes, D is the pore diameter, and a is the lattice dimension (substitute with $d_{m\text{-}m}$ for paracrystalline systems). For cubic crystal systems, alpha values are expected to range from 0.5-1.5 when the walls are measured as the shortest path between pores, or from 0.87-2.45 when measured using an inscribed circle.[1] Similarly, the d-spacing was modeled using:

$$r = d_{m-m}\sqrt[3]{\frac{3\gamma}{4\pi}}\left(x\beta_{mct} + 1 + \frac{f_{corona}}{1 - f_{corona}}\right)^{-\frac{1}{3}} \quad \text{(A.2)}$$

where r is the template radius (half of the pore diameter), $d_{m\text{-}m}$ is the micelle-to-micelle spacing, γ accounts for unit cell distortion, x is the Material:Template ratio, f_{corona} is the volume fraction of the corona block (PEO). Finally, the SAXS d-spacing (structure factor) was related to the SEM micelle-to-micelle spacing ($d_{m\text{-}m}$) using:

$$S = \frac{d_{m-m}}{d_{spacing}} = \frac{q d_{m-m}}{2\pi} \quad \text{(A.3)}$$

Table A.1. ^{1}H NMR and GPC data of PEO-*b*-PHA.

Polymer	Number Average Molecular Weight, M_n (kg mol^{-1})	Molar mass dispersity, $Đ_M$
PEO-*b*-PHA	20.0 (PEO Block), 46.1 (PHA block)	1.53

Table A.2. Fit parameters established from a dataset that included the SEM measurements and all SAXS data.

Parameter	Value
α	1.26[a]
β	0.534[a]
PEO (vol%)	30.3[b]
S	1.011[c]
γ	0.668[a]
Pore Size (nm)	108.55[d]

[a)] determined by least squares fitting within PMT window [b)] determined by NMR analysis of block polymer composition and reported bulk density values [c)] S value was determined by comparing SEM and SAXS data [d)] average of pore size diameter measured by SEM

Table A.3. Density values of polymer blocks used to calculate PEO volume fraction.

Polymer Block	Density (g cm^{-3})
Poly(ethylene oxide)[2]	1.064
Poly(hexyl acrylate)[3]	1.065

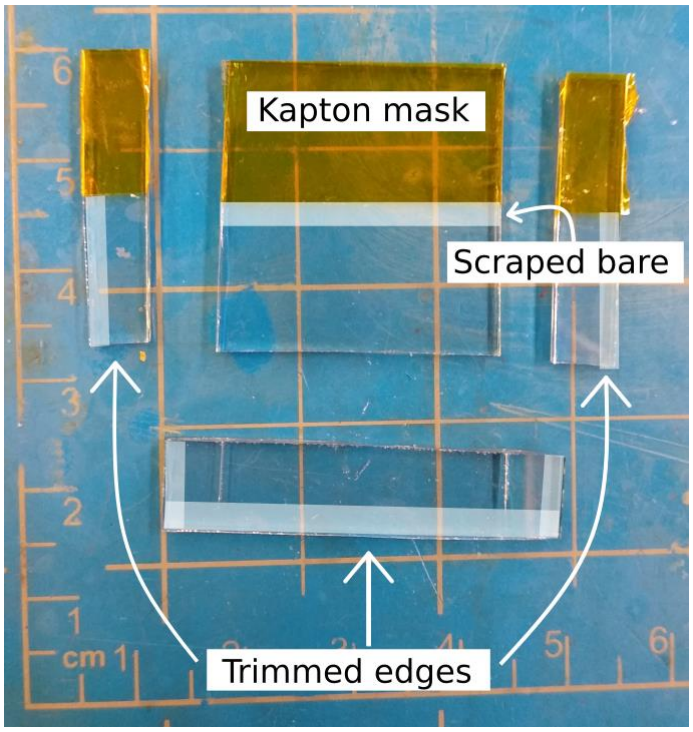

Figure A.5. Photo showing the preparation of electrodes from a spin coated substrate. The regions indicated with white lines were removed by trimming the edges and scraping the meniscus line such that the measured nanostructure was uniform.

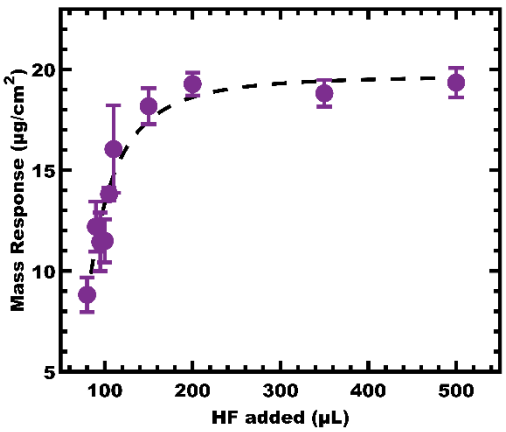

Figure A.6. ICP-MS mass response as a function of 22 M HF volume used to digest a 1 cm^2 sample on an FTO substrate. These data correspond to sample condition MT3.0. Reported values are the average ± the standard-error-of-the-mean. Dashed line is a guide for the eye.

The volume fraction of pores was calculated as

$$f_{pores} = 1 - \frac{m_{film} \,/\, (A_{film} * l_{film})}{\rho_{Nb_2O_5}} \quad \text{(A.4)}$$

where m_{film} is the area-corrected mass of film derived from ICP-MS average values for each M:T condition, A_{film} is the photo-derived area of the film, l_{film} is thickness of the film from cross-sectional SEM, and ρ_{Nb2O5} is the bulk density of T-Nb_2O_5 of 4.6 g cm^{-3}.

A.2 Supporting Information References

[1] K. A. Lantz, N. B. Clamp, W. van den Bergh, A. Sarkar, M. Stefik, *Small* **2019**, *15*, 1900393.

[2] L. J. Fetters, D. J. Lohse, D. Richter, T. A. Witten, A. Zirkel, *Macromolecules* **1994**, *27*, 4639.

[3] H. N. Lokupitiya, A. Jones, B. Reid, S. Guldin, M. Stefik, *Chem. Mater.* **2016**, *28*, 1653.

Appendix B: Supporting Information for Chapter 3

[1]van den Bergh, W.; Larison, T.; Fornerod, M. J.; Guldin, S.; Stefik, M., **2022** *In Review*.

B.1 Supporting Information for Chapter 3

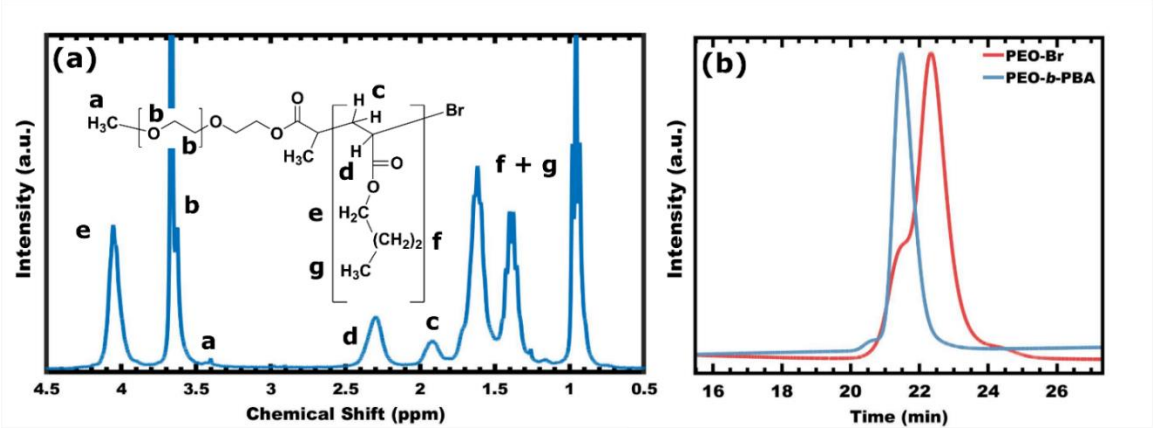

Figure B.1. (a) ^{1}H NMR spectra of poly(ethylene oxide-*b*-butyl acrylate) (PEO-*b*-PBA) block polymer and (b) GPC of PEO-OH vs PEO-*b*-PHA. ^{1}H NMR of PEO-*b*-PBA (300 MHz, $CDCl_3$) δ (ppm): 4.05 (COOC**H**$_2$), 3.67 (O–C**H**$_2$C**H**$_2$–O), 2.30 (C**H**COO), 1.92 (−C**H**$_2$CH−), convolved peaks 1.62 (−C**H**$_2$–, −C**H**$_3$), 1.39 (−C**H**$_2$–, −C**H**$_3$) and 0.96 (−C**H**$_2$–, −C**H**$_3$) with some contribution from 1.92 (−C**H**$_2$CH−).

Table B.1. Polymer synthesis conditions.

Polymer Name	**Temp (°C)**	**Time (hr)**	**[Initiator] : [Cu(I)Br] : [PMDETA] : [Monomer]**
PEO-*b*-PBA	70	12	1 : 0.5 : 0.5 : 100

Table B.2. Shows the molecular weight (M_n) and dispersity of the polymers used.

Polymer Name	**M_n, Number mean Molecular Weight (kg mol^{-1})**	**Molecular Mass Dispersity (Đ)**
PEO-*b*-PBA	5.0 (PEO), 23.1 (PBA)	1.24

A previously developed micelle core template (MCT) model[1] for disordered paracrystals was used to model d-spacing changes with the M:T ratio under constant micelle template size. The d-spacing was modeled using:

$$d_{spacing} = \frac{D}{2S}\sqrt[3]{\frac{3\gamma}{4\pi}}\left(x\beta_{mct} + 1 + \frac{f_{corona}}{1 - f_{corona}}\right)^{\frac{1}{3}} \quad \text{(B.1)}$$

where D is the template/pore diameter, γ accounts for unit cell distortion, x is the M:T ratio, f_{corona} is the volume fraction of the corona block (PEO), and β_{mct} is a convolved density term. Lastly S links the structure factor peak to the SEM measured micelle-to-micelle spacing ($d_{m\text{-}m}$) using:

$$S = \frac{d_{m-m}}{d_{spacing}} = \frac{q d_{m-m}}{2\pi} \quad \text{(B.2)}$$

The wall thickness was deconvolved from the micelle-to-micelle distance using:

$$w = (\alpha d_{m-m} - D) \quad \text{(B.3)}$$

where w is the wall thickness, α is a fit term to accommodate the variable distribution of wall thickness for different orientations, and D is the pore diameter. For cubic crystal systems, alpha values are expected to range from 0.87-2.45 when measured using an inscribed circle.[2]

Table B.3. Density values of polymer blocks used to calculate the PEO volume fraction.

Polymer Block	**Density [g/cm^3]**
Poly(ethylene oxide)[3]	1.064
Poly(butyl acrylate)[4]	1.033

Table B.4. PMT model best-fit parameters for each temperature series based on SEM and SAXS data.

Parameter	**280°C Series**	**380°C Series**	**600°C Series**
α [a]	1.24	1.14	1.14
β [a]	2.7135	4.1423	3.0220
PEO (vol%) [b]	30.28	30.28	30.28
S [c]	1.22	1.19	1.27
γ [a]	1	1	1
Pore Diameter (nm) [d]	18.19	19.09	21.67

[a)] determined by least squares fitting within PMT window

[b)] determined by NMR analysis of block polymer composition and reported bulk density values

[c)] S value was determined by comparing SEM and SAXS data

[d)] Mean of pore diameter measured by SEM

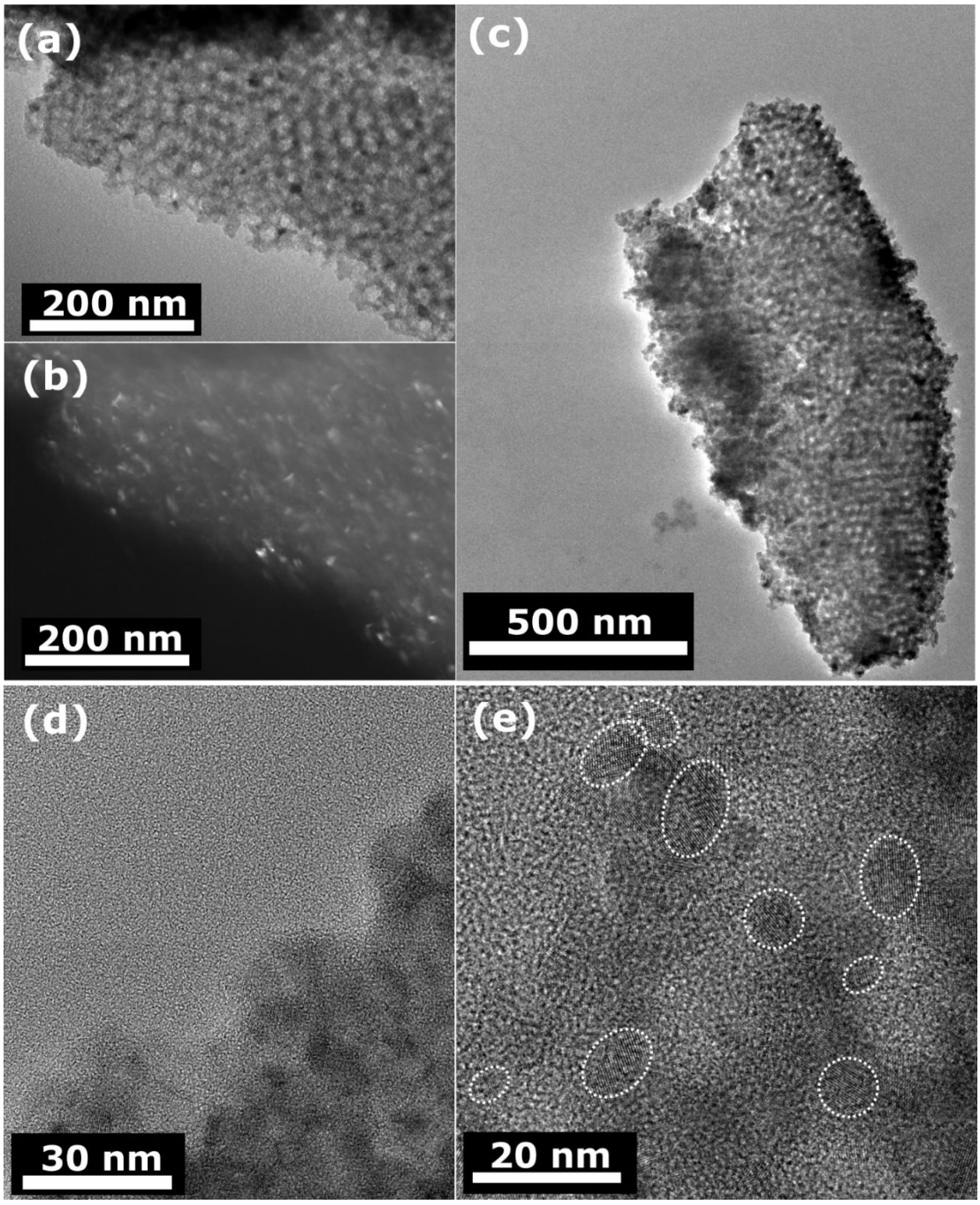

Figure B.2. TEM images of a MT1.6-600°C sample. (a) bright field and (b) dark field images of nanoscale architecture with dark field showing crystallites throughout the nanostructure. (c) HR-TEM image of segment of nanoscale architecture with subsequent magnification of nanostructure in panels (d-e). (e) HR-TEM of nanoscale architecture showing lattice fringes of crystallites highlighted with dashed rings distributed in the walls (dark region) surrounding pores (light region).

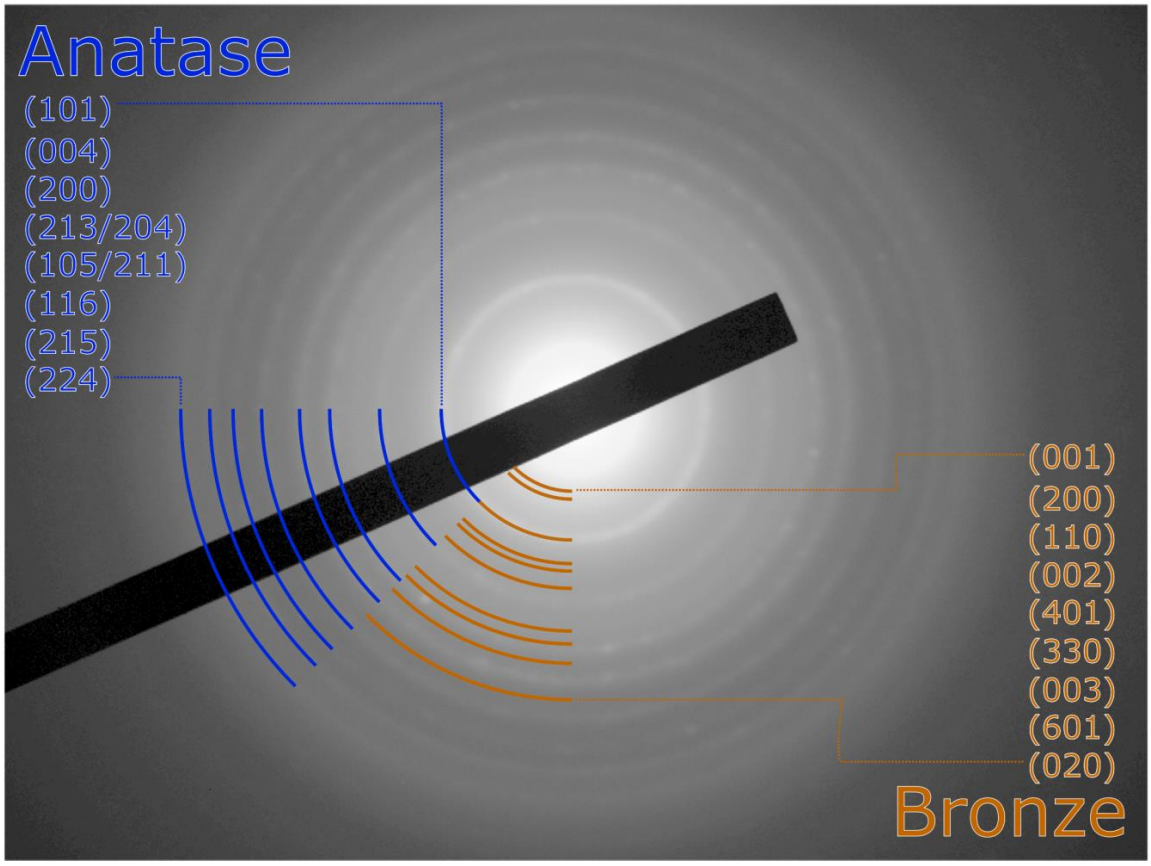

Figure B.3. TEM electron diffraction pattern of MT1.6-600°C with reference marks for anatase (PDF 65-5714) and bronze (PDF 46-1237) TiO_2 polymorphs.

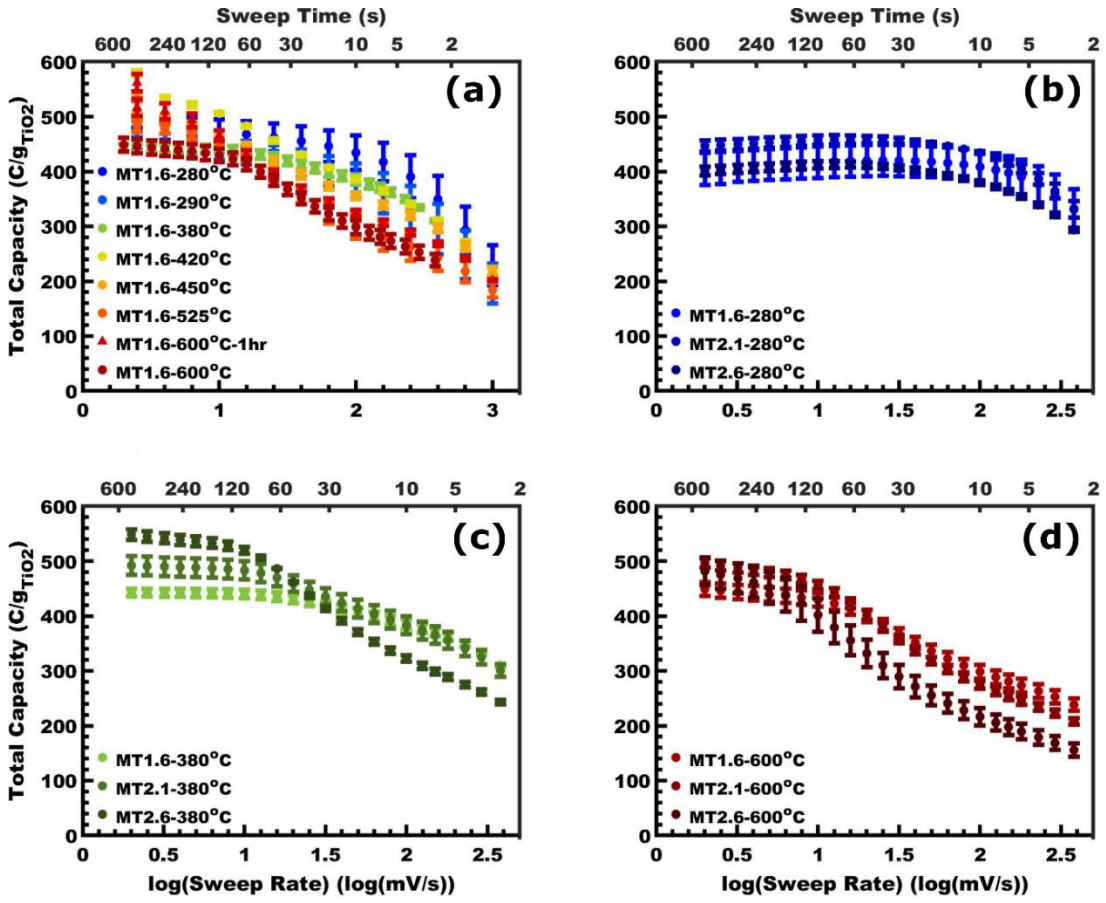

Figure B.4. Voltage sweep rate dependent lithiation capacity for (a) temperature series and (b-d) MT series conditions at (b) 280 °C, (c) 380 °C, (d) 600 °C. Values are presented as the mean ± standard error-of-the-mean.

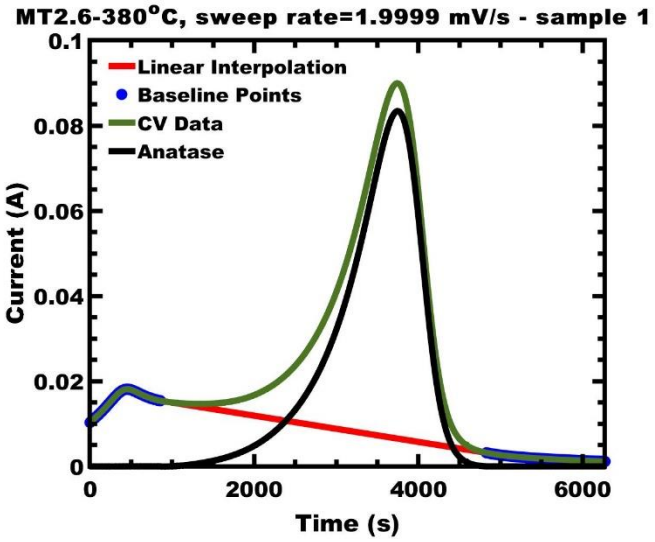

Figure B.5. Schematic showing the analysis of the anatase current contribution by using a linear baseline to model purely-amorphous TiO_2. The non-anatase data and interpolation closely resembles CV curves for purely-amorphous samples.

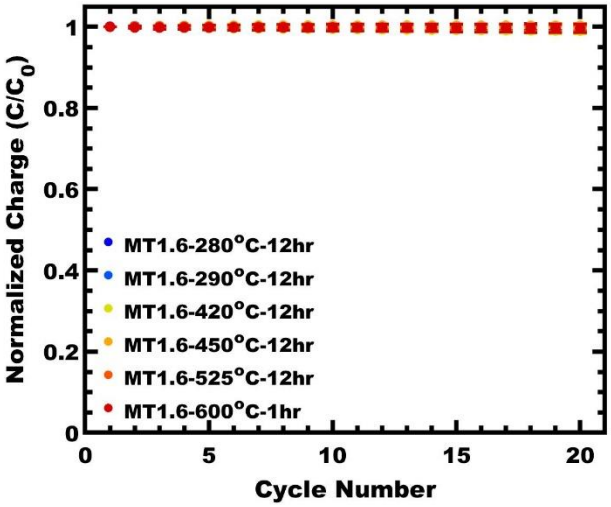

Figure B.6. The lithiation capacity of MT1.6 samples across temperature under electrochemical cycling at 25.0 mV/s. Values are presented as the mean ± standard error-of-the-mean.

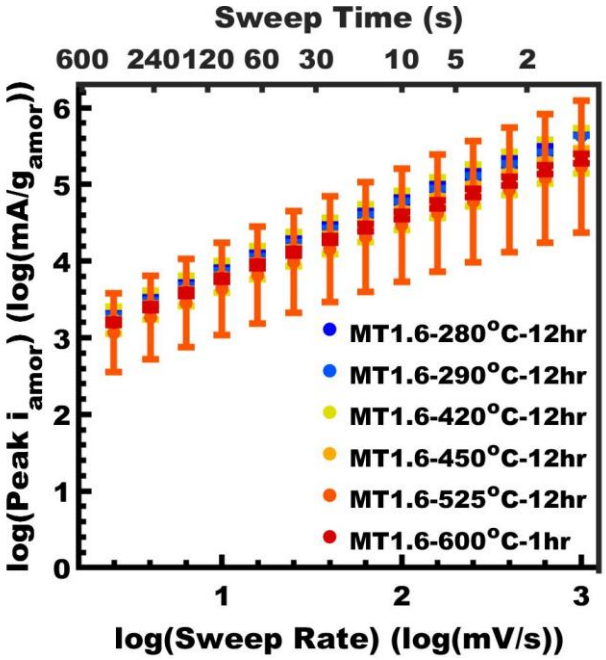

Figure B.7. Mass normalized log-log of amorphous TiO_2 anodic peak current vs voltage sweep rate for all sample conditions of the temperature series. Values are presented as the mean ± standard error-of-the-mean.

Table B.5. Electrochemical metrics for the MT1.6 temperature sample series.

Name	Amorphous ν_{SLT} (mV/s)[a)b)]	Total Capacity (C/g_{TiO2})[a)c)]	Amorphous percent by CV ($Coul.\%_{amor}$)[a)d)]
MT1.6-280°C-12hr	45.00 ± 0.21	476.8 ± 17.3	100
MT1.6-290°C-12hr	28.56 ± 0.13	455.9 ± 1	100
MT1.6-420°C-12hr	13.12 ± 0.09	579.6 ± 5.1	80.5 ± 4.4
MT1.6-450°C-12hr	12.61 ± 0.06	539.5 ± 5.5	80.2 ± 0.6
MT1.6-525°C-12hr	11.37 ± 0.07	481.8 ± 9.8	63.1 ± 10.4
MT1.6-600°C-1hr	10.80 ± 0.13	516.2 ± 15.5	72.2 ± 0.8

[a] Values presented are the mean value ± standard error-of-the-mean

[b)] Voltage sweep rate values were linearly interpolated between nearest experimental values in the lin-log coordinate space of the b-value plots. Voltage sweep rate values are reported ± the bounding limits for error propagation based on Rolle's Theorem.

[c)] Capacity is mass normalized charge at 2.5 mV/s.

[d)] Amorphous content determined by a baseline method described in experimental and Figure B.5.

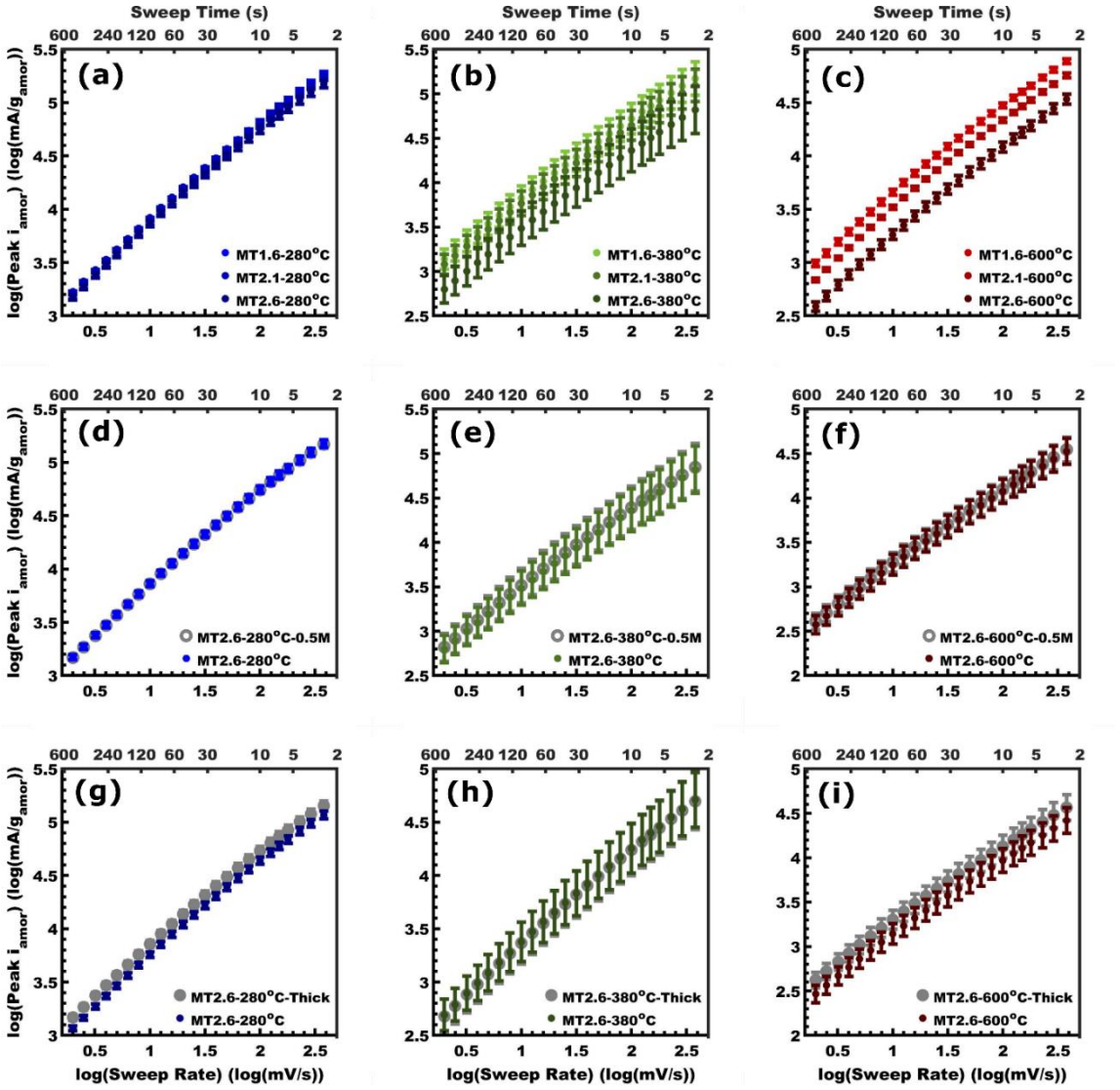

Figure B.8. Mass normalized log-log plots of amorphous TiO_2 anodic peak current vs voltage sweep rate for all sample conditions of the M:T series. Values are presented as the mean ± standard error-of-the-mean.

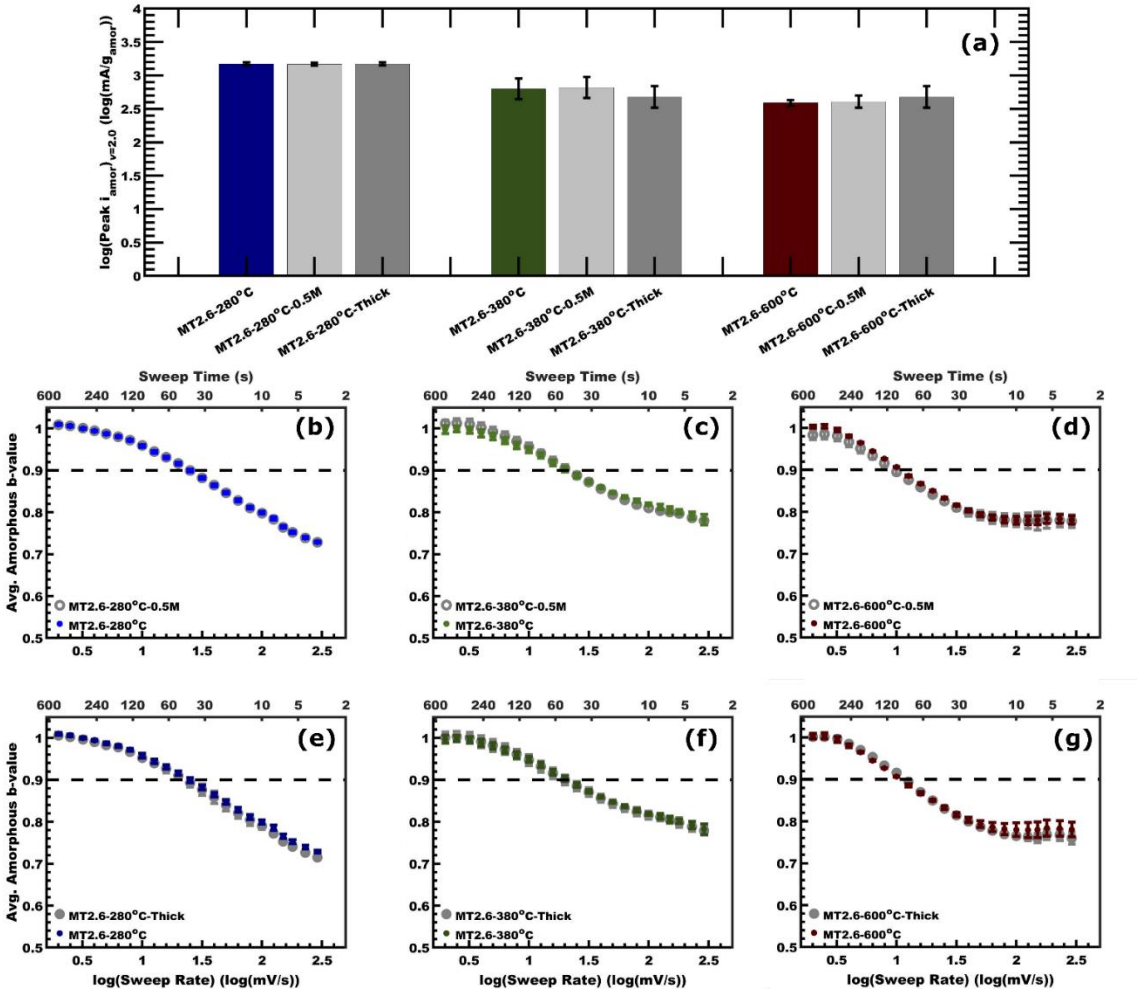

Figure B.9. Possible kinetic constraints from electrolyte transport and electron transport were examined for M:T=2.6 over a range of calcination temperatures (labelled). Comparisons include (a) the amorphous peak currents, (b-d) b-value(*v*) with 1.0 M *vs* 0.5 M electrolyte, (e-g) b-value(*v*) with standard thickness (~100 nm) vs thicker films (~28% thicker). Values are presented as the mean ± standard error-of-the-mean. The minor impact of electrolyte concentration and film thickness indicates that neither electrolyte nor electron transport is significantly rate limiting.

Table B.6. Electrochemical metrics for isomorphic series with different M:T ratios and different calcination temperatures, film thicknesses, and electrolyte concentrations.

Condition	Amorphous ν_{SLT} (mV/s)[a)b)]	Amorphous t_{SLT} (s)[a)c)]	TiO_2 $\nu_{95\%}$ (mV/s)[a)b)]	TiO_2 $t_{95\%}$ (s)[a)c)]	Total Capacity (C/g_{TiO2})[a)d)]	Amorphous percent by CV ($Coul.\%_{amor}$)[a)e)]
MT1.6-280°C	42.86 ± 0.04	23.33 ± 0.02	203.4 ± 2.82	4.92 ± 0.07	404.6 ± 28.9	100 ± 0
MT2.1-280°C	32.94 ± 0.08	30.36 ± 0.07	130.6 ± 0.90	7.66 ± 0.01	446.5 ± 9.8	100 ± 0
MT2.6-280°C	24.84 ± 0.08	40.26 ± 0.13	96.89 ± 0.48	10.11 ± 0.05	400.9 ± 7.8	96.1 ± 0.7
MT2.6-280°C-0.5M	23.48 ± 0.073	-	-	-	-	-
MT2.6-280°C-Thick	22.80 ± 0.06	-	-	-	-	-
MT1.6-380°C	28.30 ± 0.02	35.34 ± 0.02	30.44 ± 0.13	32.85 ± 0.14	442.6 ± 7.0	88.3 ± 3.2
MT2.1-380°C	22.30 ± 0.02	44.84 ± 0.04	16.77 ± 0.19	59.63 ± 0.68	492.0 ± 17.1	78.3 ± 2.8
MT2.6-380°C	20.79 ± 0.03	48.10 ± 0.07	10.06 ± 0.26	99.40 ± 2.57	548.3 ± 9.7	54.7 ± 3.0
MT2.6-380°C-0.5M	21.35 ± 0.03	-	-	-	-	-
MT2.6-380°C-Thick	19.95 ± 0.02	-	-	-	-	-
MT1.6-600°C	10.60 ± 0.05	94.34 ± 0.45	11.07 ± 0.18	90.33 ± 1.47	448.9 ± 12.7	59.0 ± 3.6
MT2.1-600°C	11.76 ± 0.04	85.03 ± 0.29	6.774 ± 0.077	147.62 ± 1.68	496.7 ± 8.4	48.5 ± 3.7
MT2.6-600°C	10.72 ± 0.01	93.28 ± 0.09	4.067 ± 0.021	245.88 ± 1.27	481.8 ± 25.3	45.6 ± 1.4
MT2.6-600°C-0.5M	9.458 ± 0.015	-	-	-	-	-
MT2.6-600°C-Thick	11.89 ± 0.04	-	-	-	-	-

[a)] Values represented are the value mean ± standard error-of-the-mean

[b)] Voltage sweep rate values were linearly interpolated between nearest experimental values in the lin-log coordinate space of the b-value plots. Voltage sweep rate values are reported ± the bounding limits for error propagation based on Rolle's Theorem.

[c)] Sweep times were calculated as the voltage window divided by the voltage sweep rate. Sweep times reported ± the error propagated from the voltage sweep rate.

[d)] Capacity is mass normalized charge at 2.0 mV/s.

[e)] Amorphous content determined by a baseline method described in experimental and Figure S4.

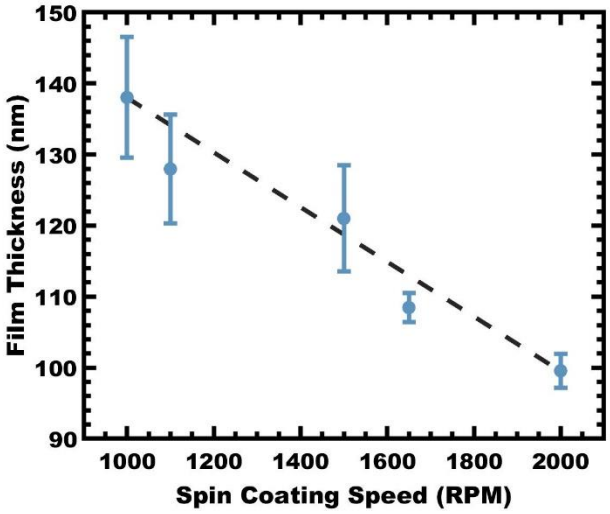

Figure B.10. Ellipsometry trend for MT2.6 samples spun at different RPM. Dashed line is a guide for the eye. Values are presented as the mean ± standard error-of-the-mean. Please note that spin-coating conditions spanning greater RPM ranges exhibit a non-linear relationship (Thickness $\propto$ $RPM^{-0.5}$)[5–7] whereas this small range of RPM values is locally linear.

Table B.7. Mean film thickness and porosity as a function of spin-coating speed determined by visible ellipsometry.

Condition name	**Spin-coating speed [rpm]**	**Film Thickness [nm][a)]**	**n_{eff}**	**n_{TiO2}[c)]**	**Porosity (vol% pore)[d)]**
MT1.6	1,100	98.33 ± 2.60	1.602 ± 0.005	2.122	55.3 ± 0.5
MT2.1	1,100	102.2 ± 4.72	1.668 ± 0.030	2.106	48.0 ± 2.8
MT2.6	2,000	99.57 ± 2.92	1.661 ± 0.014	2.040	44.3 ± 1.5
MT2.6	1,100	127.97 ± 7.67	1.674 ± 0.010	2.040	45.9 ± 1.0

[a)] Mean film thickness values were reported ± the standard error-of-the-mean

[b)] Values extracted from Semilab's software (see experimental), reported as mean ± standard error-of-the-mean

[c)] Values estimated from literature values (see experimental) and amorphous content

[d)] Mean porosities were reported ± the standard error-of-the-mean

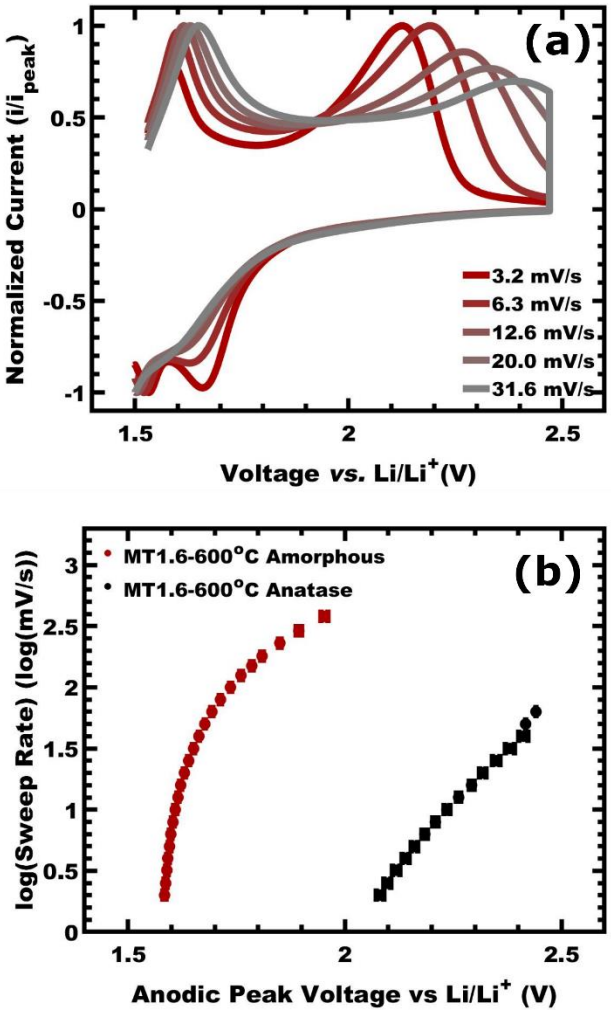

Figure B.11. (a) A representative, normalized CV of MT1.6-600°C. (b) Anodic voltage of peak current as a function of voltage sweep rate (vertical axis) for MT1.6-600°C samples. Values in panel (b) are presented as the mean ± standard error-of-the-mean.

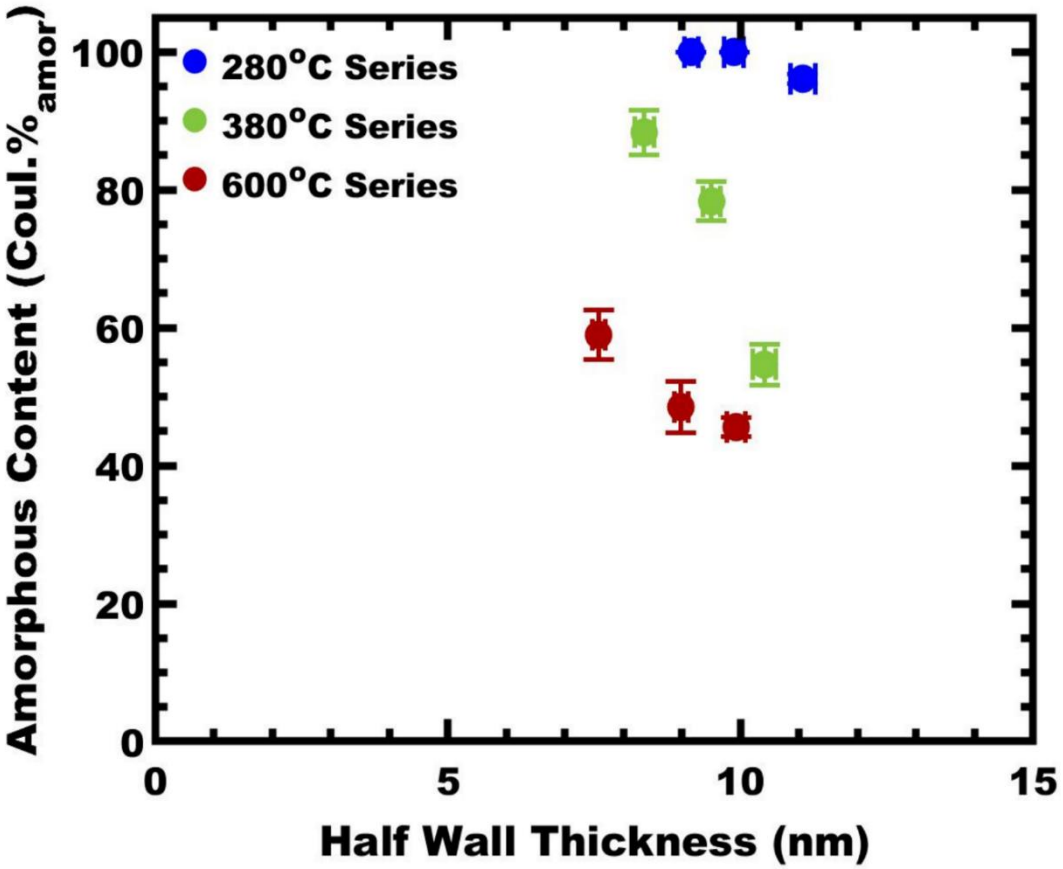

Figure B.12. Comparison of amorphous content across all conditions examined in Figure 3.8. Values are presented as the mean ± standard error-of-the-mean.

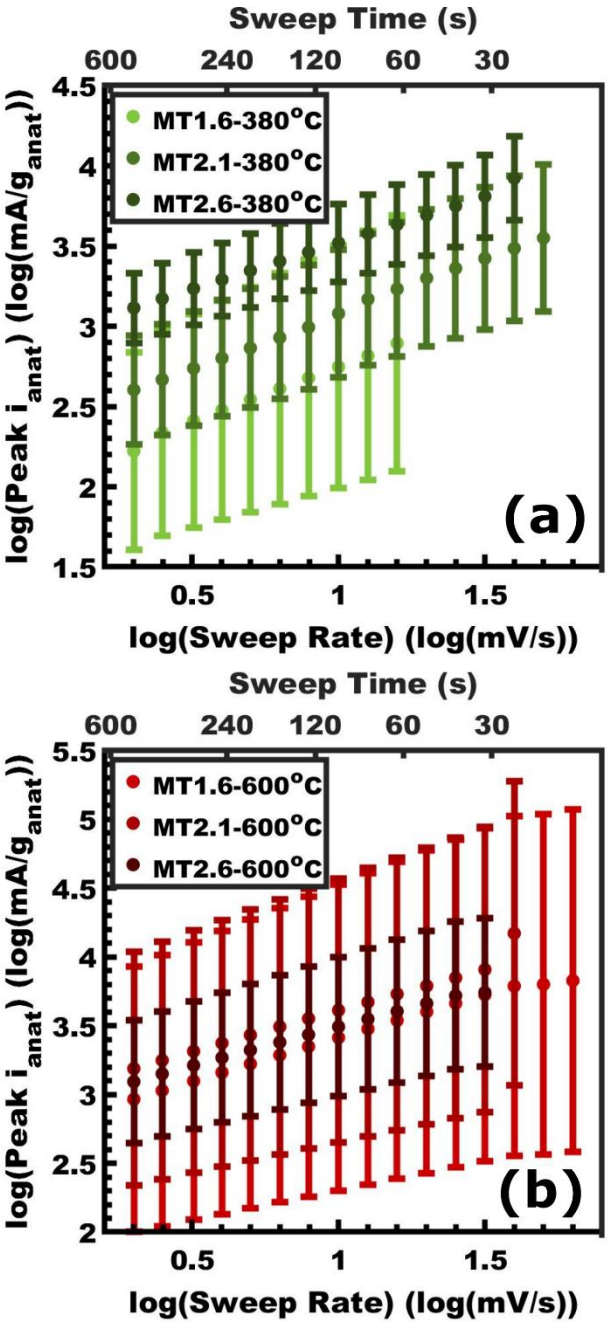

Figure B.13. Mass normalized log-log plots of anatase TiO_2 anodic peak current vs voltage sweep rate for all sample conditions of the M:T series at (a) 380 °C and (b) 600 °C. Values are presented as the mean ± standard error-of-the-mean.

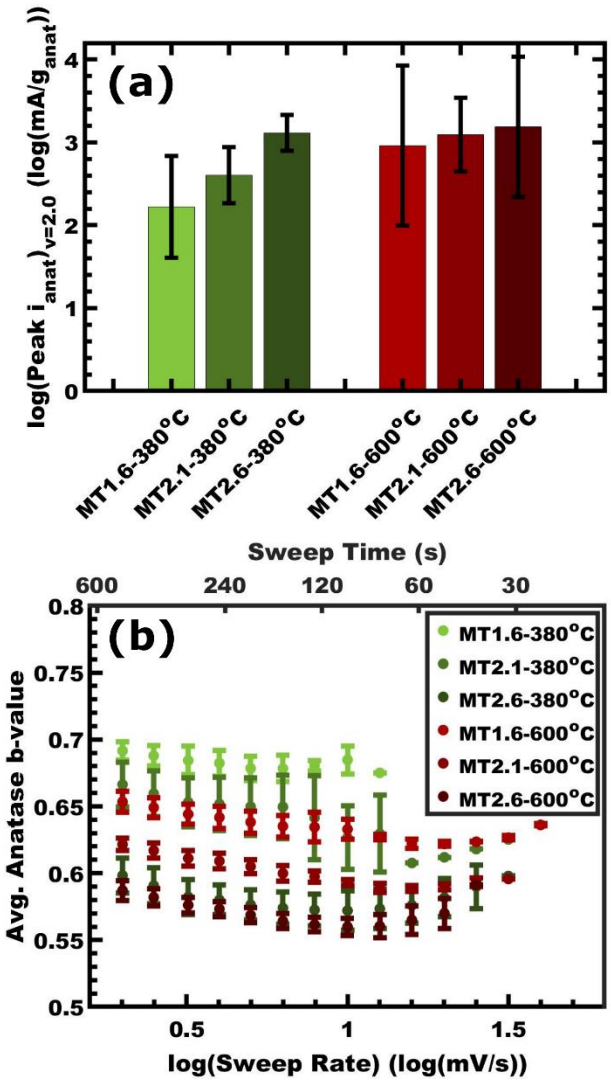

Figure B.14. Anatase TiO_2 kinetic constraints from the intercalation length (wall thickness) were examined over a range of isomorphic architectures (indicated M:T values). Comparisons include (a) amorphous peak currents and anatase b-values(*v*) for samples calcined at (b) 380 °C and 600 °C. Values are presented as the mean ± standard error-of-the-mean.

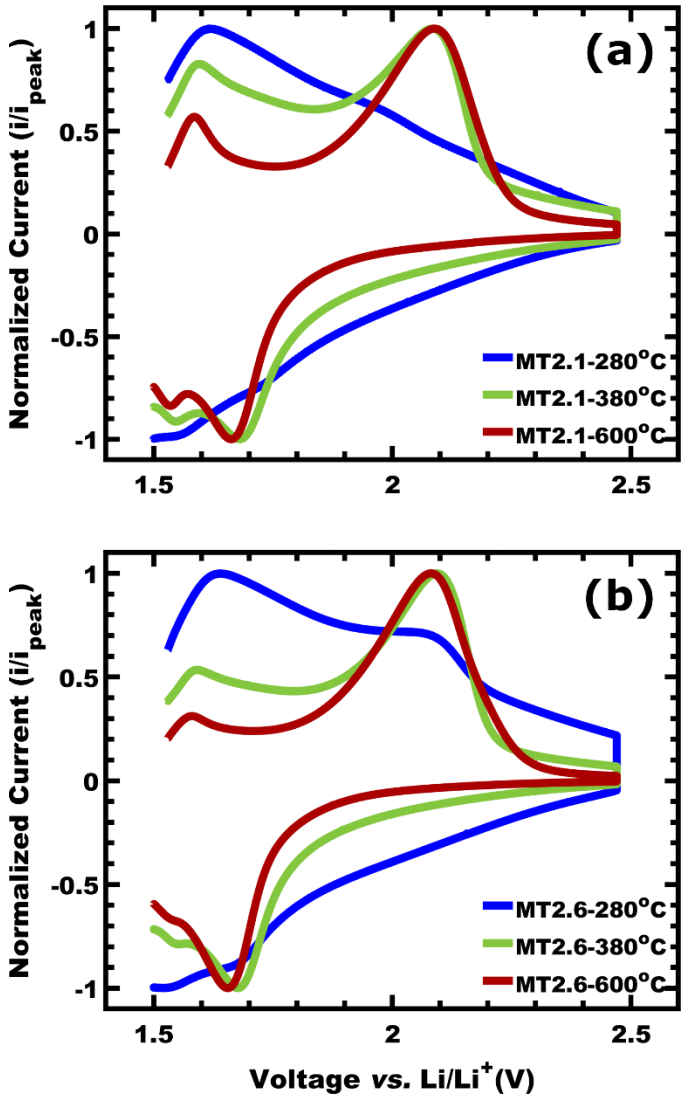

Figure B.15. Representative CVs of (a) M:T 2.1 and (b) MT2.6 for 280 °C. 380 °C, and 600 °C conditions at 2.0 mV/s.

B.2 Supporting Information References

[1] A. Sarkar, M. Stefik, *J. Mater. Chem. A* **2017**, *5*, 11840.

[2] K. A. Lantz, N. B. Clamp, W. van den Bergh, A. Sarkar, M. Stefik, *Small* **2019**, *15*, 1900393.

[3] L. J. Fetters, D. J. Lohse, D. Richter, T. A. Witten, A. Zirkel, *Macromolecules* **1994**, *27*, 4639.

[4] I. Barudio, G. Févotte, T. F. McKenna, *European Polymer Journal* **1999**, *35*, 775.

[5] D. W. Schubert, T. Dunkel, *Mater. Res.* **2003**, *7*, 314.

[6] S. Guldin, Inorganic Nanoarchitectures by Organic Self-Assembly. PhD, University of Cambridge, **2013**.

[7] H. N. Lokupitiya, Kinetic-Control of Block Copolymer Micelles for Tunable Nanomaterials Towards Energy Devices. PhD, University of South Carolina, **2017**.

Appendix C: Supporting Information for Chapter 4

[1] v. d. Bergh, W.; Wechsler, S.; Lokupitiya, H. N.; Jarocha, L.; Kim, K.; Chapman, J.; Kweon, K. E.; Wood, B. C.; Heald, S.; Stefik, M. *Batteries & Supercaps*, 2022, ASAP.

C.1 Supporting Information for Chapter 4

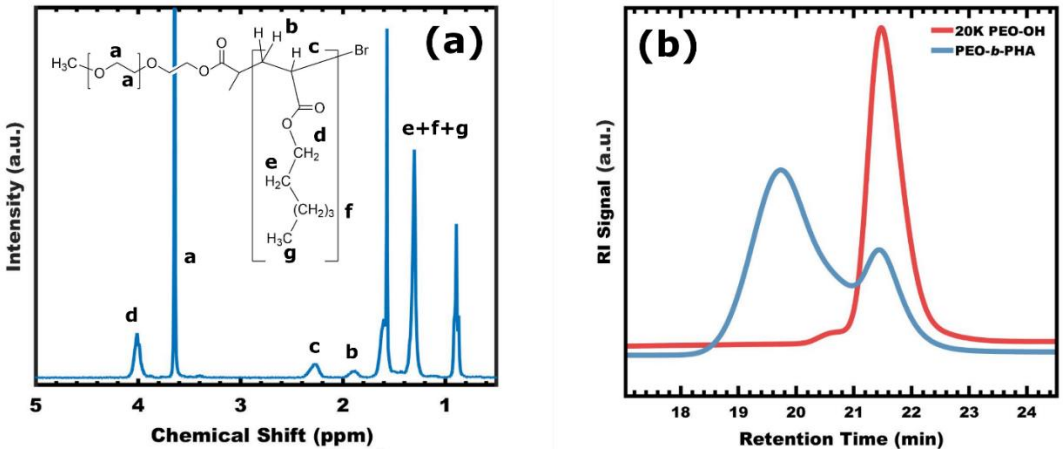

Figure C.1. (a) ^{1}H NMR spectra of PEO-b-PHA block copolymer and (b) GPC of PEO-OH vs PEO-b-PHA. ^{1}H NMR (300 MHz, $CDCl_3$, δ), 4.05 (m, 2H, $COOCH_2$), 3.65 (s, 4H, CH_2CH_2O), 2.30 (s, CH), 1.90 (s, 2H, CH_2), 1.55 (m, 2H, CH_2), 1.30 (m, 6H, CH_2), 0.90 (m, 3H, CH_3). Note that peaks b, e, f, and g have some convolution.

Table C.1. ^{1}H NMR and GPC data of PEO-*b*-PHA.

Polymer	**Number Average Molecular Weight, M_n [kg mol^{-1}]**	**Molar mass dispersity, $Đ_M$**
PEO-*b*-PHA	20.0 (PEO block), 46.1 (PHA block)	1.53

A previously developed micelle core template (MCT) model[1] for disordered paracrystals was used to model d-spacing changes with the M:T ratio under constant micelle template size. The d-spacing was modeled using:

$$d_{spacing} = \frac{D}{2S}\sqrt[3]{\frac{3\gamma}{4\pi}}\left(x\beta_{mct} + 1 + \frac{f_{corona}}{1 - f_{corona}}\right)^{\frac{1}{3}} \quad \text{(C.1)}$$

where D is the template (pore) diameter, γ accounts for unit cell distortion, x is the M:T ratio, f_{corona} is the volume fraction of the corona block (PEO), and β_{mct} is a convolved density term. Lastly S links the structure factor peak to the SEM measured micelle-to-micelle spacing ($d_{m\text{-}m}$) using:

$$S = \frac{d_{m-m}}{d_{spacing}} = \frac{q d_{m-m}}{2\pi} \quad \text{(C.2)}$$

The wall thickness was deconvolved from the micelle-to-micelle spacing using:

$$w = (\alpha d_{m-m} - D) \quad \text{(C.3)}$$

where w is the wall thickness, α is a fit term to accommodate the variable distribution of wall thickness for different orientations, and D is the pore diameter. For cubic crystal systems, alpha values are expected to range from 0.87-2.45 when wall thicknesses are measured using an inscribed circle.[2]

Table C.2. Density values of polymer blocks used to calculate the PEO volume fraction

Polymer Block	**Density [g cm^{-3}]**
Poly(ethylene oxide)[3]	1.064
Poly(hexyl acrylate)[4]	1.065

Table C.3. PMT model best-fit parameters for each temperature series based on SEM and SAXS data

Parameter	520 °C Series	535 °C Series	600 °C Series
α [a]	0.955	0.955	0.955
β [a]	1.44	1.24	1.51
PEO (vol%) [b]	30.28	30.28	30.28
S [c]	1.13	1.09	1.15
γ [a]	0.71	0.79	0.76
Pore Diameter (nm) [d]	91.41	95.96	96.97

[a)] determined by least squares fitting within PMT window

[b)] determined by NMR analysis of block polymer composition and reported bulk density values

[c)] S value was determined by comparing SEM and SAXS data

[d)] Average of pore diameter measured by SEM

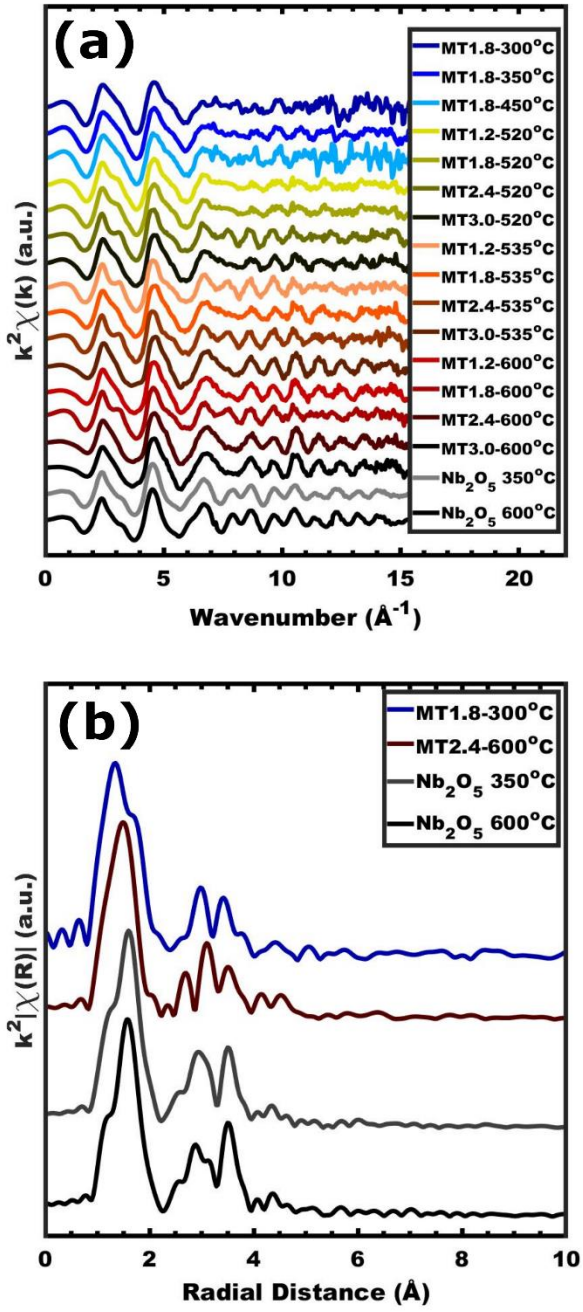

Figure C.2. (a) k^2-weighted $\chi(k)$ spectra of all samples measured including solid-state synthesized standards[5] at 350 °C and 600 °C. (b) k^2-weighted Fourier-transformed Nb K-edge EXAFS of samples used in linear combination analyses. The solid-state synthesized[5] Nb_2O_5 samples calcined at 350 °C and 600 °C did not resolve the third component discussed in main text.

Table C.4. EXAFS linear combination fit corresponding weights to each standard (sum = 1), R-factor, and reduced χ^2 values for M:T samples.

Condition	**R-factor** [a]	**Reduced χ^2** [b]	**MT1.8-300°C Weight**	**TT-Nb_2O_5 Weight**	**T-Nb_2O_5 Weight**
MT1.2-520°C	0.200	4.33473	0.46	0	0.54
MT1.2-535°C	0.179	2.78336	0.51	0	0.49
MT1.2-600°C	0.162	3.41639	0.31	0	0.69
MT1.8-520°C	0.081	0.8838	0.75	0	0.25
MT1.8-535°C	0.100	1.32838	0.66	0	0.34
MT1.8-600°C	0.152	2.10655	0.59	0	0.41
MT2.4-520°C	0.182	2.76509	0.45	0	0.55
MT2.4-535°C	0.169	2.57256	0.50	0	0.50
MT2.4-600°C	0.240	6.43973	0.26	0	0.74
MT3.0-520°C	0.103	1.46714	0.61	0	0.39
MT3.0-535°C	0.252	6.95468	0.29	0	0.71
MT3.0-600°C	0.193	4.74638	0.18	0	0.82

[a] R-factor is a measure of the mean square sum of residuals at each data point

[b] Reduced χ^2 is a statistical measure, used here to indicate if standards fit data well with $\chi^2 > 1$ indicative of data not fully captured by fit

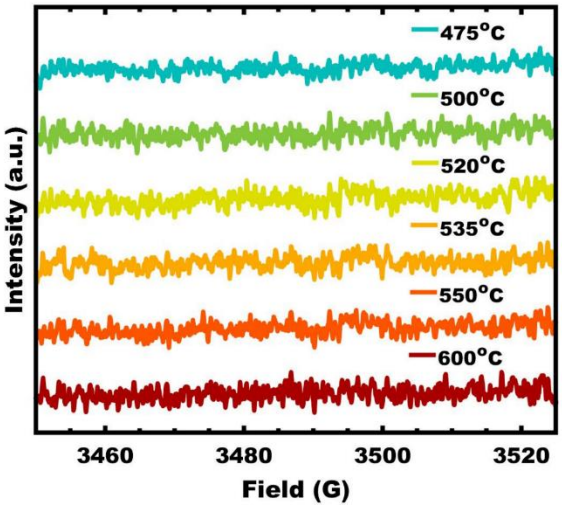

Figure C.3. X-band EPR data demonstrating no detectable signal consistent with oxygen vacancies which are expected around 3487 G. Data represented as an average of 16 measurements which were baseline corrected using measurements made in an empty resonator.

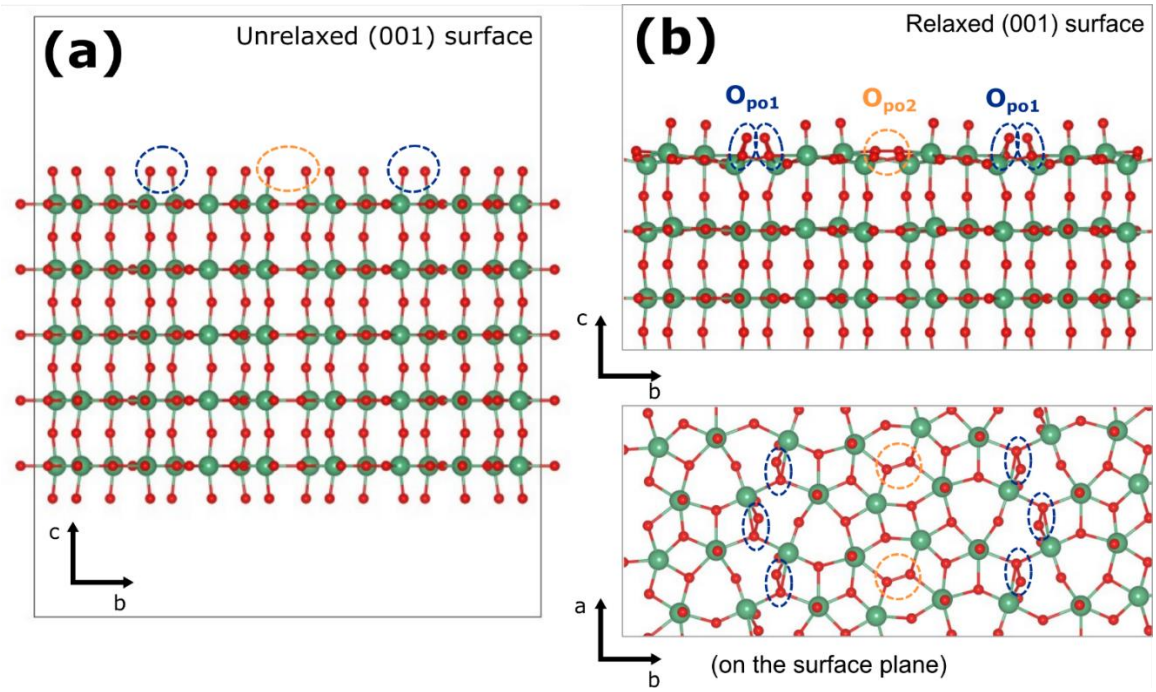

Figure C.4. (a) Slab models for unrelaxed and (b) relaxed O-rich (001) Nb_2O_5 surface were calculated using DFT. (b) The view from the [100] direction (top panel) and the [001] direction (bottom panel). The green and red balls represent Nb and O atoms, respectively. Two different peroxide (O_2^{2-}) configurations (denoted as O_{po1} and O_{po2}) are formed on the relaxed surface.

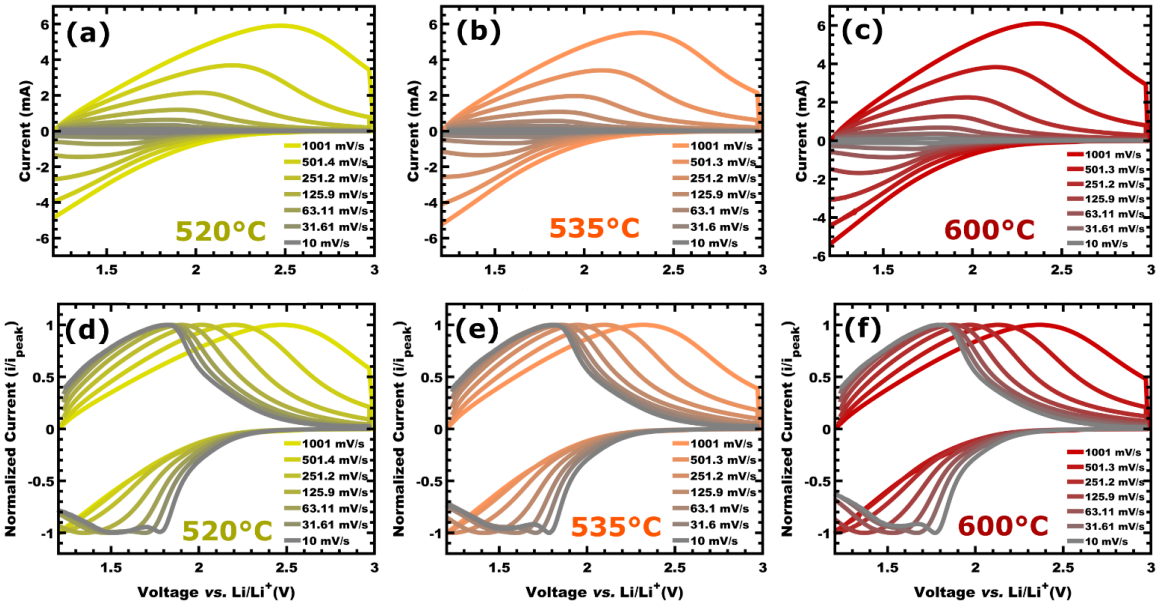

Figure C.5. (a-c) Cyclic voltammetry data from representative MT1.2 samples for each calcination condition showing voltage sweep rates ranging from 1,000 to 10 mV/s. (d-f) The corresponding normalized current plots better reveal the peak shifts.

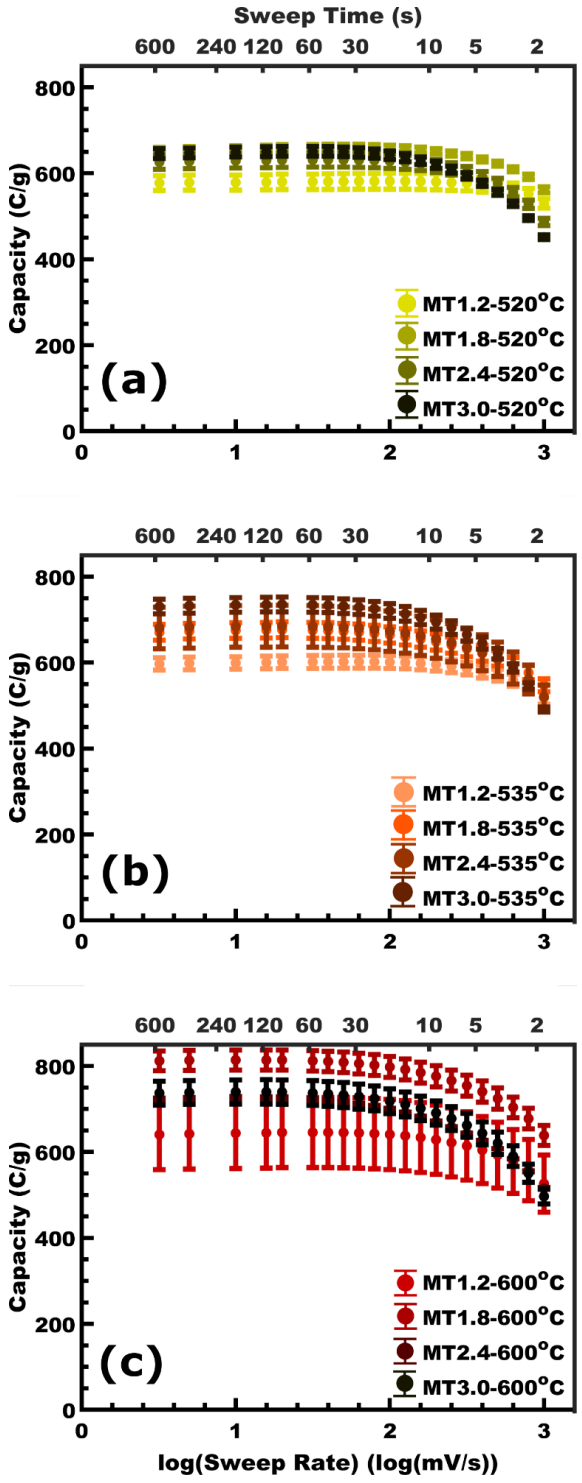

Figure C.6. Voltage sweep-rate dependent lithiation capacity for sample series calcined at (a) 520 °C, (b) 535 °C, (c) 600 °C. Values presented as mean ± standard error-of-the-mean.

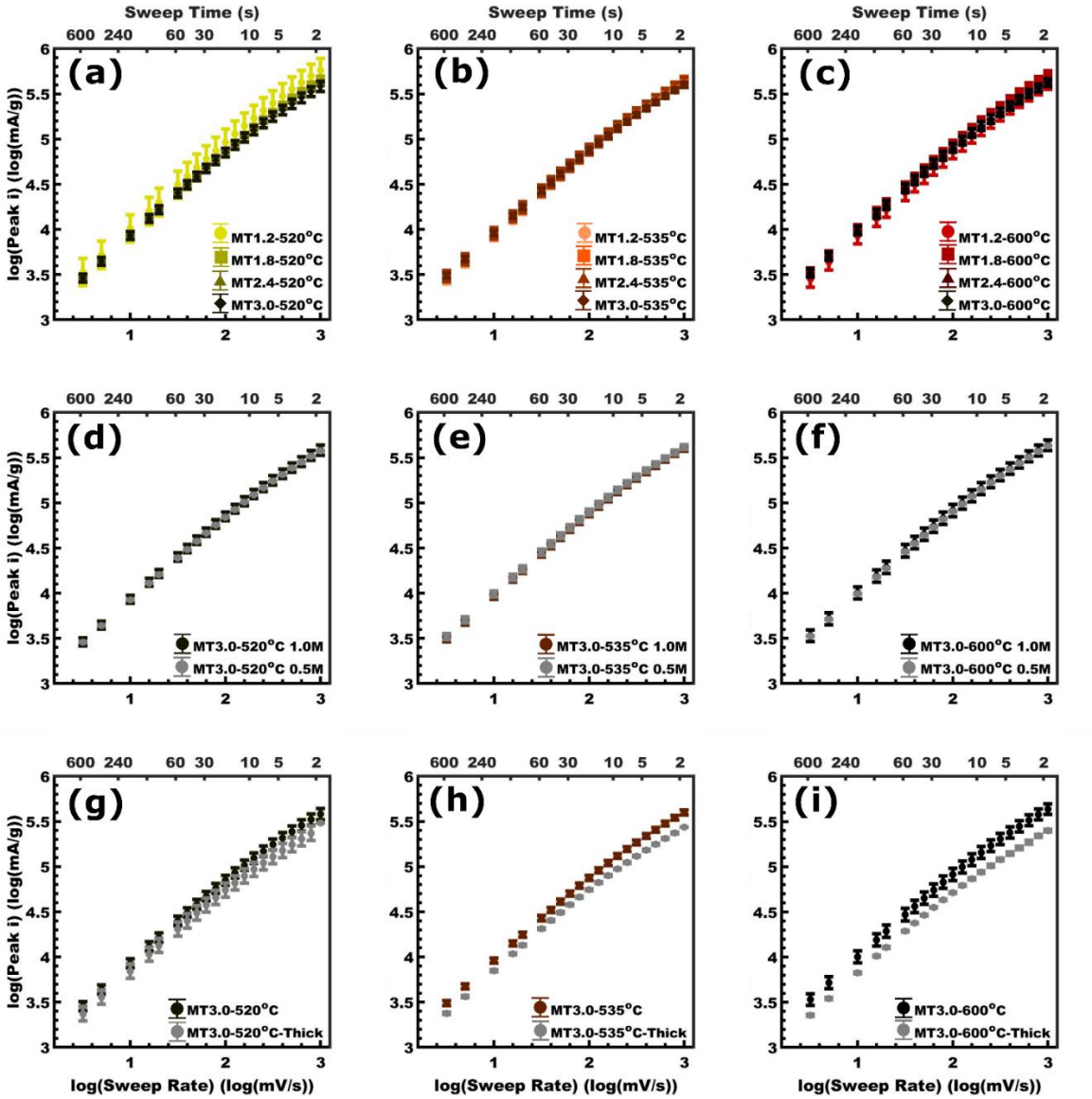

Figure C.7. Plots of anodic peak current versus voltage sweep rate for all samples conditions on a log-log plot. Values presented as mean ± standard error-of-the-mean.

Table C.5. Statistical measures of average film thickness as a function of spin-coating speed determined by cross-sectional SEM.

Condition name	**Spin-coating speed [rpm]**	**Film Thickness [nm]**[a)]
MT1.2-600°C	1,000	80.4 ± 2.2
MT1.8-600°C	1,500	78.6 ± 2.7
MT2.4-600°C	2,000	66.7 ± 1.4
MT3.0-600°C	2,150	65.2 ± 2.6
MT3.0-600°C-Thick	400	163.0 ± 4.9

[a)] Average film thickness values were reported ± the standard error of the mean

Table C.6. Voltage sweep rates and corresponding sweep times at the surface-limited threshold for all sample conditions.

Condition name	v_{SLT} **(**b **= 0.9) [mV/s]** [a)b)]	t_{SLT} **[s]** [a)c)]
MT1.2-520°C	136.3 ± 2.1	13.21 ± 0.21
MT1.8-520°C	122.5 ± 2.9	14.69 ± 0.34
MT2.4-520°C	75.2 ± 2.3	23.94 ± 0.75
MT3.0-520°C	56.0 ± 0.5	32.11 ± 0.30
MT3.0-520°C-Thick	40.6 ± 0.3	44.34 ± 0.33
MT1.2-535°C	122.0 ± 2.4	14.75 ± 0.29
MT1.8-535°C	105.0 ± 0.6	17.14 ± 0.09
MT2.4-535°C	72.1 ± 0.8	24.96 ± 0.27
MT3.0-535°C	53.4± 0.3	33.72 ± 0.18
MT3.0-535°C-Thick	38.3 ± 0.8	47.00 ± 1.01
MT1.2-600°C	87.1 ± 0.3	20.66 ± 0.08
MT1.8-600°C	84.7 ± 0.5	21.26 ± 0.12
MT2.4-600°C	59.1 ± 0.1	30.46 ± 0.05
MT3.0-600°C	51.4 ± 0.2	35.19 ± 0.17
MT3.0-600°C-Thick	32.8 ± 0.4	54.84 ± 0.65

a) Values presented are the mean value ± standard error-of-the-mean

b) Voltage sweep rate values were linearly interpolated between nearest experimental values in the lin-log coordinate space of b-value plots. Voltage sweep rate values are reported ± the bounding limits for error propagation based on Rolle's Theorem.

c) Sweep times were calculated as the voltage window divided by the voltage sweep rate. Sweep times reported ± the error propagated from the voltage sweep rate.

Table C.7. Sweep rates and corresponding sweep times at the surface-limited threshold (SLT) for each calcination condition in the MT1.8 temperature series.

Sample Name	v_{SLT} (b = 0.9) [mV/s] [a)b)]	t_{SLT} [s] [a)c)]
MT1.8-300°C	275.2 ± 0.4	6.540 ± 0.009
MT1.8-350°C	322.5 ± 0.6	5.582 ± 0.009
MT1.8-400°C	303.0 ± 0.9	5.941 ± 0.018
MT1.8-450°C	350.1 ± 1.5	5.142 ± 0.021
MT1.8-475°C	313.1 ± 1.0	5.749 ± 0.018
MT1.8-500°C	309.1 ± 1.1	5.823 ± 0.021
MT1.8-520°C	122.5 ± 2.9	14.69 ± 0.35
MT1.8-535°C	105.0 ± 0.6	17.14 ± 0.09
MT1.8-550°C	82.6 ± 0.4	21.79 ± 0.11
MT1.8-600°C	84.7+- 0.5	21.26 +- 0.12

a) Values presented are the mean value ± standard error-of-the-mean

b) Voltage sweep rate values were linearly interpolated between nearest experimental values in the lin-log coordinate space of the b-value plots. Voltage sweep rate values are reported ± the bounding limits for error propagation based on Rolle's Theorem.

c) Sweep times were calculated as the voltage window divided by the voltage sweep rate. Sweep times reported ± the error propagated from the voltage sweep rate.

C.2 Derivation of Series-Model for Current Analysis

In the spirit of the popular parallel model for current analysis, the impedance of a surface-limited step (b = 1.0) and diffusion-limited step (b = 0.5) are related to v^b. The impedance of the surface-limited process such as a capacitor is:

$$Z_{surf} = -\frac{jk_1}{v} \tag{C.4}$$

where v is the voltage sweep rate, k_1 is a fit parameter, and j is $(-1)^{0.5}$. Similarly, the impedance of the diffusion-limited process is:

$$Z_{diff} = \frac{(1-j)k_2}{\sqrt{v}} \tag{C.5}$$

Where k_2 is a fit parameter. The impedance of a resistor (R) is:

$$Z_R = R \tag{C.6}$$

For series-circuits the total impedance is additive where here:

$$Z_{total} = Z_{surf} + Z_{diff} + Z_R = \left(\frac{k_2}{\sqrt{v}} + R\right) - j\left(\frac{k_1}{v} + \frac{k_2}{\sqrt{v}}\right) \tag{C.7}$$

The magnitude of this total impedance is:

$$|Z_{total}| = \sqrt{\left(\frac{k_2}{\sqrt{v}} + R\right)^2 + \left(\frac{k_1}{v} + \frac{k_2}{\sqrt{v}}\right)^2} \tag{C.8}$$

Thus, the current is modeled using the inverse of the magnitude of the impedance where the voltage dependency and phase angle are not explicitly addressed and are accommodated by the existing fit parameters (similar to the parallel model):

$$i = \frac{1}{\sqrt{\left(\frac{k_2}{\sqrt{v}} + R\right)^2 + \left(\frac{k_1}{v} + \frac{k_2}{\sqrt{v}}\right)^2}} \tag{C.9}$$

It is noted that an alternative and related expression can be found by re-arrangement of the terms of the parallel model while neglecting interactions within the complex plane:

$$i = \frac{1}{\frac{k_1}{v} + \frac{k_2}{\sqrt{v}} + R} \tag{C.10}$$

This equation also very closely matches the presented experimental current data and b-value trends.

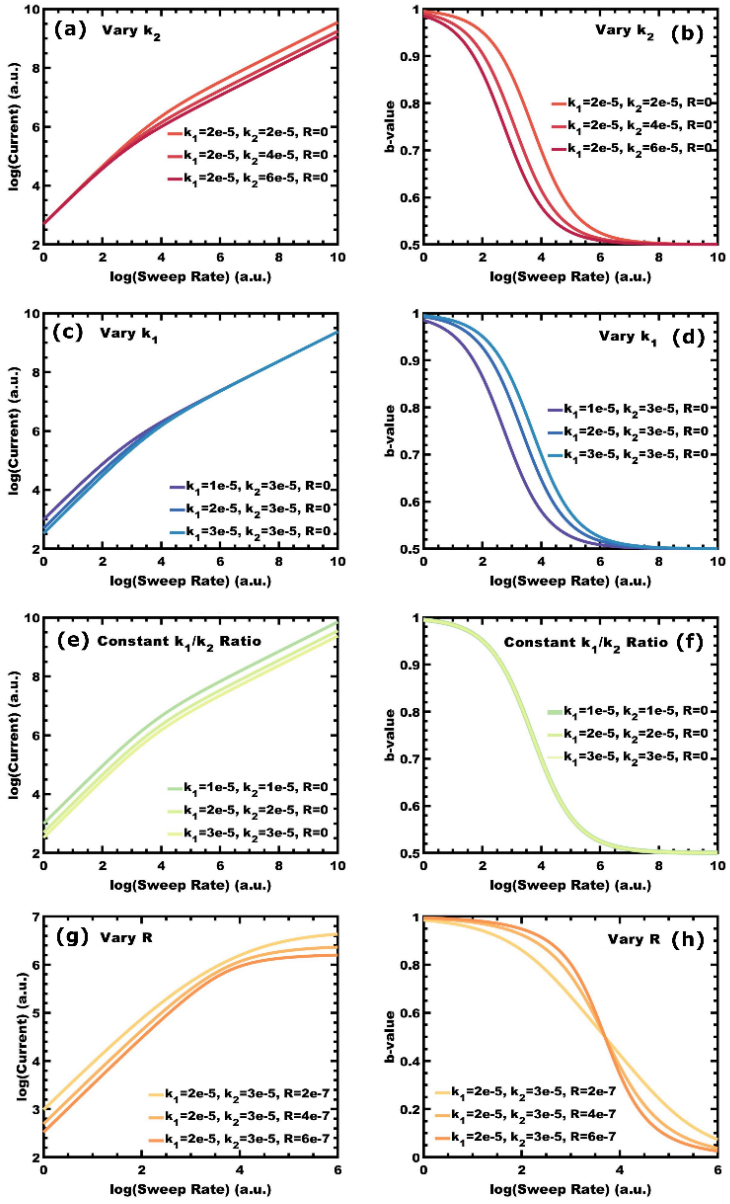

Figure C.8. The effects of series-model parameters upon the current (left) and the b-value trend (right) with varying (a,b) k_2, (c,d) k_1, (e,f) varying k_1 and k_2 with constant k_1/k_2 ratio, and (g,h) varying R.

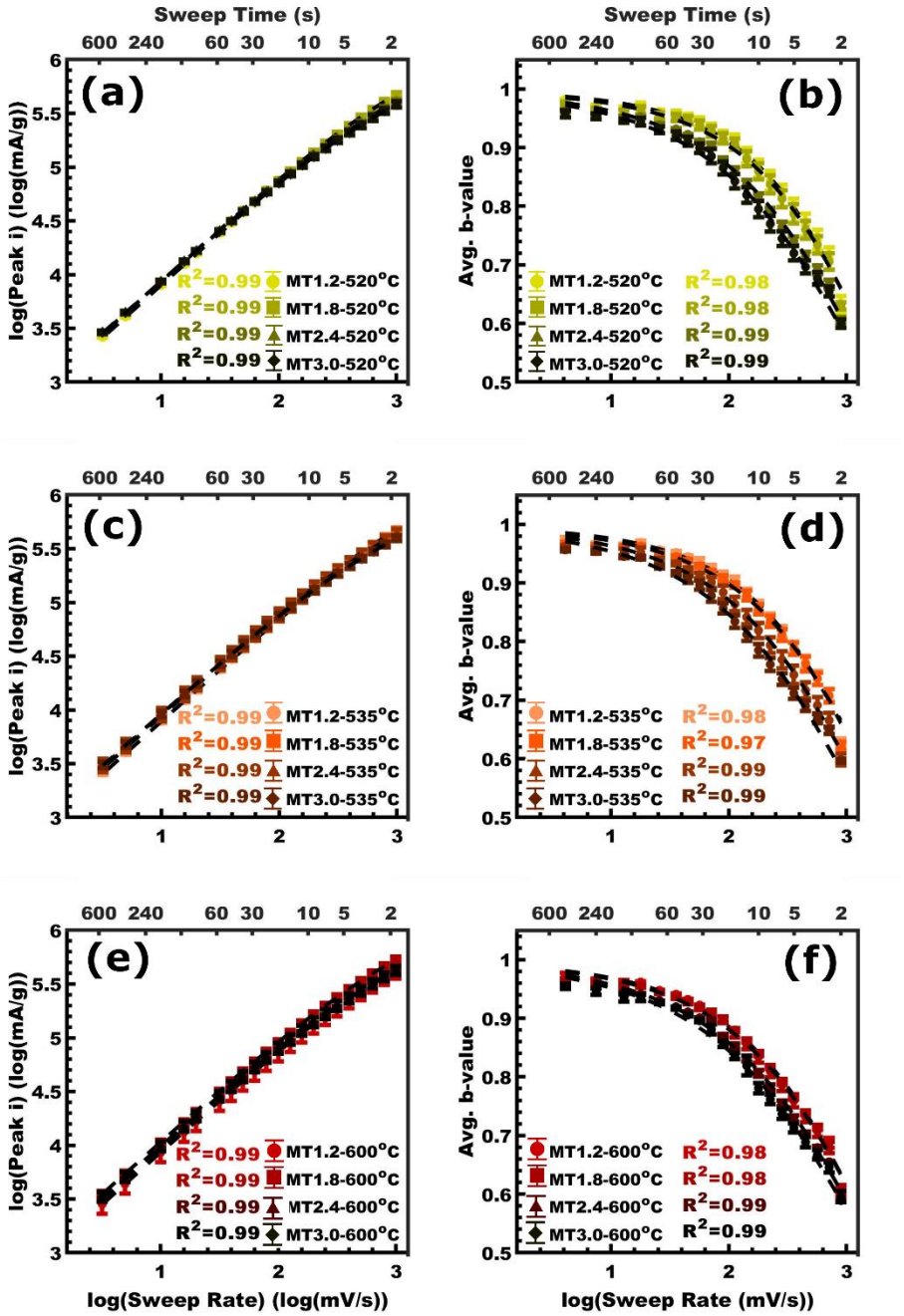

Figure C.9. The best-fits of the series model are shown for each sample series calcined at (a-b) 520 °C, (c-d) 535 °C, (e-f) 600 °C. The best-fits were performed with respect to peak current and the corresponding derivative of the best-fits are shown relative to the experimental b-values. Values are presented as mean ± standard error-of-the-mean.

C.3 Supporting Information References

[1] A. Sarkar, M. Stefik, J. Mater. Chem. A 2017, 5, 11840.

[2] K. A. Lantz, N. B. Clamp, W. van den Bergh, A. Sarkar, M. Stefik, *Small* 2019, *15*, 1900393.

[3] L. J. Fetters, D. J. Lohse, D. Richter, T. A. Witten, A. Zirkel, *Macromolecules* 1994, *27*, 4639.

[4] H. N. Lokupitiya, A. Jones, B. Reid, S. Guldin, M. Stefik, *Chem. Mater.* 2016, *28*, 1653.

[5] K. J. Griffith, A. C. Forse, J. M. Griffin, C. P. Grey, *J. Am. Chem. Soc.* 2016, *138*, 8888.

Appendix D: Supporting Information for Chapter 5

[1]van den Bergh, W.; Williams, E.; Vest, N.; Chiang, P.-H.; Stefik, M. *Langmuir*, 2021, 37(44), 12874–12886

D.1 Supporting Information for Chapter 5

Table D.1. Polymer synthesis conditions.

Polymer Name	Temp (°C)	Time (hr)	[Initiator] : [Cu(I)Br] : [PMDETA] : [Monomer]
PEO-*b*-PBA	70	12	1 : 0.5: 0.5 : 100
PEO-*b*-PS	110	6	1 : 1.125 : 1.125 : 200

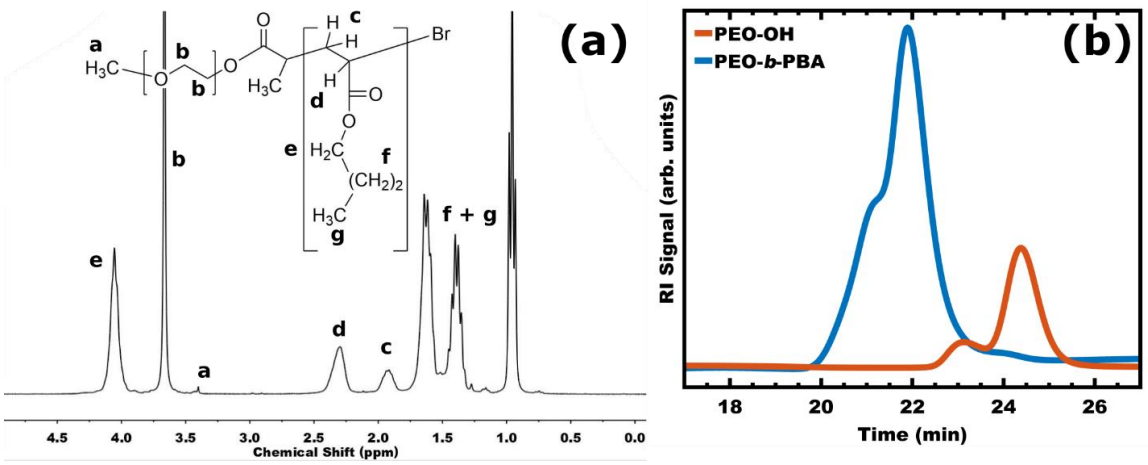

Figure D.1. ^{1}H-NMR (a) and GPC (b) analysis of PEO-*b*-PBA.

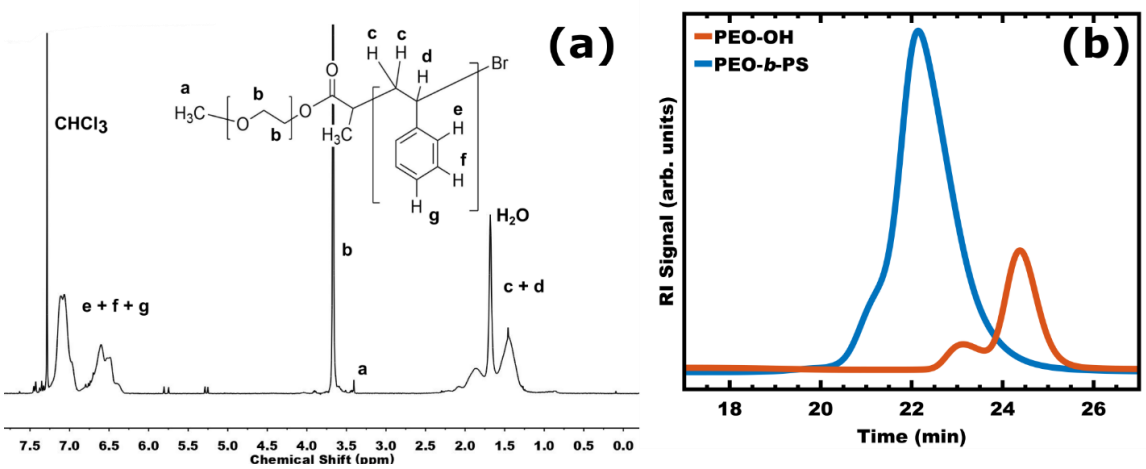

Figure D.2. ^{1}H-NMR (a) and GPC (b) analysis of PEO-*b*-PS.

Table D.2. Shows the molecular weight (M_n) and dispersity of the polymers used.

Polymer Name	M_n, Number average Molecular Weights (kg mol^{-1})	Molecular Mass Dispersity ($Đ$)
PEO-*b*-PBA	5.0 (PEO), 23.1 (PBA)	1.24
PEO-*b*-PS	5.0 (PEO), 17.2 (PS)	1.18

The "microparticle M:T" used in PMT model (*vide infra*) was fitted to SAXS data to account for material partitioning using an empirical formula:

$$x = (M:T)^C \quad \text{(D.1)}$$

Where (M:T) is the total mass ratio of material precursors to block polymer templates and x is the corresponding ratio that for only the material located within the microparticles, and C is a fit parameter.

A previously developed micelle core template (MCT) model[1] (termed here "PMT model") for disordered paracrystals was used to model d-spacing changes with the M:T ratio under constant micelle template size. The d-spacing was modeled using:

$$d_{spacing} = \frac{D}{2S}\sqrt[3]{\frac{3\gamma}{4\pi}}\left(x\beta_{mct} + 1 + \frac{f_{corona}}{1 - f_{corona}}\right)^{\frac{1}{3}} \quad \text{(D.2)}$$

where D is the template/pore diameter, γ accounts for unit cell distortion, x is the microparticle M:T ratio, f_{corona} is the volume fraction of the corona block (PEO), and β_{mct} is a convolved density term. Lastly S connects the structure factor peak to the SEM measured micelle-to-micelle spacing ($d_{m\text{-}m}$) using:

$$S = \frac{d_{m-m}}{d_{spacing}} = \frac{q d_{m-m}}{2\pi} \quad \text{(D.3)}$$

The wall thickness was deconvolved from the micelle-to-micelle distance using:

$$w = (\alpha d_{m-m} - D) \quad \text{(D.4)}$$

where w is the wall thickness, α is a fit term to accommodate the variable distribution of wall thickness for different orientations, and D is the pore diameter. For cubic crystal systems, alpha values are expected to range from 0.87-2.45 when measured using an inscribed circle.[2]

Table D.3. Density values of polymer blocks used to calculate the PEO volume fraction.

Polymer Block	Density [g cm^{-3}]
Poly(ethylene oxide)[3]	1.064
Poly(butyl acrylate)[4]	1.033
Poly(styrene)[3]	0.969

Table D.4. PMT model best-fit parameters for PEO-*b*-PS sample series determined using SEM and SAXS data.

α [a]	β [a]	PEO (vol%) [b]	S [c]	γ [a]	Pore Diameter (nm) [d]	C
1.08	6.28	20.9	1.07	1.0	13.6 ± 0.1	0.463

[a] determined by least squares fitting within PMT window

[b] determined by NMR analysis of block polymer composition and reported bulk density values

[c] S value was determined by comparing SEM and SAXS data

[d] Average of pore diameter measured by SEM

The β_{mct}=6.28 value found here was larger than the previous β_{mct}=4.66 value found for TiO_2 PMT thin films.[2] The β_{mct} term is a convolved density parameter that combines polymer densities with the material density at the time of structure rigidification:

$$\beta_{mct} = \frac{\rho_{core} + \frac{f_{corona}}{1 - f_{corona}} \rho_{corona}}{\rho_{material}} \quad \text{(D.5)}$$

The block polymer templates had similar PEO (corona) volume fraction (21.0%) and the polymer densities were largely similar. Thus this relative change in β_{mct} is likely associated

largely with material density at the point of rigidification. These β_{mct} values all correspond to lower than expected material densities and were attributed to the presence of residual solvent volume which is not separately accounted for, as previously noted.[5] Thus it is reasonable to expect thin film processing, which includes rapid removal of residual solvent and short solvent diffusion lengths, to result in more dense materials.

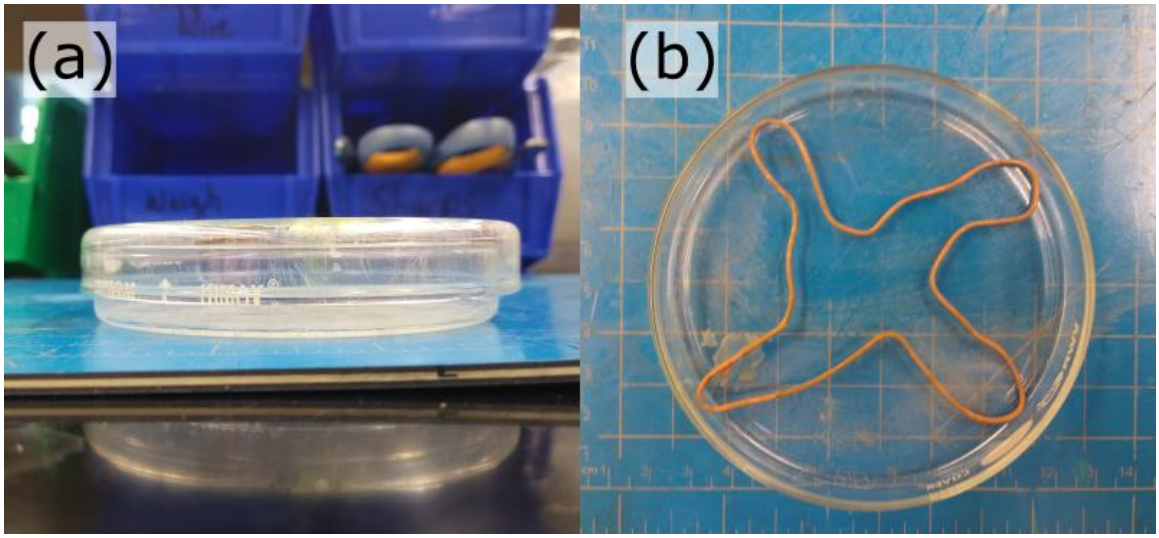

Figure D.3. Photos showing the glass casting dish with the cover (a) and the cover with a 16G wire spacer (b).

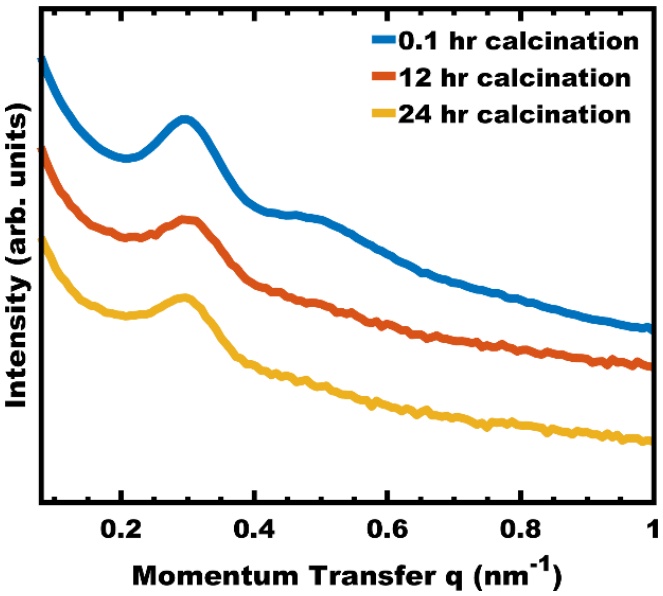

Figure D.4. SAXS data after different calcination times at 450 °C. The template was PEO-*b*-PBA with M:T=2.5.

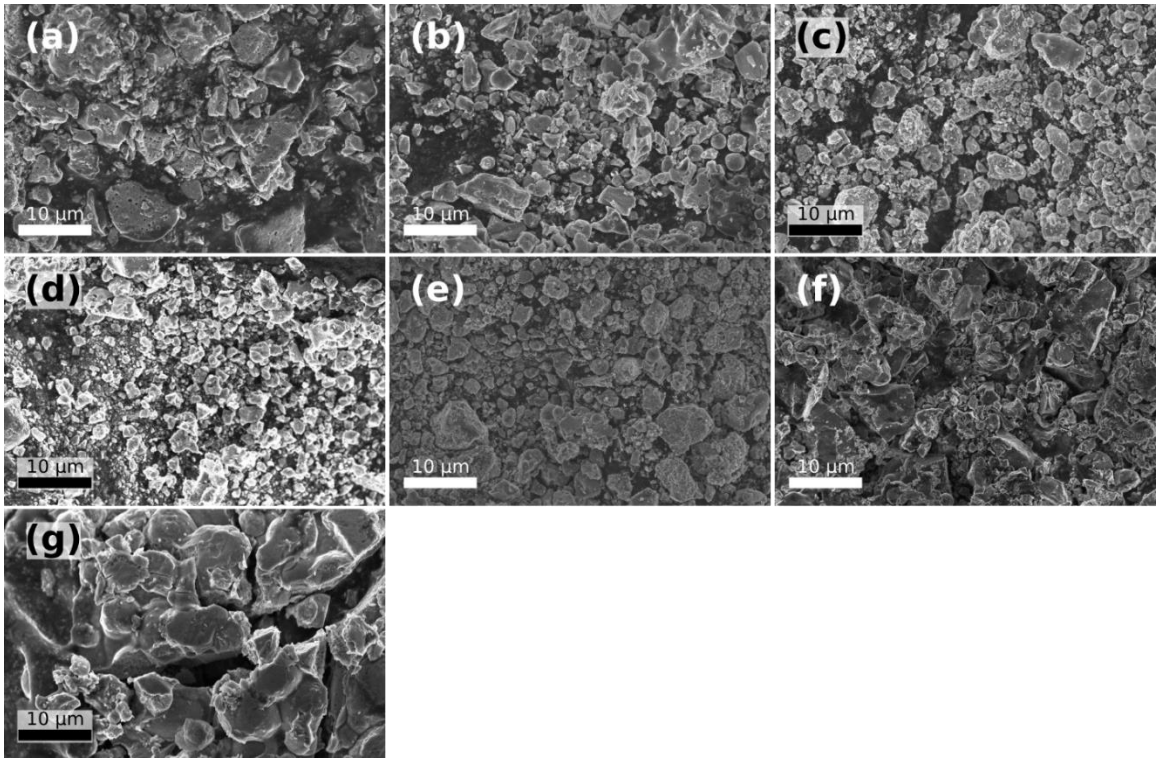

Figure D.5. SEM images of microparticles prepared with different PPO:Block Polymer mass ratios at (a) 2.5x, (b) 5.0x, (c) 7.5x, (d) 10x, (e) 15x, (f) 20x, (g) 40x, respectively. The template was PEO-*b*-PBA with M:T=2.5.

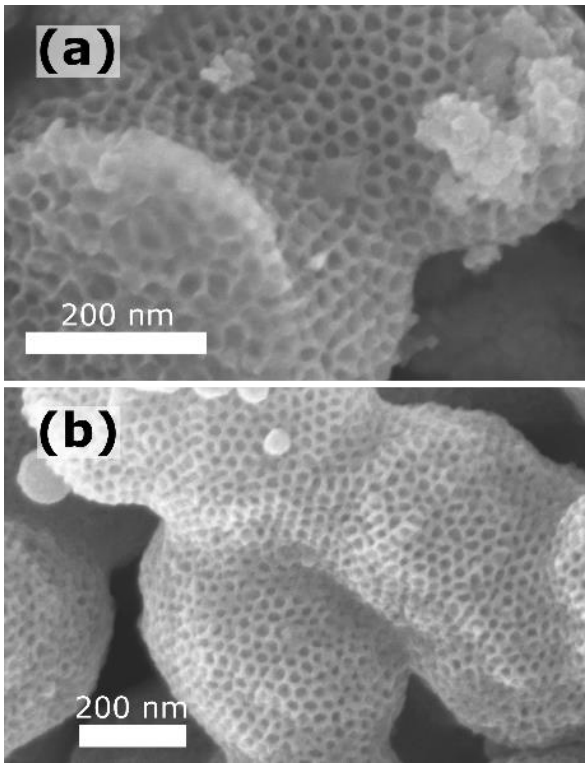

Figure D.6. SEM images of pore morphology cast with 20x PPO:Block Polymer at 5% wt% (a) and 10% wt% (b) water content, respectively. The template was PEO-*b*-PBA with M:T=2.5.

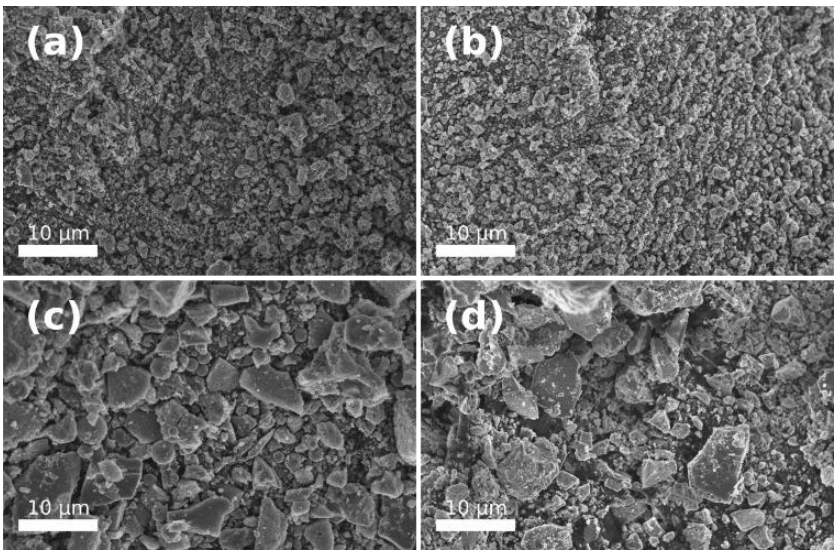

Figure D.7. SEM images of microparticles prepared using different wt% water cast in glass dishes: (a) 5% wt%, (b) 10% wt%, and (c) 15% wt%, (d) 20% wt%, respectively. The template was PEO-*b*-PBA with M:T=2.5.

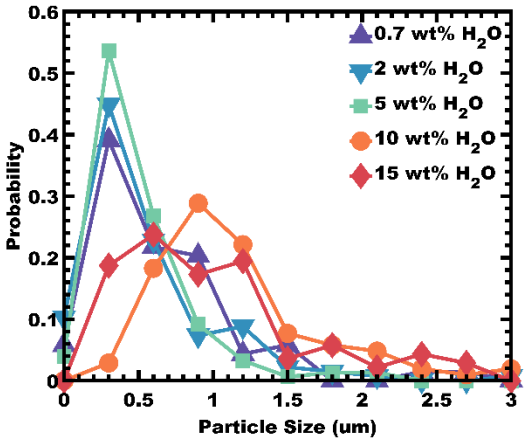

Figure D.8. Microparticle size distribution of different samples as a function of solution wt% water when cast in Teflon dishes. Template was PEO-*b*-PBA with M:T=2.5.

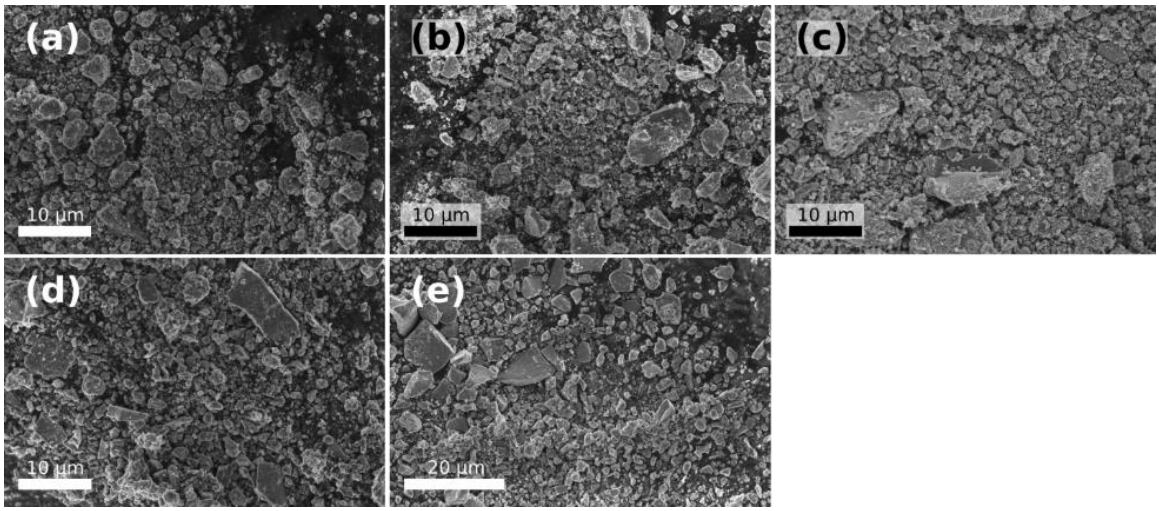

Figure D.9. SEM images of microparticles prepared using different wt% water cast in Teflon dishes: (a) 0.7% wt%, (b) 2% wt%, and (c) 5% wt%, (d) 10% wt%, (e) 15% wt%, respectively. The template was PEO-*b*-PBA with M:T=2.5.

Table D.5. Statistical measurements of average microparticle size in relation to water content of template solutions cast in Teflon dishes using PEO-*b*-PBA with M:T=2.5.

Water content (wt% of soln)	Average Particle Size (μm)*	Standard Deviation (μm)
0.7	0.79 ± 0.06	0.49
2.0	0.70 ± 0.05	0.53
5.0	0.63 ± 0.03	0.36
10.0	1.40 ± 0.08	0.85
15.0	1.21 ± 0.06	0.70

*Values are reported as an average ± standard-error-of-the-mean

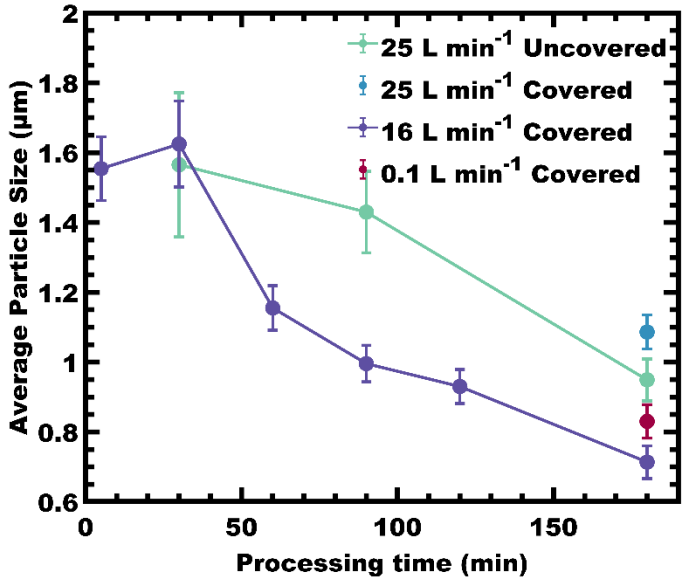

Figure D.10. Microparticle size as a function of processing time. Values are reported as the mean ± the standard-error-of-the-mean. The template was PEO-*b*-PBA with M:T=2.5.

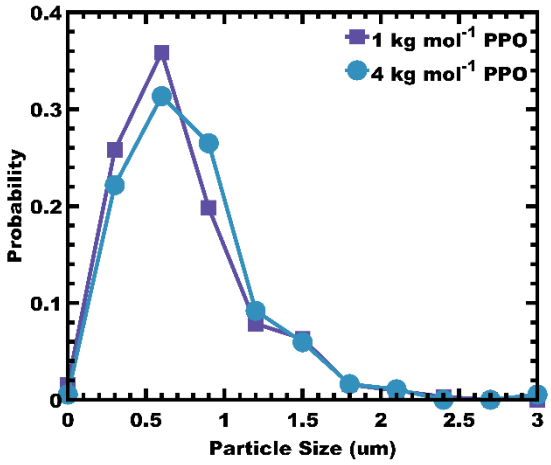

Figure D.11. Microparticle size distributions determined using measurements on SEM images as a function of PPO homopolymer molecular weight. The template was PEO-*b*-PBA with M:T=2.5.

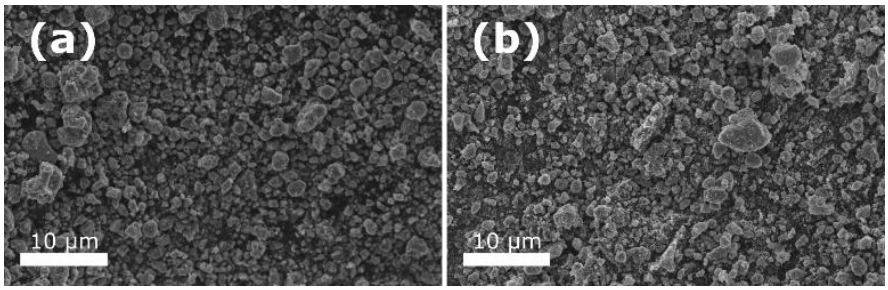

Figure D.12. SEM images of microparticles prepared using different PPO molecular weights: (a) 1 kg mol^{-1}, (b) 4 kg mol^{-1}. The template was PEO-*b*-PBA with M:T=2.5.

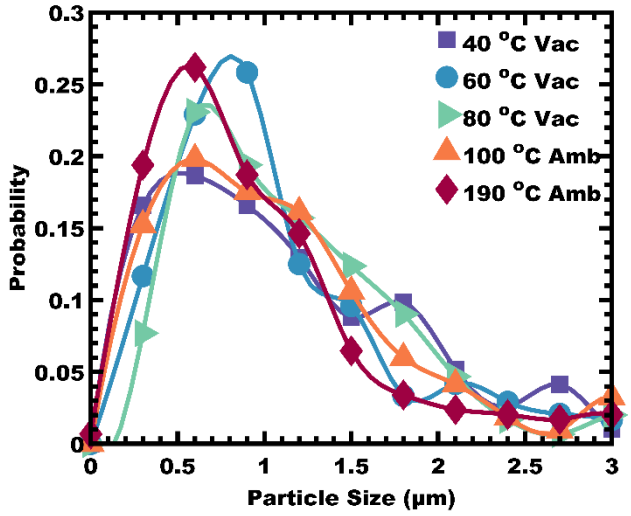

Figure D.13. Microparticle size distributions were determined using measurements on SEM images as a function of the material aging treatment. The template was PEO-*b*-PBA with M:T=2.5.

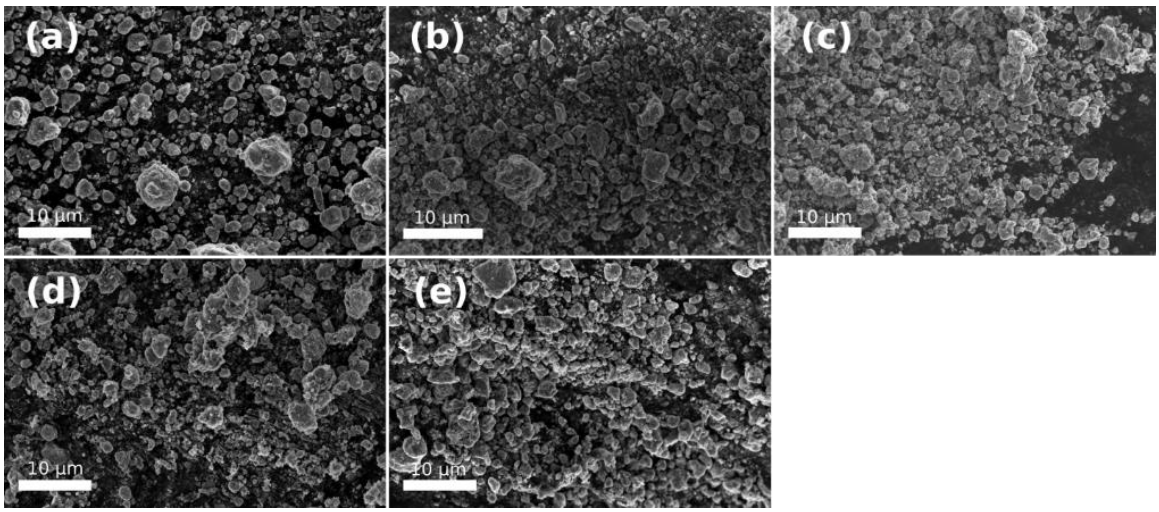

Figure D.14. SEM images of microparticles prepared using different aging conditions: (a) 40 ºC under vacuum, (b) 60 ºC under vacuum, and (c) 80 ºC under vacuum, (d) 100 ºC, (e) 190 ºC, respectively. The template was PEO-b-PBA with M:T=2.5.

Table D.6. Statistical measurements of average microparticle size as a function of aging treatment for PEO-*b*-PBA with M:T=2.5.

Aging Condition	Average Particle Size (μm)*	Standard Deviation (μm)
40 °C under Vacuum	1.40 ± 0.06	0.89
60 °C under Vacuum	1.34 ± 0.06	0.95
80 °C under vacuum	1.37 ± 0.05	0.80
100 °C	1.44 ± 0.08	1.23
190 °C	1.18 ± 0.05	0.80

*Values are reported as an average ± standard-error-of-the-mean

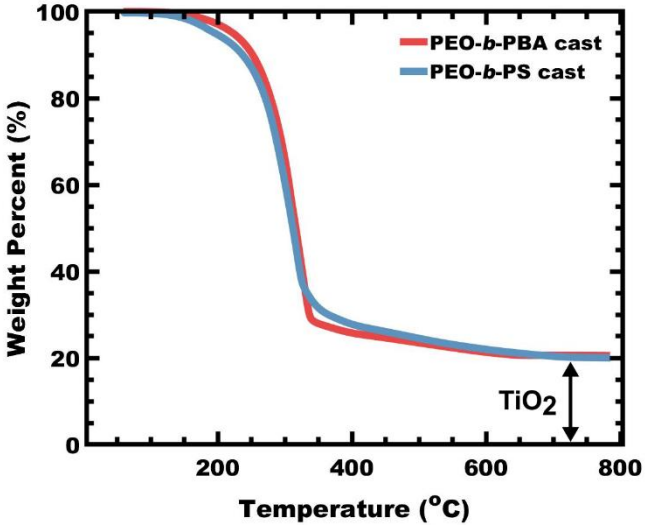

Figure D.15. TGA analysis of mesoporous TiO_2 microparticle prepared with different block polymers with M:T=2.5. TGA analysis commenced after the aging step at 80°C under vacuum.

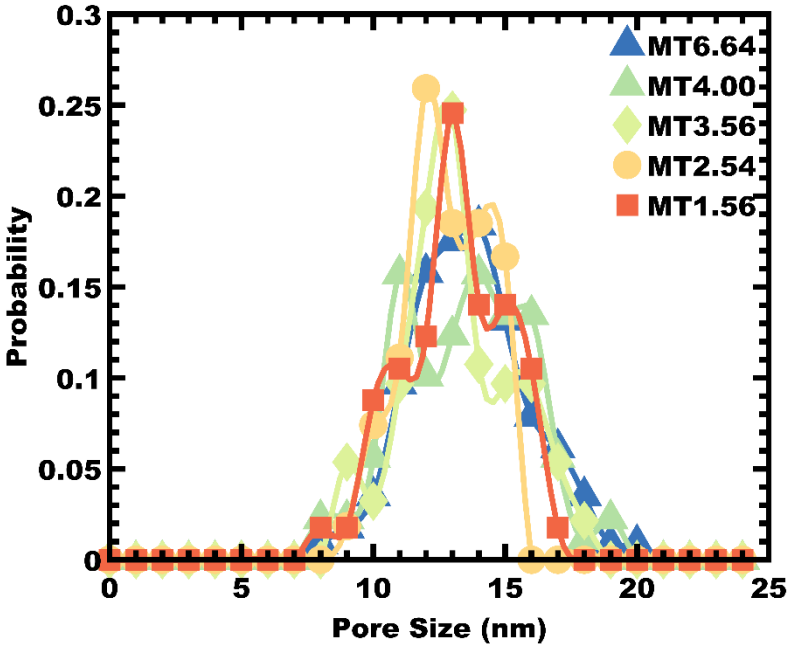

Figure D.16. Pore size distribution determined from SEM measurements of PEO-*b*-PS samples with various M:T values.

D.2 Supporting Information References

[1] Sarkar, A. & Stefik, M. *J. Mater. Chem. A* **5**, 11840–11853 (2017).

[2] Lantz, K. A., Clamp, N. B., Bergh, W. van den, Sarkar, A. & Stefik, M. *Small* **15**, 1900393 (2019).

[3] Fetters, L. J., Lohse, D. J., Richter, D., Witten, T. A. & Zirkel, A. *Macromolecules* **27**, 4639–4647 (1994).

[4] Barudio, I., Févotte, G. & McKenna, T. F. *European Polymer Journal* **35**, 775–780 (1999).

[5] Sarkar, A., Evans, L. & Stefik, M. *Langmuir* **34**, 5738–5749 (2018).